Universidade do Porto

FEUP Faculdade de Engenharia

The Radial Point Interpolation Meshless Method Extended to Axisymmetric Plates and Non-linear Continuum Damage Mechanics

by

Behzad Vasheghani Farahani

Thesis submitted to

Faculty of Engineering, University of Porto

as a requirement to obtain the Master`s degree in Computational Mechanics

under the supervision of

Professor Jorge Américo Oliveira Pinto Belinha

and

Professor Francisco Manuel Andrade Pires

University of Porto

July 2015

The Radial Point Interpolation Meshless Method Extended to Axisymmetric Plates and Non-linear Continuum Damage Mechanics

by

Behzad Vasheghani Farahani

Thesis submitted to

Faculty of Engineering, University of Porto

as a requirement to obtain the Master`s degree in Computational Mechanics

under the supervision of

Professor Jorge Américo Oliveira Pinto Belinha

Faculty of Engineering, University of Porto

and

Professor Francisco Manuel Andrade Pires

Faculty of Engineering, University of Porto

University of Porto

July 2015

Preface

An enormous number of challenges, thrown out by rapid development in science and technology, have made me choose engineering profession. I take this opportunity to increase my educational background and career objectives that motivated me to pursue a research career in *Mechanical Engineering*. I completed my Bachelor`s degree in Mechanical Engineering. My graduate education has provided a thorough exposure to the various specialties available in *Computational Mechanics*, thus stimulating interests in advanced research.

To be able to achieve my goals it is likely that the engineer will need to consider the recent academic criterion. Currently, analysis involves computer simulation of the structural behavior with non-linear characteristics, because of the availability and development of the commercial computer software.

The *Meshless Method* has been chosen as the fundamental part of my current R&D interest due to its unique nature and potential applications in *Computational Mechanics*. On the other hand, since the state-of-art lacks a detailed study on RPIM meshless method combined with the axisymmetric deformation theory and continuum damage mechanics, it motivated me to put my focus on this field in order to conduct my Master`s research.

However, the current work has been structured as my **Master`s Thesis** in *Computational Mechanics* course, providing great opportunities for my future work either in the academic word or the industrial areas.

It attempts to describe all the aspects in the simplest way to be easily understandable by other students and researchers who are enthusiastic in meshless method and continuum damage mechanics.

Behzad Vasheghani Farahani

July 2015 Porto, Portugal

Abstract

In this work an advanced discretization meshless technique, the radial point interpolation method (RPIM), is extended to the elasto-static analysis of circular plates using the 2D axisymmetric deformation theory. Both concepts are revised and more adequate parameters are found for the 2D axisymmetric RPIM approach. Here, several benchmark circular plate examples are solved and the results are compared with finite element solutions and analytical solutions, showing that RPIM is capable to obtain accurate and smooth variable fields.

In addition, RPIM is applied to analyse concrete structures using an elastic rate-independent continuum damage constitutive model. Here, the theoretical basis of the material model and the computational procedure are fully presented. The plane stress meshless formulation is extended to a rate-independent damage criteria where both compressive and tensile damage evolution are established based on a Helmholtz free energy function. Within the return-mapping damage algorithm, the required variable fields, such as the damage variables, localized damage parameters and the displacement field, are obtained. This study uses the Newton-Raphson non-linear solution algorithm to achieve the non-linear damage solution. The verification, where the performance is assessed, of the proposed non-local and localized models is demonstrated by relevant numerical examples available in the literature.

Keywords. Radial Point Interpolation Method, Finite Element Method, Axisymmetric Plates, Rate-independent Continuum Damage Mechanics, Non-local Damage, Localized Damage, Linear Elastic Fracture Mechanics.

Acknowledgments

I would like to express profound gratitude to my supervisors ***Professor Jorge Belinha*** and ***Professor Francisco Pires*** for their invaluable support, encouragement, great supervision and useful recommendations throughout this Master's thesis. Their great aegis and continuous guidance enabled me to complete my work successfully.

I sincerely thank to ***Professor José César de Sá***, senior scientist, (the chairman of Computational Mechanics course in Faculty of Engineering, University of Porto) who has organized this Master`s course effectively.

I acknowledge with thanks the kind of patience, love and patronage that I received from my lovely future wife ***Parisa***.

Lastly, I cannot ever express my appreciation to my parents and brothers for their moral, economical and heartfelt support throughout my M.Sc. Course and most importantly what they have been doing for the past years of my life. I hope that I will pay up their favors in the near future as they really deserve.

Behzad Vasheghani Farahani

Table of Contents

Nomenclature

Abbreviations

FEM	*Finite Element Method*
RPIM	*Radial Point Interpolation Method*
XFEM	*Extended Finite Element Method*
PIM	*Point Interpolation Method*
SSSS	*Simply Supported*
CCCC	*Clamped*
CPL	*Circular Punctual Load*
UDL	*Uniform Distributed Load*
MQRBF	*Multiquadrics Radial Basis Function*
LEDM	*Linear Elastic Damage Mechanics*
LEFM	*Linear Elastic Fracture Mechanics*
RBF	*Radial Basis Function*
EFGM	*Element-free Galerkin Method*

Operators and mathematical symbols

$\|\|.\|\|$	*Euclidean norm*
$\otimes$	*Dyadic product*
$:$	*Tensor Multiplication*
$\langle . \rangle$	*Macaulay bracket*
$tr(.)$	*Trace of a set matrix*
∂	*Partial derivatives*
$\mathbb{N}$	*Natural numbers*
$\mathbb{R}$	*Real numbers set*
ξ	*Generic variable*
$x\ y\ z$	*Cartesian direction*
$i\ j\ k$	*Referent to the standard basis vectors in Cartesian coordination*
$r\ z\ \theta$	*Cylindrical direction*

Geometric parameters

L	*Length*
D	*Width*
e	*Thickness*

R	*Radius of circular plate*
H	*Thickness of circular plate*
r	*Distance between node and center of circular plate*
b	*Radius*
a_0	*Initial crack length*
a	*Equivalent crack length*
λ	*Irregularity parameter*
l_{ch}	*Characteristic length*
h	*Average distance between nodes*
ΔA	*Area of the element*
ΔV	*Volume of the element*
RGP	*Radius of the Gauss points circle*
g	*Vertical dimension of the hole*
A	*Deflection*
q	*Hole mouth opening*

Stress and strain components

$\bar{\tau}^+, \bar{\tau}^-$	*Effective norm in tension, compression*
$\overline{\boldsymbol{\sigma}}^+, \overline{\boldsymbol{\sigma}}^-$	*Effective stress in tension, compression*
r^+, r^-	*Damage threshold in tension, compression*
r_0^+, r_0^-	*Initial tensile , compressive threshold*
ε_0^+	*Maximum uniaxial tensile strain*
ε_0^-	*Maximum uniaxial compressive strain*
$\tilde{\bar{\sigma}}$	*Equivalent von Mises effective stress*
$\tilde{\sigma}$	*Equivalent von Mises stress*
$\tilde{\varepsilon}$	*Equivalent von Mises strain*
σ_{oct}	*Normal octahedral stress*
τ_{oct}	*Shear octahedral stress*
$\sigma_{xx}, \sigma_{yy}, \sigma_{zz}$	*Normal stress components in Cartesian coordinate system*
$\tau_{xy}, \tau_{zx}, \tau_{zy}$	*Shear stress components in Cartesian coordinate system*
$\varepsilon_{xx}, \varepsilon_{yy}, \varepsilon_{zz}$	*Normal strain components in Cartesian coordinate system*
$\gamma_{xy}, \gamma_{zx}, \gamma_{zy}$	*Shear strain components in Cartesian coordinate system*
$\sigma_{rr}, \sigma_{zz}, \sigma_{\theta\theta}$	*Normal stress components in cylindrical coordinate system*
$\tau_{rz}, \tau_{z\theta}, \tau_{r\theta}$	*Shear stress components in cylindrical coordinate system*
$\varepsilon_{rr}, \varepsilon_{zz}, \varepsilon_{\theta\theta}$	*Normal strain components in cylindrical coordinate system*
$\gamma_{rz}, \gamma_{z\theta}, \gamma_{r\theta}$	*Shear strain components in cylindrical coordinate system*
I	*Stress invariants*
f_c'	*Compressive strength*

Solid Mechanics

$\boldsymbol{C}$	*Second order constitutive matrix*
$\boldsymbol{\sigma}$	*Cauchy stress tensor*
$\boldsymbol{\varepsilon}$	*Strain tensor*
$\boldsymbol{K}$	*Stiffness matrix*
$\boldsymbol{u}$	*Displacement vector*
$\boldsymbol{B}$	*Deformation matrix*
$\boldsymbol{L}$	*Differentiation matrix*
$\boldsymbol{b}$	*Body force vector*
$\boldsymbol{t}$	*External traction force vector*
$\boldsymbol{f_b}, \boldsymbol{f_t}, \boldsymbol{f_q}$	*Force vectors*
$\boldsymbol{S_t}$	*External force vector*
L	*Lagrangian functional*
T	*Kinetic energy*
U	*Strain energy*
$\boldsymbol{W_f}$	*Work done by external force*
u	*Enforced Displacement*
$\bar{u}$	*Normalized displacement*
$\hat{\boldsymbol{n}}$	*Principal directions*
$\boldsymbol{N}$	*Principal vector*
$\boldsymbol{T_{oct}}$	*Octahedral vector*

Meshless characteristics

n	*Number of nodes*
$\boldsymbol{n_Q}$	*Number of integration (Gauss) points*
T	*Function space*
$\boldsymbol{\Omega}$	*Problem domain*
$\boldsymbol{u^h(x)}$	*Shape functions*
$\boldsymbol{x_I}$	*Interest point*
$\boldsymbol{N_I}$	*Vector of nodes inside influence domain*
$\boldsymbol{\Omega_I}$	*Influence domain*
$\boldsymbol{X}$	*Nadal set vector*
h	*Density of the nodal set*
$\boldsymbol{r(x)}$	*Radial basis function*
$\boldsymbol{p(x)}$	*Polynomial basis function*
$\boldsymbol{a_i}$	*Non-constant coefficient for radial basis*
$\boldsymbol{b_i}$	*Non-constant coefficient for polynomial basis*
$\boldsymbol{a^T}, \boldsymbol{r(x)^T}$	*Vectors of radial basis function*
$\boldsymbol{b^T}, \boldsymbol{p(x)^T}$	*Vectors of polynomial basis function*
$\boldsymbol{d_{iI}}$	*Distance between interest point and nodes*
$\boldsymbol{c}, \boldsymbol{p}$	*MQRBF shape parameter*
$\boldsymbol{G}$	*Moment matrix*
$\boldsymbol{Z}$	*Null matrix*
$\boldsymbol{z}$	*Null vector*

$\boldsymbol{R}$	*Radial moment matrix*
$\boldsymbol{P}$	*Polynomial moment matrix*
$\boldsymbol{\Phi}$	*Interpolation function vector*
$\boldsymbol{\Psi}$	*Residual vector*
$\boldsymbol{r}(\boldsymbol{x_I})$	*MQ-RBF vector*
$\boldsymbol{gp}$	*Gauss point vector*
N_{gp}	*Total number of Gauss points*
W_{gp}	*Weight of Gauss points*

Material property

E	*Young`s Modulus*
ν	*Poisson's ratio*
G_t	*Fracture energy per unit area*
f_0^+	*Maximum uniaxial tensile strength*
f_0^-	*Maximum uniaxial compressive strength*
G_f^+	*Tensile fracture energy*
G_f^-	*Compressive fracture energy*
β	*Compressive material property*
K	*Compressive material property*
$\bar{H}^+$	*Tensile Material property*

Damage Property

g^+, g^-	*Damage criteria in tension, compression*
d^-	*Non-local compressive damage*
d^+	*Non-local tensile damage*
d	*Total damage*
A^+	*Tensile coefficient*
A^-, B^-	*Compressive coefficients*
G^+, G^-	*Monotonic increasing function in tension, compression*
ψ_0	*Free elastic energy*
ψ_0^+, ψ_0^-	*Free elastic energy in tension, compression*
$d^-_{localized}$	*Localized compressive damage*
$d^+_{localized}$	*Localized tensile damage*
$w^{\pm}_{total}$	*Total weight of integration points*
$w^{\pm}_{d}$	*Weighted Damage parameter*
n_p	*Localized damage parameter*

List of Figures

List of Tables

List of Boxes

Chapter 1

1 Introduction

Currently, the industrial structural design relies mainly on the finite element method (FEM) (O. C. Zienkiewicz and R. L. Taylor, 1994) analysis to obtain efficiently accurate solutions. This status quo can be explained with the vast number of commercial FEM software packages available in the market and with the robustness and reliability of the FEM. However, this fact cannot hide some of the FEM drawbacks, such as the dependency on the element mesh discretization (due to the mesh-based interpolation) or the reduced continuity of its shape functions.

Several industrial components, such as pressure vessels, turbo-alternator group and circular plate and shell structures, are frequently designed considering an axisymmetric configuration, i.e. the three-dimensional solid is obtained with the rotation of a two-dimensional cross section around an axis of symmetry. Additionally, all the mentioned industrial components are commonly subjected to axisymmetric loads during operation.

Thus, since axial symmetry can be found in the solid geometry and in its boundary conditions, instead of using a full three-dimensional deformation theory, generally the structural analysis of those components is performed using a two-dimensional simplification – the axisymmetric deformation theory – which permits to reduce the computational cost of the analysis.

In addition, numerous challenging fields in computational mechanics involve the study of the numerical non-linear damage solution of concrete materials using finite element method (FEM) formulations (Voyiadjis & Taqieddin, 2009)(R. Faria, Oliver, & Cervera, 1998)(Cervera, Oliver, & Faria, 1995; Cervera, Oliver, & Manzoli, 1996; He, Wu, Liew,

& Wu, 2006; Lee & Fenves, 2001; Oliver, Cervera, Oller, & Lubliner, 1990; Yu, Ruiz, & Chaves, 2008). Distinct aspects of the continuum damage mechanics field have been investigated by researchers to obtain the experimental solution (Tao & Phillips, 2005)(J. Y. Wu, Li, & Faria, 2006).

The first works combining the FEM and the axisymmetric formulation were published back in the 1970's (Klie, Lung, & Mahrenholtz, 1974); (Pedersen & Megahed, 1975); (Hinton, 1976) . Then, other FEM formulations were suggested to solve efficiently the axisymmetric problems, such as the nonconforming element method and the hybrid element method (Wanji & Cheung, 1996), which were able to obtain respectively nonconforming variable fields.

The axisymmetric formulation possesses a well-known singularity, which occurs when the element or its nodes are near to the revolution axis. Thus, in order to increase the accuracy of the element stiffness matrix when a discretization entity (node or element) is close to the symmetry axis, or coincident with it, Clayton and Rencis (Clayton & Rencis, 2000) proposed two numerical integration schemes based on cubic transformations and high-order Gauss quadrature schemes. Even nowadays the scientific community devotes some effort into the numerical improvement of classic finite element formulations in order to enhance the FEM behaviour in the axisymmetric formulation, such as the work of Sze and Wu (Sze & Wu, 2011) on several transition element families or the research developed by Puccio and Celi (Di Puccio & Celi, 2012) regarding the comparison between the several versions of the quadrilateral element available in the commercial FE software.

Indeed, several demanding non-linear solid mechanics problems were analysed with the axisymmetric formulation, such as elastoplasticity (Klie et al., 1974), the dynamic transient analysis of circular plates (Hinton, 1976) and, more recently, the large strain analysis considering elastoplastic materials (Castelló & Flores, 2008) and hyperelastic materials (G. H. Liu & Sze, 2010).

Generally, in damage models, the degradation of the constitutive model under tensile and compressive enforced displacement states include various principal stress terms (Lee & Fenves, 2001).

The return-mapping algorithm permits to obtain the non-linear damage solution (Lee & Fenves, 2001). The most inconvenient feature of this approach is the repetitive calculations of principal terms in a pseudo-time stepping scheme, which appears due to the usage of the general stress tensor (J. Simo & Taylor, 1986).

However, the most recent approach of the return-mapping stage relies on the decomposition of the trial stress, which leads to the separation of the return-mapping algorithm proposed by Simo (J.C. Simo, 1992). This study focuses on the enhancement of a return-mapping algorithm for a rate-independent elastic damage model to simulate concrete materials, adapted to the unique characteristics of the meshless method here considered.

Alternatively to the FEM, advanced methods of discretization (commonly known as meshless techniques) have been developed since the middle 1990`s (J. Belinha, 2014) (V. P. Nguyen, Rabczuk, Bordas, & Duflot, 2008). The field functions are determined through an approximation within an adaptable influence domain surrounding an interest point (generally an integration point), instead a fixed element. Hence, the nodes have the potential to discretize the problem domain in a random distribution. A detailed description of the advantages of meshless method techniques compared to FEM can be found in the literature (Liew, Zhao, & Ferreira, 2011) (J. Belinha, 2014) (Belinha, Dinis, & Natal Jorge, 2013b).

Meshless methods are capable to analyse complex structural models; the high-order continuity of the constructed test functions permits to achieve smoother internal variables, such as the strain/stress fields; can be efficiently used to solve large deformation problems and; permit to insert locally more nodes where the mesh refinement is required, without any extra computational cost (J. Belinha, 2014).

Generally, the system of equations is developed from the strong or weak formations. The majority of meshless methods adopt the weak formulations, particularly the Galerkin weak

form as in FEM. Commonly, meshless methods using the weak formulation are classified in two categories: meshless methods using approximation functions to produce the shape functions (Nayroles, Touzot, & Villon, 1992) (Belytschko, Lu, & Gu, 1994) (W. K. Liu, Jun, & Zhang, 1995) (Randles & Libersky, 1996) (Atluri & Zhu, 1998) and; meshless methods that construct the shape functions using interpolation functions (Oñate, Idelsohn, Zienkiewicz, & Taylor, 1996) (Wang, Liu, & Wu, 2001)(Liew et al., 2011)(Belinha, Dinis, & Natal Jorge, 2013b) (G. R. Liu, 2001)(Wang & Liu, 2002a) (Wang & Liu, 2002b) (Idelsohn & Pin, 2003) (Belinha, Dinis, & Natal Jorge, 2013b).

Although approximate meshless methods have been successfully applied in computational mechanics, there were several problems not completely solved. One of those problems, and perhaps the most important unsolved issue, was the lack of the Kronecker delta property on the approximation functions, which increases the computational complexity on the imposition of essential and natural boundary conditions (J. Belinha, 2014).

This work uses the radial point interpolation method (RPIM) (Wang & Liu, 2002a, 2002b) to analyse circular plates using the axisymmetric formulation. Besides, RPIM is extended to a rate-independent damage constitutive model for concrete structures (Cervera et al., 1996) (Voyiadjis & Taqieddin, 2009) (Malvar & Warren, 1988). Here, the damage process is controlled by the elastic strain term.

The RPIM started with the Point Interpolation Method (PIM) (G. R. Liu & Gu, 2001), which involve the construction of polynomial interpolants based only on a group of arbitrarily distributed points. Later, the PIM evolved and the RPIM (Wang & Liu, 2002a) was fully developed. The main difference between the PIM and the RPIM is the inclusion of a Radial Basis Function (RBF) to obtain the interpolation function, which permits to stabilize the construction procedure. The RPIM's first works concluded that the multiquadric RBF is the most efficient RBF for the RPIM formulation (Wang & Liu, 2002a, 2002b). The RBF was firstly applied to solve partial differential equations in the work of Kansa (Kansa, 1990a, 1990b). However the RPIM uses, unlike Kansa's algorithm, the concept of "influence-domain" instead of "global-domain", which permits to generate sparse and banded stiffness matrices, more adequate to complex geometry problems

Presently, it is possible to find in the literature several versions of the original RPIM, such as the Natural Neighbour RPIM (L.M.J.S. Dinis, Jorge, & Belinha, 2007; L. M J S Dinis, Jorge, & Belinha, 2010; L. M. J. S. Dinis, Natal Jorge, & Belinha, 2011;), the nodal integration RPIM (G. R. Liu et al., 2007), the linearly conforming RPIM (Zhao et al., 2008, 2009), the cell-based smoothed RPIM (G. R. Liu, Jiang, Chen, Zhang, & Zhang, 2011) and the Natural Radial Element Method (Belinha, Dinis, & Jorge, 2013; Belinha, Dinis, & Natal Jorge, 2013a, 2013b).

Several works are available using the RPIM (G. R. Liu, 2009), however the state-of-art lacks a detailed study on the RPIM combined with the axisymmetric deformation theory. Other meshless methods were extended to this topic with success. Raju and Chen (I S Raju & Chen, 2003; I.S. Raju & Chen, 2001) extended the Meshless Local Petrov-Galerkin Method (MLPG) to the elasto-static analysis of axisymmetric structures and Ferronato et al (Ferronato, Mazzia, Pini, & Gambolati, 2007) applied the MLPG to the analysis of poro-elastic materials. More recently, Sladek (Sladek, Sladek, & Zhang, 2008), assuming the local integral equations, compared the performance of three numerical approaches in the analysis of the two-dimensional axisymmetric problems: the FEM, the PIM and the element-free Galerkin method (EFGM). Regarding the EFGM, Hayati (Hayati, Ahmadi, & Sadrnejad, 2012) presented in 2012 a short communication on the topic.

It is possible to find some experimental tests reporting the behaviour of concrete materials, such as softening response of concrete under monotonic uniaxial tension test (Gopalaratnam & Shah, 1985), the behaviour of concrete under compressive enforced displacement (Karsan & Jirsan, 1969), the response of concrete under biaxial stress states (Kupfer, Hilsdorf, & Rusch, 1969) and the three point bending tests on single-edge notched beams (Malvar & Warren, 1988).

Various demanding isotropic non-linear damage models for concrete structures were analysed with the FEM formulations, such as linear elastic models (Khan, Al-Gadhib, & Baluch, 2007) (Mazars & Pijaudier-Cabot, 1989) (Tao & Phillips, 2005) (Willam, Rhee, & Beylkin, 2001) (Comi & Perego, 2001) (Labadi & Hannachi, 2005), rate-dependent models (Cervera et al., 1996) (Cervera et al., 1995), viscous-damage models (R. Faria et al., 1998)

and, more recently, elasto-plastic damage models for crack propagation using Extended Finite Element Method(XFEM) formulations (Roth, Léger, & Soulaïmani, 2015).

However the state-of-the-art lacks a study on meshless methods combined with a non-linear damage constitutive model.

Thus, this work aims to fulfil a gap in the RPIM state-of-art, presenting an extensive and complete numerical study of the RPIM regarding the analysis of axisymmetric plate structures and continuum damage mechanics theory. All the important features of the RPIM are addressed and verified for the two-dimensional axisymmetric approach and rate-independent elastic damage model: the size of the influence-domain; the optimal integration scheme; the tolerance to the irregularity of the mesh; the convergence trend; the global efficiency; the internal fields and damage variables.

1.1 Thesis Organization

To facilitate the comprehension, it is outlined how this thesis is structured.

Chapter 2: Meshless Method

The Radial Point Interpolation Method (RPIM) numerical characteristics are presented, such as the integration scheme, the nodal connectivity, radial point interpolators and others.

Chapter 3: Solid Mechanics

The elastic plane stress formulations according to the variational fields are introduced. Furthermore, the corresponding solid mechanics theory is defined for the RPIM technique in both 2D plane stress and axisymmetric discrete systems. Besides the principal stress and directions are reviewed due to their importance in the damage mechanics. The Equivalent von Mises criteria is also presented in addition to the octahedral shear and normal stresses.

Chapter 4: Rate-independent Elastic damage Formulations

The rate-independent elastic damage formulations based on a Helmholtz free energy function connected to the damage energy release are represented. Moreover, the non-linear return-mapping stage of the numerical implementation is also introduced here. Subsequently the former formalism is extended to the localized damage theory which will be implemented after.

Chapter 5: Numerical Applications on Axisymmetric Plates

Several distinct benchmarks for axisymmetric plates are solved. A series of convergence studies is figured out to evaluate the performance of RPIM formulations extended with the axisymmetric deformation theory.

Chapter 6: Validation of the Proposed Nonlocal Damage Model

Concrete structures are studied in the scope of various monotonic tests and particularly three point bending beam test. They are solved with the proposed numerical approach in non-local damage criteria. The results are compared to the experimental and finite element solutions available in the literature.

Chapter 7: Numerical Benchmarks on the Localized Damage Formalism

This chapter is devoted to the applications of localized damage mechanics with regard to the rate-independent elastic damage theory. Two distinct relevant examples are studied here; three point bending beam and compact tension tests. In the former one, several optimization studies are done in order to obtain the optimum localized damage parameters. Subsequently, these values are applicable for the second benchmark and the obtained results are verified with the experimental solution.

Chapter 8: Discussion and Conclusion

Consequently, the final remarks and conclusions are emphasized.

1.2 Related Publications

The research conducted on the scope of this thesis permitted to publish scientific contributions. The publications have been either submitted to the related international journals or are currently in final preparation for submission. Therefore, they are listed as follows:

[1] Behzad V. Farahani, F.M. Andrade Pires, Jorge Belinha, "*A Non-linear Rate-independent Continuum Damage Mechanics Model: From Non-local to the Localized Issues within Meshless Method Formulations*", In Preparation.

[2] Behzad V. Farahani, F.M. Andrade Pires, Jorge Belinha, "*A Radial Point Interpolation Meshless Method Extended for an Elastic Rate-independent Continuum Damage Model for Concrete Materials*", Under submission.

[3] Behzad V. Farahani, José M. V. Berardo, Rafał Drgas, José César de Sá, Antonio Ferreira, Jorge Belinha, "*The Axisymmetric Analysis of Circular Plates using the Radial Point Interpolation Method*", International Journal for Computational Methods in Engineering Science & Mechanics, Under reviewing.

Conference proceedings

[1] Behzad V. Farahani, F.M. Andrade Pires, José César de Sá, A. J. M. Ferreira, Jorge Belinha, "*An Isotropic Elastic Damage Model for Concrete Material using a Meshless Method* " in the 2015 Congress on Numerical Methods in Engineering, 29 June – 2 July 2015, Lisbon, Portugal.

[2] Behzad V. Farahani, José M. V. Berardo, Rafał Drgas, José César de Sá, Antonio Ferreira, Jorge Belinha, "*Análise Axissimétrica de Placas Circulares Usando o Método de Interpolação Radial Pontual*" in the 2015 Congress on Numerical Methods in Engineering, 29 June – 2 July 2015, Lisbon, Portugal.

[3] Behzad V. Farahani, F.M. Andrade Pires, Jorge Belinha, "*A Rate-Independent Isotropic Damage Model is Formulated within a Radial Point Interpolation Meshless Method*" in the 1st Doctoral Congress in Engineering, 11-13 June 2015, Porto, Portugal.

[4] Behzad V. Farahani, F.M. Andrade Pires, Jorge Belinha, "*A Return-mapping Algorithm for Elastic Damage Model in Concrete Materials using Radial Point Interpolation Meshless Method"* in the 8th Encontro Investigacao Jovem da Universidade do Porto, 13-15 May 2015, Porto, Portugal.

Chapter 2

2 Meshless Method

The Radial Point Interpolation Method –RPIM– is a meshless method (J. Belinha, 2014) (Wang & Liu, 2002a) (Wang & Liu, 2002b) . In order to force the nodal connectivity, the RPIM uses the concept of the "influence-domain". The Gauss Legendre quadrature principle and integration cells are applied to numerically integrate the integro-differential equations governing the physical phenomenon.

Meshless methods discretize the problem domain and respective boundaries with a nodal set. This nodal set cannot be considered a mesh, because no previous information regarding the relation between each node is required to build the interpolation functions for the unknown variational fields.

2.1 Nodal connectivity and Numerical Integration

Several meshless methods use the concept of influence-domain due to its simplicity.

The meshless methods are discrete numerical methods, as the Finite Element Method (FEM). However, instead of discretizing the problem domain in elements and nodes, meshless methods discretize the problem domain only using nodes or points.

The predefined finite element mesh assures the nodal connectivity in the FEM. The nodes belonging to the same element interact directly between each other and with the boundary nodes of neighbour finite elements. In opposition, since there is no predefined nodal

interdependency, in meshless methods the nodal connectivity is determined after the nodal discretization (J. Belinha, 2014) , being obtained by the overlap of the influence-domain of each node. These influence-domains can be determined by searching radially enough nodes inside a fixed area or a fixed volume, respectively for the 2D problems and for the 3D problems. Because of its simplicity many meshless methods use this concept (Belytschko et al., 1994) (W. K. Liu et al., 1995) (Atluri & Zhu, 1998) (Wang & Liu, 2002a) (V. P. Nguyen et al., 2008) (J. Belinha, 2014). However, the size or shape variation of these influence-domains along the problem domain affects the performance and the final solution of the meshless method. It is important that all the influence domains in the problem contain approximately the same number of nodes. Irregular domain boundaries or node clusters in the nodal mesh can lead to unbalanced influence-domains (J. Belinha, 2014). Regardless the used meshless technique, previous works suggest that each 2D influence-domain should possess between $n = [9,16]$ nodes (Belytschko et al., 1994) (W. K. Liu et al., 1995) (Atluri & Zhu, 1998) (Wang & Liu, 2002a) (V. P. Nguyen et al., 2008) (J. Belinha, 2014). Figure 1 shows the influence domain with regard to the interest point.

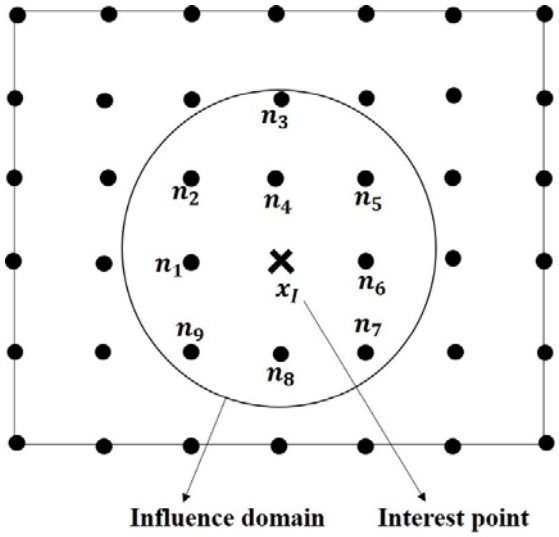

Figure 1: The schematic view of the Influence domain with regard to the interest point

In discrete numerical methods using a variational formulation, such as the Galerkin weak formulation, the numerical integration process, required to determine the system of equations based on the integro-differential equations ruling the studied physical phenomenon, represents a significant percentage of the total computational cost of the

analysis. In the FEM the integration mesh is coincident with the element mesh. Since the FEM shape functions are known polynomial functions, the number of integration points per integration cell can be pre-determined using accurate well-known relations (O. C. Zienkiewicz and R. L. Taylor, 1994) (Bathe, 1982). In meshless methods the shape function degree is generally unknown, thus it is not possible to accurately define a priori the background integration mesh.

The numerical integration scheme used in this work follows the suggestion of previous RPIM works (Wang & Liu, 2002a, 2002b). The solid domain is divided in a regular grid forming quadrilateral integration cells. Then, each grid-cell is filled with integration points, respecting the Gauss-Legendre quadrature rule (J. Belinha, 2014).

In the literature it is possible to find several works using the RPIM, however the state-of-art lacks a detailed study on the RPIM combined with the axisymmetric deformation theory. Thus, in this work a complete axisymmetric-RPIM calibration study is performed in order to determine: the optimal number of nodes forming each influence-domain and; the most accurate spatial disposition of the integration cells, and respective integration order.

2.2 Radial Point Interpolators

The RPIM shape functions are obtained using the Radial Point Interpolators (RPI), which combine radial basis functions with polynomial basis functions. Thus, consider a function space T defined in the analysed domain $\Omega \subset \Re^d$. The finite dimensional space $T_h \subset T$ discretising the domain Ω is defined by: $T_h := \left\langle r(x-x_i) : i \in \Re \wedge i \leq N \right\rangle + p_m(x)$, where $r : \Re^d \mapsto \Re$ is at least a C^1-function and $p_m : \Re^d \mapsto \Re$ is defined in the space of polynomials of degree less than m. In this work only simplified two-dimensional domains $\Omega \subset \Re^2$ are studied, therefore it is considered an interpolation function $u^h(\boldsymbol{x})$ defined in an influence-domain $\Omega_I \subset \Omega$ of an interest point $x_I \in \Re^2$ and discretised by a set of N arbitrarily distributed nodes $\boldsymbol{N}_I = \{n_1, n_2, ..., n_N\}$. The nodal set is defined in the two-

dimensional space by $X=\{x_1,x_2,...,x_N\}\wedge x_i\in\Re^2$, being n the number of nodes in the influence-domain of $\boldsymbol{x}_I$. The density of $\boldsymbol{X}$ is identified by h,

$$h=min\left\|\boldsymbol{x}_j-\boldsymbol{x}_i\right\|,\forall\{i,j\}\in N:\{i,j\}\leq N\ \wedge i\neq j \tag{1}$$

Being $\|\cdot\|$ the Euclidean norm.

The RPI constructs the interpolation function $u^h(\boldsymbol{x})\in T$ capable to pass through all nodes within the influence-domain, meaning that since the nodal function value is assumed to be u_i at the node $\boldsymbol{x}_i$, $u_i=u(\boldsymbol{x}_i)$, consequently $u^h(\boldsymbol{x}_i)=u(\boldsymbol{x}_i)$. Using a radial basis function $r(\boldsymbol{x})$ and polynomial basis function $p(\boldsymbol{x})$, the interpolation function $u^h(\boldsymbol{x})\in T$ can be defined at the interest point $x_I\in\Re^d$ (not necessarily coincident with any $\boldsymbol{x}_i\in\boldsymbol{X}$) by,

$$u^h(\boldsymbol{x}_I)=\sum_{i=1}^{n}r_i(\boldsymbol{x}_I)a_i+\sum_{j=1}^{m}p_j(\boldsymbol{x}_I)b_j=\boldsymbol{r}(\boldsymbol{x}_I)^{\mathrm{T}}\boldsymbol{a}+\boldsymbol{p}(\boldsymbol{x}_I)^{\mathrm{T}}\boldsymbol{b}=u(\boldsymbol{x}_I) \tag{2}$$

where a_i is the non-constant coefficient of $r_i(\boldsymbol{x}_I)$ and b_j the non-constant coefficient for $p_j(\boldsymbol{x}_I)$. The integers n and m are the number of nodes inside the influence-domain of the interest point $\boldsymbol{x}_I$. The vectors are defined as,

$$\boldsymbol{a}^{\mathrm{T}}=\{a_1,a_2,...,a_n\} \tag{3}$$

$$\boldsymbol{b}^{\mathrm{T}}=\{b_1,b_2,...,b_m\} \tag{4}$$

$$\boldsymbol{r}(\boldsymbol{x})^{\mathrm{T}}=\{r_1(\boldsymbol{x}),r_2(\boldsymbol{x}),...,r_n(\boldsymbol{x})\} \tag{5}$$

$$\boldsymbol{p}(\boldsymbol{x})^{\mathrm{T}}=\{p_1(\boldsymbol{x}),p_2(\boldsymbol{x}),...,p_m(\boldsymbol{x})\} \tag{6}$$

being $\boldsymbol{x}_i=\{x_i,y_i\}$. This work uses the Multiquadrics Radial Basis Function (MQ-RBF) (Belinha, Dinis, & Jorge, 2013; Belinha, Dinis, & Natal Jorge, 2013a) (J. Belinha, 2014), which can be defined by $\boldsymbol{r}_i(\boldsymbol{x}_I)=\boldsymbol{s}(d_{iI})=\left(d_{iI}^2+c^2\right)^p$, where d_{iI} is a distance between the interest point $\boldsymbol{x}_I=\{x_I,y_I\}$ and the node $\boldsymbol{x}_i=\{x_i,y_i\}$, being $d_{iI}=\sqrt{\left(x_i-x_I\right)^2+\left(y_i-y_I\right)^2}$. The c and p variables are the MQ-RBF shape parameters, which are fixed values

determined in previous works (Wang & Liu, 2002a, 2002b) . The variation of these parameters can affect the performance of the MQ-RBFs. In the work of Wang and Liu (Wang & Liu, 2002a) (Wang & Liu, 2002b), it was shown that the optimal values are $c = 1.42$ and $p = 1.03$, which are the values used in this work. The original RPI formulation requires a complete polynomial basis function, which for the two-dimensional space can be defined by,

$$\boldsymbol{p}(\boldsymbol{x}_i)^{\mathrm{T}} = \{1, x_i, y_i, x_i^2, x_i y_i, y_i^2, \ldots\} \tag{7}$$

However, it was shown in previous RPI research works (J. Belinha, 2014) (L.M.J.S. Dinis et al., 2007) (L. M J S Dinis, Natal Jorge, & Belinha, 2008) that using a simple constant basis increases the RPI formulation efficiency. Thus, in this work only the constant basis is considered $\boldsymbol{p}(\boldsymbol{x}_i) = \{1\}$, for which the number of monomial terms is defined by $m = 1$. The coefficients a_i and b_j in equation (2) are determined by enforcing the interpolation to pass through all n nodes within the influence-domain (J. Belinha, 2014). The interpolation at the k^{th} node is defined by,

$$u^h(x_k, y_k) = \sum_{i=1}^{n} r_i(x_k, y_k) a_i + \sum_{j=1}^{m} p_j(x_k, y_k) b_j = u_k, \quad k = 1, 2, \ldots, n \tag{8}$$

The inclusion of the following polynomial term is an extra-requirement that guarantees unique approximation (J. Belinha, 2014) (L. M J S Dinis et al., 2008),

$$\sum_{i=1}^{n} p_j(x_i, y_i) a_i = 0, \quad j = 1, 2, \ldots, m \tag{9}$$

The computation of the shape functions is written in a matrix form as

$$\begin{bmatrix} \boldsymbol{R} & \boldsymbol{P} \\ \boldsymbol{P}^T & \boldsymbol{Z} \end{bmatrix} \begin{Bmatrix} \boldsymbol{a} \\ \boldsymbol{b} \end{Bmatrix} = \begin{Bmatrix} \boldsymbol{u} \\ \boldsymbol{z} \end{Bmatrix} \Leftrightarrow \boldsymbol{G} \begin{Bmatrix} \boldsymbol{a} \\ \boldsymbol{b} \end{Bmatrix} = \begin{Bmatrix} \boldsymbol{u} \\ \boldsymbol{z} \end{Bmatrix} \tag{10}$$

where $\boldsymbol{G}$ is the complete moment matrix, $\boldsymbol{Z}$ is a null matrix defined by $Z_{ij} = 0, \forall \{\{i, j\} \in \mathrm{N} : \{i, j\} \leq m\}$ and the null vector $\boldsymbol{z}$ can be represented by $z_i = 0, \forall \{i \in \mathrm{N} : i \leq m\}$. The vector for function values is defined as $u_i = u(x_i), \forall \{i \in \mathrm{N} : i \leq n\}$. The radial moment matrix $\boldsymbol{R}$ is represented as,

$$\underset{[n\times n]}{\boldsymbol{R}} = \begin{bmatrix} r_1(x_1,y_1) & r_1(x_2,y_2) & \cdots & r_1(x_n,y_n) \\ r_2(x_1,y_1) & r_2(x_2,y_2) & \cdots & r_2(x_n,y_n) \\ \vdots & \vdots & \ddots & \vdots \\ r_n(x_1,y_1) & r_n(x_2,y_2) & \cdots & r_n(x_n,y_n) \end{bmatrix} \tag{11}$$

and polynomial moment matrix $\boldsymbol{P}$ is defined as,

$$\underset{[n\times m]}{\boldsymbol{P}} = \begin{bmatrix} p_1(x_1,y_1) & p_2(x_1,y_1) & \cdots & p_m(x_1,y_1) \\ p_1(x_2,y_2) & p_2(x_2,y_2) & \cdots & p_m(x_2,y_2) \\ \vdots & \vdots & \ddots & \vdots \\ p_1(x_n,y_n) & p_2(x_n,y_n) & \cdots & p_m(x_n,y_n) \end{bmatrix} \tag{12}$$

Since the distance is directionless, $r_i(x_j,y_j) = r_j(x_i,y_i)$, i.e. $R_{ij} = R_{ji}$, matrix $\boldsymbol{R}$ is symmetric. A unique solution is obtained if the inverse of the radial moment matrix $\boldsymbol{R}$ exists,

$$\begin{Bmatrix} \boldsymbol{a} \\ \boldsymbol{b} \end{Bmatrix} = \boldsymbol{G}^{-1} \begin{Bmatrix} \boldsymbol{u} \\ \boldsymbol{z} \end{Bmatrix} \tag{13}$$

The solvability of this system is usually guaranteed by the requirements $rank(p) = m \le n$ (Wang et al., 2001).

In this work, the influence-domain will always possess enough nodes to largely satisfy the previously mentioned condition. It is possible to obtain the interpolation with

$$u^h(\boldsymbol{x}_I) = \left\{ \boldsymbol{r}(\boldsymbol{x}_I)^T ; \boldsymbol{p}(\boldsymbol{x}_I)^T \right\} \boldsymbol{G}^{-1} \begin{Bmatrix} \boldsymbol{u} \\ \boldsymbol{z} \end{Bmatrix} = \left\{ \Phi(\boldsymbol{x}_I)^T ; \Psi(\boldsymbol{x}_I)^T \right\} \begin{Bmatrix} \boldsymbol{u} \\ \boldsymbol{z} \end{Bmatrix} \tag{14}$$

where the interpolation function vector $\Phi(\boldsymbol{x}_I)$ is defined by

$$\Phi(\boldsymbol{x}_I) = \left\{ \varphi_1(\boldsymbol{x}_I) \quad \varphi_2(\boldsymbol{x}_I) \quad \cdots \quad \varphi_n(\boldsymbol{x}_I) \right\} \tag{15}$$

and the residual vector $\psi(\boldsymbol{x}_I)$, with no relevant physical meaning, is expressed as follows,

$$\Psi(\boldsymbol{x}_I) = \left\{ \psi_1(\boldsymbol{x}_I) \quad \psi_2(\boldsymbol{x}_I) \quad \cdots \quad \psi_m(\boldsymbol{x}_I) \right\} \tag{16}$$

Since

$$u^h(\boldsymbol{x}_I) = \Phi(\boldsymbol{x}_I)^T \boldsymbol{u} = \left\{\Phi(\boldsymbol{x}_I)^T ; \Psi(\boldsymbol{x}_I)^T\right\} \begin{Bmatrix} \boldsymbol{u} \\ \boldsymbol{z} \end{Bmatrix} \tag{17}$$

It is possible to obtain the partial derivatives of the interpolated field variable, with respect to a generic variable ξ which can be $\xi = x$ or $\xi = y$, with the following expression,

$$\frac{\partial u^h(\boldsymbol{x}_I)}{\partial \xi} = \frac{\partial \Phi(\boldsymbol{x}_I)^T}{\partial \xi} \boldsymbol{u} = \left\{ \frac{\partial \Phi(\boldsymbol{x}_I)^T}{\partial \xi} ; \frac{\partial \Psi(\boldsymbol{x}_I)^T}{\partial \xi} \right\} \begin{Bmatrix} \boldsymbol{u} \\ \boldsymbol{z} \end{Bmatrix} \tag{18}$$

From Equation (14) it is possible to write

$$\left\{ \frac{\partial \Phi(\boldsymbol{x}_I)^T}{\partial \xi} ; \frac{\partial \Psi(\boldsymbol{x}_I)^T}{\partial \xi} \right\} = \frac{\partial \left(\left\{ \boldsymbol{r}(\boldsymbol{x}_I)^T ; \boldsymbol{p}(\boldsymbol{x}_I)^T \right\} \boldsymbol{G}^{-1} \right)}{\partial \xi} \tag{19}$$

Since the moment matrix $\boldsymbol{G}$ does not depend on the variable $\boldsymbol{x}_I$, Equation (19) can be rewritten as,

$$\left\{ \frac{\partial \Phi(\boldsymbol{x}_I)^T}{\partial \xi} ; \frac{\partial \Psi(\boldsymbol{x}_I)^T}{\partial \xi} \right\} = \left\{ \frac{\partial \boldsymbol{r}(\boldsymbol{x}_I)^T}{\partial \xi} ; \frac{\partial \boldsymbol{p}(\boldsymbol{x}_I)^T}{\partial \xi} \right\} \boldsymbol{G}^{-1} \tag{20}$$

The partial derivatives of the MQ-RBF vector $\boldsymbol{r}(\boldsymbol{x}_I)$, with respect to a generic variable ξ, can be obtained for each component $\partial r_i(\boldsymbol{x}_I) / \partial \xi$ with the expression,

$$\frac{\partial r_i(\boldsymbol{x}_I)}{\partial \xi} = 2p(\xi_i - \xi_I)(d_{iI}{}^2 + c^2)^{p-1} \tag{21}$$

The RPI test functions $\Phi(\boldsymbol{x}_I)$ depend uniquely on the distribution of scattered nodes (J. Belinha, 2014). Previous works (Wang & Liu, 2002a) (L.M.J.S. Dinis et al., 2007) (J. Belinha, 2014) show that RPI test functions possess the Kronecker delta property. Since the obtained RPI test functions have a local compact support it is possible to assemble a well-conditioned and a banded stiffness matrix. If a polynomial basis is included, the RPI test functions have reproducing properties and possess the partition of unity property (J. Belinha, 2014).

Chapter 3

3 Solid Mechanics

The current study is based on the elasticity theory. Hence it is necessary to introduce the corresponding formulations, such as deformation theory and internal variable fields. Thus, it is prepared as follows: in Section 3.1, deformation theory for 2D case with regard to the variational fields are introduced. The Galerkin weak formalism is also presented in this Section. It covers the equations relevant to strain and stress fields, stiffness matrix and force vectors existing in the model. In Subsection 3.1.2, principal stress and principal direction are represented for the 2D and 3D cases. Subsection 3.1.3 is devoted to the equivalent von Mises stress and strain formulation for 2D and 3D cases. This part plays a significant role in the theory of damage mechanics discussed later. At the end, the formulation of octahedral shear and normal stress tensors are expressed in Subsection 3.1.4. The pattern is repeated for the axisymmetric discrete equation system in Section 3.2.

3.1 Deformation Theory for 2D Case

In this work, only 2D examples are solved. Therefore, the plane stress deformation theory is assumed. Figure 2 shows a 2D plate in the Cartesian coordinate system and the non-null components of the stress tensor are indicated. The 2D displacement field can be represented as follows:

$$\boldsymbol{u}(x,y) = \begin{Bmatrix} u_x(x,y) \\ u_y(x,y) \end{Bmatrix} \tag{22}$$

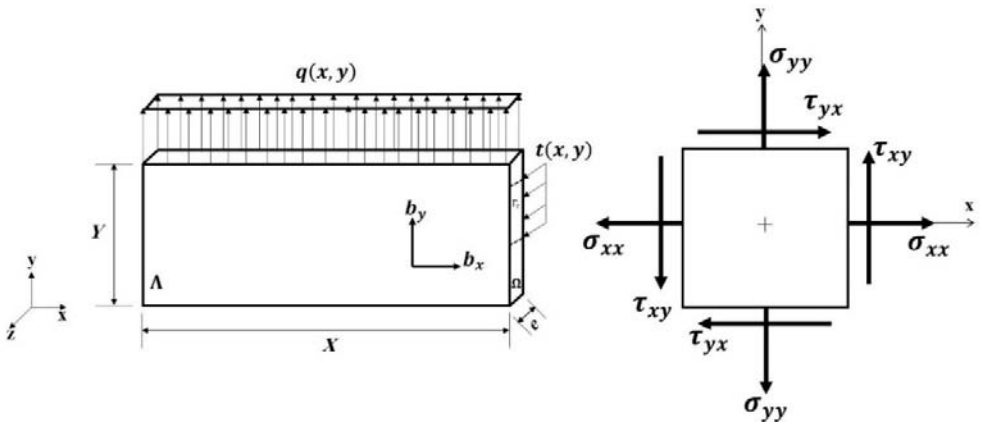

Figure 2: Left, 2D solid plate in Cartesian coordinate system, right stress components in plane stress state

The corresponding deformation field is computed with the following equation (23):

$$\boldsymbol{\varepsilon} = \begin{Bmatrix} \varepsilon_{xx} \\ \varepsilon_{yy} \\ \gamma_{xy} \end{Bmatrix} = \boldsymbol{L}\boldsymbol{u} = \begin{bmatrix} \frac{\partial}{\partial x} & 0 \\ 0 & \frac{\partial}{\partial y} \\ \frac{\partial}{\partial y} & \frac{\partial}{\partial x} \end{bmatrix} \begin{Bmatrix} u_x(x,y) \\ u_y(x,y) \end{Bmatrix} = \begin{Bmatrix} \frac{\partial u_x}{\partial x} \\ \frac{\partial u_y}{\partial y} \\ \frac{\partial u_x}{\partial y} + \frac{\partial u_y}{\partial x} \end{Bmatrix} \tag{23}$$

According to the Hooke's law, it is possible to determine the stress field with the expression:

$$\boldsymbol{\sigma} = \boldsymbol{C}\boldsymbol{\varepsilon} = \begin{Bmatrix} \sigma_{xx} \\ \sigma_{yy} \\ \tau_{xy} \end{Bmatrix} = \boldsymbol{C} \begin{Bmatrix} \varepsilon_{xx} \\ \varepsilon_{yy} \\ \gamma_{xy} \end{Bmatrix} \tag{24}$$

Being $\boldsymbol{C}$ the material constitutive matrix for plane stress case defined as follows:

$$\boldsymbol{C} = e\frac{E}{(1+\nu)(1-\nu)} \begin{bmatrix} 1 & \nu & 0 \\ \nu & 1 & 0 \\ 0 & 0 & \frac{1-\nu}{2} \end{bmatrix} \tag{25}$$

with E and ν being Young's modulus and the Poisson's ratio respectively and e the thickness of the plate.

3.1.1 Galerkin Weak-form

The discrete equation system is obtained using the Galerkin weak-form. The Lagrangian functional is defined by:

$$L = T - U + W_f \tag{26}$$

In the above relation, T and U are the kinetic and strain energy values respectively while W_f is known as the work produced by external forces. Afterwards, based on Hamilton`s principle and neglecting the dynamic effect, the minimization of the Lagrangian functional leads to the Galerkin weak form of the equilibrium equation:

$$\delta L = \int_\Lambda \delta\varepsilon^T \sigma \, d\Lambda - \int_\Lambda \delta u^T b \, d\Lambda - \int_{S_t} \delta u^T t \, dS - \int_{C_q} \delta u^T q \, dC = 0 \tag{27}$$

As seen in Figure 2, $\boldsymbol{b}$ is the body force vector, $\boldsymbol{t}$ is the external traction force vector applied on a close surface $\boldsymbol{S_t}$ and $\boldsymbol{q}$ represents the external force vector applied on a close curve $\boldsymbol{C_q}$. Besides, it is valuable to mention that $d\Lambda = dx.dy.dz$. Afterwards, the energy equation could be written as follows:

$$\int_\Omega e \, \delta\varepsilon^T \sigma \, d\Omega = \int_\Omega e \, \delta u^T b \, d\Omega + \int_\Gamma e \, \delta u^T t \, d\Gamma + e \, \delta u^T q \tag{28}$$

In the RPIM, the weak form has local support, which means that the discrete system of equations is developed firstly for every influence-domain. Then, the local system of equations is assembled to form the global system of equations, which is solved afterwards. The RPIM trial function is given by equation (14), thus for each degree of freedom it is possible to write:

$$u_x^h(\boldsymbol{x_I}) = \sum_{i=1}^n \varphi_i(\boldsymbol{x_I}) u_x(x_i) \tag{29}$$

$$u_y^h(\boldsymbol{x_I}) = \sum_{i=1}^n \varphi_i(\boldsymbol{x_I}) u_y(x_i) \tag{30}$$

In the abovementioned equations, $\varphi_i(\boldsymbol{x_I})$ represents the RPIM interpolation function while $u_x(x_i)$ and $u_y(x_i)$ are the nodal parameters of the i^{th} node belonging to the nodal set defined in the influence domain of the interest node of $\boldsymbol{x_I}$.

Subsequently, it is possible to generate a more general equation:

$$\boldsymbol{u}^h(\boldsymbol{x_I}) = \begin{Bmatrix} u_x(x_i) \\ u_y(x_i) \end{Bmatrix} = \sum_{i=1}^{n} \begin{bmatrix} \varphi_i(\boldsymbol{x_I}) & 0 \\ 0 & \varphi_i(\boldsymbol{x_I}) \end{bmatrix} \begin{Bmatrix} u(x_i) \\ v(x_i) \end{Bmatrix} = \sum_{i=1}^{n} \boldsymbol{H}_i\,(\boldsymbol{x_I})\boldsymbol{u}(x_i) \quad (31)$$

Furthermore, as a result of Equation (31), it is possible to present developed form equation of the strain field:

$$\boldsymbol{\varepsilon}(\boldsymbol{x_I}) = \boldsymbol{L}u^h(\boldsymbol{x_I}) = \boldsymbol{L}\sum_{i=1}^{n} \boldsymbol{H}_i\,(\boldsymbol{x_I})\boldsymbol{u}(x_i) \quad (32\text{-a})$$

$$\boldsymbol{\varepsilon}(\boldsymbol{x_I}) = \sum_{i=1}^{n} \boldsymbol{B}_i\,(\boldsymbol{x_I})\boldsymbol{u}(x_i) = \begin{bmatrix} \frac{\partial \varphi_i(\boldsymbol{x_I})}{\partial x} & 0 \\ 0 & \frac{\partial \varphi_i(\boldsymbol{x_I})}{\partial y} \\ \frac{\partial \varphi_i(\boldsymbol{x_I})}{\partial y} & \frac{\partial \varphi_i(\boldsymbol{x_I})}{\partial x} \end{bmatrix} \begin{Bmatrix} u_x(x_i) \\ u_y(x_i) \end{Bmatrix} \quad (32\text{-b})$$

It should be clarified that $\boldsymbol{B}$ is the deformation matrix equal to $\boldsymbol{B} = \boldsymbol{LH}$.

As mentioned before, the stress field is a function of the strain vector. Thus, the developed relation of the stress vector for an interest point $(\boldsymbol{x_I})$ could be written as follows:

$$\boldsymbol{\sigma}(\boldsymbol{x_I}) = \boldsymbol{C}\,\boldsymbol{\varepsilon}(\boldsymbol{x_I}) \quad (33)$$

In order to compute the stiffness matrix, first it is necessary to present the general integration of the weak formulation for any interest point$(\boldsymbol{x_I})$:

$$\delta u^T \int_\Omega e\boldsymbol{B}^T\boldsymbol{C}\boldsymbol{B}\,d\Omega\,\boldsymbol{u} = \delta\boldsymbol{u}^T \int_\Omega e\boldsymbol{H}^T \begin{Bmatrix} b_x \\ b_y \end{Bmatrix} d\Omega + \delta\boldsymbol{u}^T \int_\Gamma e\boldsymbol{H}^T \begin{Bmatrix} t_x \\ t_y \end{Bmatrix} d\Gamma + \delta\boldsymbol{u}^T e \begin{Bmatrix} q_x \\ q_y \end{Bmatrix} \quad (34)$$

The linear system of equations based on Equation (34) is represented below.

$$\delta u^T\left(\boldsymbol{K}\boldsymbol{u} - \boldsymbol{f}_b - \boldsymbol{f}_t - \boldsymbol{f}_q\right) = 0 \quad (35)$$

Then;

$$\boldsymbol{u} = \boldsymbol{K}^{-1}\left(\boldsymbol{f}_b + \boldsymbol{f}_t + \boldsymbol{f}_q\right) \quad (36)$$

Since the RPI test functions possess the delta Kronecker property, the essential boundary conditions are directly imposed in the global stiffness matrix.

3.1.2 Principal Stress and Principal Directions

In this section, it is focused on the principal stress and its direction in 3D state due to its application for the further parts. First of all, it should be mentioned that the principal stress and direction are derived from second order stress tensor at the specific point in the problem (Bonet & Wood, 2008) (Michael Anthony Crisfield, 1991). So, if a multidimensional vector of stress is considered as follows:

$$\sigma = \begin{bmatrix} \sigma_{xx} & \sigma_{yy} & \sigma_{zz} & \tau_{xy} & \tau_{yz} & \tau_{xz} \end{bmatrix}^T \tag{37}$$

After mapping to the second order tensor, it will be:

$$\boldsymbol{\sigma} = \begin{bmatrix} \sigma_{xx} & \tau_{xy} & \tau_{xz} \\ \tau_{yx} & \sigma_{yy} & \tau_{yz} \\ \tau_{zx} & \tau_{zy} & \sigma_{zz} \end{bmatrix} \tag{38}$$

Since, the stress tensor is symmetric, the stress invariants should be driven based on the following relations:

$$I_1 = \sigma_{xx} + \sigma_{yy} + \sigma_{zz} \tag{39-a}$$

$$I_2 = \sigma_{xx}\sigma_{yy} + \sigma_{yy}\sigma_{zz} + \sigma_{zz}\sigma_{xx} - {\tau_{xy}}^2 - {\tau_{yz}}^2 - {\tau_{xz}}^2 \tag{39-b}$$

$$I_3 = \sigma_{xx}\sigma_{yy}\sigma_{zz} + 2\tau_{xy}\tau_{yz}\tau_{xz} - \sigma_{xx}{\tau_{yz}}^2 + \sigma_{yy}{\tau_{xz}}^2 - \sigma_{zz}{\tau_{xy}}^2 \tag{39-c}$$

In order to obtain the principal stress components, the following cubic equation should be solved.

$$\sigma^3 - I_1\sigma^2 + I_2\sigma^2 - I_3 = 0 \tag{40}$$

Then, the principal stress tensor is in the following form:

$$\boldsymbol{\sigma}_p = \begin{bmatrix} \sigma_1 & 0 & 0 \\ 0 & \sigma_2 & 0 \\ 0 & 0 & \sigma_3 \end{bmatrix} \quad while \quad \sigma_1 \geq \sigma_2 \geq \sigma_3 \tag{41}$$

Since the three principal components are different, there are only three principal directions that are mutually perpendicular to each other.

$$\hat{n}_1 = \hat{n}_2 \times \hat{n}_3 \qquad \hat{n}_2 = \hat{n}_3 \times \hat{n}_1 \qquad \hat{n}_3 = \hat{n}_1 \times \hat{n}_3 \tag{42}$$

Remember that the unit vectors $\hat{n}_1, \hat{n}_2, \hat{n}_3$ corresponding to the principal direction must form a right-handed system. First, it is going to obtain the principal direction $\hat{n}_1$. So, the governing equations are presented below.

$$\hat{n}_1 = n_{x1}\hat{\imath} + n_{y1}\hat{\jmath} + n_{z1}\hat{k} \tag{43}$$

$$n_{x1}{}^2 + n_{y1}{}^2 + n_{z1}{}^2 = 0 \tag{44}$$

$$\begin{bmatrix} \sigma_{xx} - \sigma_1 & \tau_{xy} & \tau_{xz} \\ \tau_{yx} & \sigma_{yy} - \sigma_1 & \tau_{yz} \\ \tau_{zx} & \tau_{zy} & \sigma_{zz} - \sigma_1 \end{bmatrix} \begin{Bmatrix} n_{x1} \\ n_{y1} \\ n_{z1} \end{Bmatrix} = \begin{Bmatrix} 0 \\ 0 \\ 0 \end{Bmatrix} \tag{45}$$

The above system of equation is a kind of non-linear one. In order to avoid having to solve a system of equation involving a non-linear equation, the following procedure is applied. Let consider $\vec{\boldsymbol{N}}_{\boldsymbol{1}}$ as a vector parallel to the unit vector $\hat{n}_1$:

$$\vec{\boldsymbol{N}}_1 = N_1\hat{n}_1 = N_1\left(n_{x1}\,\hat{\imath} + n_{y1}\,\hat{\jmath} + n_{z1}\,\hat{k}\right) \Longrightarrow \vec{\boldsymbol{N}}_{\boldsymbol{1}} = N_{x1}\,\hat{\imath} + N_{y1}\,\hat{\jmath} + N_{z1}\,\hat{k} \tag{46}$$

$$N_1 = \left|\vec{\boldsymbol{N}}_{\boldsymbol{1}}\right| = \sqrt{N_{x1}{}^2 + N_{y1}{}^2 + N_{z1}{}^2} \qquad \text{Magnitude of } \vec{N}_1 \tag{47}$$

$$N_{x1} = N_1 n_{x1} \qquad n_{x1} = \frac{N_{x1}}{N_1} \tag{48-a}$$

$$N_{y1} = N_1 n_{y1} \qquad n_{y1} = \frac{N_{y1}}{N_1} \tag{48-b}$$

$$N_{z1} = N_1 n_{z1} \qquad n_{z1} = \frac{N_{z1}}{N_1} \tag{48-c}$$

Substituting in equation (45);

$$\begin{bmatrix} \sigma_{xx} - \sigma_1 & \tau_{xy} & \tau_{xz} \\ \tau_{yx} & \sigma_{yy} - \sigma_1 & \tau_{yz} \\ \tau_{zx} & \tau_{zy} & \sigma_{zz} - \sigma_1 \end{bmatrix} \begin{Bmatrix} N_{x1} \\ N_{y1} \\ N_{z1} \end{Bmatrix} = \begin{Bmatrix} 0 \\ 0 \\ 0 \end{Bmatrix} \tag{49}$$

Considering $N_{x1} = 1$, the other components are calculated through solving the above system of equation. The obtained values are replaced in Equation (48) and finally the first principal direction is calculated from Equation (43). This procedure is the same to compute $\hat{n}_2 \; and \; \hat{n}_3$.

It is worth nothing that the principal stress and principal direction could be also known as eigenvalues and eigenvectors in another definition respectively. In the 2D case, the stress components in *z* direction are assumed as zero but the pattern is equal to the 3D one (Michael Anthony Crisfield, 1991).

3.1.3 Equivalent von Mises Stress and Strain

It is helpful to present the equivalent von Mises relations for stress and strain fields, as extracted from (Ford, 1963) (Kazimi, 1982), due to their applications. In the 3D case, the multidimensional vectors and the second order tensor of strain and stress are considered as follows:

$$\varepsilon=\begin{Bmatrix}\varepsilon_{xx}\\ \varepsilon_{yy}\\ \varepsilon_{zz}\\ \gamma_{xy}\\ \gamma_{yz}\\ \gamma_{zx}\end{Bmatrix}\xrightarrow{Mapping\ to\ the\ tensor}\boldsymbol{\varepsilon}=\begin{bmatrix}\varepsilon_{xx} & \frac{1}{2}\gamma_{xy} & \frac{1}{2}\gamma_{xz}\\ \frac{1}{2}\gamma_{xy} & \varepsilon_{yy} & \frac{1}{2}\gamma_{yz}\\ \frac{1}{2}\gamma_{xz} & \frac{1}{2}\gamma_{zy} & \varepsilon_{zz}\end{bmatrix},\quad \boldsymbol{\sigma}=\begin{bmatrix}\sigma_{xx} & \tau_{xy} & \tau_{xz}\\ \tau_{xy} & \sigma_{yy} & \tau_{yz}\\ \tau_{xz} & \tau_{zy} & \sigma_{zz}\end{bmatrix} \tag{50}$$

According to equation (50), it is possible to apply the von Mises rule to compute the equivalent stress and strain without any restrictions in the following terms:

$$\tilde{\sigma}=\sqrt{\frac{1}{2}\left[\left(\sigma_{xx}-\sigma_{yy}\right)^2+\left(\sigma_{yy}-\sigma_{zz}\right)^2+(\sigma_{zz}-\sigma_{xx})^2+6\left(\tau_{xy}{}^2+\tau_{xz}{}^2+\tau_{zy}{}^2\right)\right]} \tag{51}$$

$$\tilde{\varepsilon}=\sqrt{\frac{2}{3}\left[\varepsilon_{xx}\varepsilon_{xx}+\varepsilon_{yy}\varepsilon_{yy}+\varepsilon_{zz}\varepsilon_{zz}+\frac{1}{2}\left(\gamma_{xy}\gamma_{xy}+\gamma_{yz}\gamma_{yz}+\gamma_{zx}\gamma_{zx}\right)\right]} \tag{52}$$

There is also another relation in the literature for computation of $\tilde{\varepsilon}$ in the 2D state as:

$$\tilde{\varepsilon}=\sqrt{\varepsilon^T:C^{-1}:\sigma} \tag{53}$$

where ***C*** is the second order constitutive matrix in plane stress presented in Equation (25). Indeed Figure 3 demonstrates a bounding surface in the 3D and 2D principal stress coordinate systems where the von Mises accounted for a constant value so called “High-Westergard Space”. It is based on the fact that any stress state can be converted into its principal values and compared to this sketch. If the resulting principal stress point in the

coordinate system is within the cylinder, then the material has not yielded. If it is on the surface, then the material has yielded and if it is outside the cylinder, it means that there was an elastic analysis of a situation that cannot in fact be correct because yielding would have long since taken place.

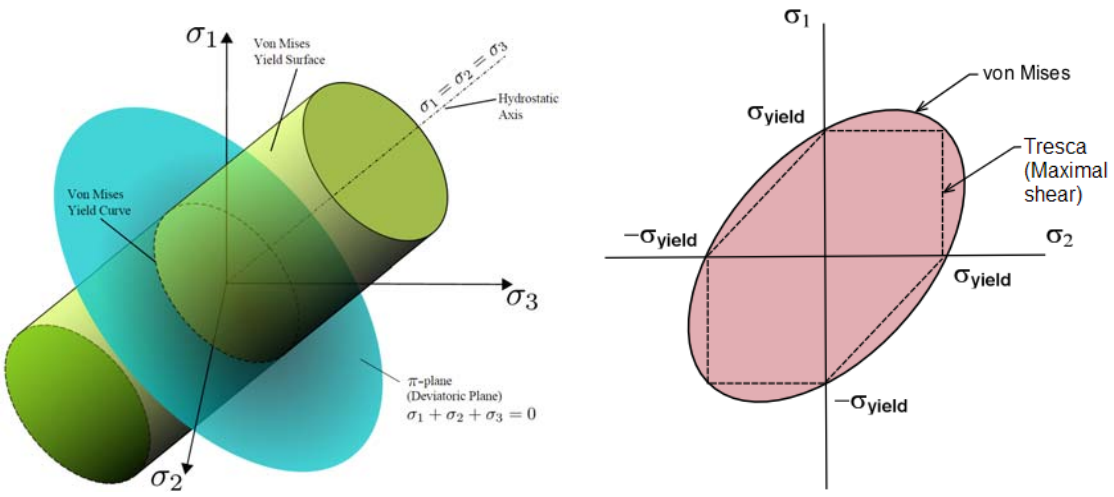

Figure 3: A bounding surface in the principal stress coordinate system; left, 3D and right, 2D case

(http://en.wikipedia.org/wiki/File:Yield_surfaces.svg)

3.1.4 Octahedral Shear and Normal Stress

Here it is presented a brief description in order to calculate the octahedral stress components based on the formulation presented by (Fung, Tong, & Bechtel, 2003) (Chen & Han, 1988).

Considering the principal directions as the coordinate axes, a plane whose normal vector makes equal angles with each of the principal axes, for example having direction cosines equal to $\left|\frac{1}{\sqrt{3}}\right|$, is called an octahedral plane. As seen in Figure 4, there are eight various octahedral planes.

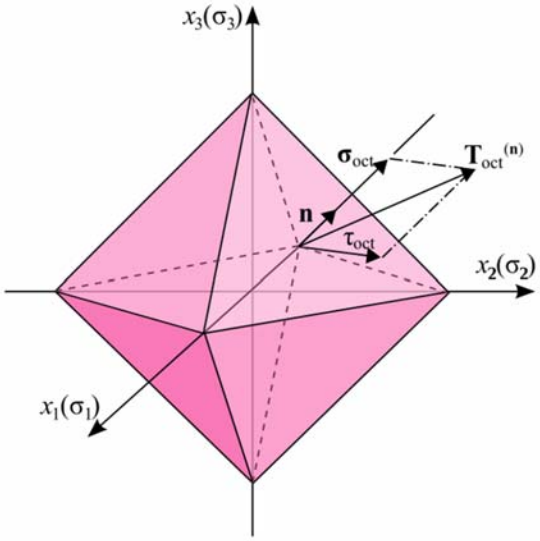

Figure 4: Octahedral stress planes

(https://commons.wikimedia.org/wiki/File:Octahedral_stress_planes.svg)

The normal and shear components of the stress tensor on these planes are called octahedral normal stress and octahedral shear stress. Thus, the stress tensor of a desirable point in the principal axes is in the following form:

$$\boldsymbol{\sigma}_{ij} = \begin{bmatrix} \sigma_1 & 0 & 0 \\ 0 & \sigma_2 & 0 \\ 0 & 0 & \sigma_3 \end{bmatrix} \tag{54}$$

The stress vector on the octahedral plane could be defined as follows:

$$\boldsymbol{T}_{oct}^{(n)} = \sigma_{ij} n_i e_j = \sigma_1 n_1 e_1 + \sigma_2 n_2 e_2 + \sigma_3 n_3 e_3 = \frac{1}{\sqrt{3}}(\sigma_1 e_1 + \sigma_2 e_2 + \sigma_3 e_3) \tag{55}$$

Thus, the normal component of the stress vector at the corresponding point on the octahedral plane is:

$$\sigma_{oct} = T_i^{(n)} n_i = \sigma_{ij} n_i n_j = \sigma_1 n_1 n_1 + \sigma_2 n_2 n_2 + \sigma_3 n_3 n_3 \tag{56}$$

$$\sigma_{oct} = \frac{1}{3}(\sigma_1 + \sigma_2 + \sigma_3) = \frac{1}{3} I_1 \tag{57}$$

The above relation presents the mean normal stress or hydrostatic stress. The procedure of calculation is the same for all the eight octahedral planes. In addition, the shear stress on the octahedral plane could be derived as follows:

$$\tau_{oct} = \sqrt{T_i^{(n)} T_i^{(n)} - \sigma_n^2} = \sqrt{\frac{1}{3}(\sigma_1^2 + \sigma_2^2 + \sigma_3^2) - \frac{1}{9}(\sigma_1 + \sigma_2 + \sigma_3)^2} \tag{58}$$

$$\tau_{oct} = \frac{1}{3}\sqrt{(\sigma_1 - \sigma_2)^2 + (\sigma_2 - \sigma_3)^2 + (\sigma_3 - \sigma_1)^2} = \frac{1}{3}\sqrt{2I_1^2 - 6I_2} \tag{59}$$

According to Equations (39-a) and (39-b), it is needed to rewrite the first and second stress invariants;

$$I_1 = tr(\sigma) = \sigma_{kk} = \sigma_1 + \sigma_2 + \sigma_3 \tag{60}$$

$$I_2 = \frac{1}{2}tr(\sigma)^2 = \sigma_1\sigma_2 + \sigma_2\sigma_3 + \sigma_3\sigma_1 \tag{61}$$

3.2 Axisymmetric Discrete Equation System

In this work, since the complete three-dimensional domain $\Lambda \subset \Re^3$ of the studied circular plates can be obtained by the revolution of a two-dimensional domain section $\Omega \subset \Re^2$ and all the natural and essential boundaries show radial symmetry, it is used the axisymmetric deformation theory. In Figure 5(a) a general example of a revolution solid is demonstrated. Therefore, it is assumed a body described by the domain $\Omega \subset \Re^2$ and bounded by Γ, where $\Gamma \in \Omega : \Gamma_u \cup \Gamma_t = \Gamma \wedge \Gamma_u \cap \Gamma_t = \varnothing$, being Γ_u the essential boundary and Γ_t the natural boundary.

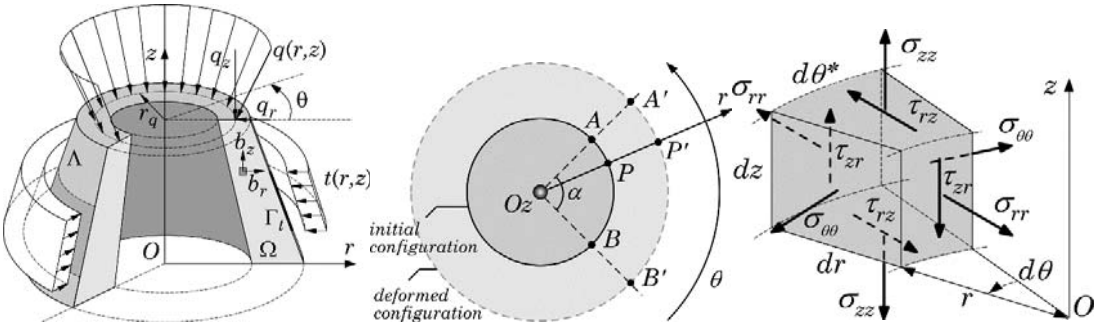

(a) (b) (c)

Figure 5 : (a) Axisymmetric solid. (b) Axisymmetric deformation. (c) Stress components in circular coordinates

3.2.1 Variable Fields

Using the cylindrical coordinate system, Figure 5(a), the complete 3D displacement field can be defined as,

$$\boldsymbol{u}(r,z)=\begin{Bmatrix} u_r(r,z) \\ u_z(r,z) \\ u_\theta(r,z) \end{Bmatrix} \tag{62}$$

The deformation field is determined with,

$$\varepsilon=\begin{Bmatrix} \varepsilon_{rr} \\ \varepsilon_{zz} \\ \varepsilon_{\theta\theta} \\ \gamma_{rz} \\ \gamma_{z\theta} \\ \gamma_{\theta r} \end{Bmatrix}=\boldsymbol{L}\,\boldsymbol{u}=\begin{bmatrix} \frac{\partial}{\partial r} & 0 & 0 \\ 0 & \frac{\partial}{\partial z} & 0 \\ 0 & 0 & \frac{\partial}{\partial \theta} \\ \frac{\partial}{\partial z} & \frac{\partial}{\partial r} & 0 \\ 0 & \frac{\partial}{\partial \theta} & \frac{\partial}{\partial z} \\ \frac{\partial}{\partial \theta} & 0 & \frac{\partial}{\partial r} \end{bmatrix}\begin{Bmatrix} u_r(r,z) \\ u_z(r,z) \\ u_\theta(r,z) \end{Bmatrix}=\begin{Bmatrix} \frac{\partial u_r}{\partial r} \\ \frac{\partial u_z}{\partial z} \\ \frac{\partial u_\theta}{\partial \theta} \\ \frac{\partial u_r}{\partial z}+\frac{\partial u_z}{\partial r} \\ \frac{\partial u_z}{\partial \theta}+\frac{\partial u_\theta}{\partial z} \\ \frac{\partial u_r}{\partial \theta}+\frac{\partial u_\theta}{\partial r} \end{Bmatrix}. \tag{63}$$

However, due to the circumferential symmetry of all problems studied in this work, the circumferential coordinate is in fact dependent on the other two coordinates,

$$u_\theta(r,z)=f(u_r,u_z), \tag{64}$$

which is one of the assumptions of the axisymmetric deformation theory. Thus, it is considered that the deformation only occurs in the Orz plane, being the displacement field described by,

$$\boldsymbol{u}(r,z)=\begin{Bmatrix} u_r(r,z) \\ u_z(r,z) \end{Bmatrix}. \tag{65}$$

Considering Figure 5(b), due to the axisymmetric conditions, the angle α between points AB on an initial configuration is the same as the angle between $A'B'$ for a deformed configuration. Additionally, the arch $A'B'$ is a homothetic arch of initial arch AB, indicating that in the circumferential direction θ there will be only volume changes ($\varepsilon_{\theta\theta}\neq 0$) and no distortions will occur ($\gamma_{z\theta}=0$ and $\gamma_{\theta r}=0$).

Therefore, the deformation components for the axisymmetric deformation theory are the following,

$$\varepsilon = \boldsymbol{L}\,\boldsymbol{u} = \begin{Bmatrix} \varepsilon_{rr} \\ \varepsilon_{zz} \\ \varepsilon_{\theta\theta} \\ \gamma_{rz} \end{Bmatrix} = \begin{bmatrix} \dfrac{\partial}{\partial r} & 0 \\ 0 & \dfrac{\partial}{\partial z} \\ \dfrac{1}{r} & 0 \\ \dfrac{\partial}{\partial z} & \dfrac{\partial}{\partial r} \end{bmatrix} \begin{Bmatrix} u_r(r,z) \\ u_z(r,z) \end{Bmatrix} = \begin{Bmatrix} \dfrac{\partial u_r}{\partial r} \\ \dfrac{\partial u_z}{\partial z} \\ \dfrac{u_r}{r} \\ \dfrac{\partial u_r}{\partial z} + \dfrac{\partial u_z}{\partial r} \end{Bmatrix}. \tag{66}$$

In order to determine the deformation in the circumferential direction θ, $\varepsilon_{\theta\theta}$ presented in Equation(66), consider point $P \in A\widehat{B}$ represented in Figure 5(b). The deformation of P occurs along the Or axis, leading to point P' and showing a radial displacement: $u_r(r_P, z_P)$. Notice that, due to the axisymmetric assumptions, the displacement field does not depend on the circumferential direction θ: $u_r(r_P, z_P) = u_r(r_A, z_A) = u_r(r_B, z_B)$. Thus, the deformation on the circumferential direction can be obtained with,

$$\varepsilon_{\theta\theta} = \frac{A'\widehat{B}' - A\widehat{B}}{A\widehat{B}} = \frac{\alpha(r + u_r) - \alpha r}{\alpha r} = \frac{u_r}{r}. \tag{67}$$

The generalized Hooke's law permits to correlate the strain field with the stress field,

$$\boldsymbol{\sigma} = \boldsymbol{C}\boldsymbol{\varepsilon} = \begin{Bmatrix} \sigma_{rr} \\ \sigma_{zz} \\ \sigma_{\theta\theta} \\ \tau_{rz} \end{Bmatrix} = \boldsymbol{C} \begin{Bmatrix} \varepsilon_{rr} \\ \varepsilon_{zz} \\ \varepsilon_{\theta\theta} \\ \gamma_{rz} \end{Bmatrix} \tag{68}$$

being $\boldsymbol{C}$ the material constitutive matrix, defined for the isotropic case as,

$$\boldsymbol{C} = \frac{E}{(1+\upsilon)(1-2\upsilon)} \begin{bmatrix} 1-\upsilon & \upsilon & \upsilon & 0 \\ \upsilon & 1-\upsilon & \upsilon & 0 \\ \upsilon & \upsilon & 1-\upsilon & 0 \\ 0 & 0 & 0 & \dfrac{1-2\upsilon}{2} \end{bmatrix} \tag{69}$$

The Young's modulus is represented by E and the Poisson's coefficient by υ.

3.2.2 Galerkin Weak-form

This part is almost similar to the one presented in Section 3.1.1 for the 2D solid cases. The differences are related to the coordinate system. Hence revising the previous equations and with regard to the cylindrical coordinate system, the discrete equation system is obtained using the Galerkin weak-form. The Lagrangian functional is defined by

$$L = T - U + W_f . \tag{70}$$

where T is the kinetic energy, U is the strain energy and W_f is the work produced by external forces. Neglecting the dynamic term, the minimization of the Lagrangian functional leads to the Galerkin weak form of the equilibrium equation,

$$\delta L = \int_\Lambda \delta \boldsymbol{\varepsilon}^T \boldsymbol{\sigma}\, d\Lambda - \int_\Lambda \delta \boldsymbol{u}^T \boldsymbol{b}\, d\Lambda - \int_{S_t} \delta \boldsymbol{u}^T \boldsymbol{t}\, dS - \int_{C_q} \delta \boldsymbol{u}^T \boldsymbol{q}\, dC = 0 . \tag{71}$$

As represented in Figure 5(a), $\boldsymbol{b}$ is the body force, $\overline{\boldsymbol{t}}$ an external force applied along a close surface S_t and $\boldsymbol{q}_i$ are external forces applied along a close curve C_t. Notice that from Figure 5(c), the infinitesimal volume $d\Lambda$ is defined as, $d\Lambda = dr \cdot dz \cdot d\theta^*$, being $d\theta^* = r \cdot \sin(d\theta) \cong r \cdot d\theta$ since $d\theta << 1$, which leads to $d\Lambda = r \cdot d\theta \cdot dr \cdot dz = r \cdot d\theta \cdot d\Omega$. Similarly, it is possible to obtain: $dS = dz \cdot d\theta^* = r \cdot d\theta \cdot dz = r \cdot d\theta \cdot d\Gamma$ and $dC = d\theta^* = r \cdot d\theta$.

Thus, Equation (71) can be represented as,

$$\begin{aligned} &\int_\Omega \int_{\theta_i}^{\theta_f} \delta \boldsymbol{\varepsilon}^T \boldsymbol{\sigma}\, r \cdot d\theta \cdot d\Omega = \\ &= \int_\Omega \int_{\theta_i}^{\theta_f} \delta \boldsymbol{u}^T \boldsymbol{b}\, r \cdot d\theta \cdot d\Omega + \int_\Gamma \int_{\theta_i}^{\theta_f} \delta \boldsymbol{u}^T \overline{\boldsymbol{t}}\, r \cdot d\theta \cdot d\Gamma + \int_{\theta_i}^{\theta_f} \delta \boldsymbol{u}^T \boldsymbol{q}\, r \cdot d\theta \end{aligned} . \tag{72}$$

The integral along the circumferential direction θ is a defined integral, and since all analysed problems in this work present a full revolution: $\theta_i = 0$ and $\theta_f = 2\pi$,

$$2\pi \int_\Omega r \left(\delta \boldsymbol{\varepsilon}^T \boldsymbol{\sigma} \right) d\Omega = 2\pi \int_\Omega r \left(\delta \boldsymbol{u}^T \boldsymbol{b} \right) d\Omega + 2\pi \int_\Gamma r \left(\delta \boldsymbol{u}^T \overline{\boldsymbol{t}} \right) d\Gamma + 2\pi r \left(\delta \boldsymbol{u}^T \boldsymbol{q} \right) . \tag{73}$$

or

$$\int_\Omega r \left(\delta \boldsymbol{\varepsilon}^T \boldsymbol{\sigma} \right) d\Omega = \int_\Omega r \left(\delta \boldsymbol{u}^T \boldsymbol{b} \right) d\Omega + \int_\Gamma r \left(\delta \boldsymbol{u}^T \overline{\boldsymbol{t}} \right) d\Gamma + r \left(\delta \boldsymbol{u}^T \boldsymbol{q} \right) . \tag{74}$$

In the RPIM, the weak form has local support, which means that the discrete system of equations is developed firstly for every influence-domain. Then, the local systems of equations are assembled to form the global system of equations, which is solved afterwards. The RPIM trial function is given by Equation (14), thus for each degree of freedom it is possible to write,

$$u_r^{\,h}(\boldsymbol{x}_I)=\sum_{i=1}^{n}\varphi_i(\boldsymbol{x}_I)\,u_r(\boldsymbol{x}_i)\ \text{ and }\ u_z^{\,h}(\boldsymbol{x}_I)=\sum_{i=1}^{n}\varphi_i(\boldsymbol{x}_I)\,u_z(\boldsymbol{x}_i) \tag{75}$$

where $\varphi_i(\boldsymbol{x}_I)$ is the RPIM interpolation function, $u_r(\boldsymbol{x}_i)$ and $u_z(\boldsymbol{x}_i)$ are the nodal parameters of the i^{th} node belonging to the nodal set defining the influence-domain of interest node $\boldsymbol{x}_I$. Both expressions in Equation (75) can be combined in one single equation,

$$\boldsymbol{u}^h(\boldsymbol{x}_I)=\begin{Bmatrix}u_r^{\,h}(\boldsymbol{x}_I)\\ u_z^{\,h}(\boldsymbol{x}_I)\end{Bmatrix}=\sum_{i=1}^{n}\begin{bmatrix}\varphi_i(\boldsymbol{x}_I) & 0\\ 0 & \varphi_i(\boldsymbol{x}_I)\end{bmatrix}\begin{Bmatrix}u(\boldsymbol{x}_i)\\ v(\boldsymbol{x}_i)\end{Bmatrix}=\sum_{i=1}^{n}\boldsymbol{H}_i(\boldsymbol{x}_I)\,\boldsymbol{u}(\boldsymbol{x}_i)\,. \tag{76}$$

Consequently, using Equation (66) and Equation (75), it is possible to develop the strain vector to the following expression,

$$\begin{aligned}\boldsymbol{\varepsilon}(\boldsymbol{x}_I)&=\boldsymbol{L}\,\boldsymbol{u}^h(\boldsymbol{x}_I)=\boldsymbol{L}\sum_{i=1}^{n}\boldsymbol{H}_i(\boldsymbol{x}_I)\,\boldsymbol{u}(\boldsymbol{x}_i)=\\ &=\sum_{i=1}^{n}\boldsymbol{B}_i(\boldsymbol{x}_I)\,\boldsymbol{u}(\boldsymbol{x}_i)=\sum_{i=1}^{n}\begin{bmatrix}\dfrac{\partial\varphi_i(\boldsymbol{x}_I)}{\partial r} & 0\\ 0 & \dfrac{\partial\varphi_i(\boldsymbol{x}_I)}{\partial z}\\ \dfrac{\varphi_i(\boldsymbol{x}_I)}{r} & 0\\ \dfrac{\partial\varphi_i(\boldsymbol{x}_I)}{\partial z} & \dfrac{\partial\varphi_i(\boldsymbol{x}_I)}{\partial r}\end{bmatrix}\begin{Bmatrix}u_r(\boldsymbol{x}_i)\\ u_z(\boldsymbol{x}_i)\end{Bmatrix},\end{aligned} \tag{77}$$

being $\boldsymbol{B}=\boldsymbol{LH}$ the deformation matrix. Using the relation between the stress state and the strain state in Equation (68), it is possible to obtain for an interest point $\boldsymbol{x}_I$: $\boldsymbol{\sigma}(\boldsymbol{x}_I)=\boldsymbol{C}\,\boldsymbol{\varepsilon}(\boldsymbol{x}_I)$ Substituting the strain vector $\boldsymbol{\varepsilon}(\boldsymbol{x}_I)$ and the stress vector $\boldsymbol{\sigma}(\boldsymbol{x}_I)$ in the first term of Equation (74) and the approximation function on Equation (76) in the other terms, it is possible to rewrite Equation (64) for an interest point $\boldsymbol{x}_I$,

$$\delta \boldsymbol{u}^T \underbrace{\int_\Omega r_I \boldsymbol{B}^T \boldsymbol{C}\, \boldsymbol{B} d\Omega}_{\boldsymbol{K}} \boldsymbol{u} = \delta \boldsymbol{u}^T \underbrace{\int_\Omega r_I \boldsymbol{H}^T \begin{Bmatrix} b_r \\ b_z \end{Bmatrix} d\Omega}_{\boldsymbol{f}_b} + \delta \boldsymbol{u}^T \underbrace{\int_{\Gamma_t} r_I \boldsymbol{H}^T \begin{Bmatrix} t_r \\ t_z \end{Bmatrix} d\Gamma_t}_{\boldsymbol{f}_t} + \delta \boldsymbol{u}^T \underbrace{r_I \begin{Bmatrix} q_r \\ q_z \end{Bmatrix}}_{\boldsymbol{f}_q} \quad (78)$$

In the end, after assembling the stiffness matrices $\boldsymbol{K}_I$ obtained for each interest point $\boldsymbol{x}_I$, Equation (78) can be represented as the following linear system of equations,

$$\delta \boldsymbol{u}^T \left[\boldsymbol{K}\, \boldsymbol{u} - \boldsymbol{f}_b - \boldsymbol{f}_t - \boldsymbol{f}_q \right] = 0 \Rightarrow \boldsymbol{K}\, \boldsymbol{u} = \boldsymbol{f}_b + \boldsymbol{f}_t + \boldsymbol{f}_q \,. \quad (79)$$

Since the RPI test functions possess the delta Kronecker property, the essential boundary conditions are directly imposed in the global stiffness matrix, $\boldsymbol{K}$.

Chapter 4

4 *Rate-independent Elastic Damage Formulation*

The continuum damage mechanics theory has the potential to link continuum mechanics with fracture mechanics in an elegant way allowing the analysis of several problems as firstly introduced by Kachanov (Kachanov, 1986) for creep-related problems. Furthermore, it is applicable to different materials such as steel, concrete, ceramics and others. [See e.g. Krajcinovic Fonseka (Krajcinovic & Fonseka, 1981)(Krajcinovic & Fonseka, 1983); Resende and Martin (Resende & Martin, 1984); Cervera et. al. (Cervera et al., 1995, 1996; R. Faria et al., 1998; Oliver et al., 1990); Voyiadjis et. al. (Voyiadjis & Taqieddin, 2009)]. Basically, the last abovementioned articles have been focused on the damage mechanics in concrete materials. The corresponding authors have presented the mathematical relations of rate-independent damage mechanics connected to the subject studied in this work. Crisfield (M.A. Crisfield, 1996), Cervera et.al. (Cervera et al., 1995, 1996; R. Faria et al., 1998; Oliver et al., 1990) adopted the suitable continuum rate-independent damage equations used in this study.

The theory of the continuum damage mechanic relies on the definition of the effective stress concept connected to the equivalent strain. This means that the strain value related to the damage state when the stress $\boldsymbol{\sigma}$ applied, is equivalent to the strain obtained from the undamaged state under the effective stress $\overline{\boldsymbol{\sigma}}$. Considering this principle, the effective stress tensor is expressed as follows:

$$\overline{\boldsymbol{\sigma}} = \boldsymbol{C}: \boldsymbol{\varepsilon} \tag{80}$$

where $\boldsymbol{C}$ is the initial or undamaged second order linear elastic constitutive tensor, $\bar{\boldsymbol{\sigma}}$ and $\boldsymbol{\varepsilon}$ are the second order tensor of the effective stress and strain respectively. Indeed, it is necessary to split the effective stress tensor into tensile and compressive components due to the application of the scalar damage model for the separation of the tensile and compressive damage parameters. So as for splitting the effective stress tensor, the following relations are applicable (Cervera et al., 1995, 1996; R. Faria et al., 1998; Oliver et al., 1990):

$$\bar{\boldsymbol{\sigma}}^{+} = \langle \bar{\sigma} \rangle = \sum_{i=1}^{3} \langle \bar{\sigma}_i \rangle \, p_i \otimes p_i \tag{81-a}$$

$$\bar{\boldsymbol{\sigma}}^{-} = \rangle \bar{\sigma} \langle = \sum_{i=1}^{3} \rangle \bar{\sigma}_i \langle \, p_i \otimes p_i \tag{81-b}$$

It should be clarified that $\otimes$ operates as the dyadic product and the sign of (+) and (-) indicates the tensile and compressive entities respectively. The Macaulay brackets $\langle \bar{\sigma} \rangle$ indicates that the expression is equal to the enclosed value when positive and zero if it is negative. Besides $\rangle \bar{\sigma} \langle$ can be determined as follows:

$$\rangle \bar{\boldsymbol{\sigma}} \langle = \bar{\boldsymbol{\sigma}} - \langle \bar{\boldsymbol{\sigma}} \rangle \tag{82}$$

It must be remarked that the split form of the stress is obtained through using the principal stress and directions referring to Section 3.1.2. The methodology will be discussed later.

Considering the split relations for the effective stress tensor, it is necessary to present the Cauchy stress tensor $\boldsymbol{\sigma}$ as the final relation characterizing the full stress tensor for the isotropic model. So;

$$\bar{\boldsymbol{\sigma}} = \bar{\boldsymbol{\sigma}}^{+} + \bar{\boldsymbol{\sigma}}^{-} \tag{83-a}$$

$$\boldsymbol{\sigma} = (1 - d^{+}) \bar{\boldsymbol{\sigma}}^{+} + (1 - d^{-}) \bar{\boldsymbol{\sigma}}^{-} \tag{83-b}$$

In Equation (83-a), the damage parameters in tension and compression are called d^{+} and d^{-}. As mentioned before, both values are scalars and they should be limited as follows:

$$0 \leq d^{+}, d^{-} \leq 1 \tag{84}$$

Thermomechanical consideration related to the non-negativeness of the dissipation might be expressed by the following expression (Cervera et al., 1996):

$$\dot{d}^{+}, \dot{d}^{-} \geq 0 \tag{85}$$

It is valuable to mention that both damage parameters have the potential to control the degradation of all the elastic material properties such as Young`s modulus, Poisson`s ratio, shear modulus and other relevant properties. Considering the damage parameters, it is possible to infer that the corresponding model could predict the mixed failure of modes I and II in addition to mode I failure. Consequently, the equivalent effective tensile and compressive norms are obtained after splitting the stress as follows:

$$\bar{\tau}^{+} = \sqrt{\bar{\boldsymbol{\sigma}}^{+} : \boldsymbol{C}^{-1} : \bar{\boldsymbol{\sigma}}^{+}} \tag{86-a}$$

$$\bar{\tau}^{-} = \sqrt{\sqrt{3}(K\bar{\sigma}_{oct}^{-} + \bar{\tau}_{oct}^{-})} \tag{86-b}$$

where **:** operates as the tensor multiplication, $\bar{\sigma}_{oct}^{-}$ and $\bar{\tau}_{oct}^{-}$ are the octahedral normal and shear stresses that should be obtained from $\bar{\sigma}^{-}$ tensor (see Section 3.1.4). Furthermore, *K* is a material property depending on the ratio between the biaxial and uniaxial compressive strengths for the concrete materials. It is obtained in the following form (Cervera et al., 1995):

$$K = \sqrt{2}(\beta - 1)(2\beta - 1) \tag{87}$$

Being β the plasticity parameter which is typically assumed as $\beta = 1.16$ for concrete material (Cervera et al., 1995). The damage criteria for tensile and compressive states are expressed as (J C Simo & Ju, 1987):

$$g^{+}(\bar{\tau}^{+}, r^{+}) = \bar{\tau}^{+} - r^{+} \leq 0 \tag{88-a}$$

$$g^{-}(\bar{\tau}^{-}, r^{-}) = \bar{\tau}^{-} - r^{-} \leq 0 \tag{88-b}$$

Equation (88-b) is known as Drucker-Prager cone for compression. The current damage thresholds are defined as r^{+} and r^{-} for tension and compression. They can control the expansion of the damaged surface. In the beginning of the damage routine, r_0^{+} and r_0^{-} are assumed as material properties connected to the uniaxial maximum strengths. In accordance with equations, it is concluded that $\bar{\sigma}_1, \bar{\sigma}_2, \bar{\sigma}_3 \geq 0$ being the 3D effective stresses corresponding to the same norm $\bar{\tau}^{+}$ identified as a quarter of an ellipsoid centered

at the origin of the principal effective stresses presenting the damage bounding surface (Oliver et al., 1990). Subsequently, Figure 6 refers to the damage bounding surface if $\bar{\sigma}_1, \bar{\sigma}_3 \geq 0$, $\bar{\sigma}_2 = 0$ and $\bar{\tau}^+ = r_0^+$ in the 2D case reported by Kupfer (Kupfer et al., 1969) as the experimental solution; while Cervera and his colleagues obtained the computational FEM solution (Cervera et al., 1996) also represented in the same figure.

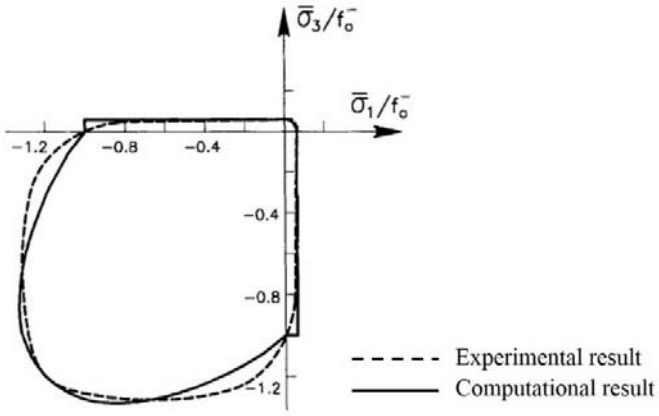

Figure 6: Initial damage bounding surface in a biaxial effective principal stress space (Cervera et al., 1996) compared with the experimental results in concrete (Kupfer et al., 1969).

Consider that f_0^+ and f_0^- are the uniaxial tensile and compressive strengths respectively (R. Faria et al., 1998).

$$r_0^+ = \sqrt{f_0^+ \frac{1}{E} f_0^+} = \frac{f_0^+}{\sqrt{E}} \tag{89-a}$$

$$r_0^- = \sqrt{\frac{\sqrt{3}}{3}\left(K - \sqrt{2}\right) f_0^-} \tag{89-b}$$

As a result, damage experiences an increasing trend if $\bar{\tau}^+ = r^+ \;\; or \;\; \bar{\tau}^- = r^-$. It will be initiated for the first time if $r_0^+ = \bar{\tau}^+ \; and \; r_0^- = \bar{\tau}^-$. Subsequently, in the case of compressive damage, the octahedral stress components could be rewritten as (R. Faria et al., 1998):

$$\sigma_{oct} = \frac{1}{3} f_0^- \tag{90-a}$$

$$\tau_{oct} = -\frac{\sqrt{2}}{3} f_0^- \tag{90-b}$$

The kinematic of the tensile and compressive internal variables are defined based on the consistency conditions for loading through Kuhn-Tucker equations as follows (J C Simo & Ju, 1987):

$$\dot{r}^+ = \dot{\bar{\tau}}^+ \geq 0, \quad \dot{d}^+ = \dot{r}^+ \frac{\partial G^+(r^+)}{\partial r^+} = \dot{G}^+(r^+) \geq 0 \tag{91-a}$$

$$\dot{r}^- = \dot{\bar{\tau}}^- \geq 0, \quad \dot{d}^- = \dot{r}^- \frac{\partial G^-(r^-)}{\partial r^-} = \dot{G}^-(r^-) \geq 0 \tag{91-b}$$

where $G^+$and G^- present the proper monotone increasing function captured from experience could determine the damage evolutions (Cervera et al., 1996). So;

$$r^+ = \max\left(r_0^+, max(\bar{\tau}^+)\right), \quad d^+ = G^+(r^+) \tag{92-a}$$

$$r^- = \max\left(r_0^-, max(\bar{\tau}^-)\right), \quad d^- = G^-(r^-) \tag{92-b}$$

Recent equations prove that the model is rate-independent and the strain is obtained in a closed form. Then, damage variables are computed within the following relations (Cervera et al., 1996):

$$d^+ = G^+(r^+) = 1 - \frac{r_0^+}{r^+}\exp\left(A^+(1 - r^+/r_0^+)\right) \quad \text{if} \quad r^+ \geq r_0^+ \tag{93-a}$$

$$d^- = G^-(r^-) = 1 - \frac{r_0^-}{r^-}(1 - A^-) - A^-\exp\left(B^-(1 - r^-/r_0^-)\right) \quad \text{if} \quad r^- \geq r_0^- \tag{93-b}$$

The damage coefficients A^- and B^- in compression and A^+ in tension will be explained later for each specific benchmark.

4.1 Assessment of the Characteristic Length

In addition to the above mentioned equations, there are some other variables and relations involved in the algorithm of damage criteria. One of the most important parameters is called ***Characteristic Length***. Cervera and his colleagues (R. Faria et al., 1998) investigated that it is known as a geometrical factor depending on the spatial discretization, and that the conservation of the energy dissipated by the material is also guaranteed by this factor. In the usual applications of the finite element, the control area (or volume) coincide with the area ΔA (or volume ΔV) associated with the integration points of each finite element in plane stress (or Gauss points). So, the definition is adopted as follows:

$$l_{ch} = \sqrt{\Delta A} \quad \text{for 2D problems} \tag{94-a}$$

$$l_{ch} = \sqrt[3]{\Delta V} \quad \text{for 3D problems} \tag{94-b}$$

Furthermore, other researchers in meshless method formulations presented different definitions of characteristic length. Ferreira et.al. (Ferreira, Kansa, Fasshauer, & Leitao, 2009) defined that the characteristic length is a parameter related to the nodal spacing in the local support domain of the interest point $(\boldsymbol{x}_I)$ and it is usually the average nodal spacing for all the nodes in the local support domain.

Moreover, Bazant (Bažant & Pijaudier-Cabot, 1989) proposed that the characteristic length of a heterogeneous brittle material such as concrete represents a material property that governs the minimum possible width of a zone of strain-softening damage in non-local continuum formulations or the minimum possible spacing of cracks in discrete fracture models. They calculated the amount of l_{ch} from test results approximately as follows:

$$l_{ch} = \frac{G_f}{W_s} \tag{94-c}$$

Consider fracture energy as $G_f = \frac{U_s}{A_0}$ where energy U_s dissipated due to fracturing in the specimen which is equal to the area below the load-displacement diagram and A_0 is related to the area of the net cross section of the specimen, so, W_s ,called deformation energy prior to fracture, is evaluated from the area below the stress-starin curve as seen in Figure 7.

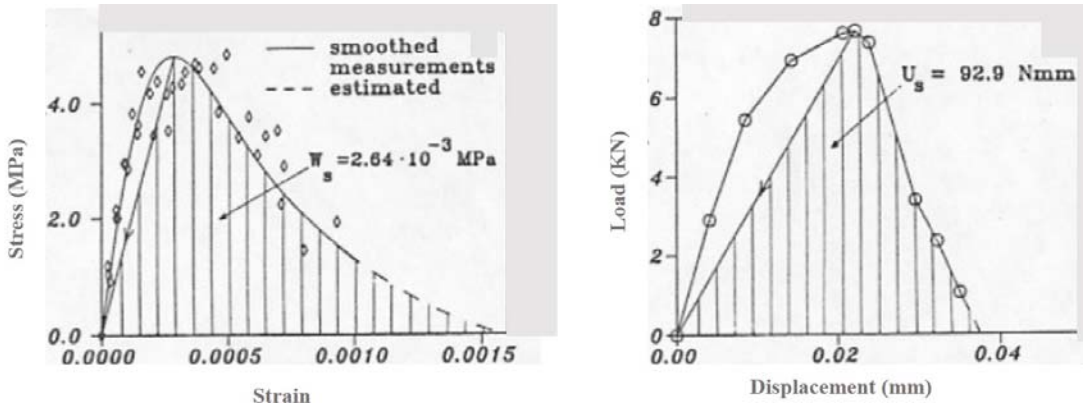

(a) (b)

Figure 7: (a): Stress-strain curve for restrained specimens; (b) Load-displacement curve for unrestrained specimens (Bažant & Pijaudier-Cabot, 1989)

Indeed, there are more scientific works focused on this definition of available in the literature reporting the different equations for the characteristic length (Ghaffarzadeh & Mansouri, 2013; Ghaffarzadeh, 2014; C. T. Wu, Hu, & Guo, 2014).

After that, it is possible to introduce the other parameters dependent on the characteristic length as proposed by Faria and coworkers (Cervera et al., 1995; R. Faria et al., 1998; R. Faria & Oliver, 1993).

$$\bar{H}^{+} = \frac{\left(r_0^{+}\right)^2}{2G_f^{+}} = \frac{\left(f_0^{+}\right)^2}{2EG_f^{+}} \tag{95-a}$$

$$l_{ch} \leq \frac{1}{\bar{H}^{+}} \tag{95-b}$$

where G_f^{+} represents the tensile fracture energy per unit area and f_0^{+} is defined as the uniaxial tensile strength which are available for concrete material in the literature. Subsequently, there is another tensile variable depending on the material property recalled A^{+} which is computed as follows:

$$A^{+} = \frac{2\bar{H}^{+} l_{ch}}{1-\bar{H}^{+} l_{ch}} \tag{96-a}$$

There is a simplified relation of A^{+} proposed by Oliver and his colleagues (Oliver et al., 1990) as follows:

$$A^{+} = \left(\frac{G_f^{+} E}{l_{ch}\left(f_0^{+}\right)^2} - \frac{1}{2}\right)^{-1} \tag{96-b}$$

There are some conditions that should be satisfied in accordance with Equations (95-a,b):

$$A^{+} \geq 0 \tag{96-c}$$

Indeed, the characteristic length controls the maximum size of the finite elements or influence domain in the mesh. It means that if the size of elements in FEM or discretization in meshless method increases, the softening branch of the response experiences an almost vertical slope and perhaps the fracture procedure is more brittle.

It is noticeable to mention that the corresponding variables are calculated at the integration points (Gauss points) in terms of local stress and strain in the field of local models, finite element analysis and meshless method.

Finally, Faria (R. M. C. M. de Faria, 1994) reported that the compressive damage parameters A^{-} and B^{-} may be defined by imposing the unidimensional experimental $(\sigma - \varepsilon)$ curve to achieve the two selected points on the curve extracted from a 1D compressive test. Considering that:

$$\boldsymbol{\sigma} = (1 - d^{-})\bar{\boldsymbol{\sigma}} = \left(\frac{r_0^{-}}{\bar{\tau}^{-}}(1 - A^{-}) + A^{-}e^{B^{-}\left(1-\frac{\bar{\tau}_1^{-}}{r_0^{-}}\right)}\right)\bar{\boldsymbol{\sigma}} \tag{97}$$

Equation (97) has to be satisfied at two particular points $(\varepsilon_1, \sigma_1)$ and $(\varepsilon_2, \sigma_2)$ of the curve $(\sigma - \varepsilon)$ obtained in a 1D compression test. Well, considering these two assumed points with the following characteristics:

Point 1:

$$Cauchy\ stress \quad \sigma_1 \ , \quad effective\ stress\ \bar{\sigma}_1(\varepsilon_1) \overset{so}{\Longrightarrow} Equivalent\ stress \quad \bar{\tau}_1^{-} \ .$$

Point 2:

$$Cauchy\ stress \quad \sigma_2 \ , \quad effective\ stress\ \bar{\sigma}_2(\varepsilon_2) \overset{so}{\Longrightarrow} Equivalent\ stress \quad \bar{\tau}_2^{-} \ .$$

Substituting in Equation (97):

$$\sigma_1 = \frac{r_0^{-}}{\bar{\tau}_1^{-}}\bar{\sigma}_1 + A^{-}\left[e^{B^{-}\left(1-\frac{\bar{\tau}_1^{-}}{r_0^{-}}\right)} - \frac{r_0^{-}}{\bar{\tau}_1^{-}}\right]\bar{\sigma}_1 \tag{98-a}$$

$$\sigma_2 = \frac{r_0^{-}}{\bar{\tau}_2^{-}}\bar{\sigma}_2 + A^{-}\left[e^{B^{-}\left(1-\frac{\bar{\tau}_2^{-}}{r_0^{-}}\right)} - \frac{r_0^{-}}{\bar{\tau}_2^{-}}\right]\bar{\sigma}_2 \tag{98-b}$$

Therefore;

$$A^{-} = \frac{\sigma_1 - \frac{r_0^{-}}{\bar{\tau}_1^{-}}\bar{\sigma}_1}{\left(e^{B^{-}\left(1-\frac{\bar{\tau}_1^{-}}{r_0^{-}}\right)} - \frac{r_0^{-}}{\bar{\tau}_1^{-}}\right)\bar{\sigma}_1} \tag{99}$$

Combining the equations:

$$\sigma_2 - \frac{r_0^{-}}{\bar{\tau}_2^{-}}\bar{\sigma}_2 = \frac{\left[e^{B^{-}\left(1-\frac{\bar{\tau}_2^{-}}{r_0^{-}}\right)} - \frac{r_0^{-}}{\bar{\tau}_2^{-}}\right]\bar{\sigma}_2}{\left[e^{B^{-}\left(1-\frac{\bar{\tau}_1^{-}}{r_0^{-}}\right)} - \frac{r_0^{-}}{\bar{\tau}_1^{-}}\right]\bar{\sigma}_1}\left(\sigma_1 - \frac{r_0^{-}}{\bar{\tau}_1^{-}}\bar{\sigma}_1\right) \tag{100}$$

$$a_1 = \left(\sigma_2 - \frac{r_0^{-}}{\bar{\tau}_2^{-}}\bar{\sigma}_2\right)\bar{\sigma}_1 \tag{101-a}$$

$$a_2 = \left(\sigma_1 - \frac{r_0^-}{\bar{\tau}_1^-}\bar{\sigma}_1\right)\bar{\sigma}_2 \qquad (101-b)$$

$$f(B^-) = a_1\left[e^{B^-\left(1-\frac{\bar{\tau}_1^-}{r_0^-}\right)} - \frac{r_0^-}{\bar{\tau}_1^-}\right] - a_2\left[e^{B^-\left(1-\frac{\bar{\tau}_2^-}{r_0^-}\right)} - \frac{r_0^-}{\bar{\tau}_2^-}\right] \qquad (102)$$

This non-linear equation which contains a single variable determination B^-, can be performed based on the iterative Newton-Raphson Method according to the recursive expression:

$$(B^-)^{i+1} = (B^-)^i - \frac{f\left((B^-)^i\right)}{f'\left((B^-)^i\right)} \qquad (103)$$

So;

$$f'\left((B^-)^i\right) = \left(\frac{\partial f}{\partial B^-}\right)' = a_1\left[1-\frac{\bar{\tau}_1^-}{r_0^-}\right]e^{B^-\left(1-\frac{\bar{\tau}_1^-}{r_0^-}\right)} - a_2\left[1-\frac{\bar{\tau}_2^-}{r_0^-}\right]e^{B^-\left(1-\frac{\bar{\tau}_2^-}{r_0^-}\right)} \qquad (104)$$

Afterwards, it is needed to compute the vector of unique damage parameter in the material which is a combination of tensile and compressive damage values obtained from the end of algorithm. If it is considered as a vector $\boldsymbol{d}_{n+1}$ with the size of number of integration points, it should be updated for each integration point at the end of each displacement enforcement increment based on the following equations:

$$\boldsymbol{\sigma_{n+1}} = (1-d_{n+1})[\boldsymbol{C}]\{\boldsymbol{\varepsilon_{n+1}}\} = (1-d_{n+1})[\bar{\boldsymbol{\sigma}}_{\boldsymbol{n+1}}] \qquad (104)$$

Since the unique damage parameter *(d)* is a scalar value, it should be calculated in accordance with the equivalent von Mises stress in each integration point. In Subsection 3.1.3, considering Equation (51), it is possible to rewrite the last equation in the following form:

$$d_{n+1} = 1 - \frac{\tilde{\sigma}_{n+1}}{\bar{\tilde{\sigma}}_{n+1}} \qquad (105)$$

Through application of the above relation at the end of the damage stage, the scalar damage vector is updated for each integration point.

It must be remarked that the characteristic length will be modified within convergence studies in this work based on the different presented examples since it is a demanding

variable. Indeed the tensile parameters A^+ and $\bar{H}^+$ are also changed due to their dependency on the characteristic length.

It is worth to mention that the abovementioned equations are relevant to the non-local damage formulations. They will be extended to the localized damage one discussed in Subsection 4.3.

4.2 Helmholtz Free Energy Relations

Since the continuum damage mechanics is an irreversible process in the sense of thermodynamics, the defined constitutive model should be related to a free energy potential such as Helmholtz free energy. The Helmholtz free energy potential is known as a function of the internal variables indicating the compressive and tensile behaviour of concrete materials as reported by Lubliner (Lubliner, 1972), Salari et. al.(Salari, Saeb, Willam, Patchet, & Carrasco, 2004), Shao et. al. (Shao, Jia, Kondo, & Chiarelli, 2006)and Faria et. al. (R. Faria & Oliver, 1993).

The current damage model is based on the uncoupled elasticity theory proposed by Faria and Oliver (R. Faria & Oliver, 1993). The total free energy is split into the elastic and plastic parts in the process. Since the elastic damage model is used here, regardless the plasticity effects, the form of Helmholtz energy relation is presented as follows:

$$\psi(\varepsilon, d^+, d^-) = (1 - d^+)\psi_0^+(\varepsilon) + (1 - d^-)\psi_0^-(\varepsilon) \tag{106}$$

If ψ_0^+ and ψ_0^- represent the free elastic energies in tension and compression states, respectively, Equations (107-a) and (107-b), the tensor multiplications, are proposed:

$$\psi_0^+\left(\bar{\sigma}(\varepsilon)\right) = \frac{1}{2}\bar{\boldsymbol{\sigma}}^+ : \boldsymbol{C^{-1}} : \bar{\boldsymbol{\sigma}} \tag{107-a}$$

$$\psi_0^-\left(\bar{\sigma}(\varepsilon)\right) = \frac{1}{2}\bar{\boldsymbol{\sigma}}^- : \boldsymbol{C^{-1}} : \bar{\boldsymbol{\sigma}} \tag{107-b}$$

According to Equation (107-a), it is obvious that the damage phenomenon influences only the elastic behaviour and does not have any influences on the plastic properties. It means that the internal variables are constituted by the elastic strain tensor with regard to damage variables in tension and compression in the rate-independent elastic damage model. Indeed,

$\boldsymbol{C}^{-1}$ represents the (undamaged) linear elasticity second order tensor and could be defined based on the Kronecker delta property as follows:

$$\boldsymbol{C}^{-1}_{ijkl} = \boldsymbol{C}^{-1}_{klij} = \frac{1}{E}\left[\frac{1+\nu}{2}\left(\delta_{ik}\delta_{jl} + \delta_{il}\delta_{jk}\right) - \nu\delta_{ij}\delta_{kl}\right] \tag{108}$$

where E and ν are the undamaged Young's modulus and Poisson's ratio.

In another definition, if the damage and plasticity effects are neglected, the free Helmholtz energy should be fulfilled the elastic free energy ψ_0. This decomposition is derived from Equations (106) and (107) with regard to $d^+ = d^- = 0$ and $\overline{\boldsymbol{\sigma}} = \boldsymbol{C}:\boldsymbol{\varepsilon}$ (La Borderie, Berthaud, & Pijaudier-Cabot, 1990; Mazars & Pijaudier-Cabot, 1989).

$$\psi_0 = \psi_0^+ + \psi_0^- = \frac{1}{2}(\overline{\boldsymbol{\sigma}}^+ + \overline{\boldsymbol{\sigma}}^-):\boldsymbol{C^{-1}}:\overline{\boldsymbol{\sigma}} = \frac{1}{2}\boldsymbol{\varepsilon}:\boldsymbol{C}:\boldsymbol{\varepsilon} \tag{109}$$

Faria et. al. (R. Faria & Oliver, 1993) extended the free energy equation based on the effective stress tensor, in the following form:

$$\psi_0^+ = \frac{1+\nu}{2E}\overline{\boldsymbol{\sigma}}^+:\overline{\boldsymbol{\sigma}} - \frac{\nu}{2E}tr(\bar{\sigma})tr(\bar{\sigma}^+) \tag{110}$$

Where $\overline{\boldsymbol{\sigma}}$ is split in the tensile and compressive components, then $tr(\overline{\boldsymbol{\sigma}}) = tr(\overline{\boldsymbol{\sigma}}^+) + tr(\overline{\boldsymbol{\sigma}}^-)$ and afterwards, the following condition must be satisfied: $\overline{\boldsymbol{\sigma}}^+:\overline{\boldsymbol{\sigma}}^- = 0$

It is also possible to rewrite the recent equation of tensile elastic free energy in terms of the total energy and compressive one.

$$\psi_0^+ = \frac{1+\nu}{2E}\overline{\boldsymbol{\sigma}}^+:\overline{\boldsymbol{\sigma}}^+ - \frac{\nu}{2E}tr^2(\overline{\boldsymbol{\sigma}}^+) - \frac{\nu}{2E}tr(\overline{\boldsymbol{\sigma}}^-)tr(\overline{\boldsymbol{\sigma}}^+) \tag{111-a}$$

$$\psi_0^+ = \frac{1}{2}\overline{\boldsymbol{\sigma}}^+:\boldsymbol{C^{-1}}:\overline{\boldsymbol{\sigma}}^+ + \left(-\frac{\nu}{2E}tr(\overline{\boldsymbol{\sigma}}^-)tr(\overline{\boldsymbol{\sigma}}^+)\right) \tag{111-b}$$

It is visible that $\overline{\boldsymbol{\sigma}}^+$and $\overline{\boldsymbol{\sigma}}^-$accounted for the positive and negative values due to their split form effective stress tensor in tension and compression respectively. So, the multiplication of $tr(\overline{\boldsymbol{\sigma}}^-)tr(\overline{\boldsymbol{\sigma}}^+)$ is certainly negative leading to achieve the positive form in the second term of the right-hand side. Furthermore, the first double product of the tensile split effective stress component is obviously positive. Overall, the computation of the recent equation proves that $\psi_0^+ \geq 0$. Moreover, the same procedure and relations are applied to show that $\psi_0^- \geq 0$.

All the aforementioned relations of the Helmholtz free energy equations demonstrate that if the damage variables are placed in the range of $0 \leq d^{+} and\ d^{-} \leq 1$, the final expression of the Helmholtz free energy could be presented as follows:

$$\psi = (1 - d^{+})\psi_0^{+} + (1 - d^{-})\psi_0^{-} \tag{112}$$

As a result of Equation (112), it is shown that $\psi \geq 0$ since all the corresponding terms are non-negative as mentioned before.

Based on the work conducted by Murakami (Murakami, 1983) and Ju (Ju, 1990), it is possible to establish the damage tensor for the process of damage mechanics; but due to the nature of the rate-independent elastic damage model in this study, the scalar damage variables are considered an adequate approximation.

Furthermore, in the case of elastic damage model, the Helmholtz free energy potential is defined as a function of the effective stress tensor $\bar{\boldsymbol{\sigma}}$ in the concept of explicit scheme when the material experiences no plastic strain. But there are some studies conducted by Mazars et. al. (Mazars & Pijaudier-Cabot, 1989)and La Borderie et. al. (La Borderie et al., 1990) referring to the presence of the Cauchy stress tensor instead of the effective stress that it is usually obtained as a consequence of the algorithm.

Subsequently, it is rational to represent the simplified Equations for Helmholtz free energy potential in terms of damage variables as Faria et. al. (R. Faria & Oliver, 1993)reported as follows:

$$-\frac{\partial \psi}{\partial d^{+}} = \psi_0^{+} \quad \text{for tension state}$$

$$-\frac{\partial \psi}{\partial d^{-}} = \psi_0^{-} \quad \text{for compression state}$$

In accordance with the concept of damage mechanics (R. Faria & Oliver, 1993), it is noticeable to mention that ψ_0^{+} and ψ_0^{-} might be identified as the thermodynamic forces subjected to the tensile and compressive damage variables with the specific amount of elastic strain energy respectively.

4.3 Damage Localization Formalism

The non-local constitutive model has been formalized so far. This part is devoted to the process of localized damage mechanics. The standard local constitutive models are inappropriate for materials that exhibit strong strain softening (Jirásek, 1998). There are several ways to proceed the localization aspect. The simplest remedy is to adjust post peak slope of stress-strain curve as a function of the element size (Jirásek, 1998). More refined approaches ensuring the targets are known as localization limiters including the higher order gradient models

So, The methodology adopted in this work is as follows:

First, the non-local tensile and compressive damage values are calculated within the rate-independent continuum damage mechanics formulations. After that, a circle with a certain radius should be defined. This circle covers the integration points (neighbour points) that are going to participate in damage localization process. It is centred in the interest integration point which is being analysed.

$$RGP = n_p h \tag{113-a}$$

The radius of this circle is so-called "*RGP*" dependent on the average distance between nodes, *h*. Consider the nodes discretised in specific divisions along *x* and *y* directions, *h* is computed based on the following relation:

$$h = \frac{L}{divisions\ along\ x} = \frac{D}{divisions\ along\ y} \tag{113-b}$$

where *L* and *D* are the dimensions of the specimen along *x* and *y* directions.

Equation (113-b) shows that the nodal discretization could affect *RGP*. Indeed, n_p is a constant value depended on the order of the weight function discussed later.

Any Gauss point locating at each integration cell is identified by the following vector:

$$\boldsymbol{gp_{ii}} = \begin{Bmatrix} x_{ii}^{gp} \\ y_{ii}^{gp} \\ W_{ii}^{gp} \end{Bmatrix} \tag{114}$$

where x_{ii}^{gp} and y_{ii}^{gp} are defined as the dimensions in *x* and *y* directions respectively; and W_{ii}^{gp} is related to the weight of the corresponding Gauss point. It should be noted that the size of the above mentioned vector is 3 by the total number of the integration points discretized on the geometry.

Afterwards, in order to detect the distance between the interest point and its neighbours, it is mandatory to define a condition as follows:

$$d_{ij} = \sqrt{\left(gp(1,ii) - gp(1,jj)\right)^2 + \left(gp(2,ii) - gp(2,jj)\right)^2} \tag{115-a}$$

Where *d* is the distance between two integration point (the interest and neighbour ones), the terms with *ii* and *jj* are relevant to the interest and neighbour integration points. The corresponding neighbour points are selected if:

$$d_{ij} < RGP \tag{115-b}$$

Figure 8 clarifies the abovementioned explanation.

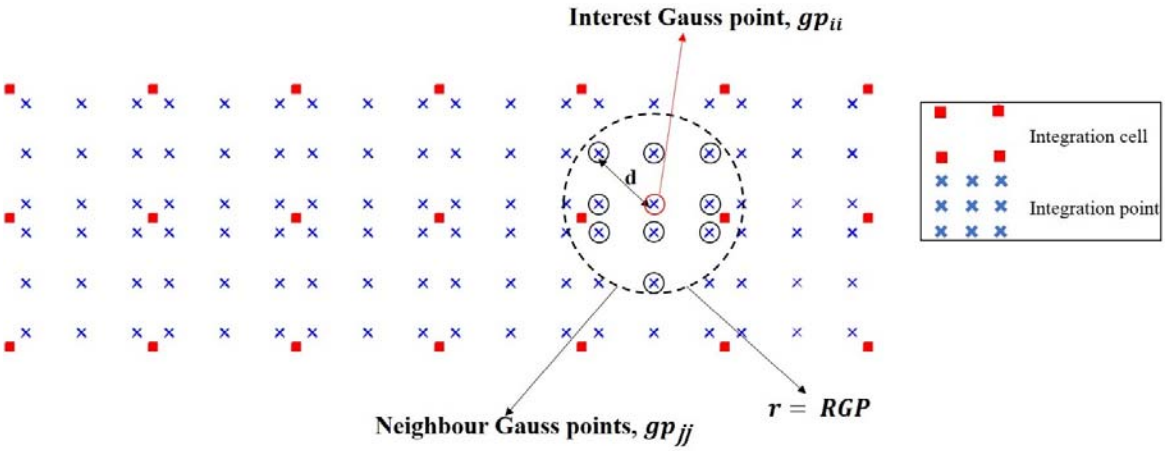

Figure 8: The schematic view of the interest and neighbor integration points in three point bending beam

Subsequently, after detecting the points satisfied the above conditions, it is necessary to define the weight function leading to sharing the damage value on the interest point with

the neighbours. There are some weight functions identified in different orders. The ones used in this analysis are presented on Table 1.

Table 1: Weight function for localization process

Order	Weight function
0	$w = 1$
2nd	$w = -\frac{(d_{ij})^2}{RGP^2} + 1$
3rd	$w = 2\frac{(d_{ij})^3}{RGP^3} - 3\frac{(d_{ij})^2}{RGP^2} + 1$

Afterwards, the collected neighbour points participate in the damage localization so that the damage value of the interest point is distributed between them in accordance with their weights and it should be summed for all the points. It means that the summation is obtained within an iterative process. The weight of integration points resulted from Table 1 is updated for each acceptable neighbour points (satisfied Equation (115-b)) in tensile and compressive states based on the below summation:

$$w_{total}^{+/-} = \sum_{n=1}^{jj} w(jj) \tag{116}$$

Subsequently, another function should be defined which is the weighted damage parameter on the neighbour points. This is the step that the damage sharing process starts. The following relation is adopted within the below summation:

$$w_d^{+/-} = \sum_{n=1}^{jj} d^{+/-}(jj) * w(jj) \tag{117}$$

Where d^+ and d^- are the non-local tensile and compressive damage parameters belonging to the jj^{th} integration point and $w^+$and w^- are the tensile and compressive weight functions.

At the end, the new damage value of the interest point is obtained based on the divided product of the total summation of damage over the total weights. So, the damage is localized for that specific interest point as:

$$d^{+}_{localized} = \frac{w^{+}_{d}}{w^{+}_{total}} \qquad (118-a)$$

$$d^{-}_{localized} = \frac{w^{-}_{d}}{w^{-}_{total}} \qquad (118-b)$$

The numerical algorithm of the damage localization is presented in Box 1.

Step $n = 0$

(i) Set $w^{+}_{total} = 0$ and $w^{-}_{total} = 0$

(ii) Set $w^{+}_{d} = 0$ and $w^{-}_{d} = 0$

(iii) Defining *RGP* Equation (113-a)

Step *n+1*, loop over all integration points

For the ii^{th} interest point

(iv) Loop over all the other integration points (neighbours)

Check the distance $d_{ij} < RGP$ Equation (115)

If yes, it is the acceptable neighbour point

Use the weight function (*W*) based on table 1

Update w^{+}_{total} and w^{-}_{total} Equation (116)

Update w^{+}_{d} and w^{-}_{d} Equation (117)

If no, the neighbour integration point is outside the circle, go for the next integration point.

(v) Calculation of the localized damage

$(d^{+}_{localized})_{ii} = \frac{w^{+}_{d}}{w^{+}_{total}}$ For tension, Equation (118-a)

$(d^{-}_{localized})_{ii} = \frac{w^{-}_{d}}{w^{-}_{total}}$ For compression, Equation (118-b)

(vi) Updating the vector of localized tensile and compressive damage for all the interest points

End of test

Box 1: The numerical algorithm to obtain localized damage parameters

After the damage localization stage, it is possible to calculate the Cauchy stress tensor based on the following relation developed form of Equation (83-b) (M.A. Crisfield, 1996):

$$\boldsymbol{\sigma} = (1 - d^{+}_{localized})\overline{\boldsymbol{\sigma}}^{+} + (1 - d^{-}_{localized})\overline{\boldsymbol{\sigma}}^{-} \tag{119}$$

Where $\overline{\boldsymbol{\sigma}}^{+}$ and $\overline{\boldsymbol{\sigma}}^{-}$ are the effective stress tensor in tension and compression respectively. To calculate the total damage parameter, it is required to use the equivalent von Mises stress since the damage is a scalar parameter. Thus, Equation (51) is applicable here.

$$\tilde{\bar{\sigma}} = (1 - d)\tilde{\sigma} \tag{120}$$

$$d = 1 - \frac{\tilde{\bar{\sigma}}}{\tilde{\sigma}} \tag{121}$$

Where d is the total damage value calculated for each integration point and $\tilde{\bar{\sigma}}$ and $\tilde{\sigma}$ are the equivalent von Mises stress in effective and total (Cauchy stress) terms (M.A. Crisfield, 1996). It is noticeable that the obtained total damage is a result of localized tensile and compressive damage parameters.

At the end of the procedure, the vector of total damage $(d)$is updated for each interest point, to be used in the further calculations.

4.4 Computational Implementation of the Constitutive Law

The strain field is determined when the routine performs for each step of displacement enforcement, then the internal variables are updated directly as the outcome of the algorithm. This mechanism relies on the strain-driven formalism of the corresponding constitutive model. Box 2 presents the return-mapping algorithm of rate-independent elastic damage for evaluation of Cauchy Stress Tensor with regard to a given strain tensor for any pseudo-time stepping scheme in the enforcement of displacement using RPIM meshless formulations. Indeed this algorithm is based on the mathematical relations for non-local damage mechanics presented in previous sections.

It should be noted that return-mapping algorithm is applied with the non-linear Newton-Raphson method to acquire the non-linear damage solution. The principal effective stress tensor is adopted instead of the general form.

Step $n = 0$

(i) **Set** $r_n^+ = r_0^+ \, , r_n^- = r_0^-$ Stress norms

$d_n^+ = 0 \;\; , \; d_n^- = 0$ Scalar damage variables

Step $n + 1$

(ii) Evaluate $\boldsymbol{\varepsilon_{n+1}}$ Trial strain, Eq. (23)

Then, compute $\bar{\boldsymbol{\sigma}}_{\boldsymbol{n+1}} = \boldsymbol{C} : \boldsymbol{\varepsilon_{n+1}}$ Effective stress of damage routine, Eq. (80)

Principal stress and directions refer to Section 3.1.2

(iii) Split $\bar{\boldsymbol{\sigma}}_{\boldsymbol{n+1}}$ into $\bar{\boldsymbol{\sigma}}_{\boldsymbol{n+1}}^+$ and $\bar{\boldsymbol{\sigma}}_{\boldsymbol{n+1}}^-$ Effective tensile and compressive stress, Eq. (81)

Obtain $\sigma_{oct}^-, \tau_{oct}^-$ Referring to Section 3.1.4, Equations (57) and (59)

(iv) Calculate $\bar{\tau}_{n+1}^+$ and $\bar{\tau}_{n+1}^-$ Tensile and compressive equivalent stress, Eq. (86)

Test for tensile and compressive damage

(v) If $\bar{\tau}_{n+1}^+ > r_n^+$,set $r_{n+1}^+ = max\{r_n^+, \bar{\tau}_{n+1}^+\}$ Update tensile damage threshold, Eq. (92-a)

If $\bar{\tau}_{n+1}^- > r_n^-$, set $r_{n+1}^- = max\{r_n^-, \bar{\tau}_{n+1}^-\}$ Update compressive damage threshold, Eq. (92-b)

Update of damage variables

(vi) $d_{n+1}^+ = G^+(r_{n+1}^+)$ Tensile damage parameter, Eq. (93-a)

$d_{n+1}^- = G^-(r_{n+1}^-)$ Compressive damage parameter, Eq. (93-b)

Compute the final Cauchy stress tensor

(vii) $\boldsymbol{\sigma_{n+1}} = (1 - d_{n+1}^+)\bar{\boldsymbol{\sigma}}_{\boldsymbol{n+1}}^+ + \; (1 - d_{n+1}^-)\bar{\boldsymbol{\sigma}}_{\boldsymbol{n+1}}^-$ Based on Eq. (83-b)

End of test.

Box 2: Algorithm to evaluate the stress tensor for the elastic damage model – non-local state

As mentioned before, it is possible to present the return-mapping algorithm with regard to the damage localization formalism (Section 4.3). Box 3 represents the return mapping algorithm to calculate the localized damage parameters with regard to the damage localization concept.

Step $n = 0$

(i) **Set** $r_n^+ = r_0^+ , r_n^- = r_0^-$ Stress norms

$d_n^+ = 0 \ , \ d_n^- = 0$ Scalar damage variables

Step $n + 1$

(ii) Evaluate $\boldsymbol{\varepsilon_{n+1}}$ Trial strain, Eq. (23)

Then, compute $\bar{\boldsymbol{\sigma}}_{\boldsymbol{n+1}} = \boldsymbol{C} : \boldsymbol{\varepsilon_{n+1}}$ Effective stress of damage routine, Eq. (80)

Principal stress and directions Refer to Section 3.1.2

(iii) Split $\bar{\boldsymbol{\sigma}}_{\boldsymbol{n+1}}$ into $\bar{\boldsymbol{\sigma}}_{\boldsymbol{n+1}}^+$ and $\bar{\boldsymbol{\sigma}}_{\boldsymbol{n+1}}^-$ Effective tensile and compressive stress, Eq. (81)

Obtain $\sigma_{oct}^-, \tau_{oct}^-$ Referring to Section 3.1.4, Equations (57) and (59)

(iv) Calculate $\bar{\tau}_{n+1}^+$ and $\bar{\tau}_{n+1}^-$ Tensile and compressive equivalent stress, Eq. (86)

Test for tensile and compressive damage

(v) If $\bar{\tau}_{n+1}^+ > r_n^+$,set $r_{n+1}^+ = max\{r_n^+, \bar{\tau}_{n+1}^+\}$ Update tensile damage threshold, Eq. (92-a)

If $\bar{\tau}_{n+1}^- > r_n^-$, set $r_{n+1}^- = max\{r_n^-, \bar{\tau}_{n+1}^-\}$ Update compressive damage threshold, Eq. (92-b)

Update of damage variables

(vi) $d_{n+1}^+ = G^+(r_{n+1}^+)$ Tensile damage parameter, Eq. (93-a)

$d_{n+1}^- = G^-(r_{n+1}^-)$ Compressive damage parameter, Eq. (93-b)

(vii) Go to Box 1, obtain the localized tensile and compressive damage parameters

(viii) Compute the final Cauchy stress tensor

$$\boldsymbol{\sigma_{n+1}} = \left(1 - (d_{n+1}^+)^{Localized}\right)\bar{\boldsymbol{\sigma}}_{\boldsymbol{n+1}}^+ + \left(1 - (d_{n+1}^-)^{Localized}\right)\bar{\boldsymbol{\sigma}}_{\boldsymbol{n+1}}^- \quad \text{Equation (119)}$$

(ix) Computation of total damage parameter

$$d = 1 - \frac{\tilde{\bar{\sigma}}}{\tilde{\sigma}} \quad \text{Equation (121)}$$

End of test.

Box 3: Algorithm to evaluate the damage parameter for the elastic localized rate-independent damage model

The differences between the algorithms presented in Box 2 and Box 3 are related to the stage where the tensile and compressive damage terms are updated in. Then, the Cauchy stress tensor is computed based on the localized tensile and compressive damage variables and finally the total damage is obtained.

Chapter 5

5 *Numerical Applications on Axisymmetric Deformation Theory*

In this chapter, first the RPIM is calibrated and validated for the axisymmetric deformation theory using the Galerkin weak formulation. Afterwards, three distinct examples of circular plates with different boundary conditions are analysed. All the examples are compared with the FEM solution obtained with the commercial FEM software ANSYS. In the FEM analysis it was used the PLANE182 element, which is a linear four-node axisymmetric element.

In this work the transversal centre displacement of the circular plate in full magnitude is chosen, $u_z(r=0)$ and the normalized value, $\overline{u}_z(r=0)$ which can be determined with:

$$\overline{u}_z(0) = 100 \times u_z(0) \times \left(\frac{E\ H^3}{R^4\ q} \right) \tag{122}$$

where q is the magnitude of external force applied on the circular plate and E the material elasticity modulus. The scalars R and H represent the radius and the thickness of the plate respectively.

Additionally, the first order local error on the centre of the plate is presented in all tables,

$$error = \frac{u_z(r=0)^{RPIM} - u_z(r=0)^{exact}}{u_z(r=0)^{exact}}, \tag{123}$$

being $u_z(r=0)^{RPIM}$ the solution obtained with the meshless method and $u_z(r=0)^{exact}$ the solution obtained with the considered exact solution.

Regarding the material properties, in all examples are considered: Elasticity modulus $E = 10^6\, Pa$ and Poisson's coefficient $\upsilon = 0.3$.

5.1 Circular Plate under Uniform Distributed Load

In this section it is studied a circular plate under a uniform distributed load (UDL) with magnitude: $q = 100 N/m^2$. Two distinct boundary conditions are studied, which include simply supported (SSSS) and clamped (CCCC) contours. The analytical solution of the circular plate for the displacement of the circular SSSS plate under an UDL is obtained from the following expression (Timoshenko & Woinowsky-Krieger)

$$u_z(r) = \frac{q\left(R^2 - r^2\right)\left[\left(\frac{5+\upsilon}{1+\upsilon}\right)R^2 - r^2\right]}{\frac{64\,E\,H^3}{12\left(1-\upsilon^2\right)}}. \tag{124}$$

The analytical solution of the circular CCCC plate submitted to a UDL is obtained with,

$$u_z(r) = \frac{q\left(R^2 - r^2\right)^2}{\frac{64\,E\,H^3}{12\left(1-\upsilon^2\right)}}. \tag{125}$$

where r is defined as the distance between the interest point P and the centre of the plate, Figure 9.

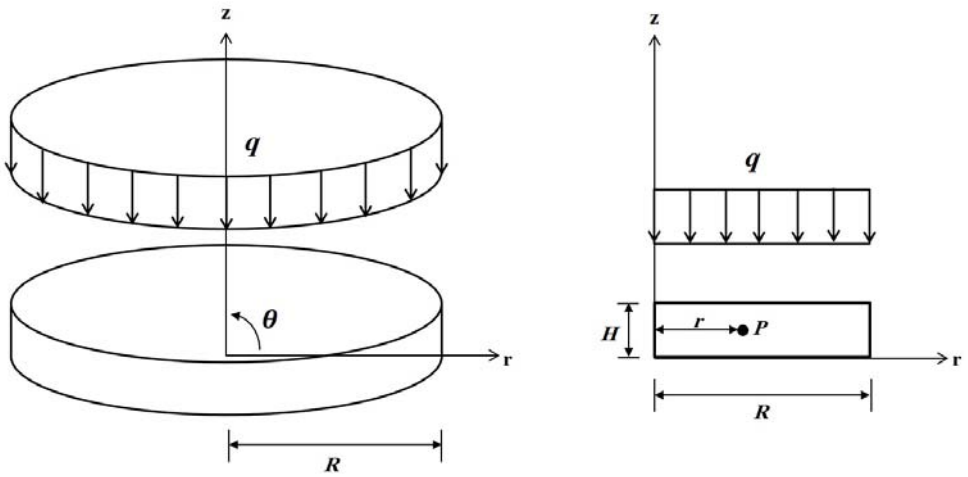

Figure 9 : Circular plate under circular uniform distributed load

5.1.1 Convergence Study

In this subsection the convergence rate of the RPIM is studied. Consider the two-dimensional domain presented in Figure 9. In this study it is considered the following dimensions: $R = 20m$ and $H = 1m$. The problem domain is discretized in a regular mesh of $n_r \times n_z$ nodes, being n_r the number of nodes along the direction r and n_z the number of nodes on direction z. The problem was analysed using the RPIM and the FEM. Both numerical solutions are compared with the analytical exact solution for the SSSS circular plate, Equation (124), and for the CCCC circular plate, Equation (125).

The results regarding the convergence study are shown in Table 2 and Table 3 respectively for the SSSS and the CCCC cases. The results show that the final converged values of the RPIM solutions and the FEM solutions are very close to each other, Figure 10. Additionally, it is visible that using more than 123 nodes permits to obtain errors below 1%.

Table 2 : Transversal displacement values of exact solution, RPIM and FEM, with the variation of the number of nodes in each direction for the SSSS case.

nodes			u_z (m) – transversal displacement			$\overline{u}_z$ – normalized displacement			Error (%)	Error (%)
n_z	n_r	total	exact	RPIM	FEM	exact	RPIM	FEM	RPIM-exact	FEM-exact
3	41	123	11.1300	10.9613	11.1570	69.5625	68.5079	69.7313	1.5160	0.2426
5	81	405	11.1300	11.0887	11.1560	69.5625	69.3041	69.7250	0.3714	0.2336
9	161	1449	11.1300	11.1452	11.1560	69.5625	69.6575	69.7250	0.1366	0.2336
17	321	5457	11.1300	11.1602	11.1560	69.5625	69.7512	69.7250	0.2713	0.2336

Table 3 : Transversal displacement values of exact solution, RPIM and FEM, with the variation of the number of nodes in each direction for the CCCC case.

nodes			u_z (m) – transversal displacement			$\overline{u}_z$ – normalized displacement			Error (%)	Error (%)
n_z	n_r	total	exact	RPIM	FEM	exact	RPIM	FEM	RPIM-exact	FEM-Exact
3	41	123	2.7300	2.5823	2.7480	17.0625	16.1392	17.1750	5.4111	0.6593
5	81	405	2.7300	2.7086	2.7518	17.0625	16.9291	17.1988	0.7821	0.7985
9	161	1449	2.7300	2.7432	2.7539	17.0625	17.1449	17.2119	0.4830	0.8755
17	321	5457	2.7300	2.7521	2.7548	17.0625	17.2009	17.2175	0.8111	0.9084

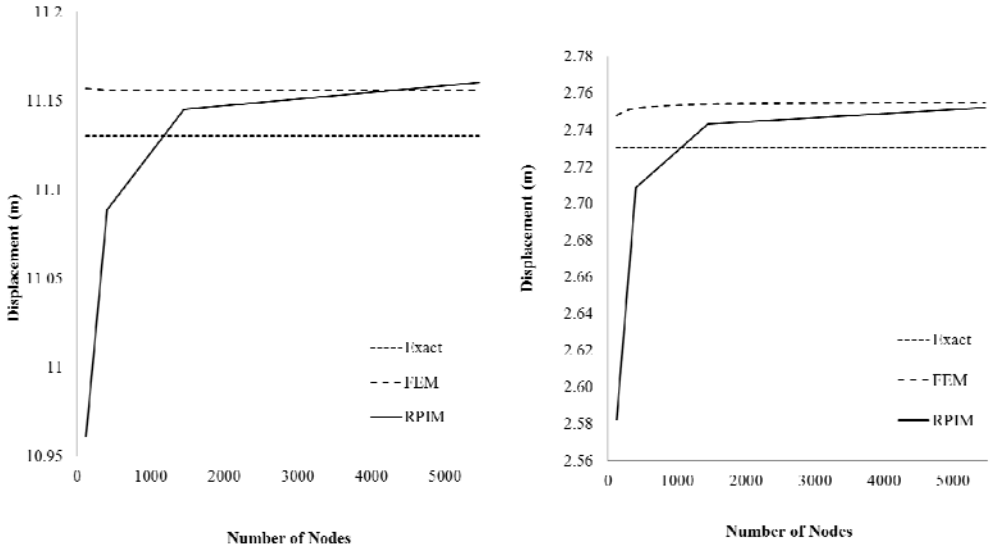

(a) (b)

Figure 10 : Transversal displacement values obtained from exact, RPIM and FEM methods regarding of number of nodes for (a) SSSS, (b) CCCC.

5.1.2 Numerical Integration Scheme

In order to determine the optimal number of integration points inside every integration cell, it is required to perform a transversal study on the several quadrature schemes of Gaussian points inside the integration cell.

Consider Figure 11 , in which a general example of an integration cell is presented. Inside the integration cell are inserted 3×3 integration points respecting the Gauss-Legendre quadrature scheme. In this study all the integration cells respect the geometric disposition shown in Figure 11, i.e. all integration cells contain 9 nodes and $n_Q \times n_Q$ integration points respecting the Gauss-Legendre quadrature scheme. Aiming to determine the optimal number of integration points inside each integration cell, the value n_Q was varied between 2 and 10. All the material, geometrical and loading conditions considered in Subsection 5.1.1 are assumed. The results for the SSSS and the CCCC cases are shown respectively in Table 4 and Table 5.

The values on the tables indicate that the solution starts to stabilize to integration schemes using $n_Q > 5$. However, the increase of n_Q increases the computational cost of the RPIM analysis. Thus, in this work, in all further examples it is used 3×3 integration points inside each integration cell (see Figure 11), since with this integration scheme it is possible to obtain solutions showing acceptable errors (below 0.8%) without increasing significantly the computational cost of the analysis.

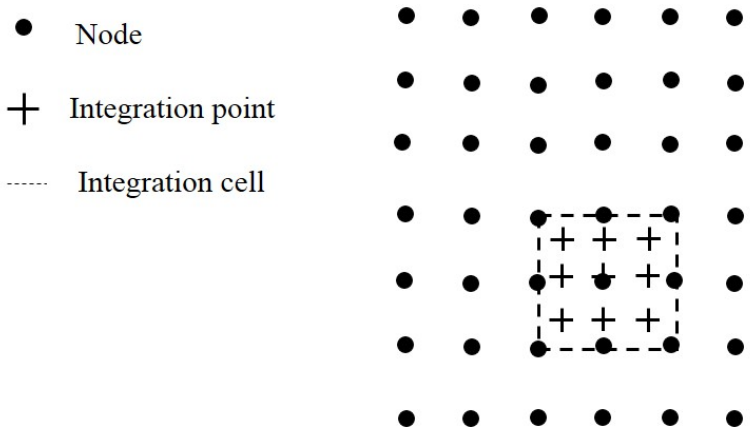

Figure 11: An integration cell with 3x3 integration points in the discrete model

Table 4 : Transversal displacement values obtained for each integration scheme for the exact solution, RPIM and FEM methods for the SSSS case.

discretization			u_z (m) – transversal displacement			$\overline{u}_z$ – normalized displacement			Error (%)	Error (%)
Integration scheme	n_z	n_r	exact	RPIM	FEM	exact	RPIM	FEM	RPIM-exact	FEM-exact
2x2	5	81	11.1300	11.0987	11.1560	69.5625	69.3669	69.7250	0.0028	0.2336
3x3	5	81	11.1300	11.0887	11.1560	69.5625	69.3041	69.7250	0.0037	0.2336
4x4	5	81	11.1300	11.0863	11.1560	69.5625	69.2895	69.7250	0.0039	0.2336
5x5	5	81	11.1300	11.0781	11.1560	69.5625	69.2379	69.7250	0.0047	0.2336
6x6	5	81	11.1300	11.0900	11.1560	69.5625	69.3123	69.7250	0.0036	0.2336
7x7	5	81	11.1300	11.0901	11.1560	69.5625	69.3130	69.7250	0.0036	0.2336
8x8	5	81	11.1300	11.0903	11.1560	69.5625	69.3144	69.7250	0.0036	0.2336
9x9	5	81	11.1300	11.0874	11.1560	69.5625	69.2960	69.7250	0.0038	0.2336
10x10	5	81	11.1300	11.0899	11.1560	69.5625	69.3119	69.7250	0.0036	0.2336

Table 5 : Transversal displacement values obtained for each integration scheme for the exact solution, RPIM and FEM methods for the CCCC case.

discretization			u_z (m) – transversal displacement			$\overline{u}_z$ – normalized displacement			Error (%)	Error (%)
Integration scheme	n_z	n_r	exact	RPIM	FEM	exact	RPIM	FEM	RPIM-exact	FEM-exact
2x2	5	81	2.7300	2.6881	2.7539	17.0625	16.8006	17.2119	1.5347	0.8755
3x3	5	81	2.7300	2.7086	2.7539	17.0625	16.9291	17.2119	0.7821	0.8755
4x4	5	81	2.7300	2.7018	2.7539	17.0625	16.8861	17.2119	1.0337	0.8755
5x5	5	81	2.7300	2.7005	2.7539	17.0625	16.8780	17.2119	1.0816	0.8755
6x6	5	81	2.7300	2.7038	2.7539	17.0625	16.8985	17.2119	0.9610	0.8755
7x7	5	81	2.7300	2.7056	2.7539	17.0625	16.9098	17.2119	0.8952	0.8755
8x8	5	81	2.7300	2.7044	2.7539	17.0625	16.9027	17.2119	0.9365	0.8755
9x9	5	81	2.7300	2.7041	2.7539	17.0625	16.9004	17.2119	0.9498	0.8755
10x10	5	81	2.7300	2.7043	2.7539	17.0625	16.9021	17.2119	0.9401	0.8755

5.1.3 Influence-domain

This part purposes to determine the optimal number of nodes inside the influence-domains. Thus, first it is assumed a circular plate showing the same geometrical properties of previous parts. The material properties and the external load conditions are coincident as well. The problem domain is then discretized in a regular mesh of 81x5 nodes and an integration background mesh is constructed, as described in Subsection 5.1.2, Figure 11. Afterwards each integration point $\boldsymbol{x}_I$ searches for the closest N_I nodes. These N_I nodes: $N_I = \{n_1, n_2, ..., n_{N_I}\}$, form the influence-domain of interest point $\boldsymbol{x}_I$. In order to obtain the optimal value for N_I, the described example was studied considering 34 integer values for $N_I = \{8, 9, ..., 40, 41\}$ (see Figure 1 referring to the influence domain definition).

The transversal centre displacements of each study is presented in Figure 12(a) for the SSSS circular plate and in Figure 12(b) for the CCCC circular plate. For comparison purposes it is presented also the FEM solution and the analytical solution (which are constant since both do not depend on N_I). To both graphs it was added an adjustment curve using the moving-least squares with a cubic polynomial basis – "cubic approximation". These curves are adjusted to the RPIM values, and show the solution trend. In Figure 12(a) and (b), it is visible that the minimum of the cubic approximation

function is obtained on the vicinity of $N_I = 20$. Thus, future examples in this work are analysed considering $N_I = 20$ nodes inside each influence-domain.

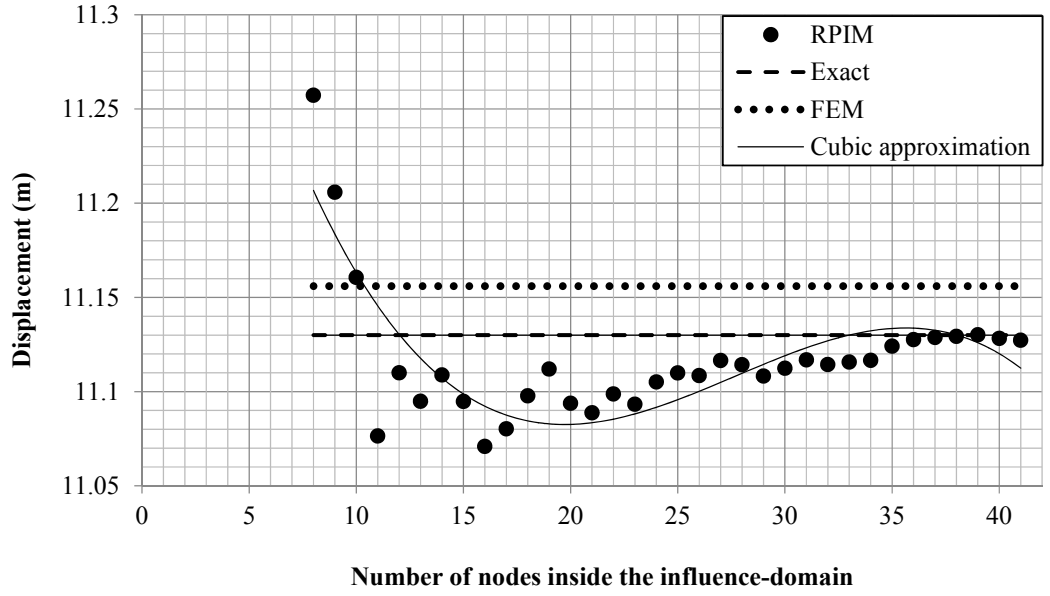

(a)

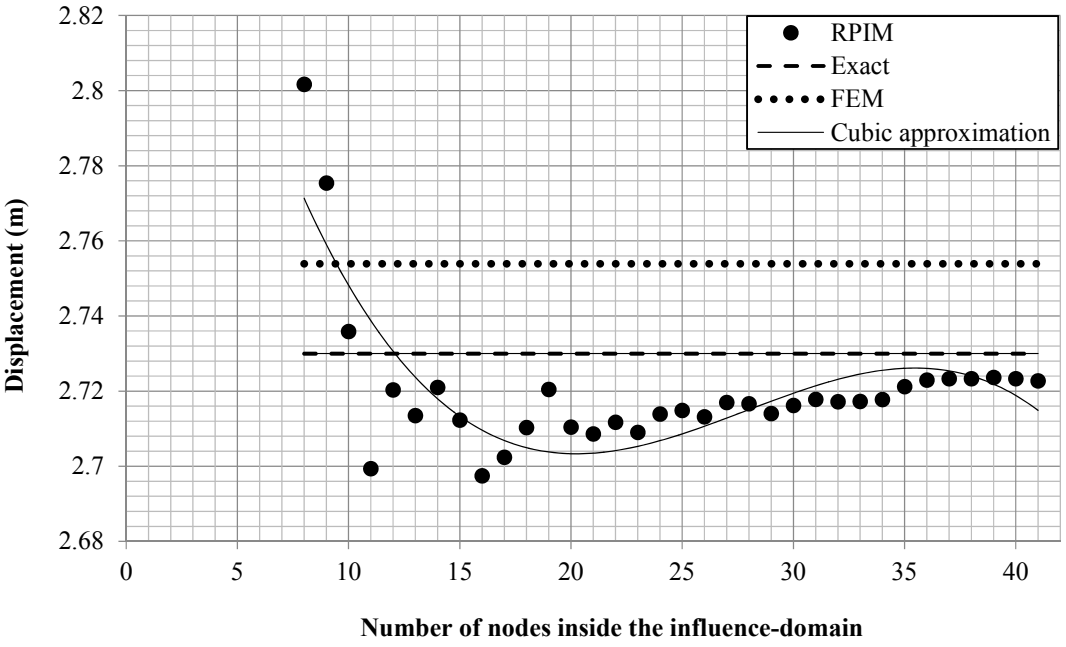

(b)

Figure 12 : Transversal displacement values obtained from RPIM, exact and FEM regarding the number of nodes inside the influence-domain for (a) SSSS case and (b) CCCC cases.

5.1.4 RPIM Behavior with Irregular Meshes

It is important to determine the influence of the mesh irregularity on the RPIM performance. Thus, this part studies the behaviour of the RPIM when random irregular nodal meshes are used in the analysis.

In order to generate an irregular mesh the following procedure is considered. First, a regular mesh is constructed, with all nodes equally spaced and aligned as the mesh example in Figure 13(a), afterwards all the nodes $\boldsymbol{x} \in \Omega \setminus \Gamma$ are affected with,

$$\begin{aligned} x_i^{new} &= x_i + \frac{\tilde{r}_1 \cdot h}{\lambda} cos\left(2\tilde{r}_2 \cdot \pi\right) \\ y_i^{new} &= y_i + \frac{\tilde{r}_2 \cdot h}{\lambda} sin\left(2\tilde{r}_2 \cdot \pi\right) \end{aligned}, \tag{126}$$

being $\boldsymbol{x}_i$ the initial coordinates of node n_i, $\boldsymbol{x}_i^{new}$ the new coordinates obtained for node n_i and h is the inter-nodal distance shown in Figure 13(a). The random coefficient is defined by $\tilde{r} \approx N(0,1)$ and λ is a parameter that controls the irregularity level of the mesh. The effect of the irregularity parameter λ is shown in Figure 13. Notice that if $\lambda = \infty$ the mesh is perfectly regular, Figure 13(a), and with the decrease of λ the mesh becomes more and more irregular, Figure 13(b) and (c).

The same circular plate described in the previous section was analysed considering several irregular nodal meshes with $n_r \times n_z = 81 \times 5$ nodes, varying the irregularity parameter from $\lambda = 100$ to $\lambda = 2$. Each constructed irregular mesh was used to analyse the problem considering the RPIM. The obtained results are presented in Figure 14(a) for the SSSS circular plate case and in Figure 14(b) for the CCCC circular plate case.

The results show that the SSSS and CCCC solutions only start to show significant instabilities for meshes constructed with $\lambda < 4$, which are in fact extremely irregular meshes. For $\lambda \geq 4$ the results are stable and accurate. This example shows that, for the axisymmetric formulation, the RPIM permits to obtain accurate results using highly irregular meshes, therefore showing robustness.

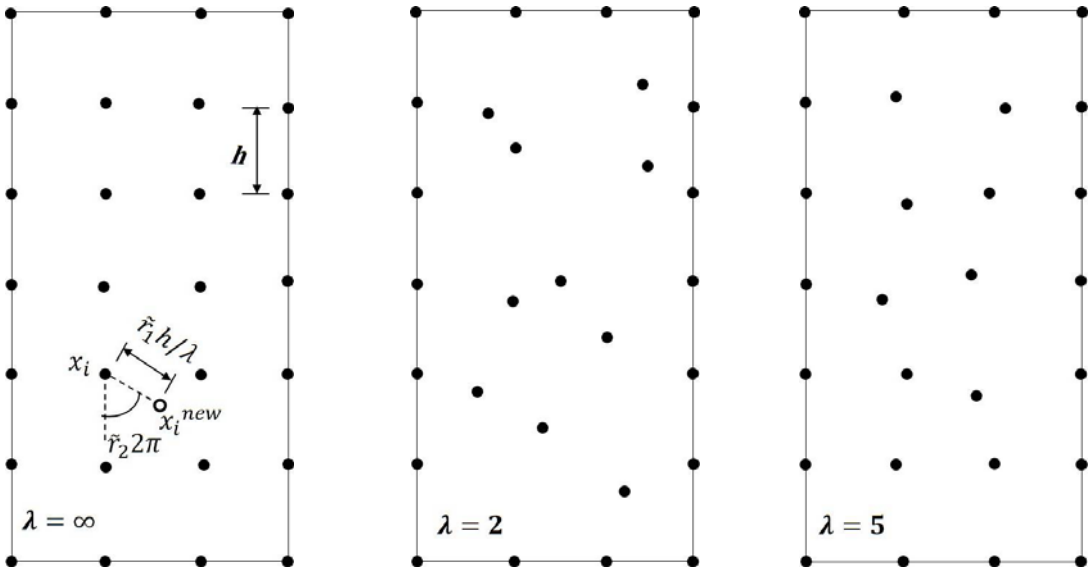

(a) (b) (c)

Figure 13 : (a) 7×4 regular mesh, (b) irregular mesh with λ=2 and (c) irregular mesh with λ=5.

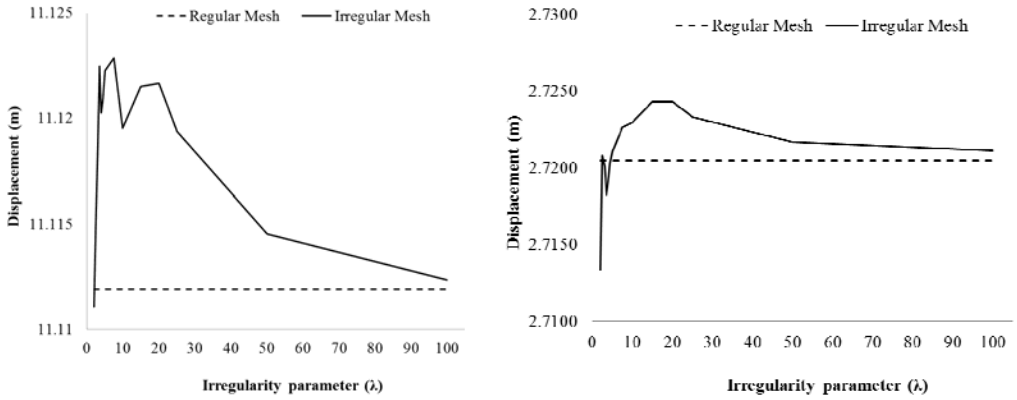

(a) (b)

Figure 14 : Transversal centre displacements obtained from RPIM varying the irregularity parameter for the (a) SSSS and (b) CCCC case.

5.1.5 Variation of R/H

In this section several R/H ratios are considered and analysed. Consider the generic circular plate under the UDL $q = 100N/m^2$ presented in Figure 9. Four distinct circular plates are considered, each one with a distinct radius $R = \{10, 20, 50, 100\}m$ and all of them with the same thickness $H = 1.0m$. Thus, each of the four circular plates is analysed considering the RPIM and the FEM with axisymmetric formulation.

The results regarding the SSSS circular plate are presented in Table 6 and the results obtained for the CCCC circular plate are shown in Table 7.

Both tables show that the RPIM solution is very close with the exact analytical solution and the FEM solution, permitting to demonstrate the RPIM accuracy.

Table 6 : Transversal displacement values obtained with the variation of the R/H ratio for the SSSS case.

discretization			u_z (m) – transversal displacement			$\overline{u}_z$ – normalized displacement			Error (%)	Error (%)	Error (%)
R/H	n_z	n_r	exact	RPIM	FEM	exact	RPIM	FEM	RPIM-exact	RPIM-FEM	FEM-exact
10	9	81	0.6956	0.7037	0.7023	69.5625	70.3718	70.2290	1.1635	0.2034	0.9581
20	9	161	11.1300	11.1537	11.1560	69.5625	69.7107	69.7250	0.2131	0.0205	0.2336
50	9	401	434.7656	434.5531	434.9200	69.5625	69.5285	69.5872	0.0489	0.0844	0.0355
100	9	801	6956.2500	6946.8230	6956.9000	69.5625	69.4682	69.5690	0.1355	0.1448	0.0093

Table 7 : Transversal displacement values obtained with the variation of the R/H ratio for the CCCC case.

discretization			u_z (m) – transversal displacement			$\overline{u}_z$ – normalized displacement			Error (%)	Error (%)	Error (%)
R/H	n_z	n_r	exact	RPIM	FEM	exact	RPIM	FEM	RPIM-exact	RPIM-FEM	FEM-exact
10	9	81	0.1770	0.1706	0.1775	17.0625	17.6962	17.7470	3.7137	0.2865	4.0117
20	9	161	2.7471	2.7300	2.7539	17.0625	17.1695	17.2119	0.6273	0.2460	0.8755
50	9	401	106.4844	106.6406	106.7200	17.0625	17.0375	17.0752	0.1465	0.2208	0.0745
100	9	801	1702.2440	1706.2500	1706.1000	17.0625	17.0224	17.0610	0.2348	0.2260	0.0088

5.2 Circular Plate under Circular Punctual Load

In this part, the circular plate submitted to a circular punctual load (CPL) $q = 100N/m$ presented in Figure 15(a) is studied. The circle in which the punctual load is applied presents a radius b. In this study three distinct analyses, with three different radius b, are considered: $b = \{0.25R, 0.5R, 0.75R\}$.

Regarding the essential boundary conditions, in the present example two distinct cases are once more considered: the complete contour of the plate simply supported (SSSS), Figure 15(b), and the full plate's contour clamped (CCCC), Figure 15(c).

The exact analytical solution for the SSSS plate with a CPL can be found in (S. Timoshenko & Woinowsky-Krieger, n.d.).

$$u_z(r) = \begin{cases} \dfrac{2\pi qb}{\left(\dfrac{8\pi EH^3}{12(1-\upsilon^2)}\right)}\left[\left(R^2-r^2\right)\left(1+\dfrac{1-\upsilon}{2(1+\upsilon)}\dfrac{R^2-r^2}{R^2}\right)+\log\left(\dfrac{r}{R}\right)\left(b^2+r^2\right)\right] & r>b \\ \dfrac{2\pi qb}{\left(\dfrac{8\pi EH^3}{12(1-\upsilon^2)}\right)}\left[\log\left(\dfrac{b}{R}\right)\left(b^2+r^2\right)+\left(R^2-b^2\right)\left(\dfrac{R^2\left(3+\upsilon\right)-r^2\left(1-\upsilon\right)}{2R^2(1+\upsilon)}\right)\right] & r<b \end{cases}. \quad (127)$$

The analytical solution of the circular CCCC plate submitted to a CPL is obtained with (Stephen Timoshenko & Woinowsky-Krieger, n.d.),

$$u_z(r) = \begin{cases} \dfrac{2\pi qb}{\left(\dfrac{8\pi EH^3}{12(1-\upsilon^2)}\right)}\left[\dfrac{\left(R^2+r^2\right)\left(R^2-b^2\right)}{2R^2}+\log\left(\dfrac{b}{R}\right)\left(b^2+r^2\right)\right] & r>b \\ \dfrac{2\pi qb}{\left(\dfrac{8\pi EH^3}{12(1-\upsilon^2)}\right)}\left[\dfrac{\left(R^2-r^2\right)\left(R^2+b^2\right)}{2R^2}+\log\left(\dfrac{r}{R}\right)\left(b^2+r^2\right)\right] & r<b \end{cases}. \quad (128)$$

First a convergence study is performed. For this purpose, the plate geometry is considered with $R = 20m$ and $H = 1m$. The results regarding the convergence study are presented in Table 8 for the SSSS case and in Table 9 for the CCCC case.

Analysing the obtained results, it is possible to conclude that the RPIM presents a fast convergence rate and that the last converged solution, for the transversal displacement in the centre of the plate, is very close with the exact analytical solution and the FEM solution, for both SSSS and CCCC cases.

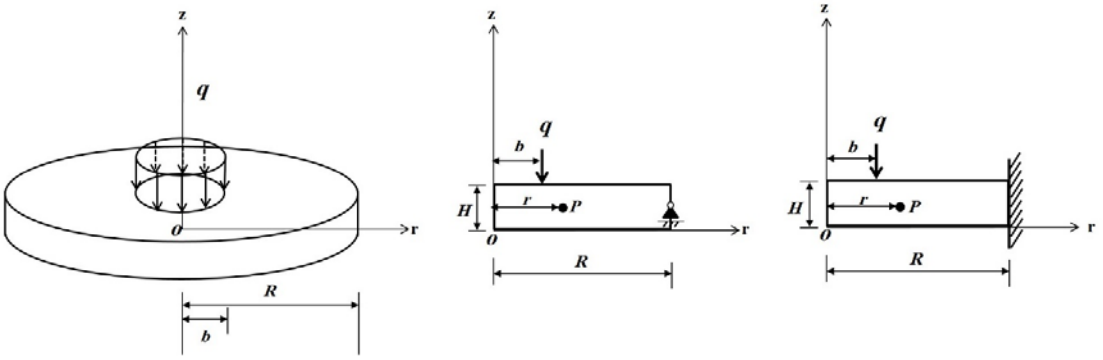

Figure 15 : (a) Circular plate under circular punctual load. (b) Simply supported boundary condition. (b) Clamped boundary condition.

Table 8 : Transversal displacement and error values for R/H=20 of the SSSS circular plate under circular punctual load.

discretization				u_z (m) – transversal displacement			$\overline{u}_z$ – normalized displacement			Error (%)	Error (%)
b	n_z	n_r	total	exact	RPIM	FEM	exact	RPIM	FEM	RPIM-exact	RPIM-FEM
R/4	3	41	123	0.6024	0.5928	0.6049	3.7649	3.7051	3.7804	1.5881	1.9932
	5	81	405	0.6024	0.6020	0.6048	3.7649	3.7625	3.7799	0.0620	0.4602
	9	161	1449	0.6024	0.6042	0.6048	3.7649	3.7761	3.7797	0.2983	0.0947
	17	321	5457	0.6024	0.6046	0.6047	3.7649	3.7790	3.7796	0.3761	0.0155
R/2	3	41	123	0.8503	0.8342	0.8528	5.3142	5.2137	5.3300	1.8914	2.1824
	5	81	405	0.8503	0.8486	0.8527	5.3142	5.3036	5.3294	0.1996	0.4839
	9	161	1449	0.8503	0.8518	0.8527	5.3142	5.3238	5.3292	0.1809	0.1010
	17	321	5457	0.8503	0.8525	0.8527	5.3142	5.3283	5.3292	0.2645	0.0176
3R/4	3	41	123	0.6445	0.6317	0.6461	4.0281	3.9482	4.0382	1.9834	2.2277
	5	81	405	0.6445	0.6429	0.6461	4.0281	4.0180	4.0378	0.2521	0.4915
	9	161	1449	0.6445	0.6454	0.6460	4.0281	4.0336	4.0377	0.1351	0.1021
	17	321	5457	0.6445	0.6459	0.6461	4.0281	4.0371	4.0378	0.2224	0.0182

Table 9 : Transversal displacement and error values for R/H=20 of the CCCC circular plate under circular punctual load.

discretization				u_z (m) – transversal displacement			$\overline{u}_z$ – normalized displacement			Error (%)	Error (%)
b	n_z	n_r	total	exact	RPIM	FEM	exact	RPIM	FEM	RPIM-exact	RPIM-FEM
R/4	3	41	123	0.2086	0.1985	0.2103	1.3039	1.2406	1.3141	4.8583	5.5913
	5	81	405	0.2086	0.2083	0.2105	1.3039	1.3017	1.3153	0.1705	1.0338
	9	161	1449	0.2086	0.2101	0.2105	1.3039	1.3129	1.3159	0.6907	0.2227
	17	321	5457	0.2086	0.2105	0.2106	1.3039	1.3155	1.3161	0.8890	0.0452
R/2	3	41	123	0.2203	0.2071	0.2214	1.3767	1.2945	1.3838	5.9710	6.4506
	5	81	405	0.2203	0.2192	0.2218	1.3767	1.3699	1.3859	0.4972	1.1564
	9	161	1449	0.2203	0.2214	0.2219	1.3767	1.3835	1.3869	0.4912	0.2511
	17	321	5457	0.2203	0.2219	0.2220	1.3767	1.3866	1.3874	0.7226	0.0529
3R/4	3	41	123	0.0933	0.0864	0.0936	0.5828	0.5398	0.5848	7.3888	7.6962
	5	81	405	0.0933	0.0926	0.0939	0.5828	0.5790	0.5868	0.6654	1.3326
	9	161	1449	0.0933	0.0938	0.0940	0.5828	0.5861	0.5878	0.5576	0.2877
	17	321	5457	0.0933	0.0941	0.0941	0.5828	0.5878	0.5882	0.8546	0.0676

Additionally, it was obtained the transversal displacement in the centre of the plate considering several R/H ratios. Thus, four distinct circular plate geometries were considered: $R=10m$ and $H=1m$; $R=20m$ and $H=1m$; $R=50m$ and $H=1m$; and $R=100m$ and $H=1m$. The results are presented in Table 10 and Table 11, respectively for the SSSS and CCCC cases.

In the tables it is possible to visualize that the RPIM error with respect to the analytical solution is always very low. Considering only the results for the thin plates $R/H \geq 20$, for the SSSS case the error is about 0.1% to 0.2% and for the CCCC case the error fluctuates around 0.2%. The RPIM's error with respect to the analytical solution for the circular plates with $R/H < 20$ (thick plate) is always higher. This phenomenon can be explained with the fact that the exact solutions presented in Equation (127) and Equation (128) are thin plate solutions. Nevertheless, from Table 10 and Table 11 it is possible to confirm that the RPIM solution is accurate, since the difference between the RPIM solution and the FEM solution is around 0.1% in the SSSS case and $0.2\% \sim 0.3\%$ in the CCCC, regardless the analysed R/H ratio.

Table 10 : Transversal displacement for distinct b and R/H values regarding the SSSS circular plate under circular punctual load.

discretization				u_z (m) – transversal displacement			$\overline{u}_z$ – normalized displacement			Error (%)	Error (%)
b	R/H	n_i	n_r	exact	RPIM	FEM	exact	RPIM	FEM	RPIM-exact	RPIM-FEM
R/4	10	9	81	0.0753	0.0764	0.0765	7.5298	7.6407	7.6493	1.4738	0.1121
	20	9	161	0.6024	0.6042	0.6048	3.7649	3.7761	3.7797	0.2983	0.0947
	50	9	401	9.4122	9.4093	9.4181	1.5060	1.5055	1.5069	0.0306	0.0933
	100	9	801	75.2975	75.2039	75.3090	0.7530	0.7520	0.7531	0.1243	0.1395
R/2	10	9	81	0.1063	0.1074	0.1075	10.6284	10.7379	10.750	1.0304	0.1126
	20	9	161	0.8503	0.8518	0.8527	5.3142	5.3238	5.3292	0.1809	0.1010
	50	9	401	13.2855	13.2781	13.2910	2.1257	2.1245	2.1266	0.0555	0.0970
	100	9	801	106.2839	106.1363	106.3000	1.0628	1.0614	1.0630	0.1388	0.1540
3R/4	10	9	81	0.0806	0.0813	0.0814	8.0562	8.1264	8.1364	0.8708	0.1229
	20	9	161	0.6445	0.6454	0.6460	4.0281	4.0336	4.0377	0.1351	0.1021
	50	9	401	10.0703	10.0638	10.0740	1.6112	1.6102	1.6118	0.0646	0.1014
	100	9	801	80.5624	80.4459	80.5700	0.8056	0.8045	0.8057	0.1447	0.1541

Table 11 : Transversal displacement for distinct b and R/H values regarding the CCCC circular plate under circular punctual load.

discretization				u_z (m) – transversal displacement			$\overline{u}_z$ –normalized displacement			Error (%)	Error (%)
b	R/H	n_z	n_r	exact	RPIM	FEM	exact	RPIM	FEM	RPIM-exact	RPIM-FEM
R/4	10	9	81	0.0261	0.0270	0.0271	2.6079	2.7044	2.7117	3.7022	0.2682
	20	9	161	0.2086	0.2101	0.2105	1.3039	1.3129	1.3159	0.6906	0.2227
	50	9	401	3.2598	3.2567	3.2634	0.5216	0.5211	0.5221	0.0976	0.2063
	100	9	801	26.0788	26.0267	26.0820	0.2608	0.2603	0.2608	0.1998	0.2121
R/2	10	9	81	0.0275	0.0284	0.0285	2.7534	2.8401	2.8486	3.1494	0.2984
	20	9	161	0.2203	0.2214	0.2219	1.3767	1.3835	1.3869	0.4912	0.2511
	50	9	401	3.4417	3.4359	3.4438	0.5507	0.5497	0.5510	0.1695	0.2294
	100	9	801	27.5339	27.4666	27.5310	0.2753	0.2747	0.2753	0.2442	0.2339
3R/4	10	9	81	0.0117	0.0121	0.0122	1.1656	1.2126	1.2168	4.0284	0.3473
	20	9	161	0.0932	0.0938	0.0940	0.5828	0.5861	0.5878	0.5576	0.2909
	50	9	401	1.4570	1.4535	1.4573	0.2331	0.2326	0.2332	0.2423	0.2614
	100	9	801	11.6562	11.6206	11.6510	0.1166	0.1162	0.1165	0.3054	0.2611

To end this study, a circular plate with $R = 5m$ and $H = 1m$ is considered. The circular plate is submitted to the same CPL previously described: $q = 100N/m$ and $b = \{0.25R, 0.5R, 0.75R\}$, and the same essential boundary conditions cases: SSSS and CCCC. The two-dimensional section domains described in Figure 15(b) and (c) are discretized in a regular mesh of 81×5 nodes. For each of the analyses the following stress fields were obtained: σ_{rr}, σ_{zz} and τ_{rz}. The results obtained with the RPIM regarding the SSSS case are presented in Figure 16. The stress fields for the CCCC case are presented in Figure 17.

The results show that the stress fields obtained with the RPIM are smooth.

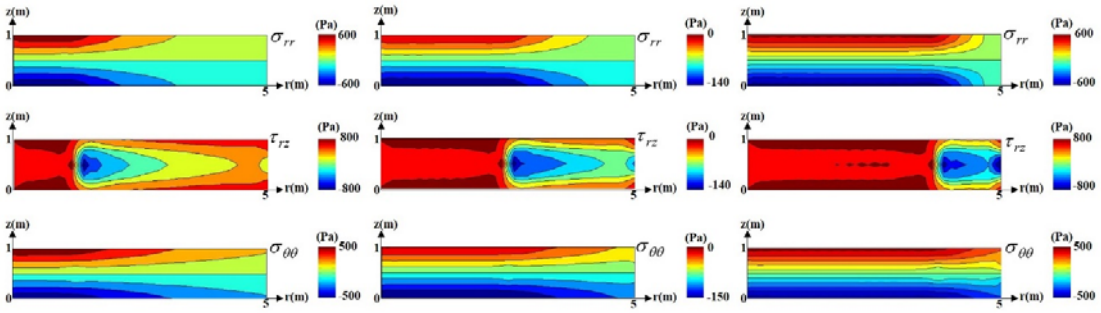

(a) (b) (c)

Figure 16 : Stress field distribution of the simply supported circular plate under circular punctual load obtained for (a) b=R/4, (b) b=R/2 and (c) b=3R/4.

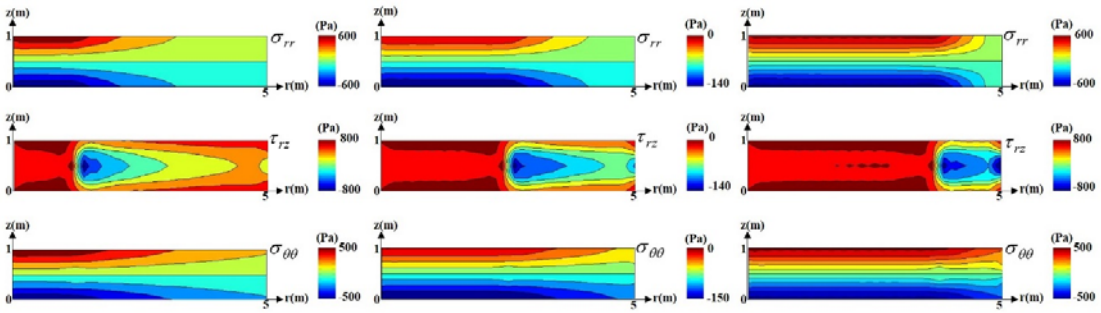

(a) (b) (c)

Figure 17 : Stress field distribution of the clamped circular plate under circular punctual load obtained for (a) b=R/4, (b) b=R/2 and (c) b=3R/4.

5.3 Circular Plate under Localized Uniform Distributed Load

The present example analyses the elasto-static behaviour of a simply supported circular plate submitted to a localized uniform distributed load $q = 100N/m^2$ (LUDL), as represented in Figure 18. The LUDL actuates on a circular area with radius b. As in the previous example, three distinct radius b are considered: $b = \{0.25R, 0.5R, 0.75R\}$.

It is possible to find in the literature (S. Timoshenko & Woinowsky-Krieger, n.d.), the exact analytical solution for the plate's centre of the present example,

$$u_z(r=0) = \frac{\pi q b^2}{\left(\frac{16\pi E H^3}{12(1-\upsilon^2)}\right)}\left[R^2\left(\frac{3+\upsilon}{1+\upsilon}\right) + b^2\log\left(\frac{b}{R}\right) - b^2\left(\frac{7+3\upsilon}{4+4\upsilon}\right)\right]. \tag{129}$$

The analysis of this example begins with a convergence study. Therefore, the circular plate geometry is considered with $R = 20m$ and $H = 1m$. The obtained results for the transversal displacement in the centre of the plate are presented in Table 12. The obtained results demonstrate once more that the RPIM presents a high convergence rate. It is also perceptible that the last converged solution is very close with the exact analytical and FEM solutions. Comparing just the final converged values, the error of the RPIM solution regarding the exact solution fluctuates between $0.3\% \sim 0.5\%$. The difference between the RPIM final converged solution and the FEM final converged solution is about $0.06\% \sim 0.08\%$.

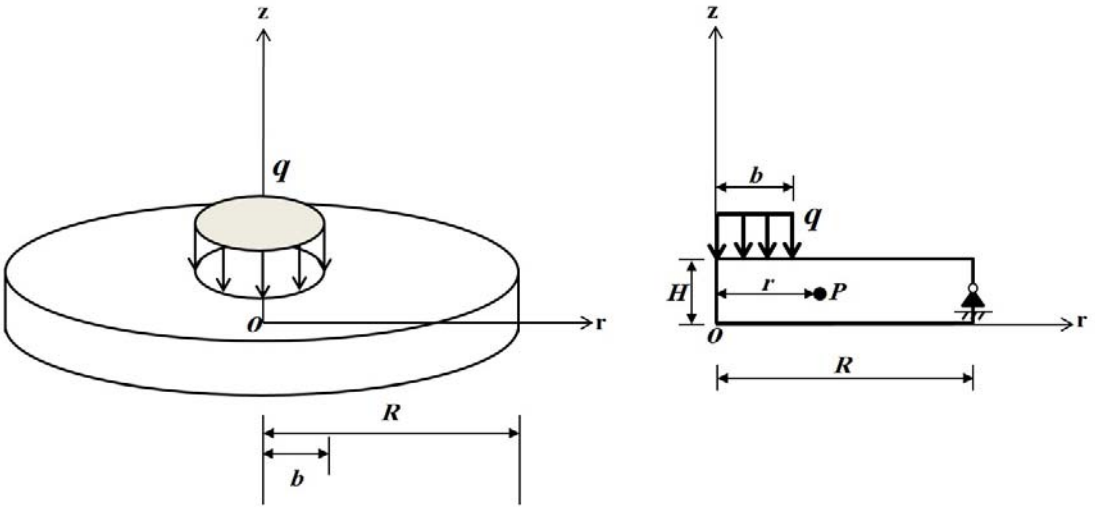

Figure 18 : Simply supported circular plate under local circular uniform distributed load.

Table 12 : Transversal displacement and error values for R/H=20 of the SSSS circular plate under circular uniform distributed load.

discretization				u_z (m) – transversal displacement			$\overline{u}_z$ – normalized displacement			Error (%)	Error (%)
b	n_z	n_r	total	exact	RPIM	FEM	exact	RPIM	FEM	RPIM-exact	RPIM-FEM
R/4	3	41	123	1.6086	1.5863	1.6152	10.0535	9.9146	10.0950	1.3816	1.7869
	5	81	405	1.6086	1.6095	1.6151	10.0535	10.0593	10.0944	0.0573	0.3478
	9	161	1449	1.6086	1.6151	1.6150	10.0535	10.0944	10.0938	0.4071	0.0068
	17	321	5457	1.6086	1.6163	1.6150	10.0535	10.1021	10.0938	0.4832	0.0825
R/2	3	41	123	5.4201	5.3305	5.4368	33.8753	33.3156	33.9800	1.6523	1.9553
	5	81	405	5.4201	5.4155	5.4364	33.8753	33.8465	33.9775	0.0850	0.3854
	9	161	1449	5.4201	5.4352	5.4362	33.8753	33.9702	33.9763	0.2801	0.0178
	17	321	5457	5.4201	5.4396	5.4362	33.8753	33.9974	33.9763	0.3604	0.0623
3R/4	3	41	123	9.3493	9.1832	9.3739	58.4333	57.3952	58.5869	1.7766	2.0340
	5	81	405	9.3493	9.3357	9.3732	58.4333	58.3484	58.5825	0.1454	0.3996
	9	161	1449	9.3493	9.3706	9.3729	58.4333	58.5663	58.5806	0.2275	0.0245
	17	321	5457	9.3493	9.3784	9.3729	58.4333	58.6147	58.5806	0.3103	0.0581

Next, another study was performed using the same benchmark example.

Considering several R/H ratios, it was obtained the transversal displacement in the centre of the plate with the RPIM and the FEM. Therefore, maintaining the circular plate thickness constant, $H = 1m$, four distinct plate radius were considered: $R = \{10, 20, 50, 100\}$. The obtained results are presented in Table 13.

Once more from the results show that the RPIM error with respect to the analytical solution is always very low. Considering only the results for the thin plates $R/H \geq 20$ the error with respect to the analytical solution is around $0.1\% \sim 0.4\%$. Similar to the previous examples, the RPIM's error with respect to the analytical solution for the thick circular plates ($R/H < 20$) is always higher, which can be explained with the same argument as before. However, the results obtained with the RPIM are in accordance with the FEM solution. Table 13 shows that the difference between the RPIM solution and the FEM solution is around $0.02\% \sim 0.2\%$, regardless the analysed R/H ratio.

Table 13 : Transversal displacement for distinct b and R/H values regarding the SSSS circular plate under circular uniform distributed load.

discretization				u_z (m) – transversal displacement			$\overline{u}_z$ – normalized displacement			Error (%)	Error (%)
b	R/H	n_z	n_r	exact	RPIM	FEM	exact	RPIM	FEM	RPIM -exact	RPIM-FEM
R/4	10	9	81	0.1005	0.1025	0.1022	10.0535	10.2445	10.2150	1.8998	0.2889
	20	9	161	1.6086	1.6151	1.6150	10.0535	10.0944	10.0938	0.4071	0.0068
	50	9	401	62.8344	62.8275	62.8750	10.0535	10.0524	10.0600	0.0110	0.0755
	100	9	801	1005.3510	1004.1450	1005.5000	10.0535	10.0415	10.0550	0.1200	0.1348
R/2	10	9	81	0.3388	0.3435	0.3428	33.8753	34.3528	34.2830	1.4094	0.2035
	20	9	161	5.4201	5.4352	5.4362	33.8753	33.9702	33.9763	0.2801	0.0178
	50	9	401	211.7208	211.6447	211.8200	33.8753	33.8635	33.8912	0.0359	0.0828
	100	9	801	3387.5330	3383.0520	3387.9000	33.8753	33.8305	33.8790	0.1323	0.1431
3R/4	10	9	81	0.5843	0.5914	0.5903	58.4333	59.1412	59.0340	1.2114	0.1816
	20	9	161	9.3493	9.3706	9.3729	58.4333	58.5663	58.5806	0.2275	0.0245
	50	9	401	365.2084	365.0377	365.3500	58.4333	58.4060	58.4560	0.0467	0.0855
	100	9	801	5843.3340	5835.2440	5843.9000	58.4333	58.3524	58.4390	0.1385	0.1481

In order to show that the RPIM is capable to produce smooth stress fields, a simply supported circular plate with $R = 5m$ and $H = 1m$ is submitted to the same LUDL previously described: $q = 100N/m^2$ and $b = \{0.25R, 0.5R, 0.75R\}$. The two-dimensional section domain described in Figure 18 are discretized in a regular mesh of 81×5 nodes. For each analyses the following stress fields were obtained: σ_{rr}, σ_{zz} and τ_{rz}. The obtained RPIM results are presented in Figure 19.

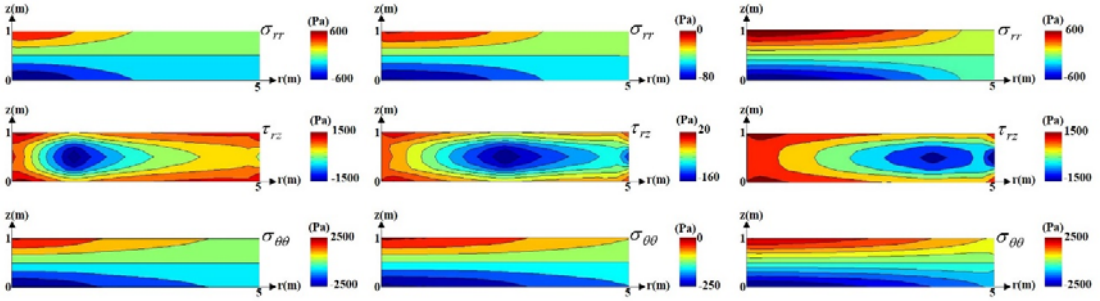

(a) (b) (c)

Figure 19 : Stress field distribution of the simply supported circular plate under local circular uniform distributed load obtained for (a) b=R/4, (b) b=R/2 and (c) b=3R/4.

Chapter 6

6 Validation of the Proposed Non-local Damage Model

In this chapter, several numerical benchmarks associated with the concrete structures are analysed using the proposed rate-independent damage model combined with the RPIM formulations (Chapter 4). The results are compared to the experimental solution from the literature ((Gopalaratnam & Shah, 1985); (Karsan & Jirsan, 1969); (Kupfer et al., 1969) and (Malvar & Warren, 1988)) and FEM solutions (Voyiadjis & Taqieddin, 2009).

6.1 Identification of the Model`s Parameters

The considered non-local damage model depends on specific material properties and damage coefficients, such as: Young's modulus and Poisson's ratio for undamaged material (E and ν); parameters for damage characterisation including characteristic length (l_{ch}), compressive and tensile coefficients ($A^{\pm}, B^{-}$); plasticity parameter (β, K) and; fracture energy in tensile and compressive states $\left(G_f^{\pm}\right)$. The corresponding parameters are determined by a series of experimental tests on concrete under tensile and compressive enforcements (Cervera et al., 1996) (He et al., 2006). The proposed rate-independent elastic damage model is based on the effective elastic constitutive model presented by M. Cervera et.al (Cervera et al., 1996). Hence, it is possible to use the parameters and coefficients values suggested by Cervera and co-workers (Cervera et al., 1996). Nevertheless, here, the characteristic length assumes another definition, due to the meshless method concept.

6.2 Monotonic Uniaxial Tensile Test

The monotonic uniaxial tensile test is studied as the first example. The arrangement of the nodes and boundary conditions are shown in Figure 20-a. The damage coefficients and material properties of concrete are defined according to the work presented by (Lee & Fenves, 1998) (Tao & Phillips, 2005)(He et al., 2006) (G. D. Nguyen & Houlsby, 2008) (Cervera et al., 1996): $E = 31\ (GPa)$, $\nu = 0.2$, $f_0^+ = 3.48\ (MPa)$ and $G_f^+ = 40\ (N/m)$. As discussed in Subsection 4.1, the characteristic length (l_{ch}) variable, which is associated with the element size and affects the degradation of the damage phenomenon, is fully defined for the FEM formulation (Cervera et al., 1996) expressed in Equations (94-a) and (94-b) for 2D and 3D respectively. Thus, since in this work it is considered a meshless method, this variable has to be adapted for the meshless method concept. In this work, the characteristic length is obtained for each integration point with the following expression,

$$l_{ch} = \sqrt{N_{gp}.W_{gp}} \tag{130}$$

Where N_{gp} is the total number of integration points defining the problem domain and W_{gp} represents the weight of the integration point (Equation (114)).

Afterwards, in order to determine the tensile damage coefficient, A^+, Equation (96-a) is considered for the rate-independent damage model (Cervera et al., 1996).

$$A^+ = \frac{2H^+ l_{ch}}{1 - H^+ l_{ch}} \geq 0$$

where (referring to Equation (95-a)),

$$H^+ = \frac{(f_0^+)^2}{2EG_f^+}$$

Being H^+ dependent on the material properties mentioned above. It is important to mention that the characteristic length restricts the maximum size of the each integration cell with the condition of $l_{ch} \leq 1/H^+$(Equation (95-b)).

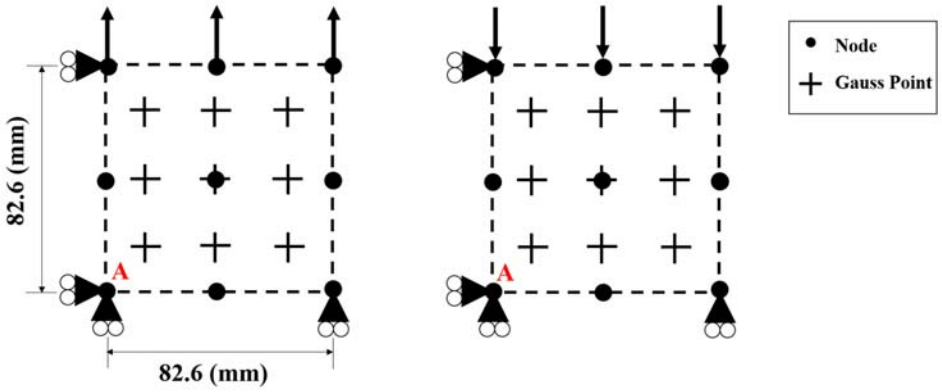

Figure 20: Quadrilateral geometry of uniaxial test under (a) tension and (b) compression

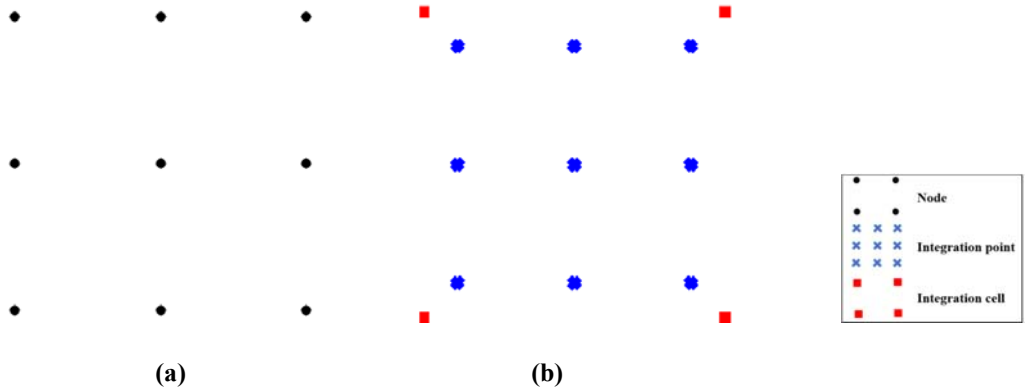

Figure 21: Regular discretization for monotonic test (a) 9 nodes and (b) 9 integration points

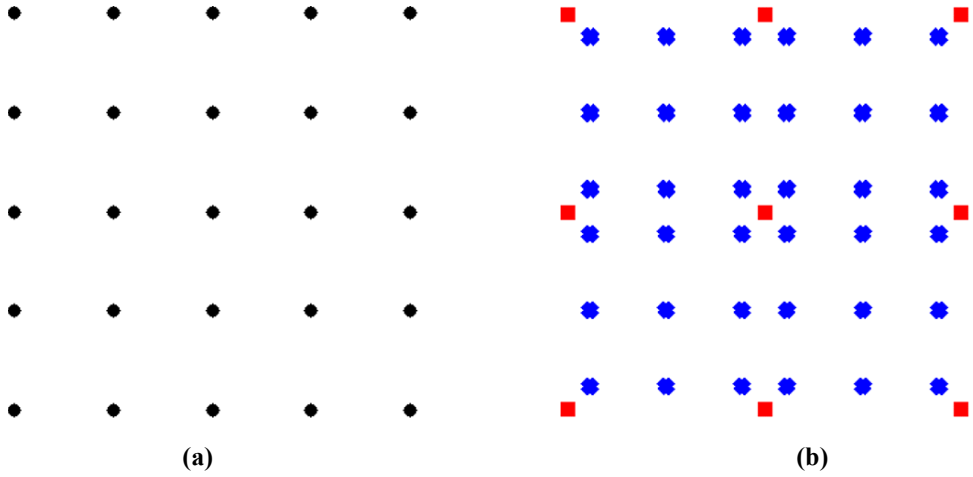

Figure 22: Regular discretization for monotonic test (a) 25 nodes and (b) 36 integration points

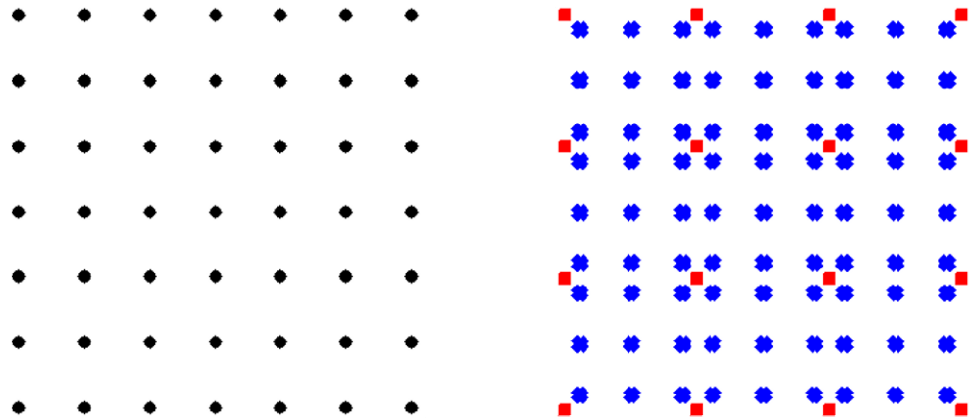

(a) (b)

Figure 23: Regular discretization for monotonic test (a) 49 nodes and (b) 81 integration points

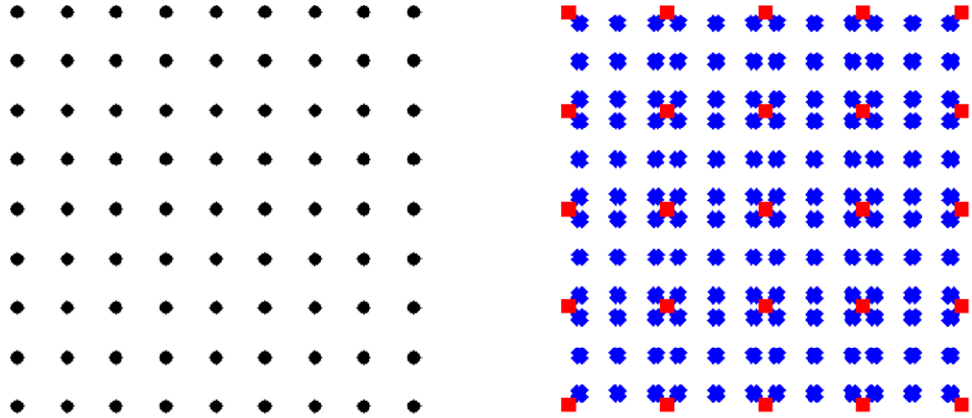

(a) (b)

Figure 24: Regular discretization for monotonic test (a) 81 nodes and (b) 144 integration points

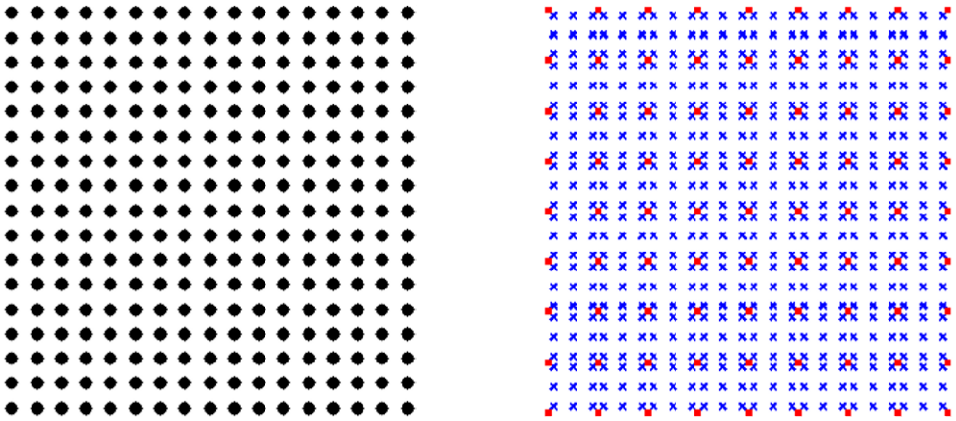

(a) (b)

Figure 25: Regular discretization for monotonic test (a) 289 nodes and (b) 576 integration points

To evaluate the performance of the constitutive damage model, the present analysis is performed using several nodal discretizations shown in Figure 21, Figure 22, Figure 23, Figure 24 and Figure 25. All the obtained results are compared with the experimental solution (Gopalaratnam & Shah, 1985) for stress-strain curve. Moreover, the behaviour of the damage variable versus strain is compared to the FEM results of Voyiadjis et.al (Voyiadjis & Taqieddin, 2009). The iterative process of pseudo-time stepping scheme is applied using a tolerance of $1e^{-7}$ and 50 incremental enforced displacement steps. The results obtained from the corresponding study are presented for the equivalent stress versus the equivalent strain in Figure 26 and the variation of the damage parameter versus the equivalent strain at integration point *A* is presented in Figure 27.

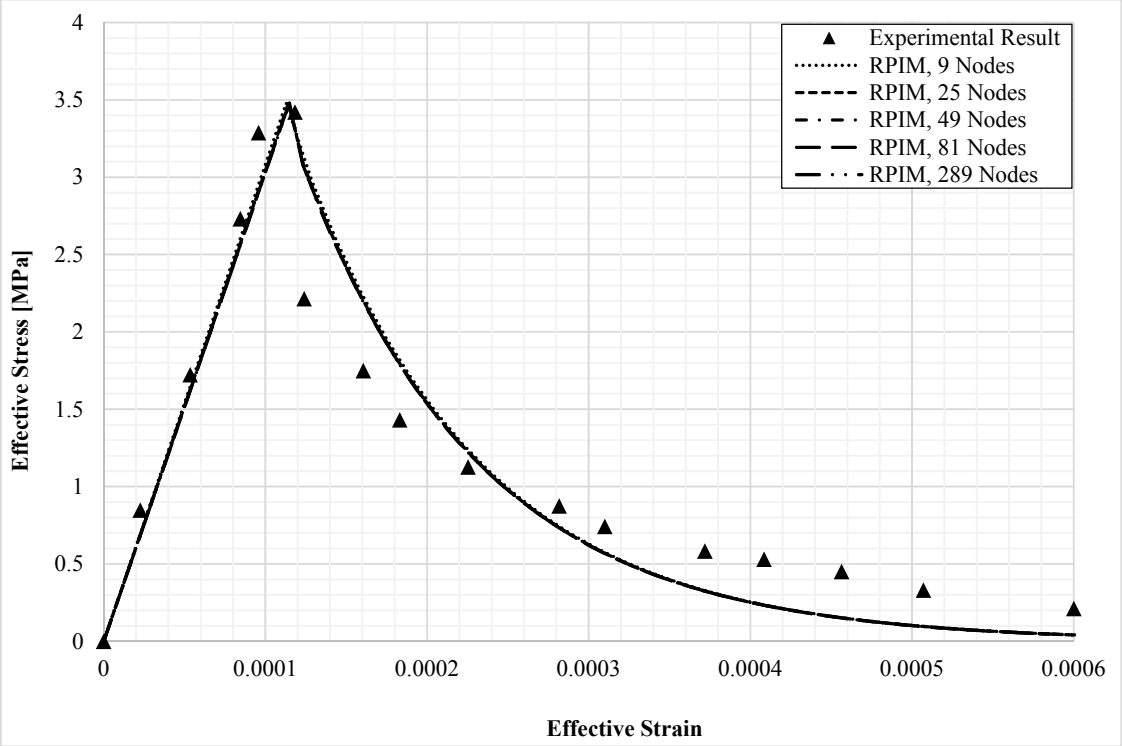

Figure 26: Effective stress-strain response for uniaxial tensile test compared to experimental result (Gopalaratnam & Shah, 1985)

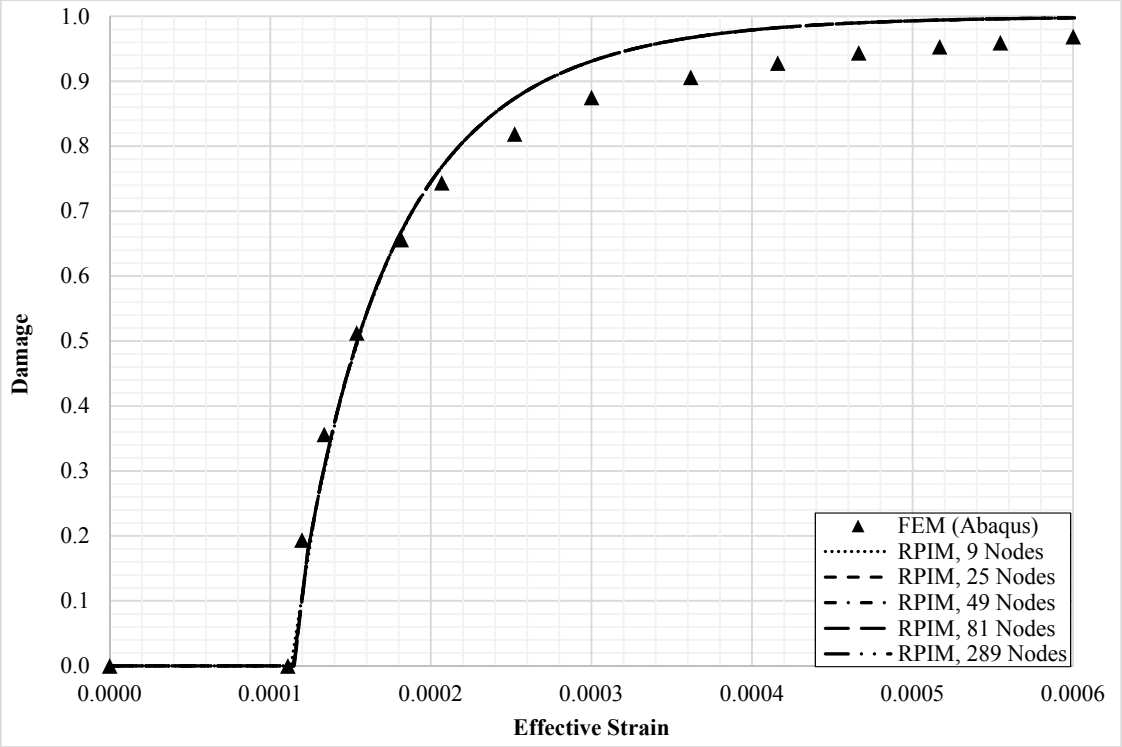

Figure 27: Damage versus effective strain at integration point *A* for uniaxial tensile test compared to FEM results (Voyiadjis & Taqieddin, 2009)

It is possible to infer that the stress versus strain curve obtained with the meshless method shows a good agreement with the experimental curve, particularly for the peak value of the stress in which the damage initiates. The behaviour of the damage variable-strain curve proves that the result is the same for the different mesh size and fixed material properties and very close with the finite element solution.

The graphical representations of the internal variables performed on the RPIM with 289 nodes are presented in Figure 28 and Figure 29. The former one is related to the first stage when half of the total displacement enforced on the geometry and the latter one is the second stage in the presence of the full enforced displacement. Moreover the profile of the compressive damage is illustrated in Figure 30. It accounted for the zero value during the full displacement enforcement.

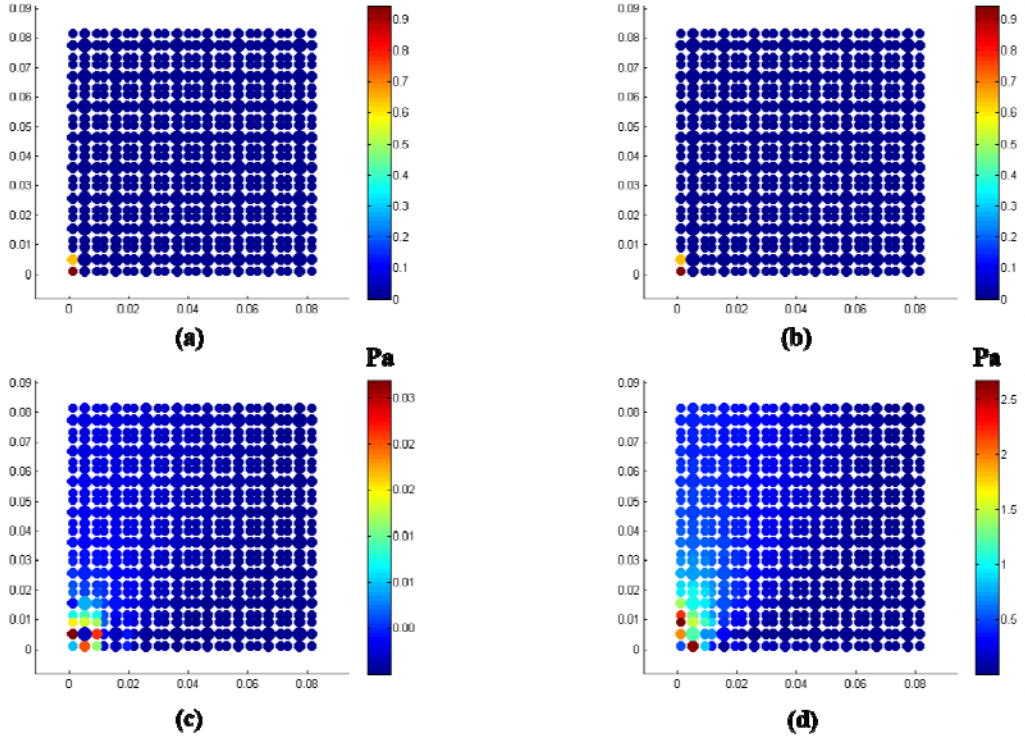

Figure 28: The profile of the internal variables for monotonic uniaxial tensile test with 289 nodes in the first displacement enforcement stage. (a) Damage, (b) tensile damage, (c) equivalent effective damaged stress and (d) equivalent effective total stress

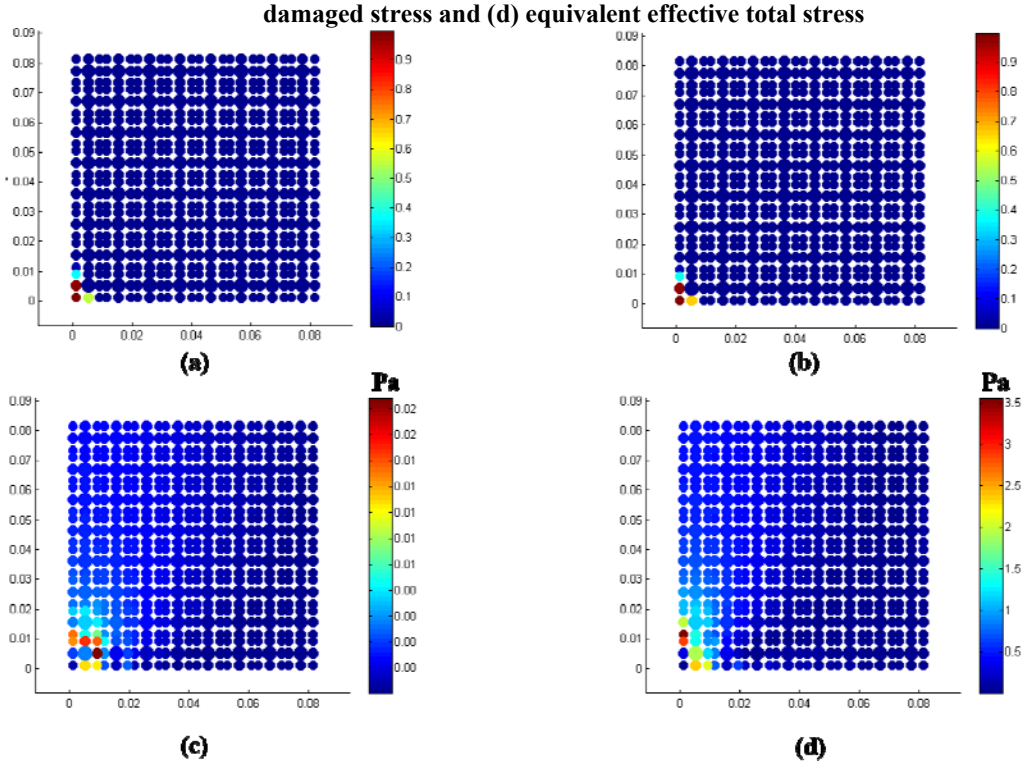

Figure 29: The profile of the internal variables for monotonic uniaxial tensile test with 289 nodes in the second displacement enforcement stage. (a) Damage, (b) tensile damage, (c) equivalent effective damaged stress and (d) equivalent effective total stress

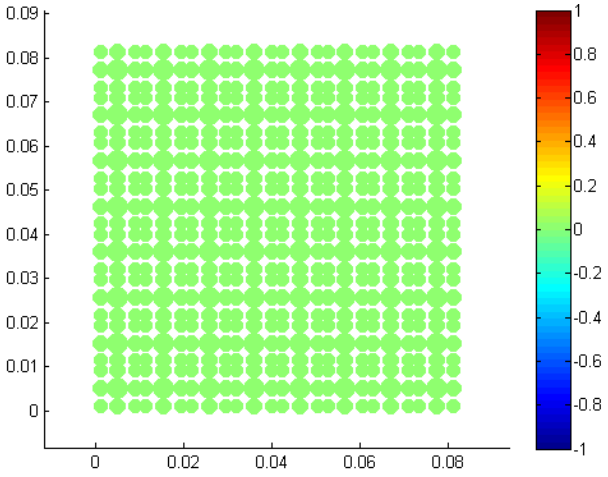

Figure 30: Compressive damage profile in monotonic uniaxial tensile test for RPIM with 289 nodes

6.3 Monotonic Uniaxial Compressive Test

The verification of the proposed model for the uniaxial compressive test is presented as the second benchmark. Figure 20-b schematically shows the discretization of the model and boundary conditions of the current analysis. The material properties used in this analysis are based on the work presented by Lee et.al. (Lee & Fenves, 1998): $E = 31\ (GPa)$, $\nu = 0.2$, $f_0^- = 10.2\ (MPa)$ and $G_f^- = 5690\ (N/m)$. By conducting a convergence study, the corresponding compressive parameters defining the compressive damage behaviour of concrete used in Equation (93-b) are: $A^- = 2.14$ and $B^- = 0.58$.

The analysis of the uniaxial test in compression is performed for several nodal discretizations (demonstrated in Figure 21, Figure 22, Figure 23, Figure 24 and Figure 25) and considering 50 enforced displacement increments (with a tolerance equal to $1e^{-8}$). The obtained results are plotted in Figure 31 and compared to the experimental solution (Karsan & Jirsan, 1969).

According to the similar numerical work using the FEM (Voyiadjis & Taqieddin, 2009), it is possible to present the curve of damage variable versus the effective strain at integration point *A* for uniaxial compressive test, which is shown in Figure 32.

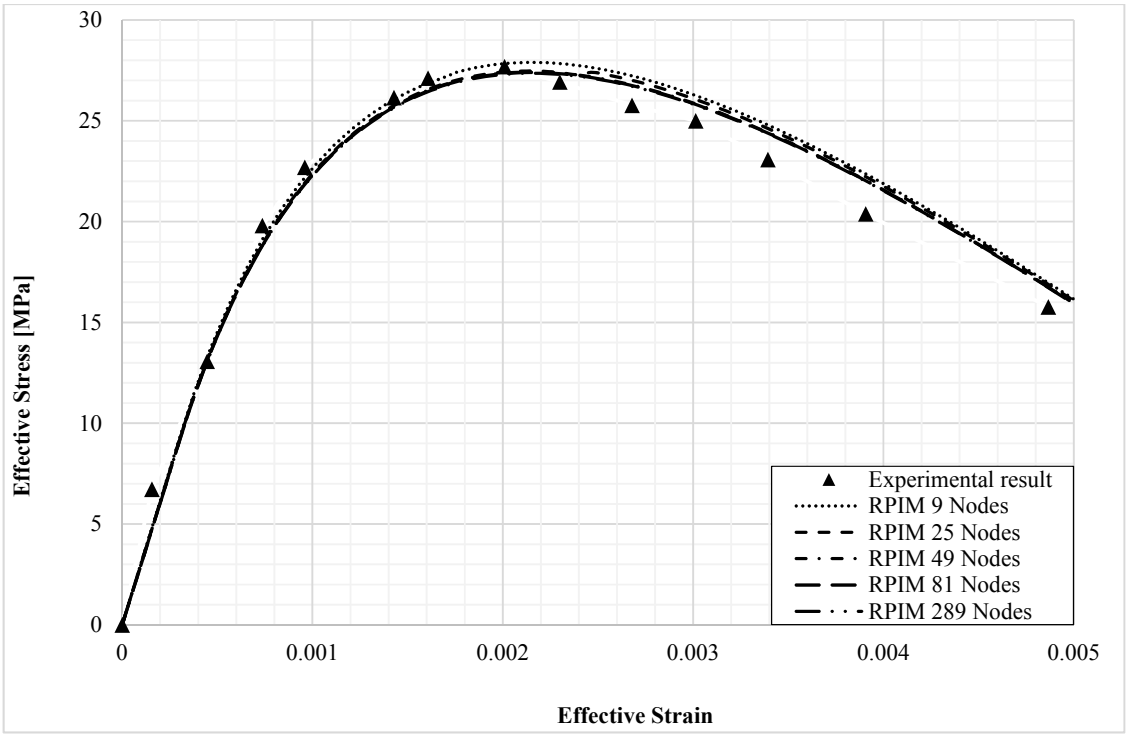

Figure 31: Effective stress-strain response for uniaxial compressive test compared to experimental result (Karsan & Jirsan, 1969)

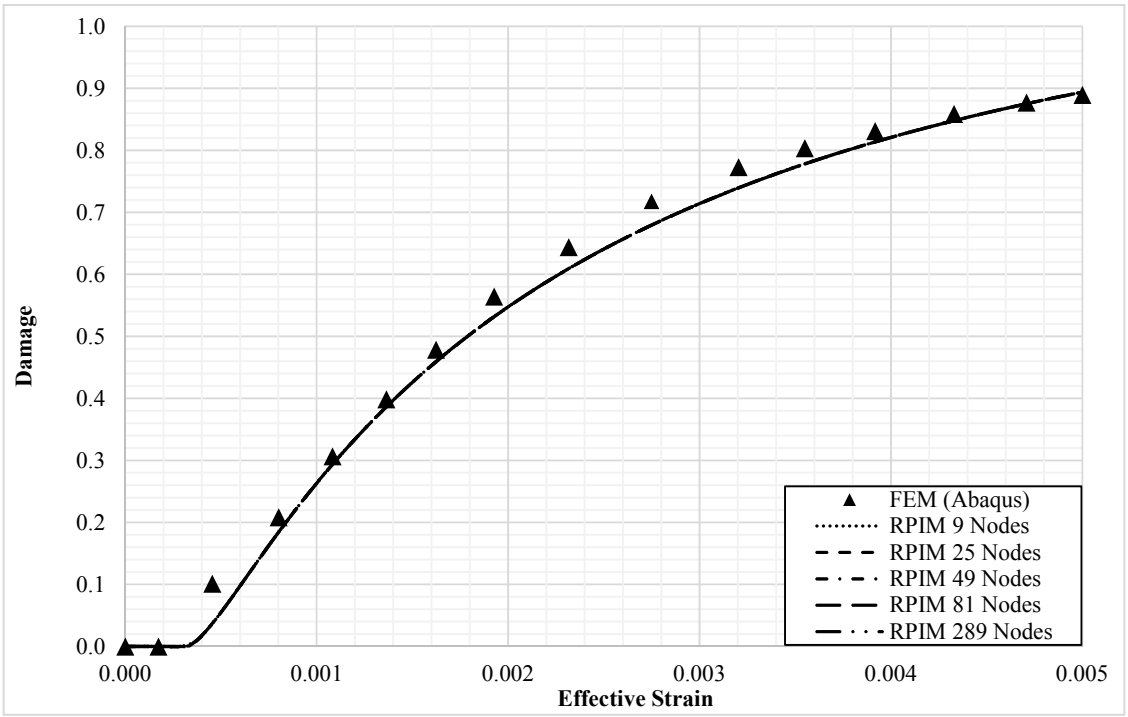

Figure 32: Damage versus effective strain at integration point A for uniaxial compressive test compared to FEM results (Voyiadjis & Taqieddin, 2009)

The obtained curves related to the uniaxial compressive test shown in Figure 31 and Figure 32, indicate that the RPIM results agree with the FEM solution and the experimental one, regardless the nodal discretizations used in the analysis.

The progress of the current analysis is demonstrated for the internal and damage variables in Figure 33 and Figure 34. The RPIM discretization with the total number of 289 nodes is considered here. The former figure is captured when half of the total displacement enforced on the material (first stage) while the latter figure is related to the stage with the full displacement enforcement (second stage).

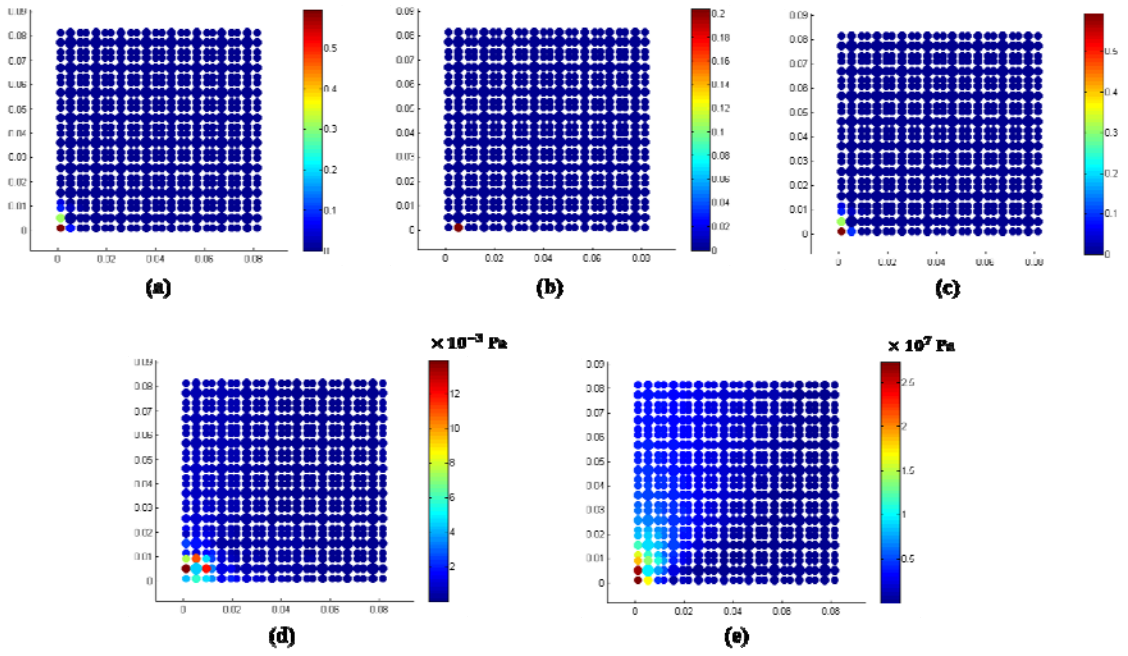

Figure 33: The profile of the variables for monotonic uniaxial compressive test with 289 nodes in the first displacement enforcement stage. (a) Compressive damage, (b) tensile damage, (c) damage (d) equivalent effective damaged stress and (e) equivalent effective total stress

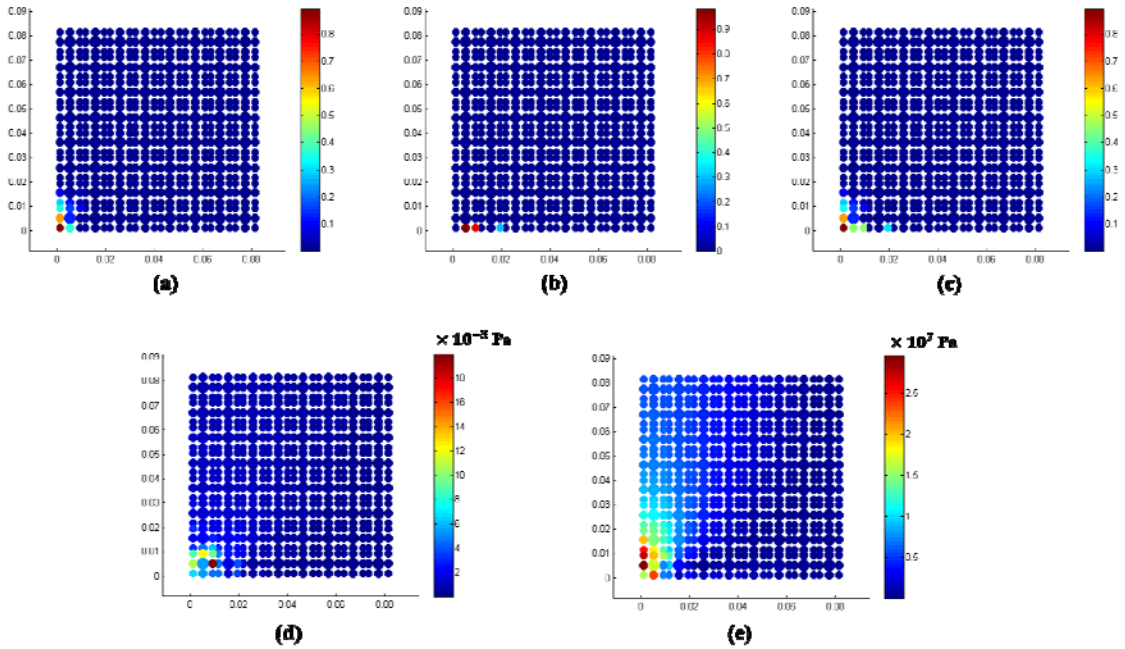

Figure 34: The profile of the variables for monotonic uniaxial compressive test with 289 nodes in the second displacement enforcement stage. (a) Compressive damage, (b) tensile damage, (c) damage (d) equivalent effective damaged stress and (e) equivalent effective total stress

6.4 Monotonic Biaxial Tensile Test

Consider now the test problem illustrated in Figure 35-a for a biaxial tensile test. The analysis is performed by enforcing a compressive displacement on the right and top edges of the body. The material properties and the damage characteristics, such as A^+ and l_{ch}, are the same as uniaxial test in tension. In the case of stress-strain response, the computational results derived from meshless method are compared to the experimental solution presented by Kupfer et. al. (Kupfer et al., 1969).

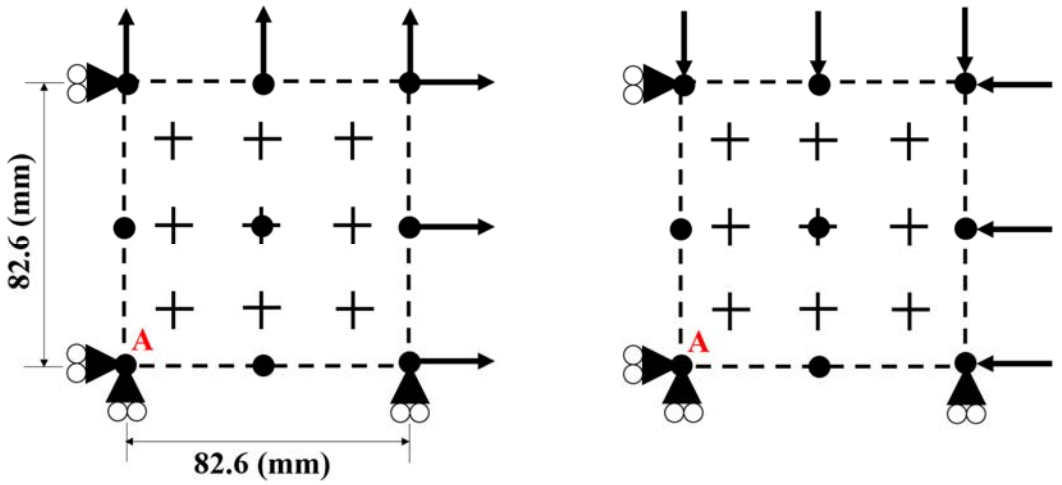

Figure 35: Quadrilateral meshless discretization of biaxial test under (a) tension and (b) compression

Figure 36 shows the behaviour of the proposed rate-independent elastic damage model in a biaxial tensile test performed with the RPIM formulation for various discretizations (refer to Figure 21, Figure 22, Figure 23, Figure 24 and Figure 25). The figure is graphed in a non-dimensional mapped stress form derived from dividing the normalized stress $\sigma_{11}$by the compressive strength $f_c' = 27.6\ (MPa)$ with regard to $R = \sigma_{11}/\sigma_{22} = 1$. The experimental results of Kupfer et. al. (Kupfer et al., 1969) are valid within the following range: $0 \leq \sigma_{11}/f_c' \leq 0.09$. The RPIM solutions are compared with the FEM results (Voyiadjis & Taqieddin, 2009).

Figure 37 shows that the results obtained with proposed elastic damage model using RPIM formulation agree with both experimental and FEM solution.

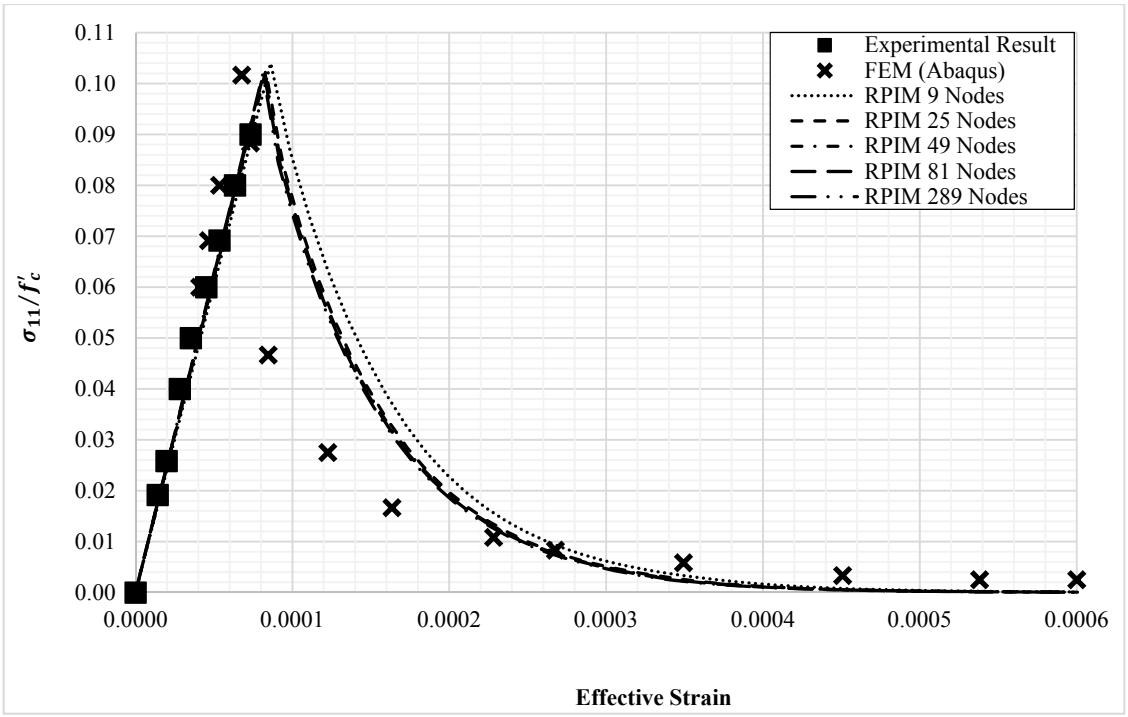

Figure 36: Effective stress-strain response for biaxial tensile test compared to experimental (Kupfer et al., 1969) and FEM (Voyiadjis & Taqieddin, 2009) results ($\sigma_{11} = \sigma_{22}$)

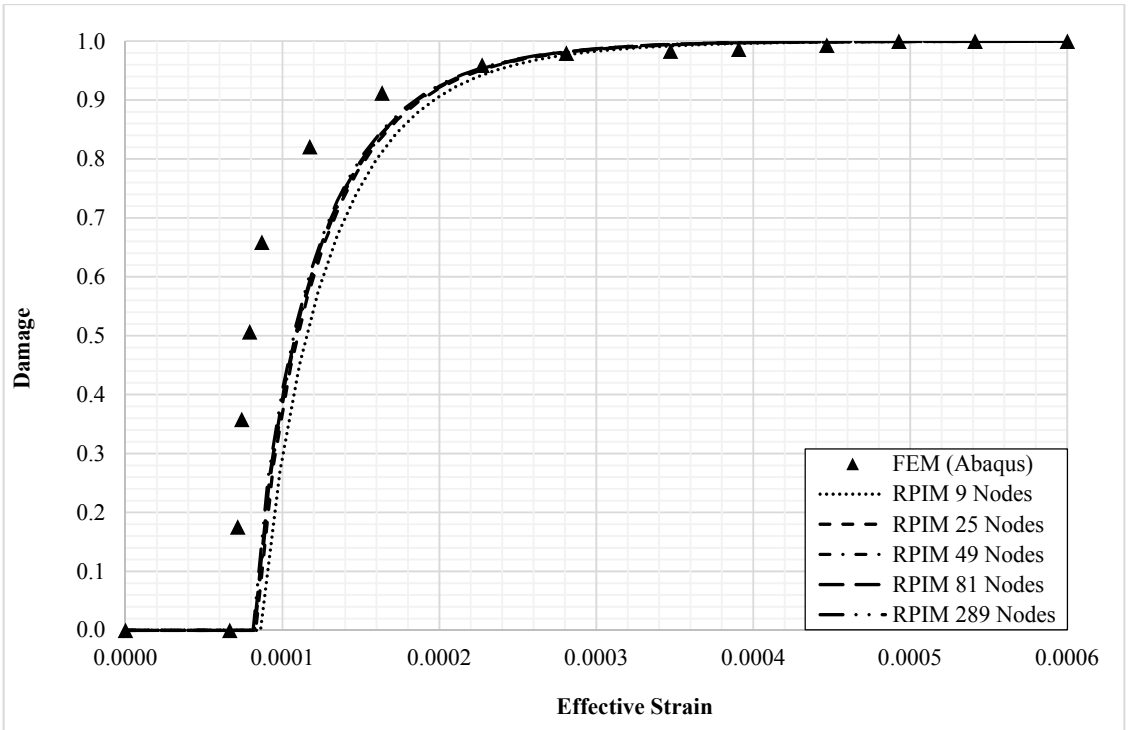

Figure 37: Damage versus effective strain at integration point A for biaxial tensile test compared to FEM result (Voyiadjis & Taqieddin, 2009)

It must be remarked that the enforced displacement has the same value in both directions and it is imposed incrementally during the analysis. The RPIM curves are very close to the FEM and experimental results.

Consider the discretization with 289 number of nodes under biaxial tensile test, the distribution of the internal variables such as equivalent effective stress in total and damaged states, in addition to the damage variables, are plotted in Figure 38, Figure 39 and Figure 40. It must be noted that the first stage is subjected to the half of total enforced displacement and the second stage is connected to the end of the analysis when the full displacement enforcement is applied on the material.

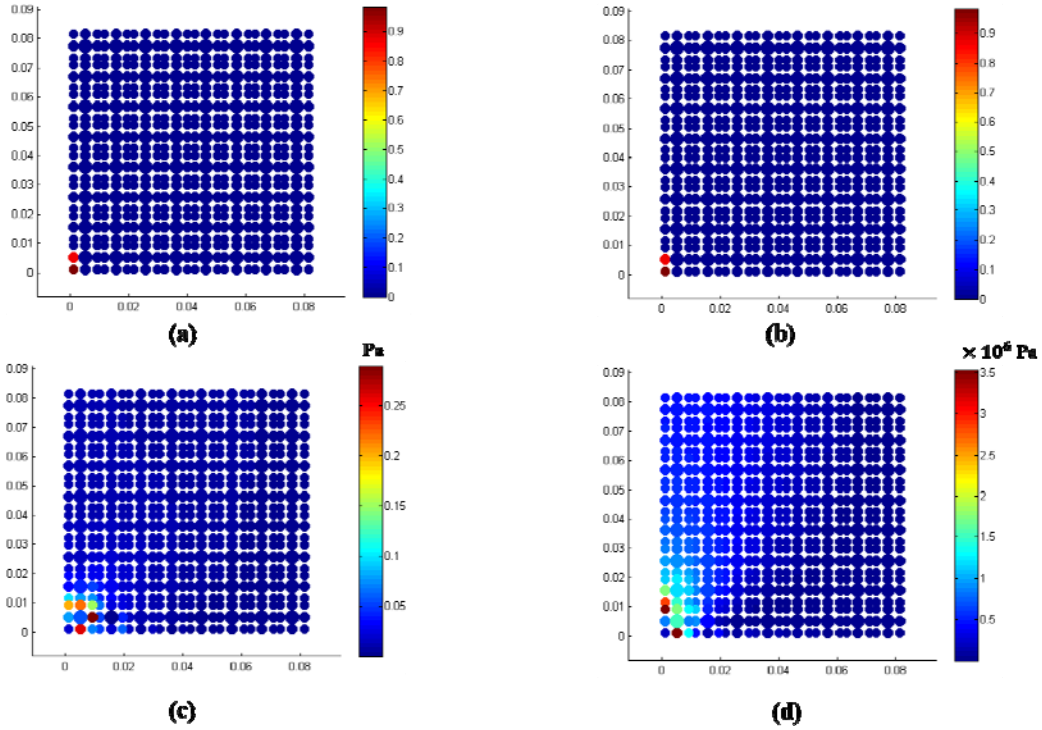

Figure 38: The profile of the internal variables for monotonic biaxial tensile test with 289 nodes in the first displacement enforcement stage. (a) Damage, (b) tensile damage, (c) equivalent effective damaged stress and (d) equivalent effective total stress

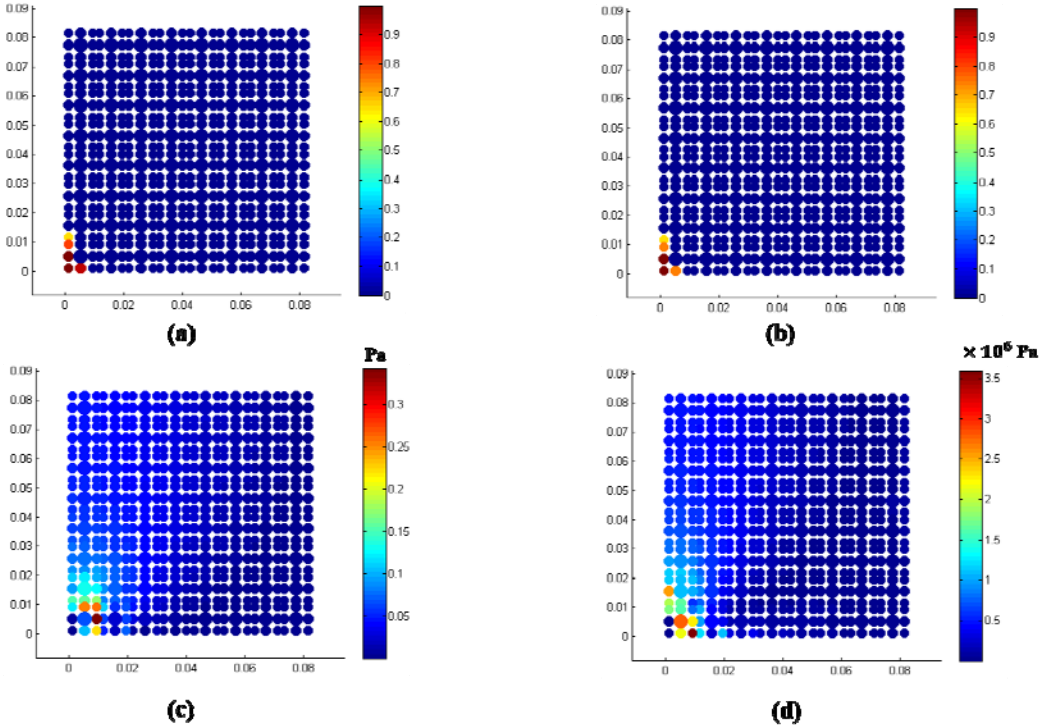

Figure 39: The profile of the internal variables for monotonic biaxial tensile test with 289 nodes in the second displacement enforcement stage. (a) Damage, (b) tensile damage, (c) equivalent effective damaged stress and (d) equivalent effective total stress

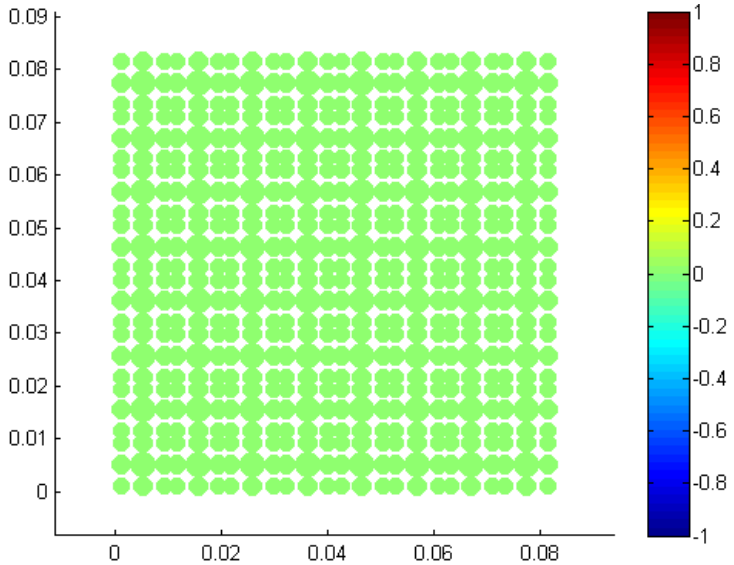

Figure 40: Compressive damage profile in monotonic biaxial tensile test for RPIM with 289 nodes

6.5 Monotonic Biaxial Compressive Test

The computational model described in the previous benchmark is now applied to the analysis of the biaxial compressive test. The RPIM geometry model for this study is shown in Figure 35-b. The material properties are the same used for uniaxial test in compression. In this example it is considered $f_0^- = 15.2(MPa)$, as recommended by Wu et.al.(J. Y. Wu et al., 2006). Within Equation (93-b), the corresponding compressive damage coefficients are adopted based on a damage study of the material: $A^- = 2.50$ and $B^- = 0.67$. In order to evaluate the accuracy of the proposed non-linear return-mapping damage stage, in this study 200 displacement increments are considered. The assumed tolerance is: $1e^{-7}$.

The RPIM result regarding the response of effective stress-strain for various number of nodes (see Figure 21, Figure 22, Figure 23, Figure 24 and Figure 25) compared to experimental observation (Kupfer et al., 1969) is plotted in Figure 41. Additionally, the values obtained for the damage variable versus the effective strain at integration point *A* are presented in Figure 42.

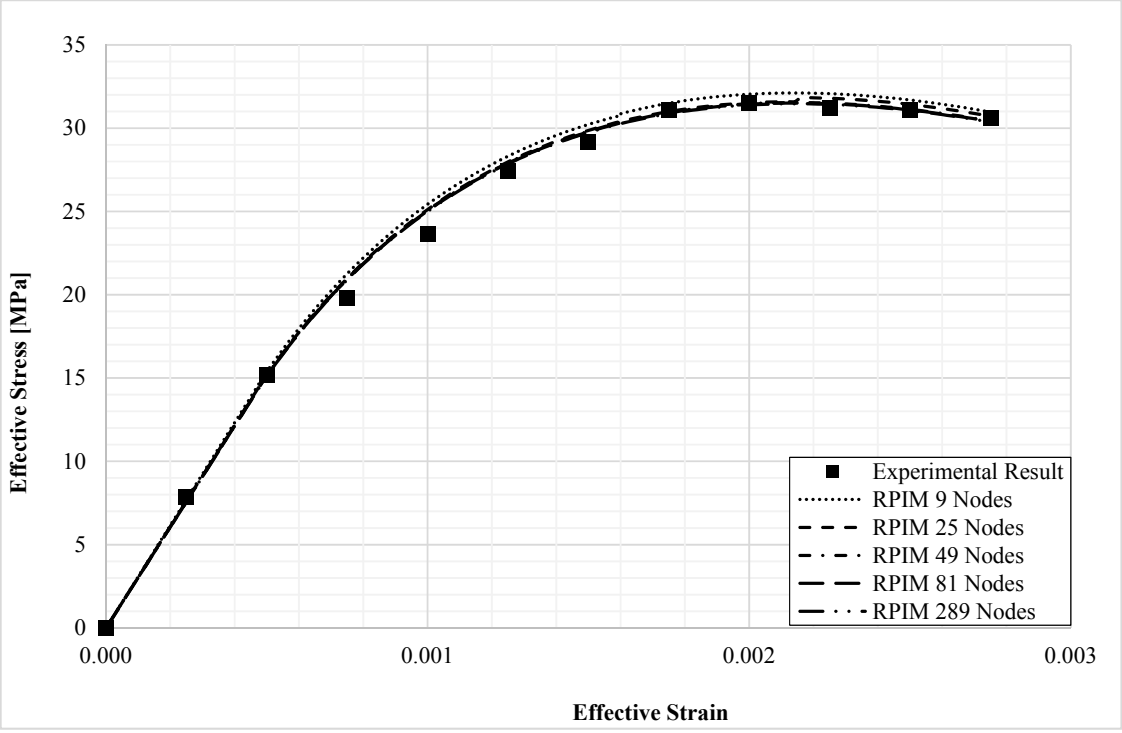

Figure 41: Effective stress-strain response for biaxial compressive test compared to experimental result (Kupfer et al., 1969)

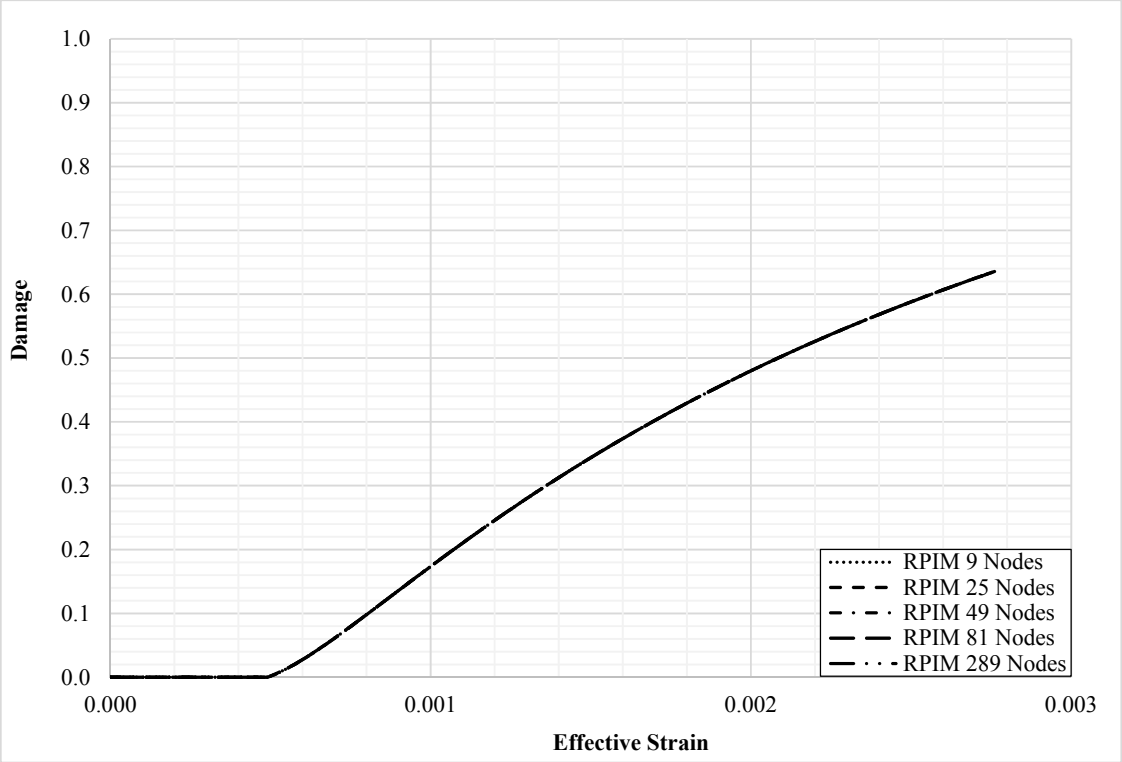

Figure 42: Damage versus effective strain integration point A for biaxial compressive test obtained from RPIM

As can be noticed, the stress-strain curve exhibits a satisfactory agreement with the experimental result. Additionally, it is possible to visualize, in Figure 41 and Figure 42 that the RPIM solution does not significantly vary with the level of the nodal discretizations.

There are some valuable observations captured in two different displacement enforcement stages. The first is related to the one that the half of total displacement enforcement governs on the material while the second stage is related to the one that full displacement enforced on the material. The discretization is assumed the one with 289 total number of nodes (the densest one). Following that the profiles of internal and damage variables are indicated in Figure 43 and Figure 44 correspond to the biaxial compressive test.

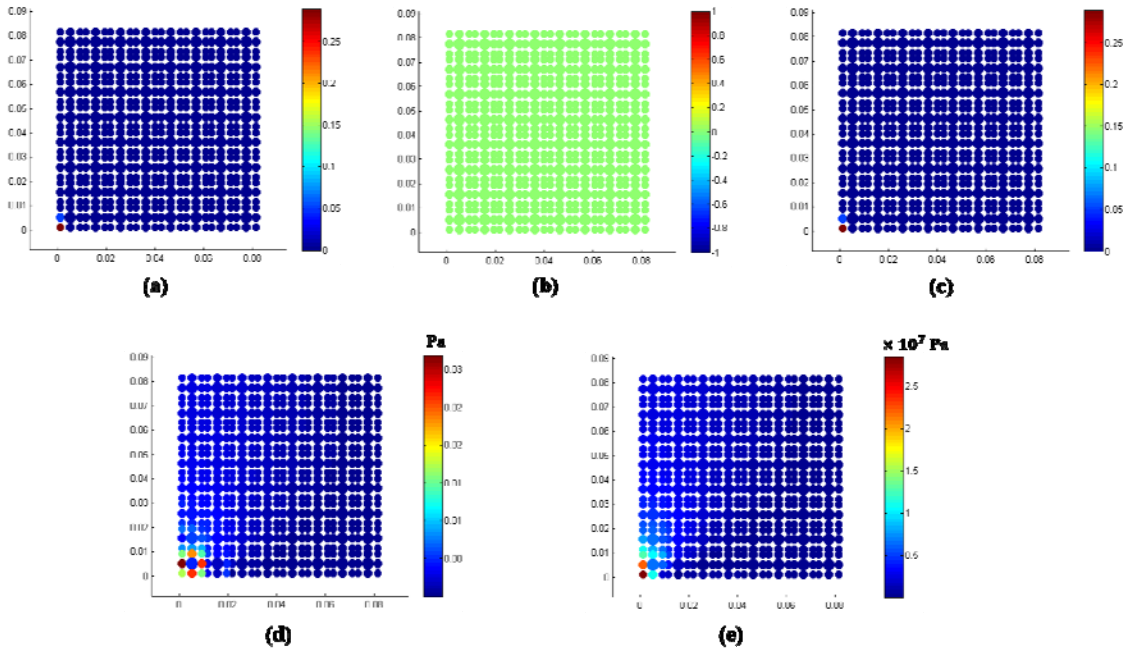

Figure 43: The profile of the variables for monotonic biaxial compressive test with 289 nodes in the first displacement enforcement stage. (a) Compressive damage, (b) tensile damage, (c) damage (d) equivalent effective damaged stress and (e) equivalent effective total stress

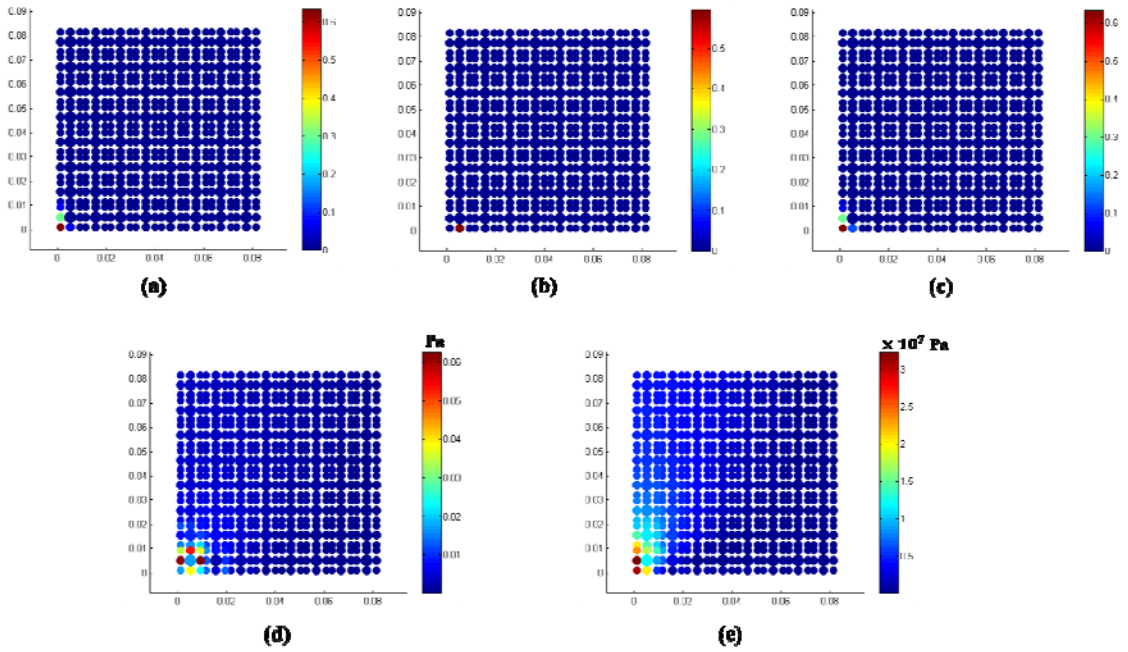

Figure 44: The profile of the variables for monotonic biaxial compressive test with 289 nodes in the second displacement enforcement stage. (a) Compressive damage, (b) tensile damage, (c) damage (d) equivalent effective damaged stress and (e) equivalent effective total stress

Furthermore, the results of the effective stress-strain and damage-effective strain for the uniaxial and biaxial tests in tension obtained with the RPIM formulation are illustrated in Figure 45 and Figure 46, respectively. The RPIM solutions are compared to the FEM one reported by Voyiadjis et.al. (Voyiadjis & Taqieddin, 2009). The RPIM results were obtained with a nodal distribution possessing 289 nodes.

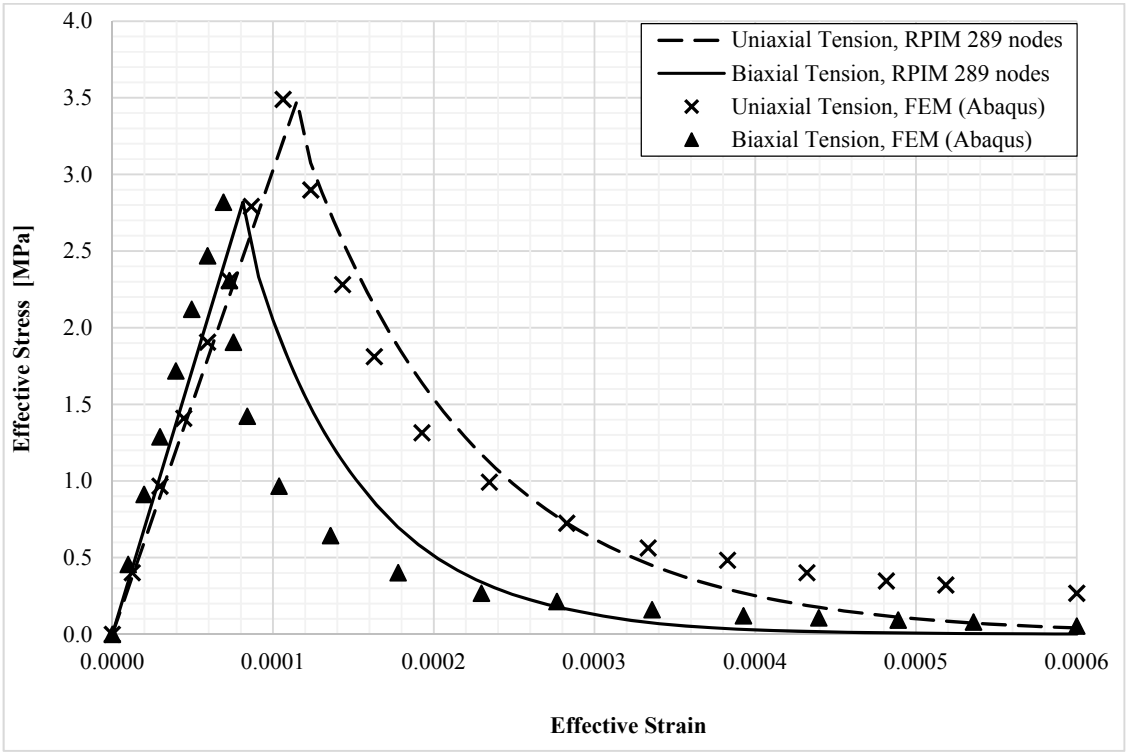

Figure 45: Comparison of the effective stress-strain response of the uniaxial and biaxial tensile tests

As can be noticed, the resistance of the material against damage phenomenon is greater in the uniaxial test compared to the biaxial test, it means that the stress reaches its peak sooner in the biaxial test.

Similarity, the response of damage variable–effective strain at integration point *A* of both tests are indicated in Figure 46. The results of the RPIM technique are compared to the FEM solution (Voyiadjis & Taqieddin, 2009).

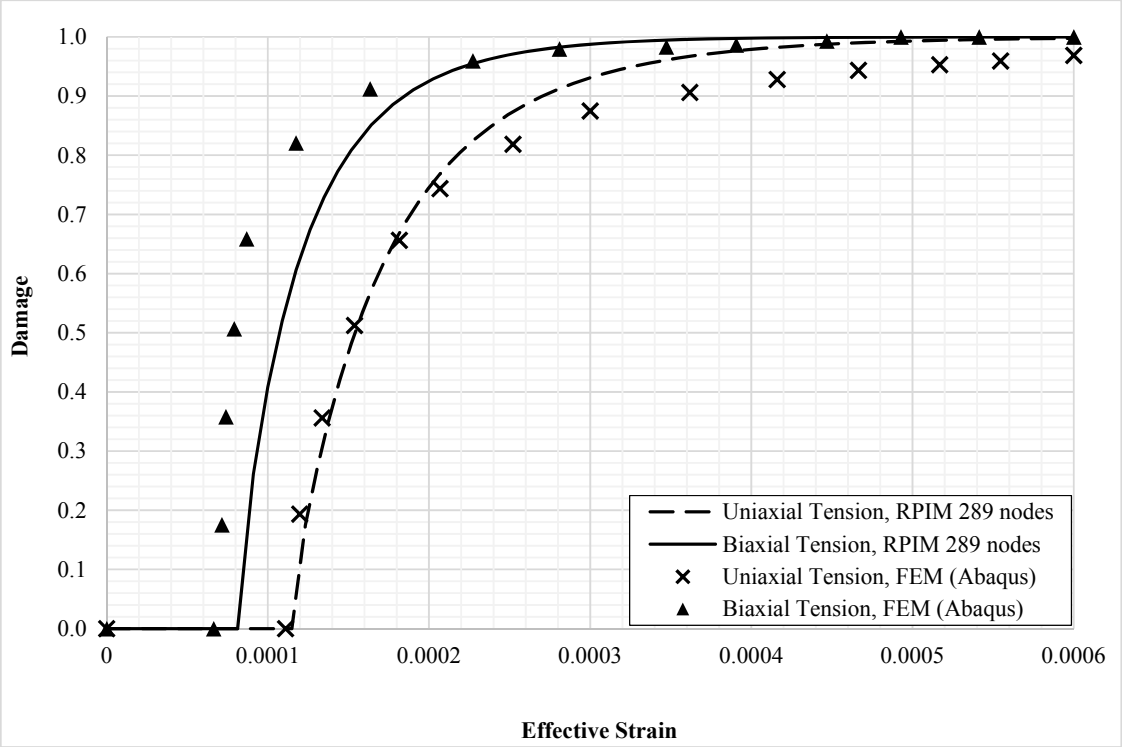

Figure 46: Comparison of damage versus effective strain integration point *A* for uniaxial and biaxial tensile tests (Voyiadjis & Taqieddin, 2009)

An important aspect of the proposed model under biaxial tension can be observed in Figure 46, the damage initiates at a sooner step and it increases rapidly to reach the maximum damage value.

Considering Figure 45 and Figure 46, it is visible that the RPIM curves exhibit an acceptable agreement with FEM curves. Indicating that the present formulation is suitable to study the damage behaviour of more demanding concrete structures.

6.6 Three Point Bending Beam

In this benchmark example a single-edge-notched concrete beam is studied using both regular and irregular nodal discretizations. The analyses are based on the experimental data from Malvar et.al. (Malvar & Warren, 1988).

Figure 47-a shows the geometry of the beam. It is possible to visualize an initial crack in the middle of the beam with the initial length of $a_0 = 51\ (mm)$ submitted to the three point bending enforcement. The material properties and damage characteristics adopted for the damage model are: Young`s Modulus $E = 21.7\ (GPa)$, Poisson's ratio $\nu = 0.2$ and a maximum uniaxial tensile and compressive strength: $f_0^+ = 2.4\ (MPa)$ and $f_0^- = 29\ (MPa)$, respectively. Moreover, the fracture energy is equal to $G_t = 30\ (N/m)$ for the current analysis. Considering Equations (93-a) and (93-b), the damage parameters for both regular and irregular discretizations are adopted as $A^+ = 0.001$ for tension (based on a convergence study performed for this work) and $A^- = 1$ and $B^- = 0.89$ in compression (Cervera et al., 1996). Here, the following characteristic length is considered: $l_{ch} = 12.6\ (mm)$(Voyiadjis & Taqieddin, 2009). Taking advantage of the symmetry of the beam, only half of the problem was analysed. Thus, the regular nodal distribution discretizing half of the problem domain is presented in Figure 47-b, corresponding to 25×19 nodes. Indeed, the total number of nodes and integration points are 475 and 972 respectively.

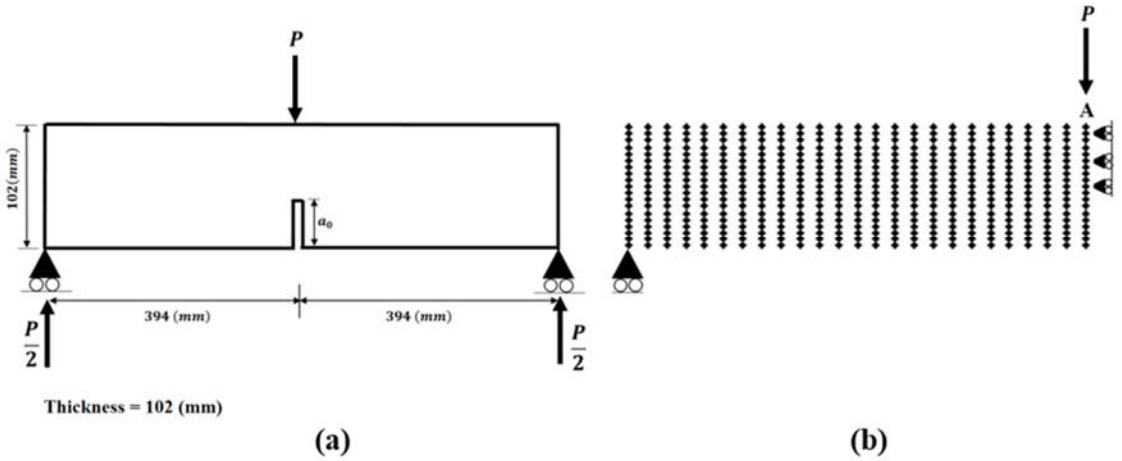

Figure 47: Three point bending test of the single-edge-notched beam; (a) the geometry of the model; and (b) 2D regular discretization of the nodes

In order to evaluate the capability of the non-linear damage algorithm for this example, it was considered a tolerance value of $1e^{-12}$ and the total number of 50 incremental steps.

The load-displacement graph for distinct nodal distributions is presented in Figure 48. The plotted load corresponds to load *P* and the displacement regards to the vertical displacement of point *A*. The obtained result is compared with the experimental solution (Malvar & Warren, 1988).

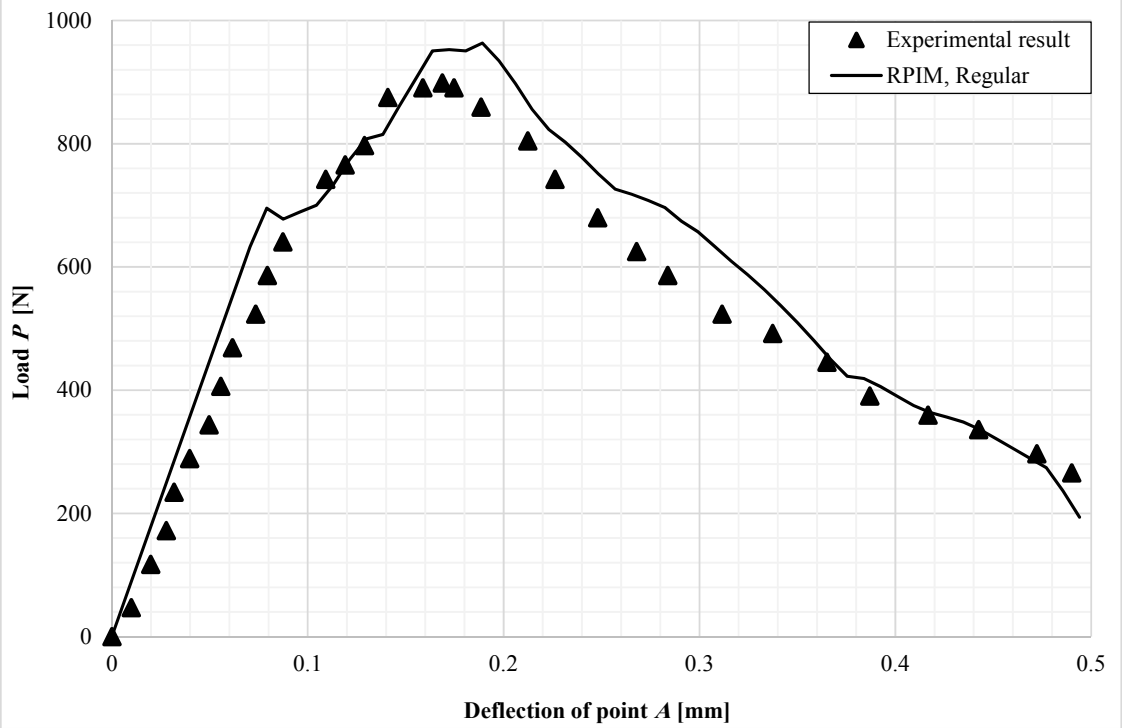

Figure 48: Load *P* in terms of deflection on point *A* for three point bending test obtained from regular RPIM mesh compared to experimental result (Malvar & Warren, 1988)

6.6.1 Irregular Mesh

It is important to determine the influence of the mesh irregularity on the performance of the RPIM formulation. Thus, the problem domain was discretized in several irregular nodal distributions with 475 nodes, Figure 49-b. The nodal discretization follows a random

distribution. The theory of RPIM irregular analysis is introduced in Subsection 5.1.4 for axisymmetric plates where Equation (126) is used with regard to Figure 13.

Additionally, in this study, the material properties and damage characteristics are the same as the analysis of the previous regular nodal distribution. Referring to Equation (126), the irregularity parameter is chosen as $\lambda = 30$.

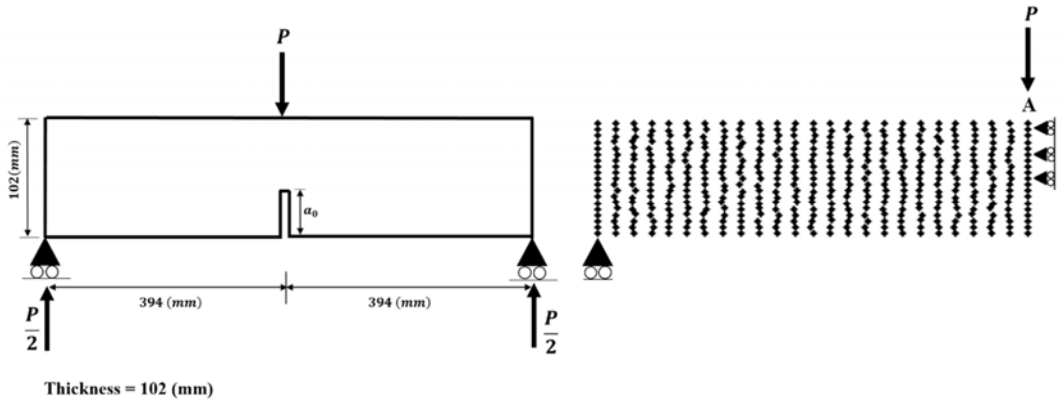

(a) (b)

Figure 49: Three point bending test of the single-edge-notched beam; (a) the geometry of the model; and (b) example of a 2D irregular mesh.

The analysis of the irregular mesh is studied for 6 random analyses. The basic results obtained for each analysis are presented in Figure 50. In Figure 51, it is presented the average RPIM solution obtained with the irregular nodal distributions and the RPIM result using a regular nodal distribution. The experimental solution indicated in Figure 51 was obtained from the literature (Malvar & Warren, 1988).

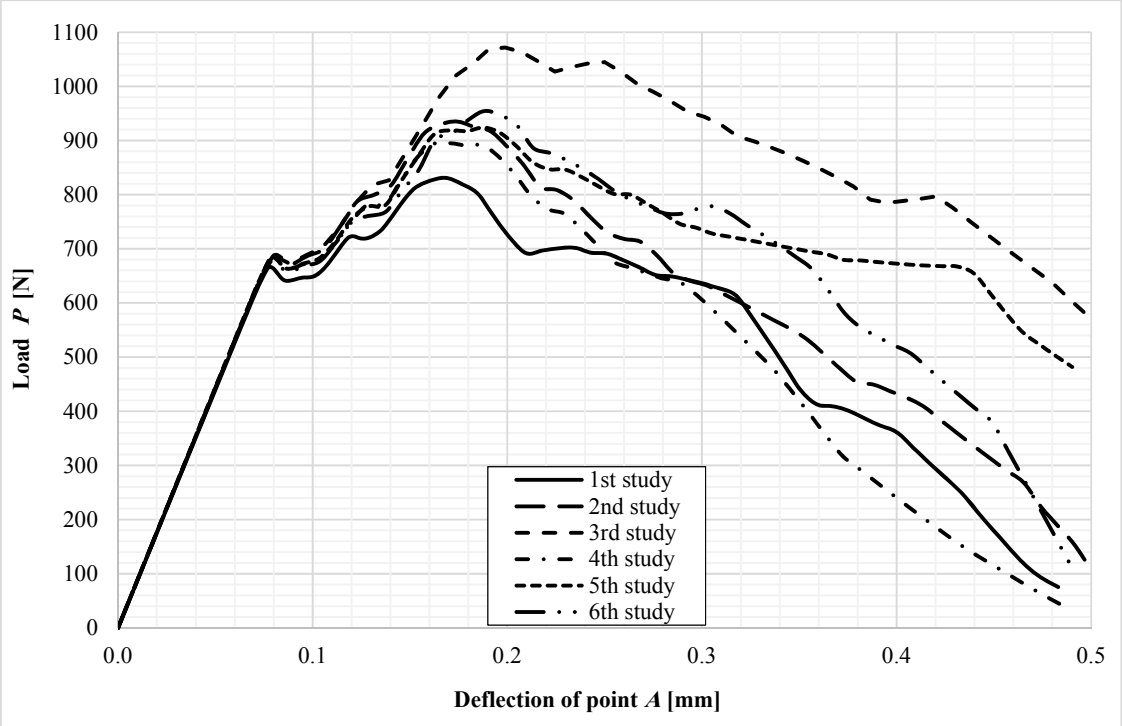

Figure 50: Study of the mesh irregularity obtained for the response of load *P* – deflection of point *A*

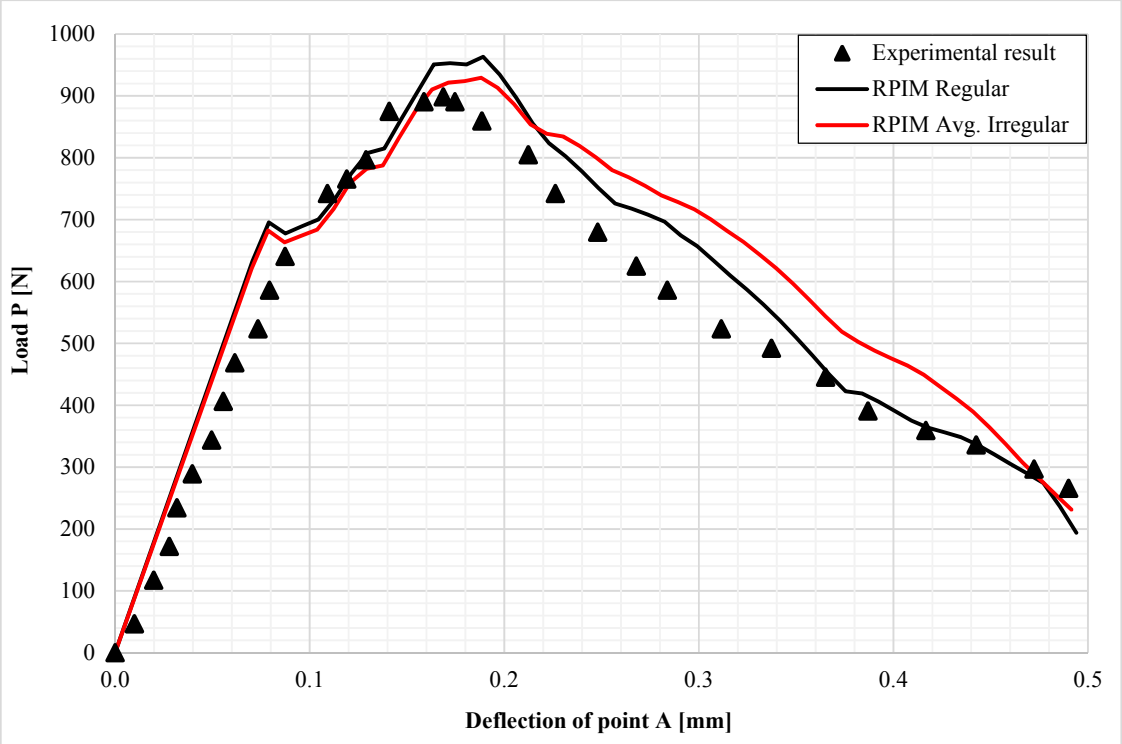

Figure 51: The response of load- deflection of point A in three point bending test obtained from RPIM regular and irregular mesh compared to experimental results (Malvar & Warren, 1988)

It should be mentioned that the non-mild behaviour of the curve, after reaching the peak load value, is due to the non-linear solution of the damage mechanics formulation for concrete materials (Voyiadjis & Taqieddin, 2009) (Feenstra, 1993) (Fichant, La Borderie, & Pijaudier-Cabot, 1998)(Lowes, 1999)(Jankowiak & Lodygowski, 2005)(Sumarac, Sekulovic, & Krajcinovic, 2003).

6.6.1.1 Graphical Representations of the Internal and Damage Variables

The following figures show the obtained distribution of the internal and damage variables for regular analysis of the concrete beam submitted to a vertical displacement enforcement in the particular displacement enforcement stages presented on Table 14.

Table 14: The corresponding displacement enforcement for three point bending beam

	First stage	Second stage	Third stage
Displacement enforcement (mm)	1.764479E-01	3.881854E-01	4.940541E-01

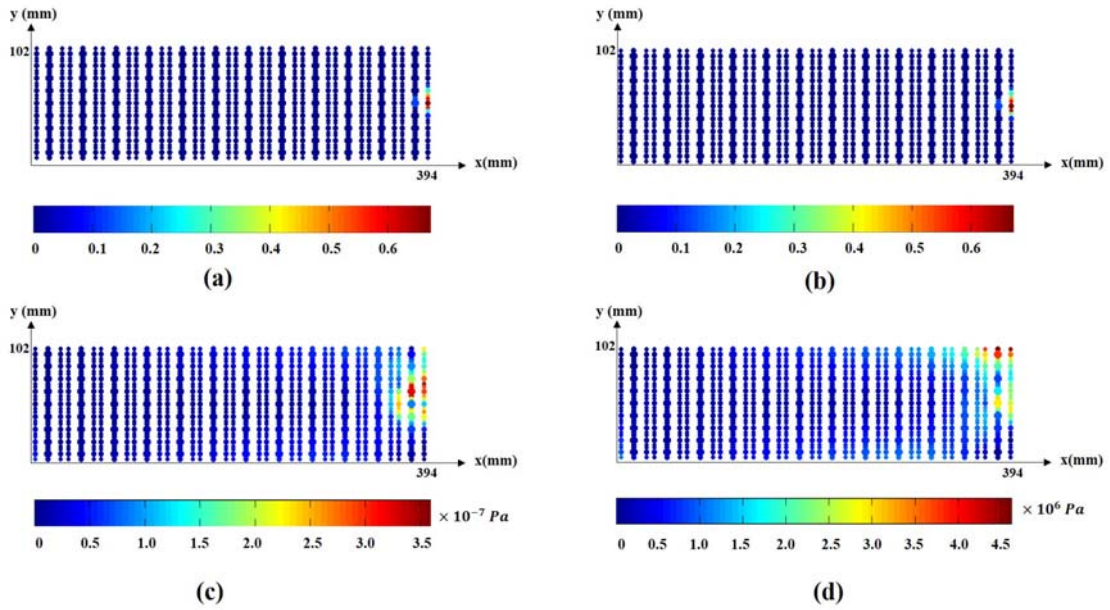

Figure 52: The graphical representations at the first displacement stage for (a) damage, (b) tensile damage, (c) equivalent effective damaged stress and (d) equivalent effective total stress

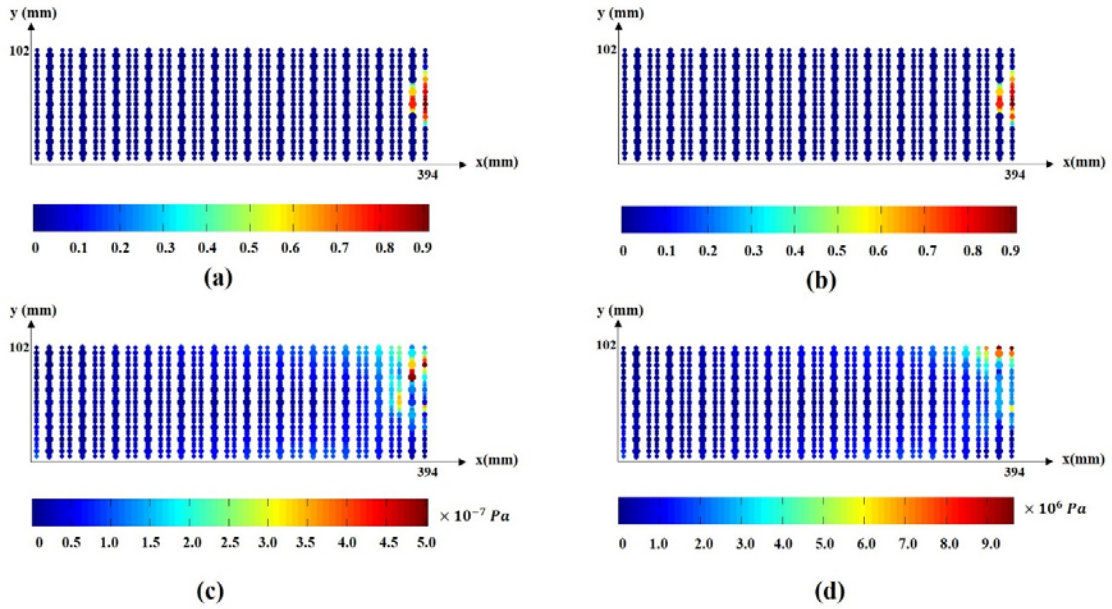

Figure 53: The graphical representations at the second displacement stage for (a) damage, (b) tensile damage, (c) equivalent effective damaged stress and (d) equivalent effective total stress

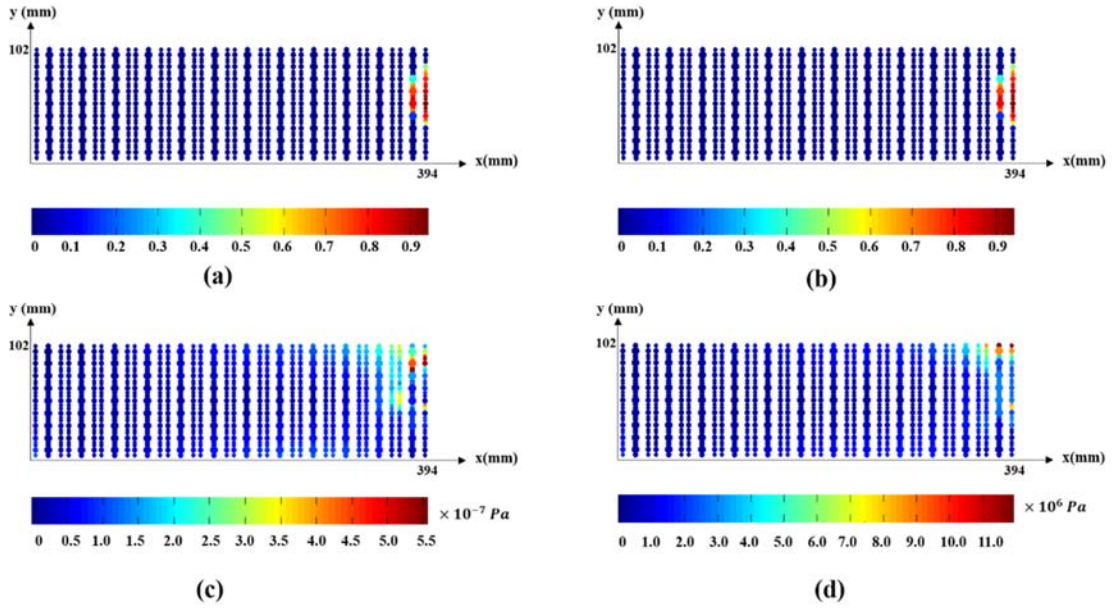

Figure 54: The graphical representations at the third displacement stage for (a) damage, (b) tensile damage, (c) equivalent effective damaged stress and (d) equivalent effective total stress

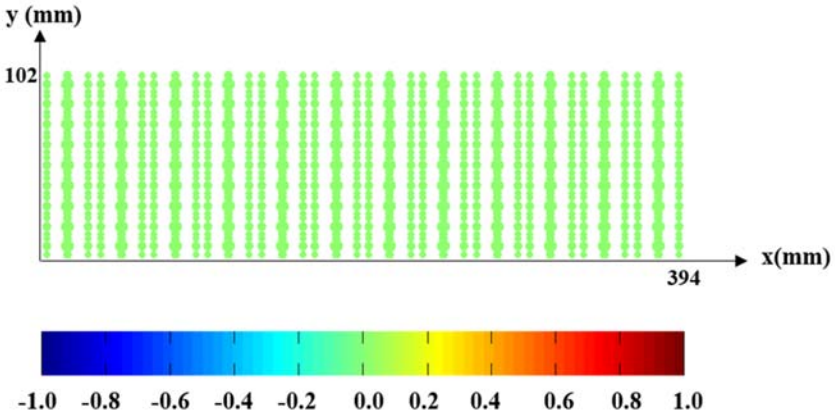

Figure 55: Distribution of compressive damage variable along the beam for all displacement enforcement stages

The damage profiles show that it is possible to predict the damaged region, near the crack tip, with the proposed algorithm. The compressive damage accounted for the zero value during all the enforced displacement stages. It is visible that the tensile damage and damage distribution possess the same profile due to the absence of the compressive one.

Additionally, it is noticeable that the crack tip zone presents higher damage values, as expected.

It must be remarked that the graphical representations for irregular mesh are the same as the regular ones, hence it is not necessary to repeat them.

Chapter 7

7 *Numerical Benchmarks on the Localized Damage Formalism*

This chapter is focused on the damage localization formulations. Two different benchmark examples are studied here, both addressing the regular and the irregular discretization patterns.

The basic equations regarding damage mechanics have been introduced in chapter 4 and the damage localization formalism was expressed in Section 4.3. Here, the algorithm presented in Box 3 is used. In this work there exist some convergence studies for the damage localization parameters.

This part is structured as the following: the three point bending beam in the normal regular discretization (the one presented in Section 6.6) is studied in Section 7.1. After that the obtained numerical results will be compared to the experimental solution reported by (Malvar & Warren, 1988) and (Voyiadjis & Taqieddin, 2009). This example has been studied before for the non-local damage formalism presented in Section 6.6. Then, a refined discretization pattern is proposed for three point bending beam .After that, in Section 7.2 , particular localized damage parameters are optimized and they will be used for the second benchmark. The graphical representations of the internal and damage variables are presented in all the case studies. Subsequently, in Section 7.3, the compact tension test is solved with regard to the optimized coefficients proposed in Section 7.2, then, the RPIM solution is compared to the experimental result extracted from the work done by (Legendre, 1984) and (Mazars & Pijaudier-Cabot, 1996). Some graphical representations of the internal fields such as stress and damage variables will be presented in details. To end this study, irregular discretizations will be analysed in Sections 7.3.3 and 7.3.4.

7.1 Three Point Bending Beam, Normal Discretization

As mentioned before, in this analysis there are some parameters that have to be optimized in order to permit to be applicable for the further examples. In order to start the analysis, it is interesting to perform the program based on the nodal distribution called "Normal Discretization" introduced in Section 6.6. So, the geometry and discretization are the same as Figure 47. All the formulations and configurations introduced in Section 6.6 are also used here. The target of this analysis is to observe the results of this example with no changes in the material and geometric properties, but in the presence of the localized damage formalism. Hence it is a trial study and we might obtain some unexpected results.

First of all, it is better to describe the whole procedure briefly. The algorithm of elasto-damage mechanics is strain driven based on the displacement enforcement at point *A* (see Box 3). According to Table 1, a trial weight function must be chosen (it is the 2nd order weight function here) for regular discretization. Afterwards, the response of load *P* versus the deflection of point *A* is compared to the experimental solution (Malvar & Warren, 1988) is plotted. The geometric properties suggested by (Malvar & Warren, 1988) are presented on Table 15. Moreover, the material properties are shown on Table 16 (Lowes, 1999) and (Lee & Fenves, 2001). In addition, the algorithm configurations and damage characteristics are shown on Table 17 and Table 18. The only parameter varying here is related to the radius of the circle containing the points to smooth their damage, which is known as *RGP*.

Regarding the characteristic length and A^+ in this analysis, it should be remarked that the latter one is assumed as its typical value here, $A^+ = 0.001$. Hence the characteristic length is computed within rewriting Equation (96-a) proposed by (Cervera et al., 1995), so, the following relation is valid:

$$l_{ch} = \frac{A^+}{H(2 + A^+)} = 1.1296 \times 10^{-4}(m)$$

Table 15: Geometric properties of three point bending beam

Parameter	Value
Length	$L = 788 \times 10^{-3}(m)$
Width	$D = 102 \times 10^{-3}(m)$
Thickness	$e = 102 \times 10^{-3}(m)$
Crack length	$a_0 = 51 \times 10^{-3}(m)$

Table 16: Material properties of the three point bending beam

Property	Value
Young`s modulus	$E = 21.7 \times 10^{9}(Pa)$
Poisson's ratio	$\nu = 0.2$
Maximum uniaxial tensile strength	$f_0^+ = 2.4 \times 10^{6}(Pa)$
Maximum uniaxial compressive strength	$f_0^- = 29 \times 10^{6}(Pa)$
Fracture energy	$G_t = 30\ (N/m)$

Table 17: Damage characteristics

Parameter	Value
In tension	$A^+ = 0.001$
In compression (Cervera et al., 1996)	$A^- = 1$
In compression (Cervera et al., 1996)	$B^- = 0.89$
Characteristic length	$l_{ch} = 1.1296 \times 10^{-4}(m)$

The amounts of A^+ and also characteristic length are assumed here, they will be optimized in the next analyses.

Table 18: Algorithm configuration

Description
Total displacement enforcement $u = 0.5 \times 10^{-3}\ (m)$
Average displacement increment = $2.11474 \times 10^{-5}\ (m)$
Tolerance = 10^{-12}
Total increment = 20
Maximum number of iteration in each increment = 500

As mentioned in Section 6.6, the nodes are discretised as 25×19 divisions along x and y directions leading to have 475 and 972 nodes and integrations points respectively. According to Equation (102-a), some trial values for n_p are chosen randomly to obtain different amounts of *RGP* which are presented on Table 19. In addition, based on Equation (102-b), the value of h corresponds to the average distance between nodes is equal to:

$$h = 0.0164\ (m)$$

Where half of the total length is considered due to its symmetric geometry.

Table 19: Variation of RGP based on different n_p for 2nd order weight function in localized damage, three point bending beam

n_p	0.2	0.3	0.5	0.55	0.6	0.7
RGP	0.0033 (m)	0.0049 (m)	0.0082 (m)	0.0090 (m)	0.0098 (m)	0.0115 (m)

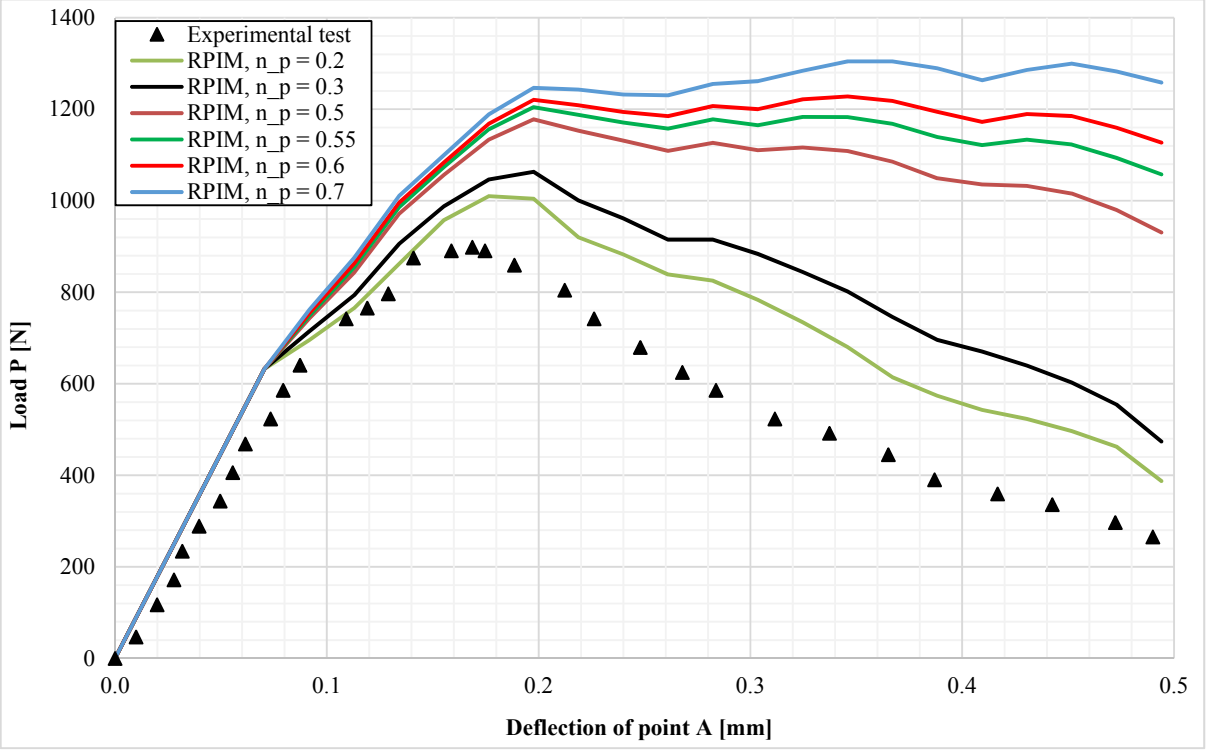

Figure 56: Response of load *P* vs. load deflection of point A for three point bending beam with normal discretization in localized damage with 2nd order weight function

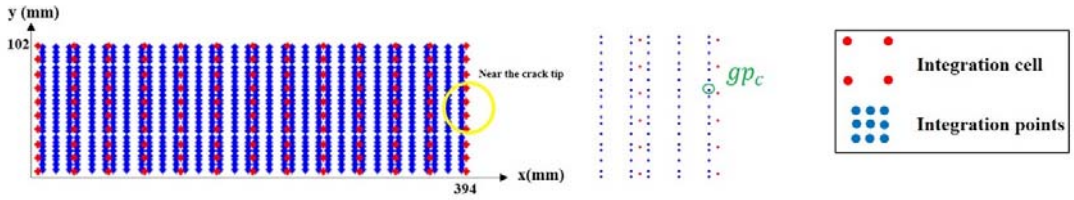

Figure 57: Integration cells and Gauss points for three point bending beam with normal discretization to detect gp_c

In order to measure the damage variables, it is necessary to select a particular integration point and then plot the damage variations for all the incremental displacement enforcements. As shown in Figure 57, this integration point is situated near the crack tip (yellow highlighted area). It is better to call it as gp_c. It should be noted that each integration cell contains 9 Gauss points.

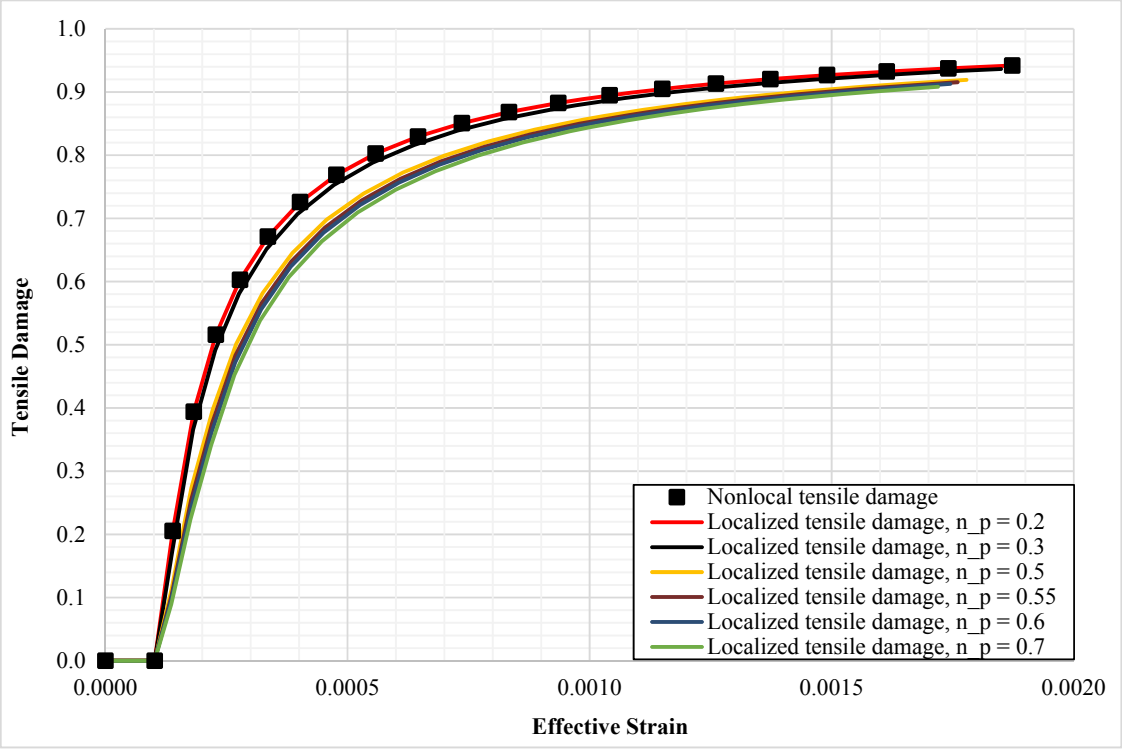

Figure 58: Tensile damage for three point bending example for different $n_p$values in the normal discretization at gp_c

Consider different values for n_p, the tensile damage curves in the both non-local and localized states at gp_c are demonstrated in Figure 58. It should be mentioned that there is no observation regarding the compressive damage, hence the total damage remains for the same values of the tensile one.

Another point resulted from this analysis is relevant to the value of n_p. It is visible that the curve of damage experiences sharper slope when the smaller n_p value is chosen. It is normal because choosing smaller n_p value produces smaller *RGP* as well. This phenomenon leads to collect lower number of integration points to damage localization process.

As a remark of this analysis, the RPIM results shown in Figure 56 do not agree well with the experimental solution. The used discretization does not permit to obtain the same spatial distribution of nodes inside the influence domain in the directions *x* and *y* (this kind of discretization leads to influence domains possessing a much higher number of nodes along the *y* direction than *x* direction).

7.2 Three Point Bending Beam, Refined Discretization

Here the nodal discretization changed in a different way. The strategy is to divide the length of the beam into two various space as [0, 3*L*/8] and [3*L*/8, *L*/2]. Then, different nodal meshes are studied to obtain the more accurate results compared to the experimental solution (Malvar & Warren, 1988). Figure 59 illustrates the refined discretization for three point bending beam with the essential boundary conditions. As it is visible in Figure 59-b, the nodal mesh represented will permit to obtain much more balanced influence domain.

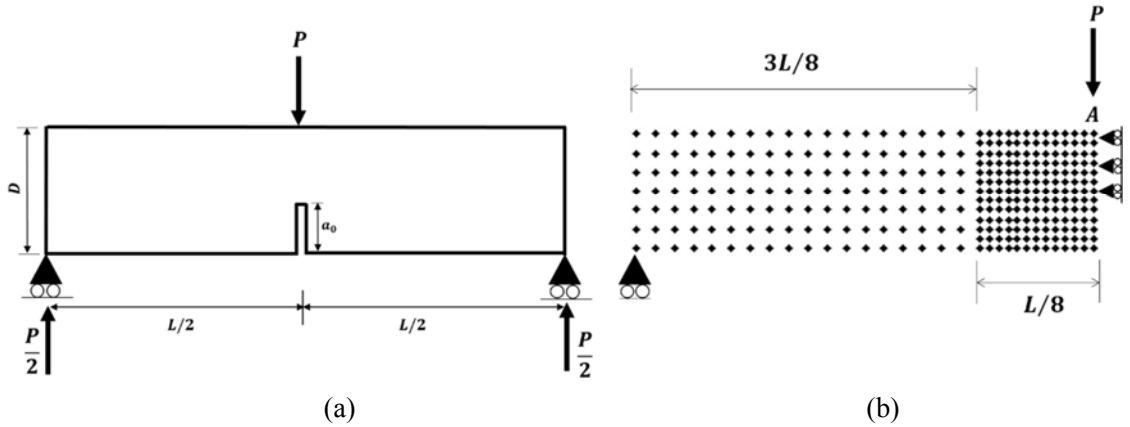

(a) (b)

Figure 59: Three point bending beam (a) geometry and (b) the refined discretization with the essential boundary conditions

7.2.1 Convergence Study on n_p

First of all, in order to check the performance of the program with the RPIM meshless formulations extended for the localized damage mechanics, it is rational to study different discretization patterns in the format shown in Figure 59. Different discretization properties are chosen to study presented on Table 20:

Table 20: Different discretization types for three point bending beam in the refined discretization

Division along x direction	Division along y direction	Total number of nodes	Total number of Gauss points
25	7	295	567
33	9	505	1008
41	11	771	1575
81	21	2941	6300

It should be mentioned that all the material and geometric properties are the same as Table 15 and Table 16 while the damage characteristics are used as Table 17. But regarding the algorithm configuration presented on Table 18, the total displacement enforcement is chosen as u = 0.26 (mm) in this study.

7.2.1.1 First Refined Disceritization

A regular mesh containing 295 and 567 nodes and integration points respectively is considered here as seen in Figure 60. It is possible to make a convergence study on n_p values differing in a range of [0.5, 2.1]. Since this part is devoted to the localized damage concept, it is necessary to obtain the response of load P versus the deflection on point A for different weight function orders such as 0, 2nd and 3rd orders (see Table 1).

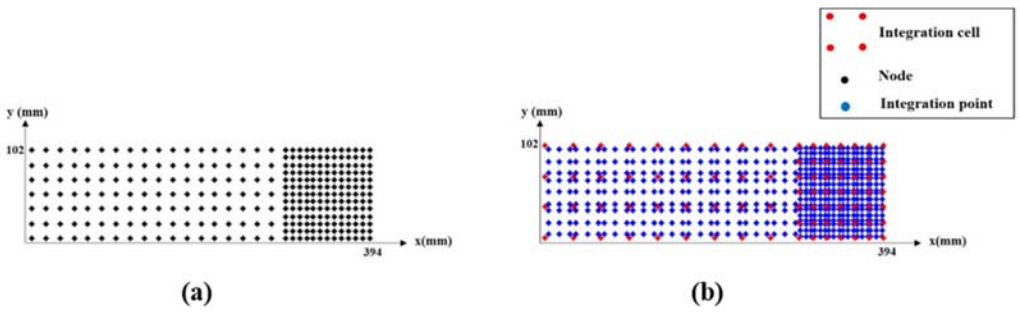

Figure 60: First refined discretization for three point bending beam: (a) 295 nodes and (b) 567 Gauss points

Consider the divisions along x direction equal to 25, According to Equation (109-b), the parameter h is computed as: $h = 0.0164\ (m)$. Furthermore, considering Equation (109-a), the variation of *RGP* based on the various n_p amounts for this study is presented on Table 21.

Table 21: Variation of RGP based on different n_p in localized damage, first refined discretization pattern

n_p	0.5	0.7	0.8	1.1	1.6	2.1
RGP	0.0082 (m)	0.0115 (m)	0.0131 (m)	0.0181 (m)	0.0263 (m)	0.0345 (m)

Considering 0-order weight function, the graph correlating the load P with the correspondent deflection on point A, for different n_p values, is presented in Figure 61. It is also interesting to capture the damage variation obtained for non-local and localized tensile states. Indeed the curves of total damage in terms of effective strain for this analysis are the same as the tensile cases.

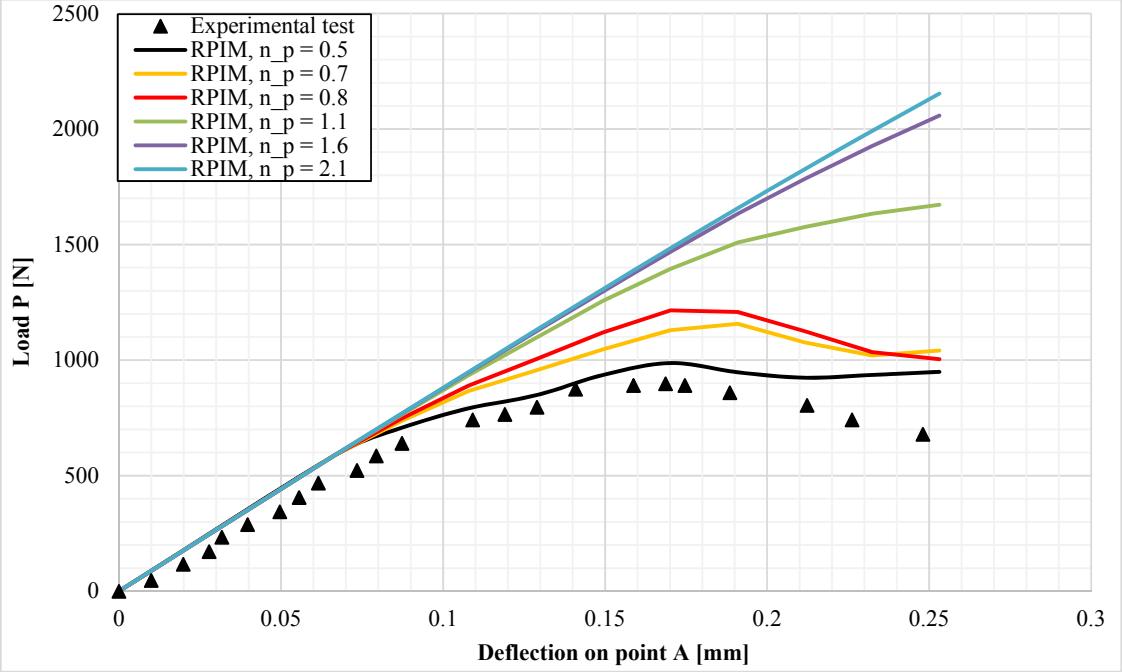

Figure 61: Response of load *P*- deflection on point *A* for the first refined discretization with regard to 0-order weight function

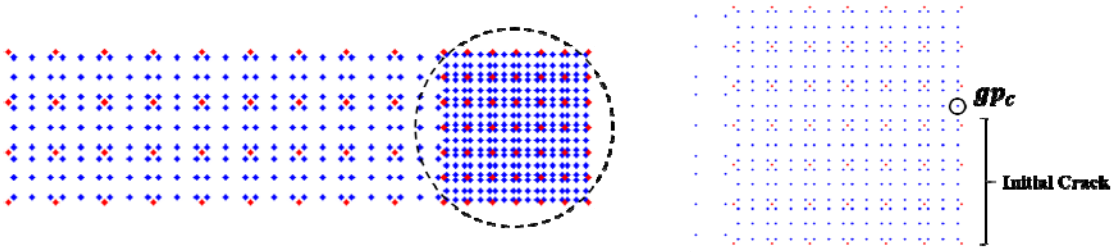

Figure 62: The detection of gp_c for the first refined discretization in three point bending beam

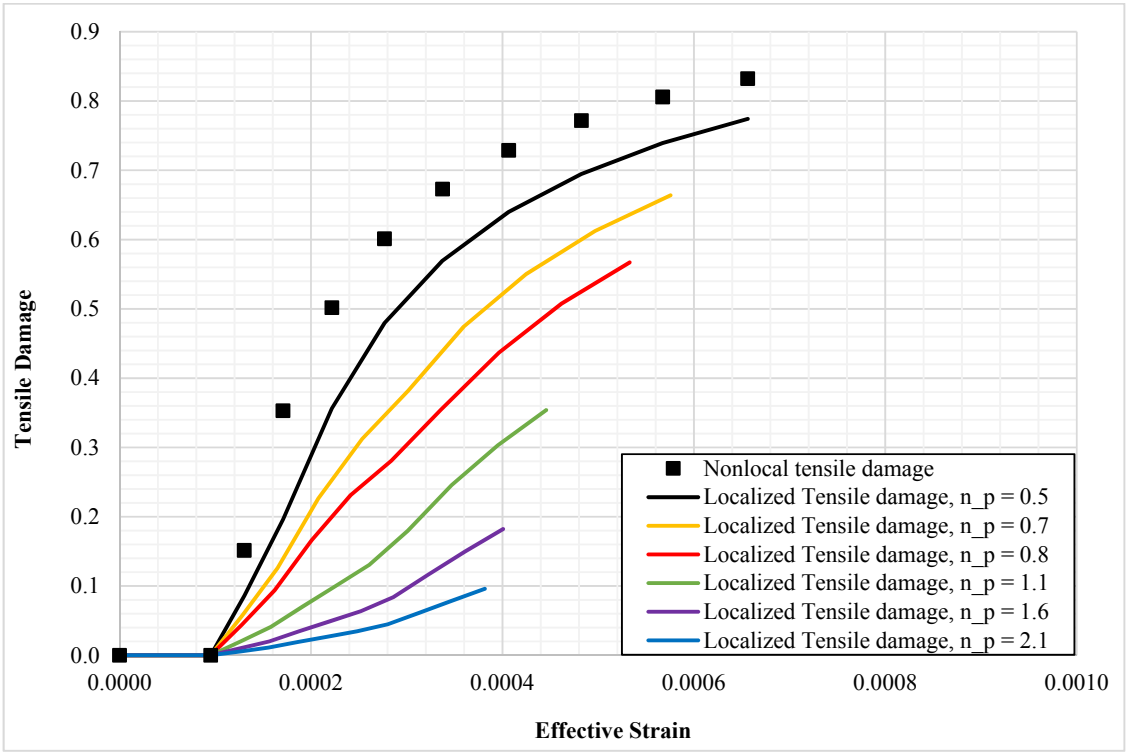

Figure 63: Variation of tensile damage vs. effective strain at gp_c for the first refined discretization with regard to 0-order weight function

Subsequently, considering 2nd-order weight function (see Table 1), the new analysis is performed and the response of load P in terms of the deflection on point A for different n_p values is presented in Figure 64.

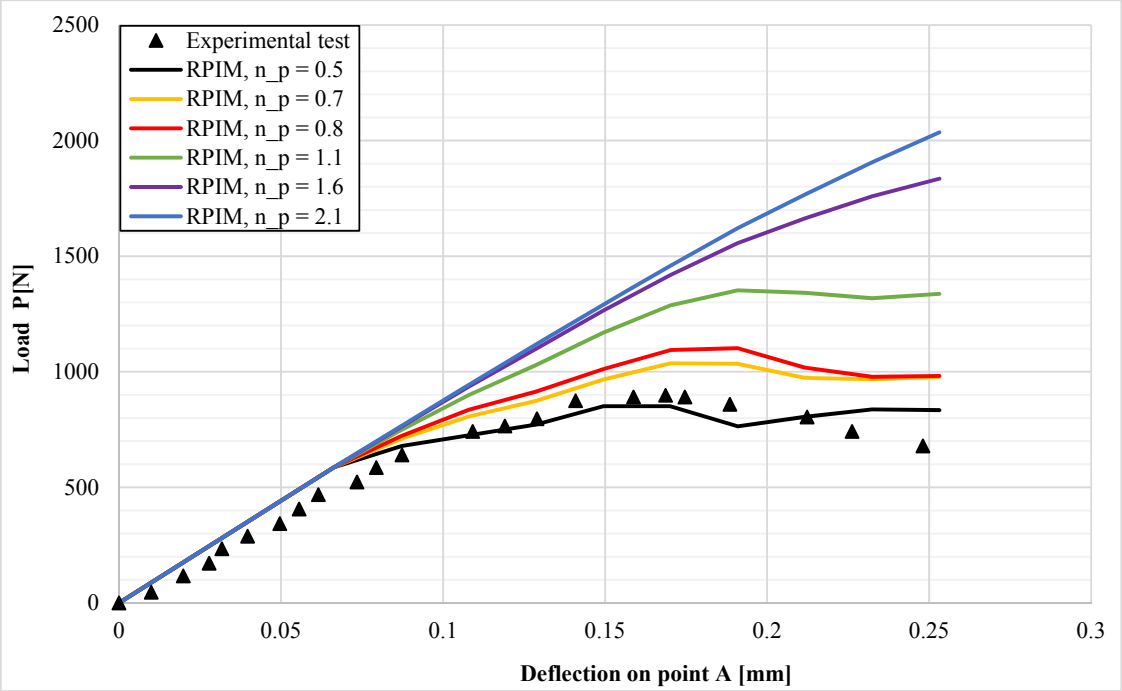

Figure 64: Response of load P- deflection on point *A* for the first refined discretization with regard to 2nd-order weight function

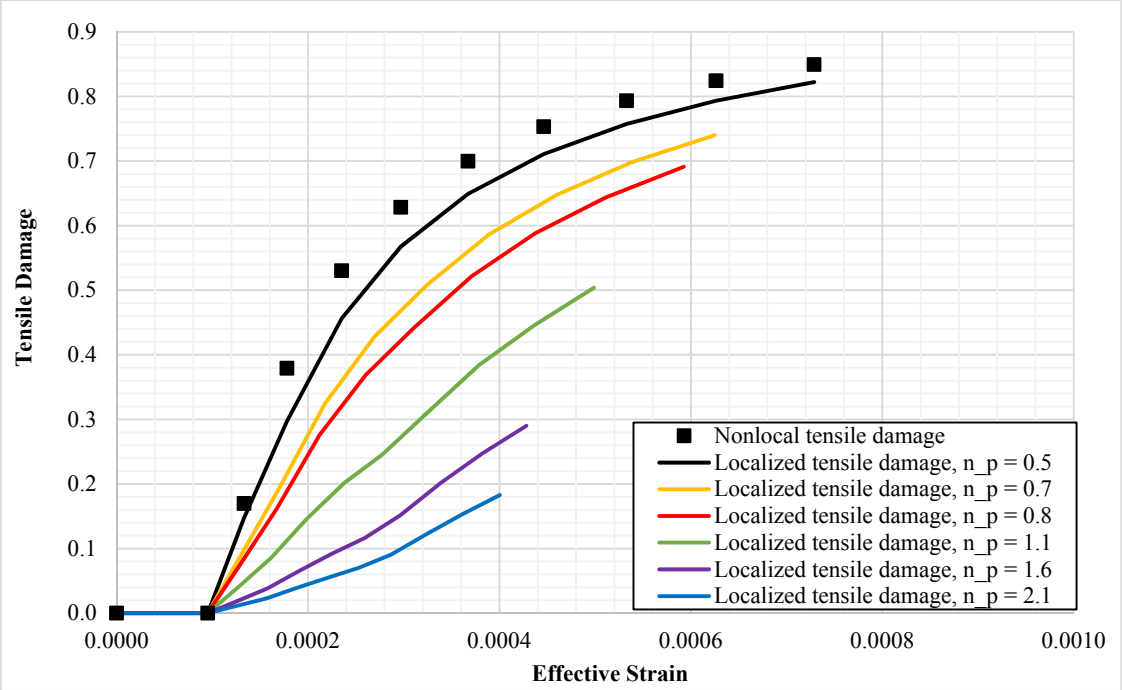

Figure 65: Variation of tensile damage vs. effective strain at gp_c for the first refined discretization with regard to 2nd-order weight function

The damage variation obtained for non-local and localized tensile states at integration point gp_c represented in Figure 65. In addition to that, it should be remarked that the total damage in terms of effective strain is the same as the tensile one. It should be noted that the damage diagrams are plotted at the particular integration point gp_c as shown in Figure 62.

To end the analysis related to the first refined discretization, the 3rd order weight function extracted from Table 1 is considered. The variation of non-local tensile damage and localized tensile damage at integration point gp_c is presented in Figure 67. In addition, the response of load *P* versus the deflection on point *A* is plotted in Figure 66.

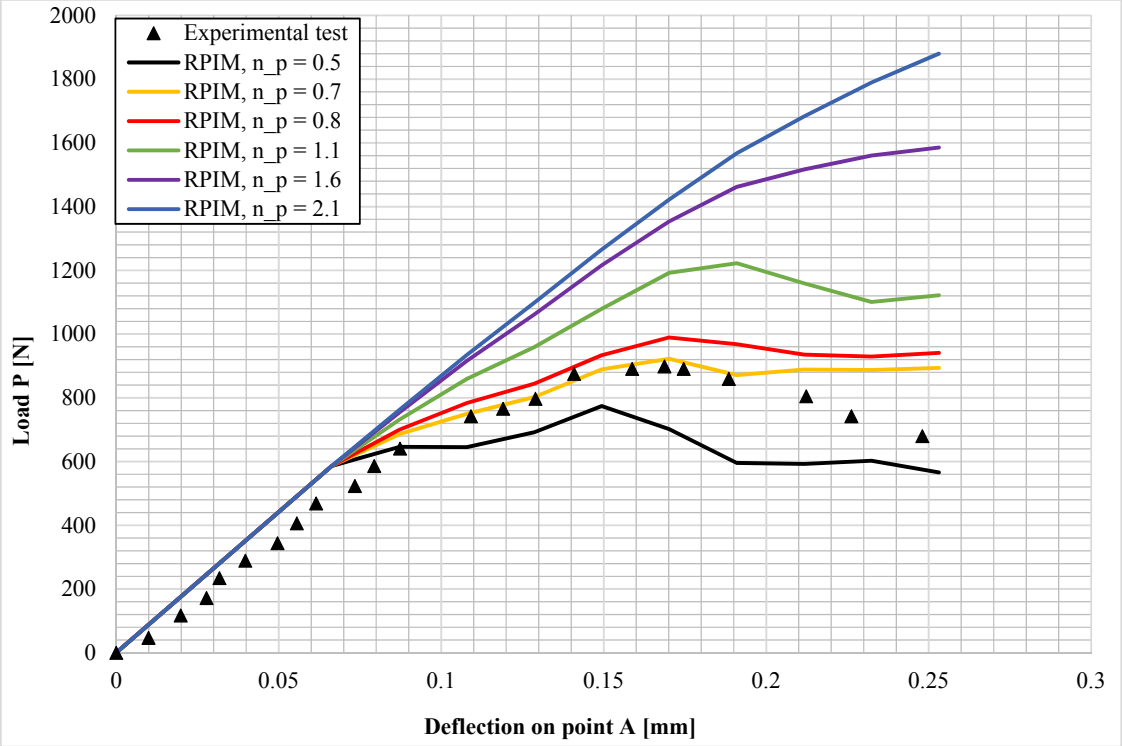

Figure 66: Response of load *P*- deflection on point *A* for the first refined discretization with regard to 3rd-order weight function

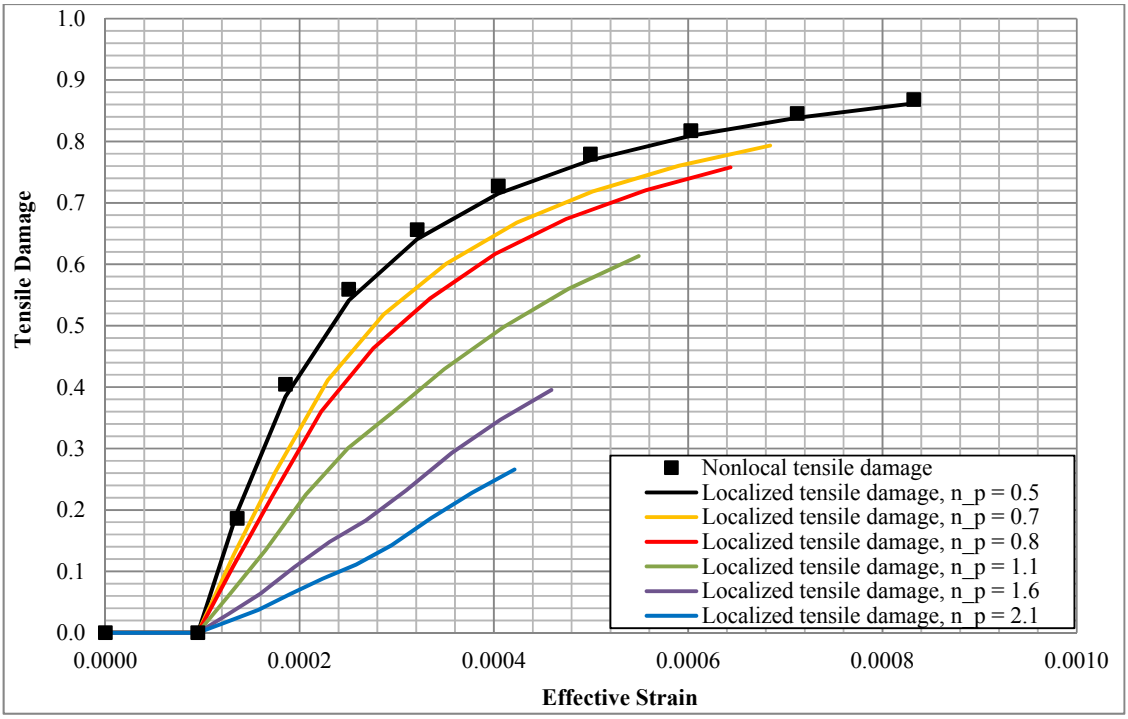

Figure 67: Variation of tensile damage vs. effective strain at gp_c for the first refined discretization with regard to 3rd - order weight function

7.2.1.2 Second Refined Disceritization

The same convergence study is conducted on another refined discretization including 505 and 1008 nodes and integration points respectively as shown in Figure 68.

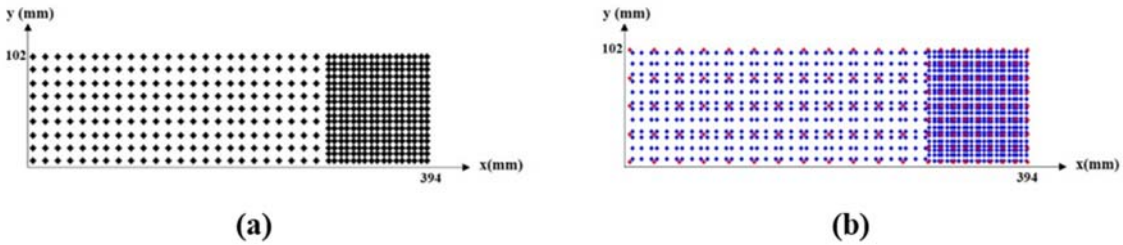

Figure 68: Second refined discretization for three point bending beam: (a) 505 nodes and (b) 1008 Gauss points

Consider the divisions along x direction being 33, regarding Equation (113-b), the parameter h is calculated as: $h = 0.0123\ (m)$. Moreover, considering Equation (113-a), the variation of *RGP* based on the various n_p amounts for this work is illustrated on Table 22.

Table 22: Variation of RGP based on different n_p in localized damage, second refined discretization pattern

n_p	0.5	0.7	0.8	1.1	1.6	2.1
RGP	0.0062 (m)	0.0086 (m)	0.0099 (m)	0.0135 (m)	0.0197 (m)	0.0259 (m)

Same as the first discretization analysis, considering 0-order weight function, the response of load P in terms of the deflection of point A for different n_p values for the second discretization pattern is presented in Figure 69 . It is also interesting to capture the damage variation obtained for non-local and localized tensile states represented in Figure 71 . Indeed the graph related to the total damage variation in terms of effective strain for this analysis is the same as Figure 71. It should be noted that the damage diagrams are plotted at a particular integration point gp_c as demonstrated in Figure 70.

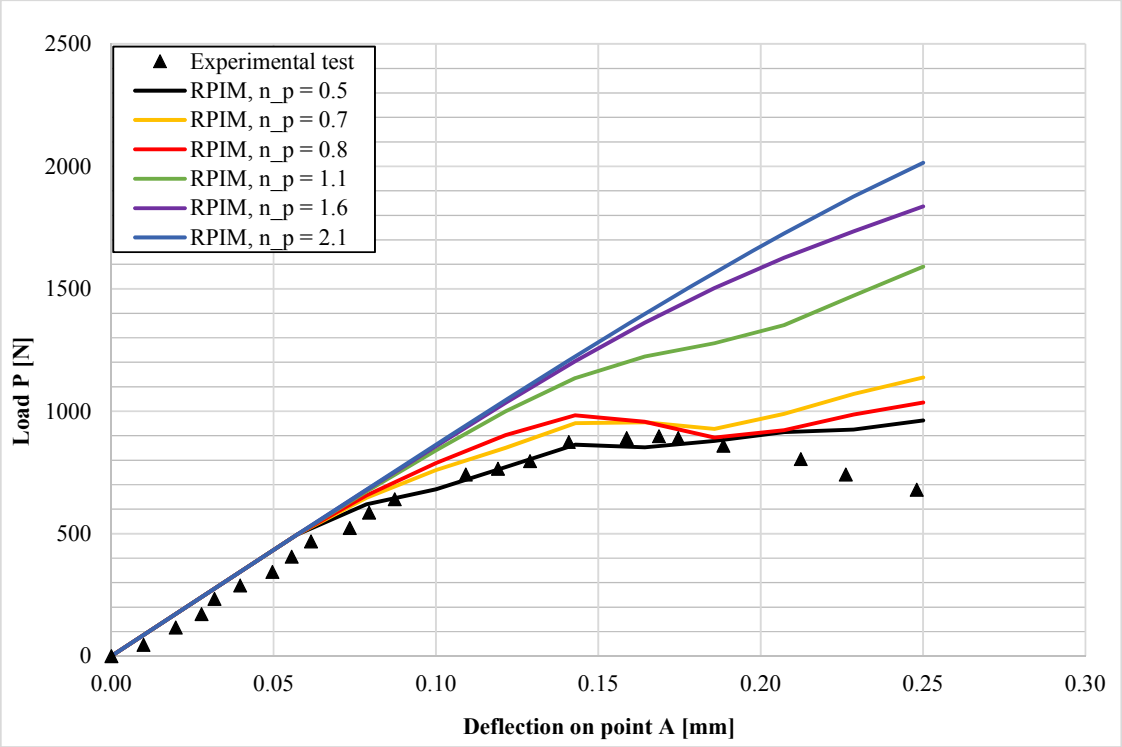

Figure 69: Response of load *P*- deflection on point *A* for the second refined discretization with regard to 0-order weight function

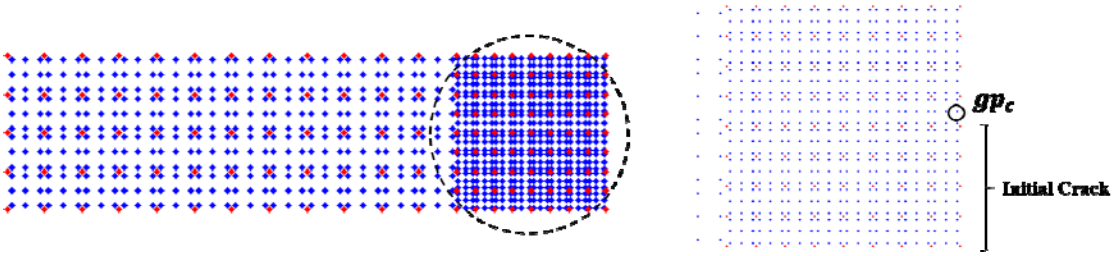

Figure 70: The detection of gp_c for the second refined discretization in three point bending beam

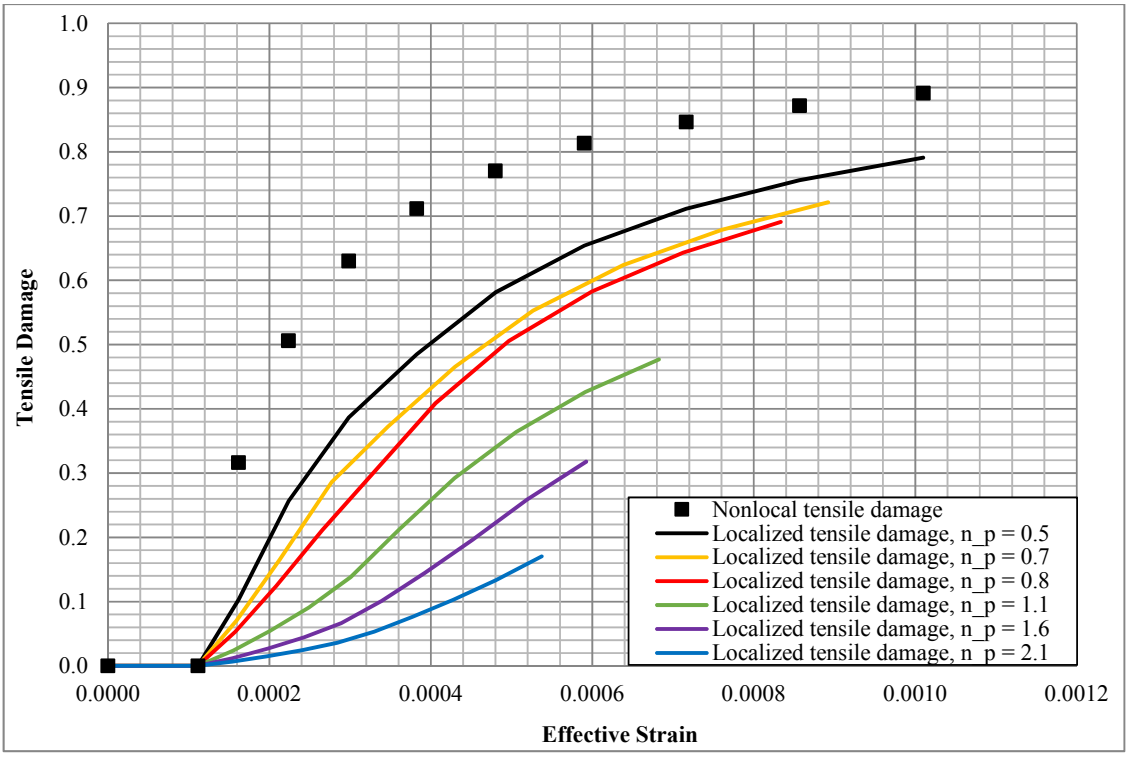

Figure 71: Variation of tensile damage vs. effective strain at gp_c for the second refined discretization with regard to 0 -order weight function

The same scenario is repeated for the 2nd order weight function in order to capture the variations of tensile damage at gp_c (see Figure 70) for the second RPIM refined discretization shown in Figure 73. The response of *P-A* for different n_p is also demonstrated in Figure 72.

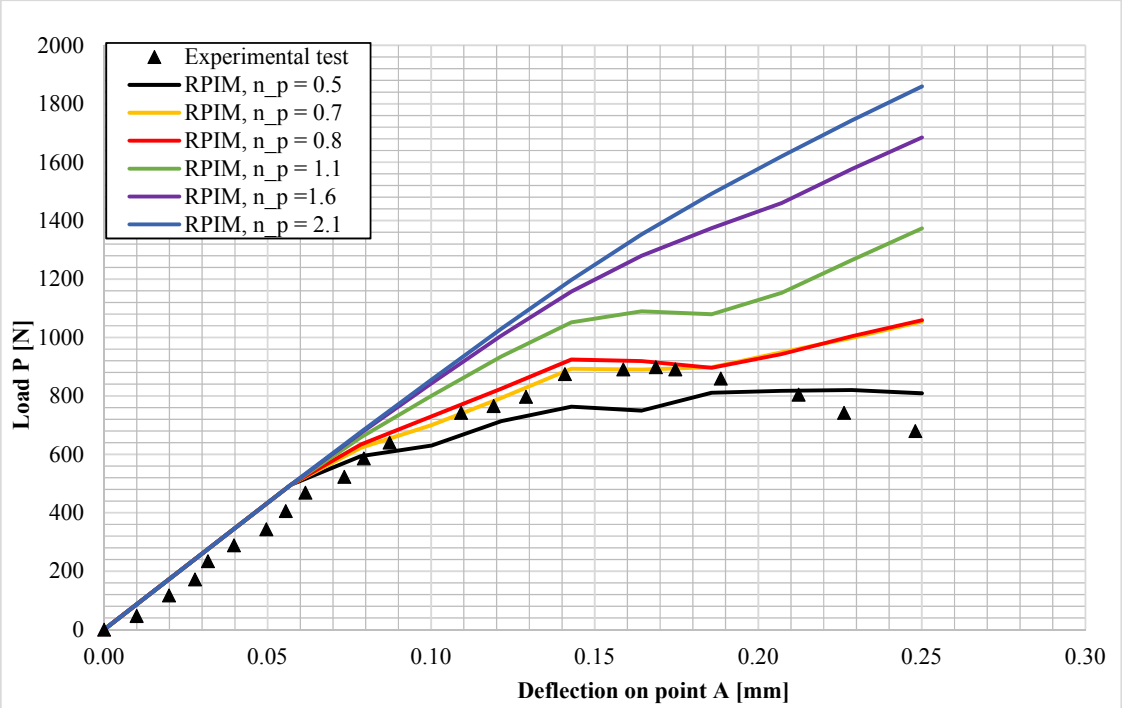

Figure 72: Response of load *P*-deflection on point *A* for the second refined discretization with regard to 2nd -order weight function

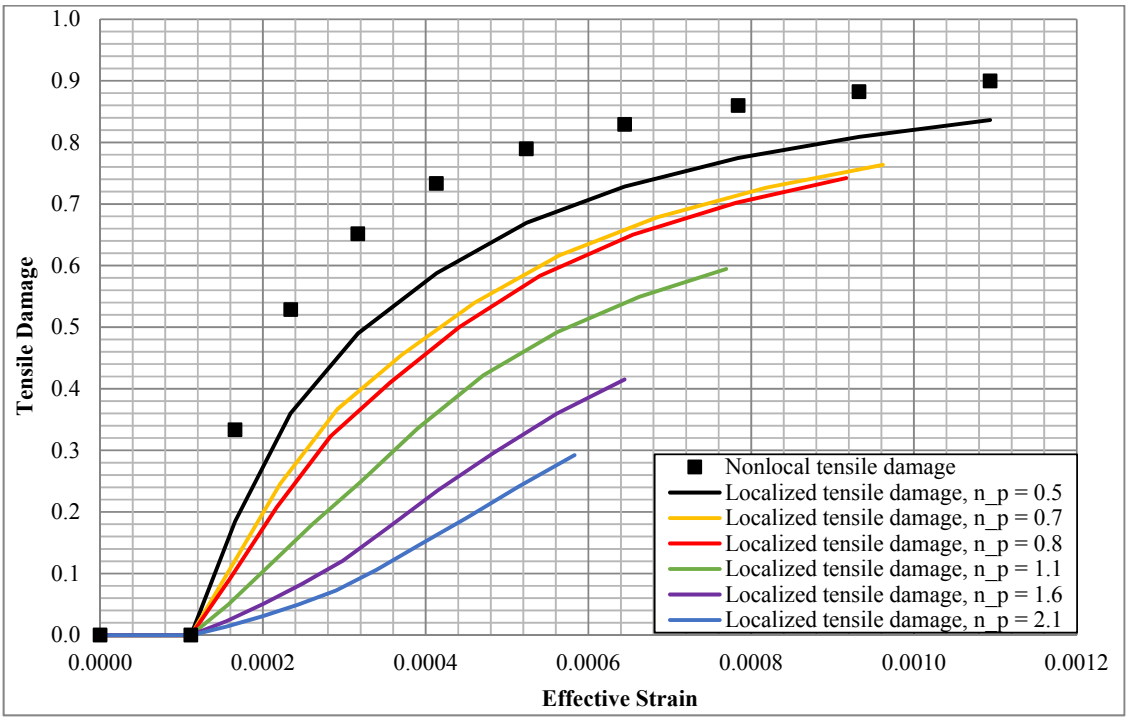

Figure 73: Variation of tensile damage vs. effective strain at gp_c for the second refined discretization with regard to 2nd -order weight function

To finish the analysis on the second refined discretization for three point bending beam, it is possible to obtain the results for the 3rd order weight function introduced on Table 1. Consider a particular integration point at gp_c as seen in Figure 70, it is possible to figure the variation of tensile damage (which is the same as total damage variation) as illustrated in Figure 75. Besides the response of load in terms of the point deflection for distinct n_p related to this analysis is presented in Figure 74 .

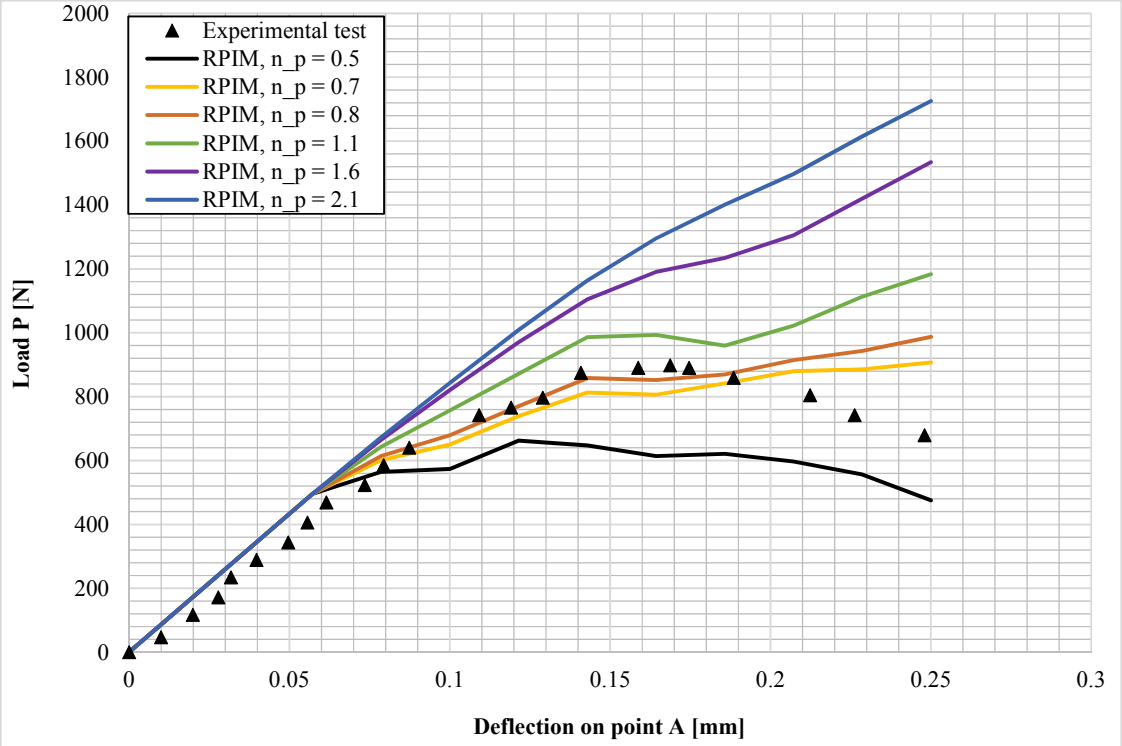

Figure 74: Response of load *P*- deflection on point *A* for the second refined discretization with regard to 3rd -order weight function

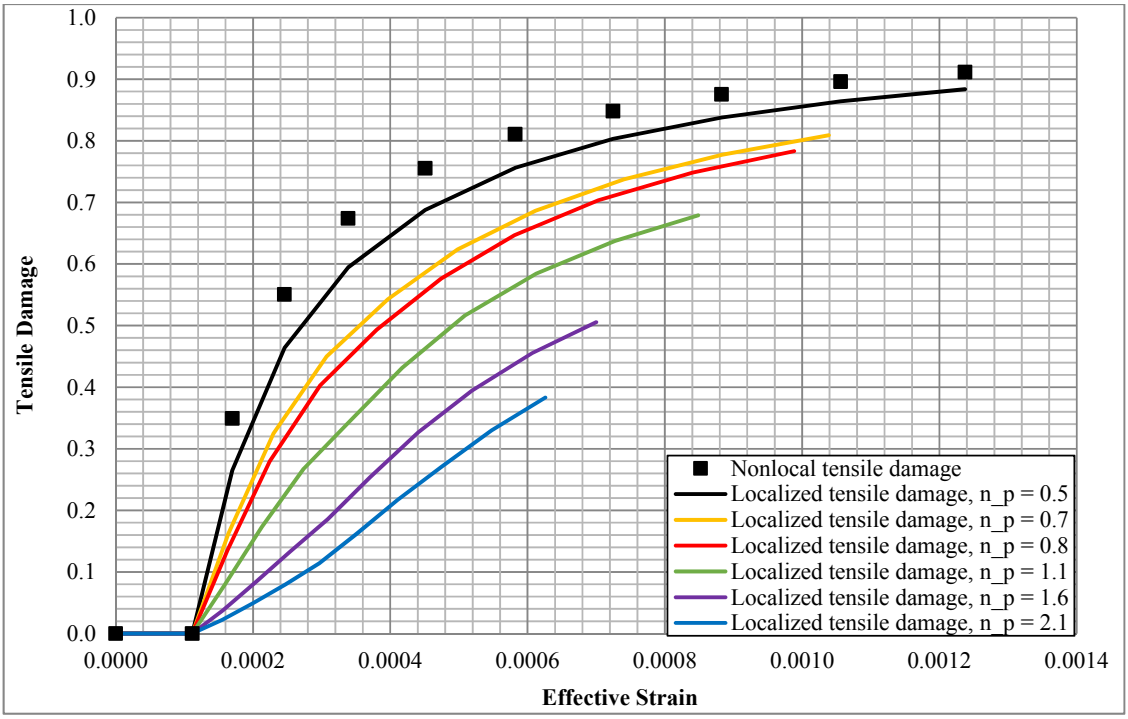

Figure 75: Variation of tensile damage vs. effective strain at gp_c for the second refined discretization with regard to 3rd -order weight function

7.2.1.3 Third Refined Disceritization

To end the convergence study on damage localization concept in the case of n_p values, the third refined discretization is analyzed using 771 nodes and 1575 integration points (see Figure 76)

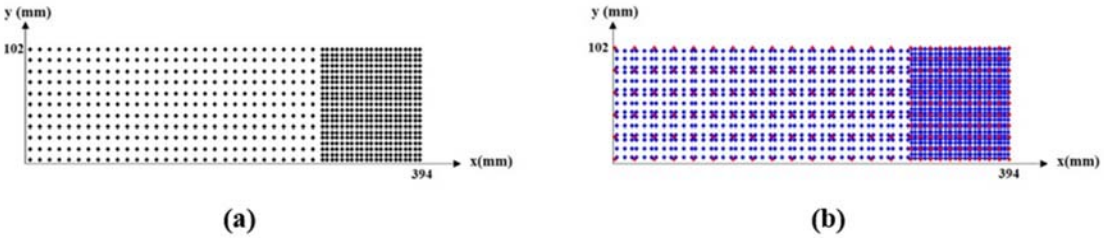

Figure 76: Third refined regular discretization for three point bending beam: (a) 771 nodes and (b) 1575 Gauss points

Consider the divisions along x direction being 41, regarding Equation (113-b), the parameter h is calculated as: $h = 0.0099\ (m)$. Moreover, considering Equation (113-a), the variation of *RGP* based on the various n_p amounts for this work is illustrated on Table 23.

Table 23: Variation of RGP based on different n_p in localized damage, the third refined discretization pattern

n_p	0.5	0.7	0.8	1.1	1.6	2.1
RGP	0.0049 (m)	0.0069 (m)	0.0079 (m)	0.0108 (m)	0.0158 (m)	0.0207 (m)

The current analysis starts with the 0-order weight function (as seen on Table 1). Then, the load response in terms of deflection is obtained for different $n_p$values. Then, the obtained solution is graphed in Figure 77. In order to plot the variation of damage parameters, a particular integration point is required. This point is selected on the crack tip known as gp_c illustrated in Figure 78. After that, the corresponding curves correspond to the damage variation are plotted in Figure 79 for tensile damage (same as the total damage).

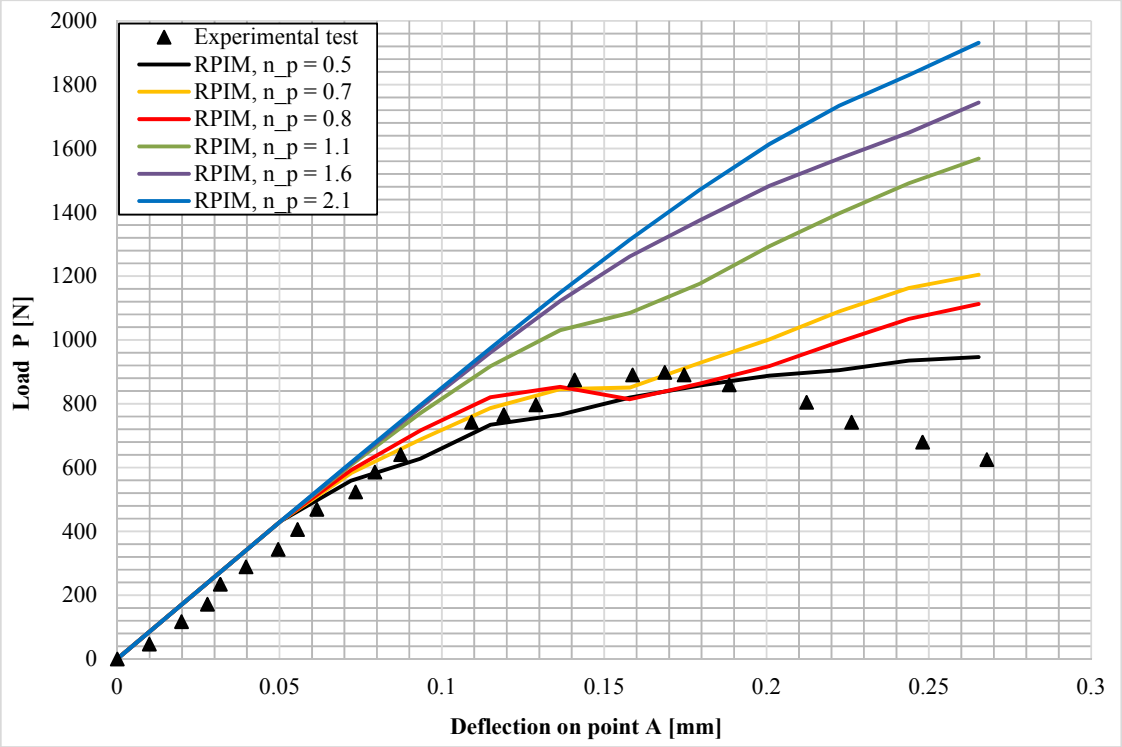

Figure 77: Response of load *P*- deflection on point *A* for the third refined RPIM discretization with regard to 0 -order weight function

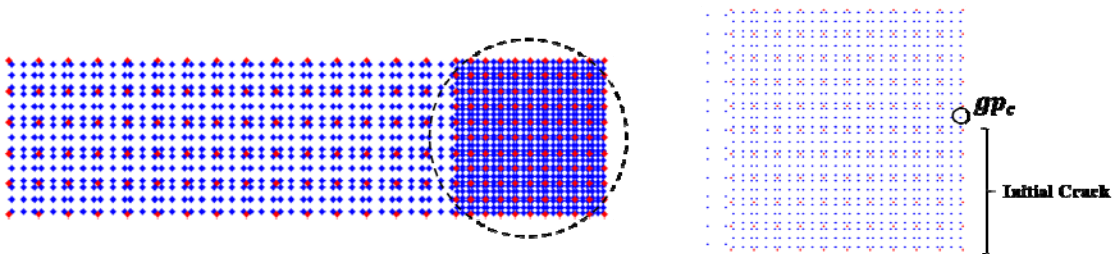

Figure 78: The detection of gp_c for the third refined discretization in three point bending beam

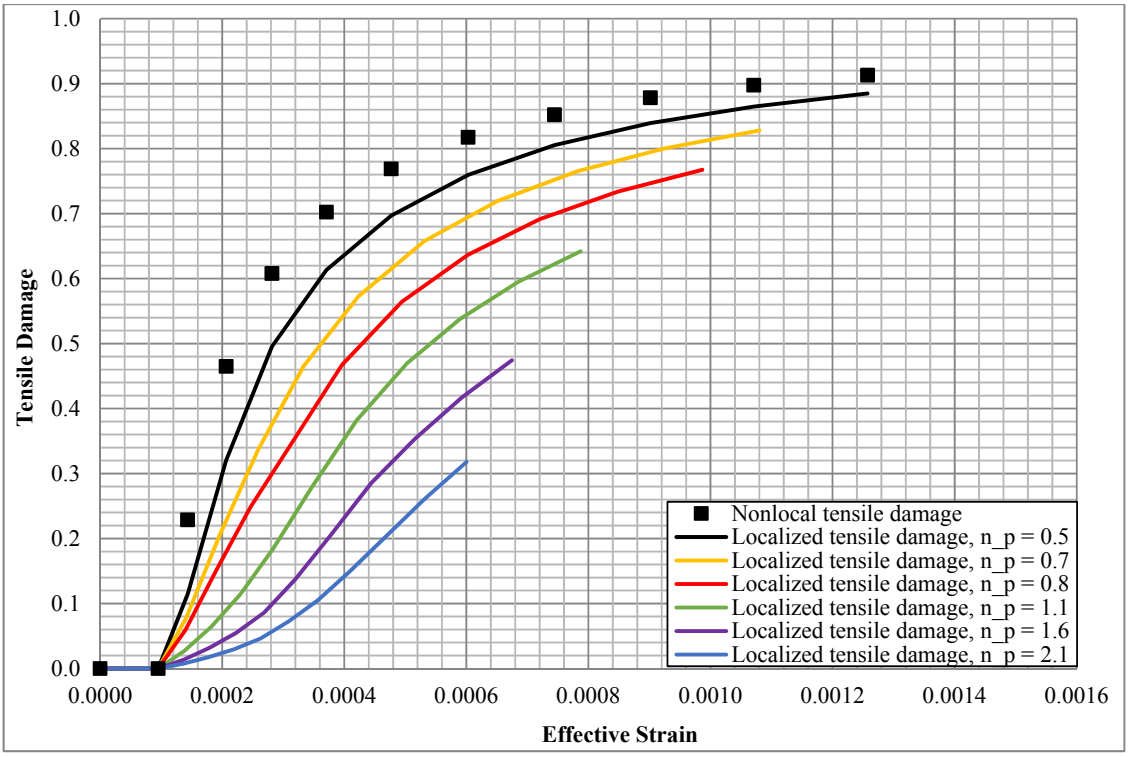

Figure 79: Variation of tensile damage vs. effective strain at gp_c for the third refined discretization with regard to 0 -order weight function

The same procedure is done for the 2nd order weight function in the presence of the third refined discretization and the response of load P versus the deflection on point A is presented in Figure 80. In the same way, the profiles of tensile damage variable are demonstrated in Figure 81. Several n_p values are performed in this analysis.

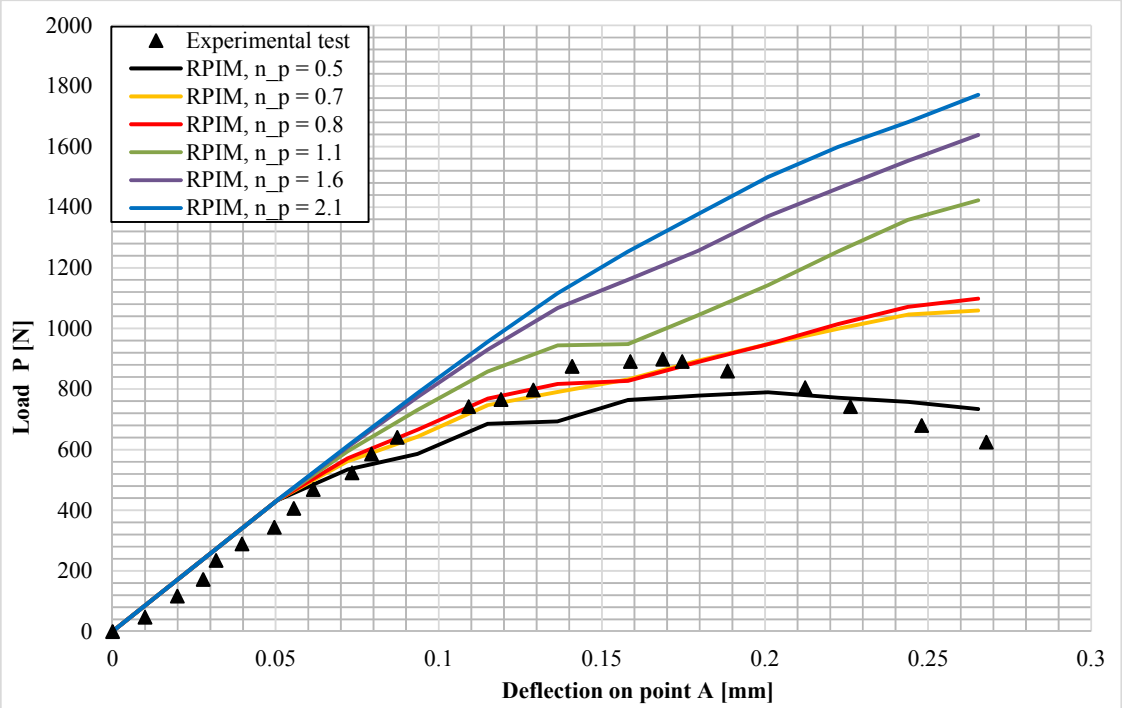

Figure 80: Response of load *P*-deflection on point *A* for the third refined discretization with regard to 2nd-order weight function

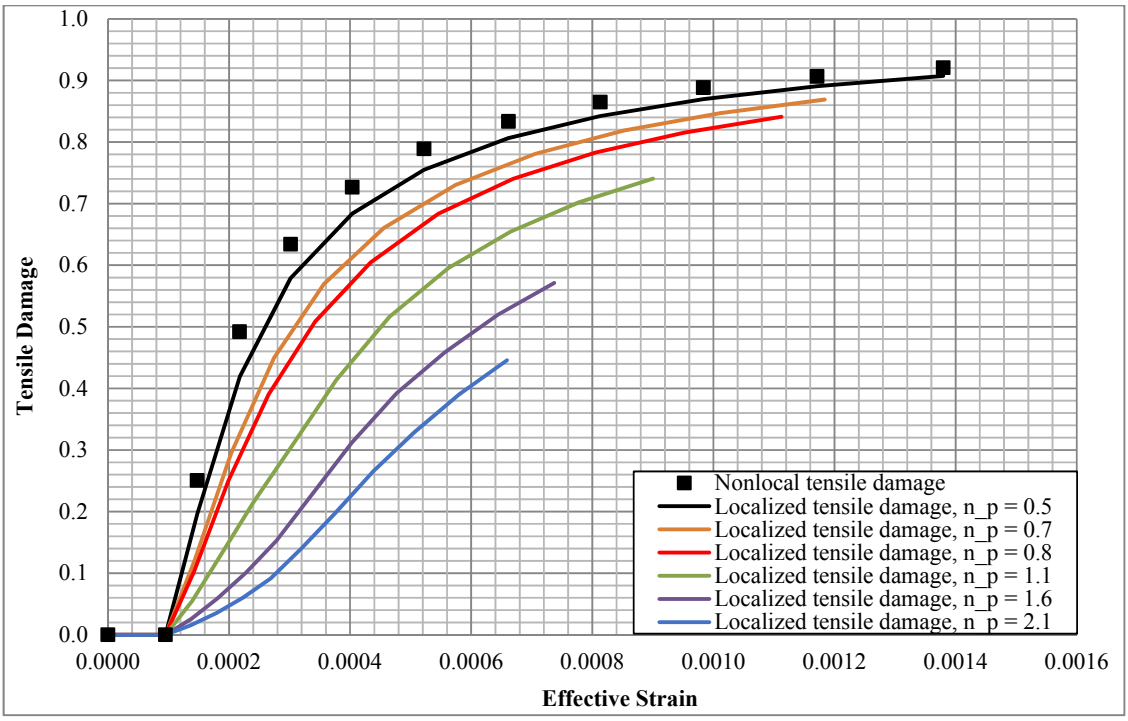

Figure 81: Variation of tensile damage vs. effective strain at gp_c for the third refined discretization with regard to 2nd-order weight function

At the end, the study on the third refined discretization for three point bending beam, the 3rd order weight function is considered to obtain the response of *P-A* as shown in Figure 82. Furthermore, consider Figure 78 in the sense of gp_c, the variation of tensile damage for non-local and several localized states is indicated in Figure 83.

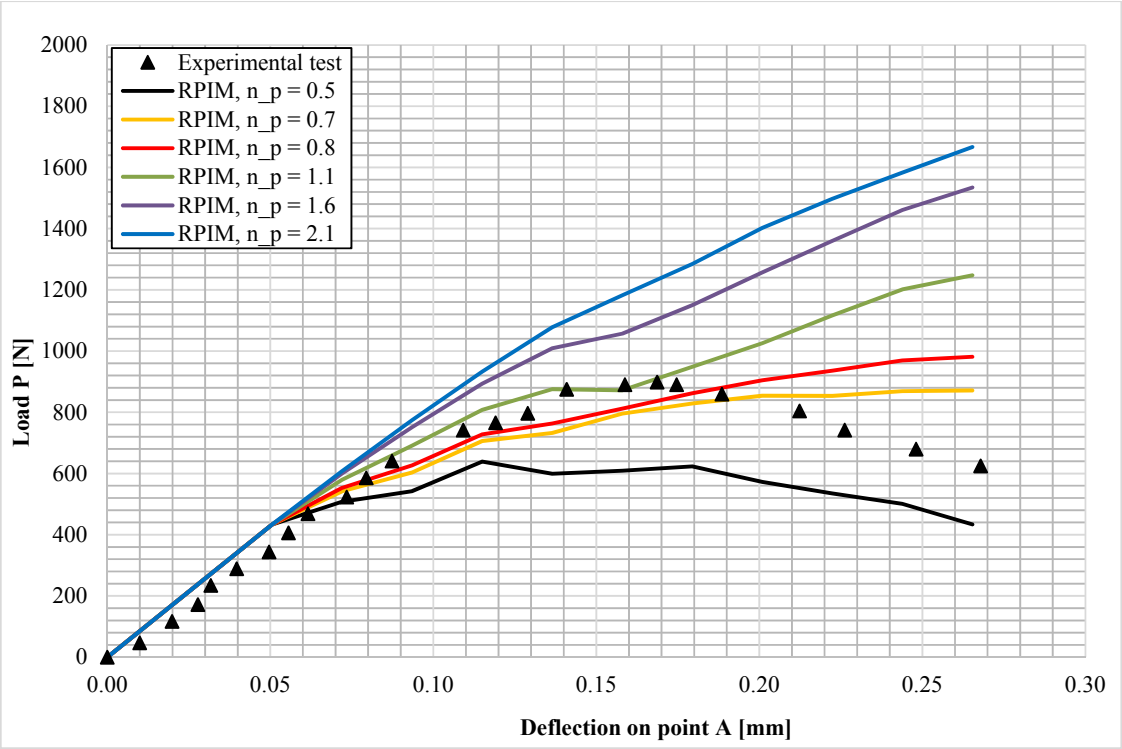

Figure 82: Response of load *P*- deflection on point *A* for the third refined discretization with regard to 3rd-order weight function

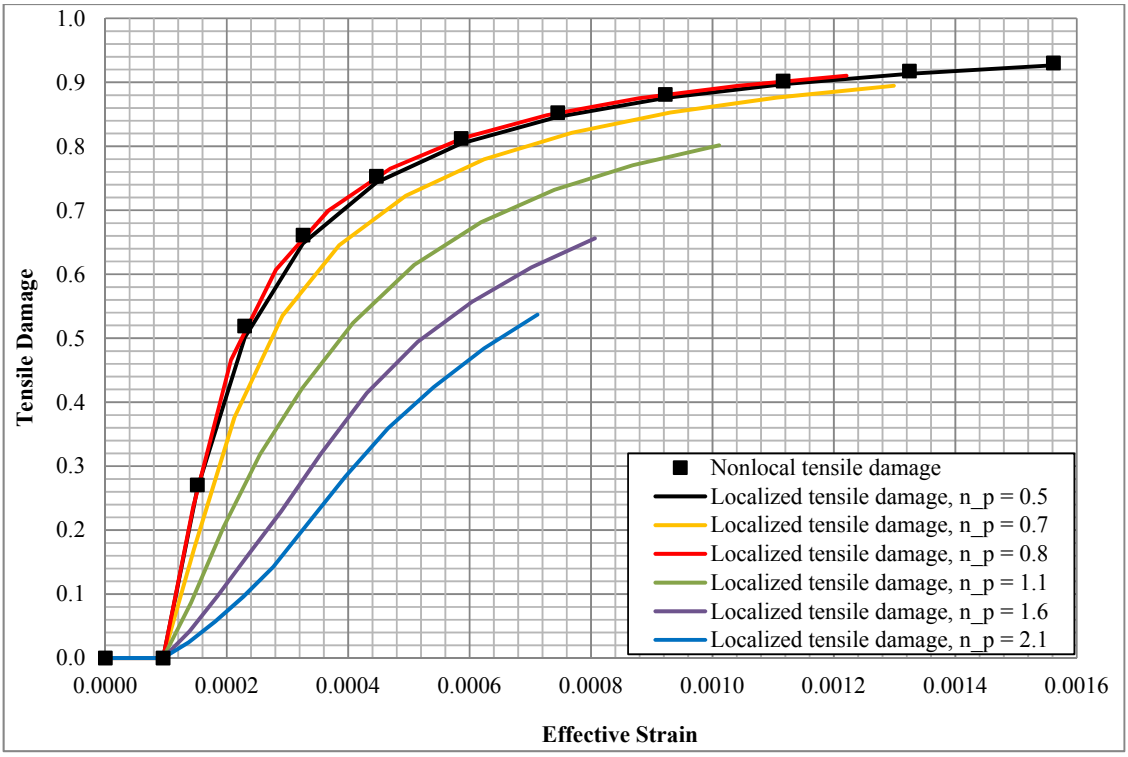

Figure 83: Variation of tensile damage vs. effective strain at gp_c for the third refined discretization with regard to 3rd-order weight function

The recent diagrams of load P in terms of the deflection on point A indicate the effect of change in n_p values leading to obtain various RGP amounts due to its dependency. In addition, the order of the weight function plays a significant role to achieve the solution for different three refined RPIM discretizations. It is visible from the corresponding figures that high values of n_p produce the results far away from the experimental one, which is not the purpose for this study. Similarly, weight function with higher order permit to obtain more satisfying solutions when compared to the experimental result.

Considering all the above-mentioned information, the localized damage parameter might be optimized as $n_p = 0.8$. Because the obtained result in the presence of $n_p = 0.8$ seem more accurate compared to the other values of n_p. Hence the resume of the analyses is presented on Table 24.

Table 24: Optimum n_p and RGP values of damage localization concept for all refined discretizations

Case study	Number of nodes	Number of integration points	n_p	Optimum RGP (m)
1st refined discretization	295	567	0.8	0.0131
2nd refined discretization	505	1008	0.8	0.0099
3rd refined discretization	771	1575	0.8	0.0079

7.2.2 Convergence Study on the Weight Function Order

Consider $n_p = 0.8$ as the optimal value, it is possible to make a convergence study on the weight function order for all the refined RPIM nodal distributions. Different weight function orders are extracted from Table 1.

The obtained results for the response of load *P* in terms of the deflection on point *A* for 0, 2nd and 3rd orders weight function are plotted in Figure 84, Figure 85 and Figure 86 respectively.

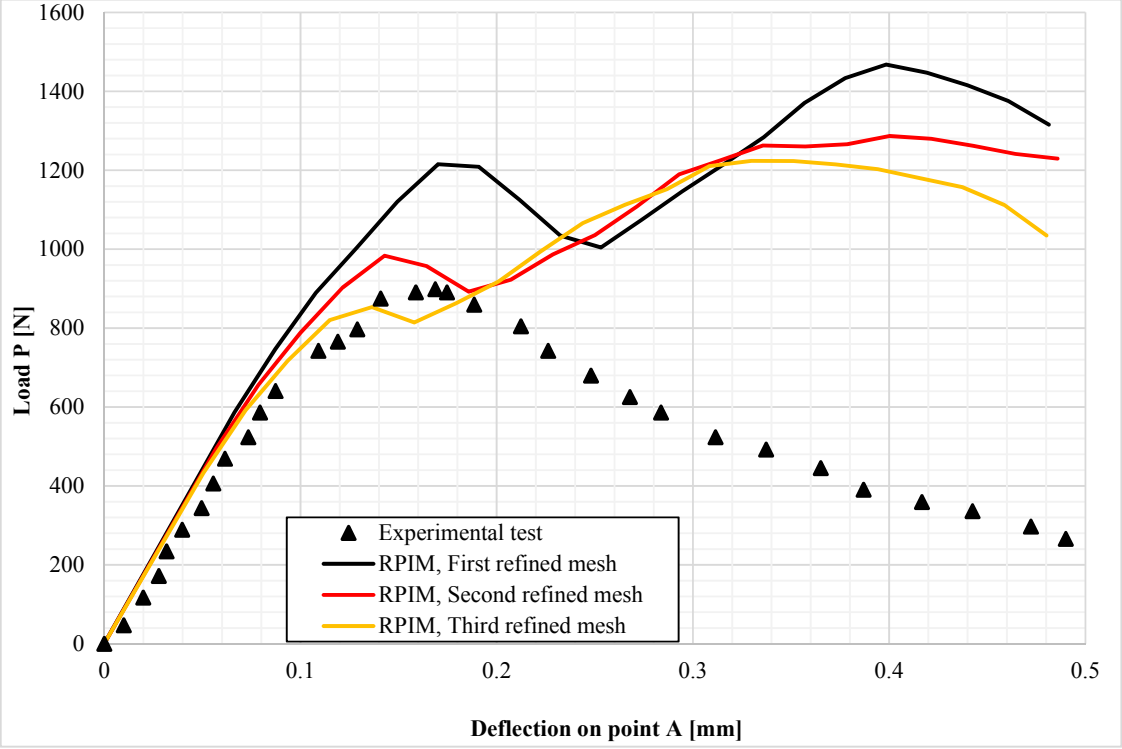

Figure 84: The response of load P versus the deflection of point A on all refined discretizations, 0 -order weight function with $n_p = 0.8$

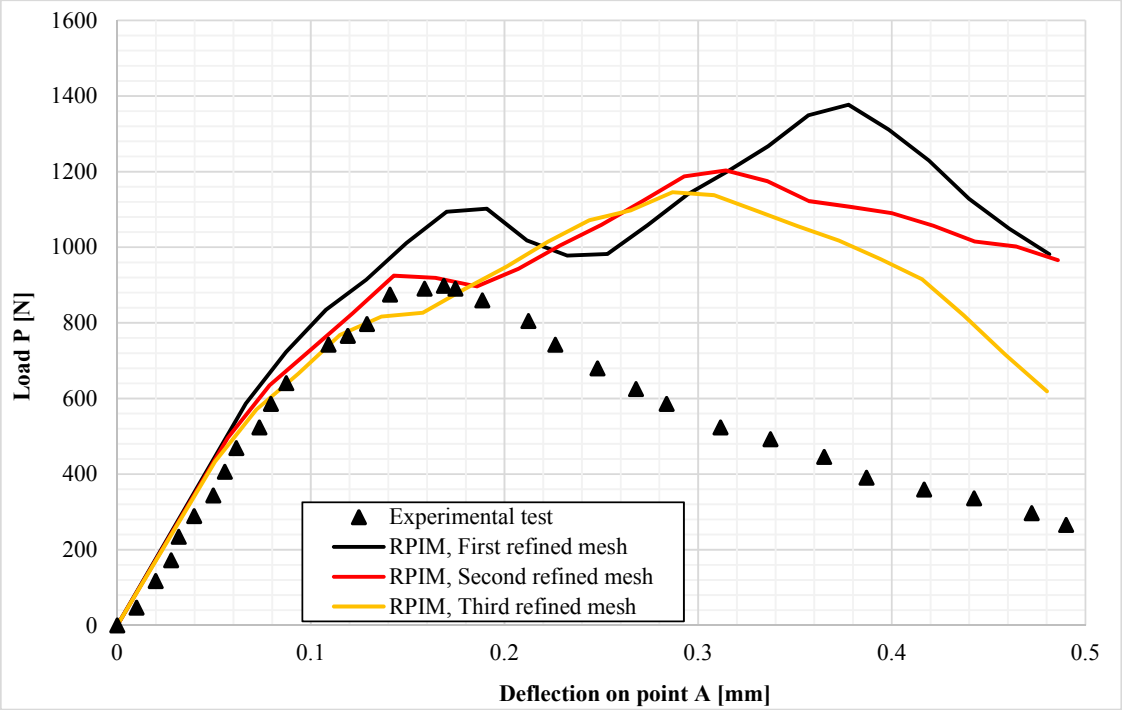

Figure 85: The response of load P versus the deflection of point A on all refined discretizations, 2nd-order weight function with $n_p = 0.8$

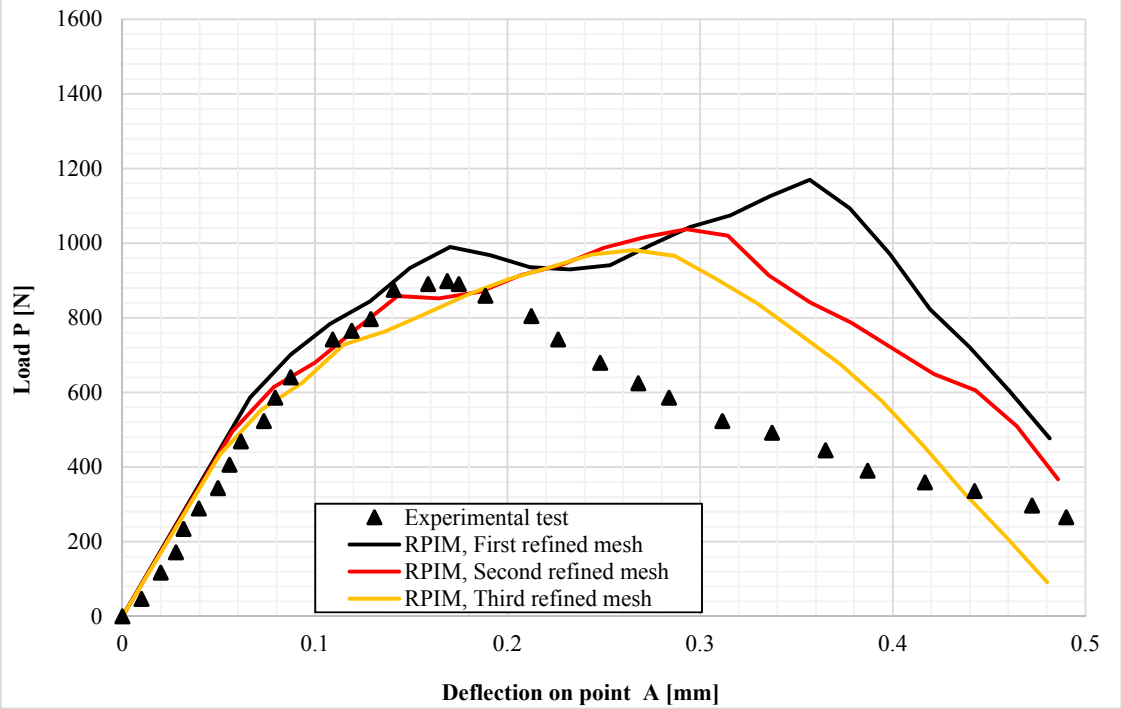

Figure 86: The response of load P versus the deflection of point A on all refined discretizations, 3rd-order weight function with $n_p = 0.8$

It is observable from the figures that the results are getting far away from the experimental solution when the 0-order weight function is performed which is not the purpose of the study. On the other hand, the RPIM solution is closer to the experimental solution when the 2nd and 3rd orders are used. However, both mentioned orders have a good agreement with the experimental curve. So, it is better to keep both of them and in the next convergence study, we might determine the best solution. Hence we discard the 0- weight function order.

7.2.3 Convergence Study on A^+

Considering the optimum value of $n_p = 0.8$, it is possible to make a convergence study on the tensile parameter A^+. So far, this value has been assumed as $A^+ = 0.001$. In this section the corresponding value will be optimized for refined discretizations with regard to the damage localization formalism. Since the characteristic length is depended on A^+ according to Equation (96-a), hence it will be possible to present the optimal value of characteristic length as well.

Indeed, the best weight function order must be determined here since it was not specified in the previous Section 7.2.2.

First the analysis starts with the 2nd-order weight function for all three refined discretizations with the properties demonstrated on Table 24.

Consider various values of A^+, the response of load versus deflection for three refined nodal distributions with regard to the 2nd order weight function is plotted in Figure 87, Figure 88 and Figure 89.

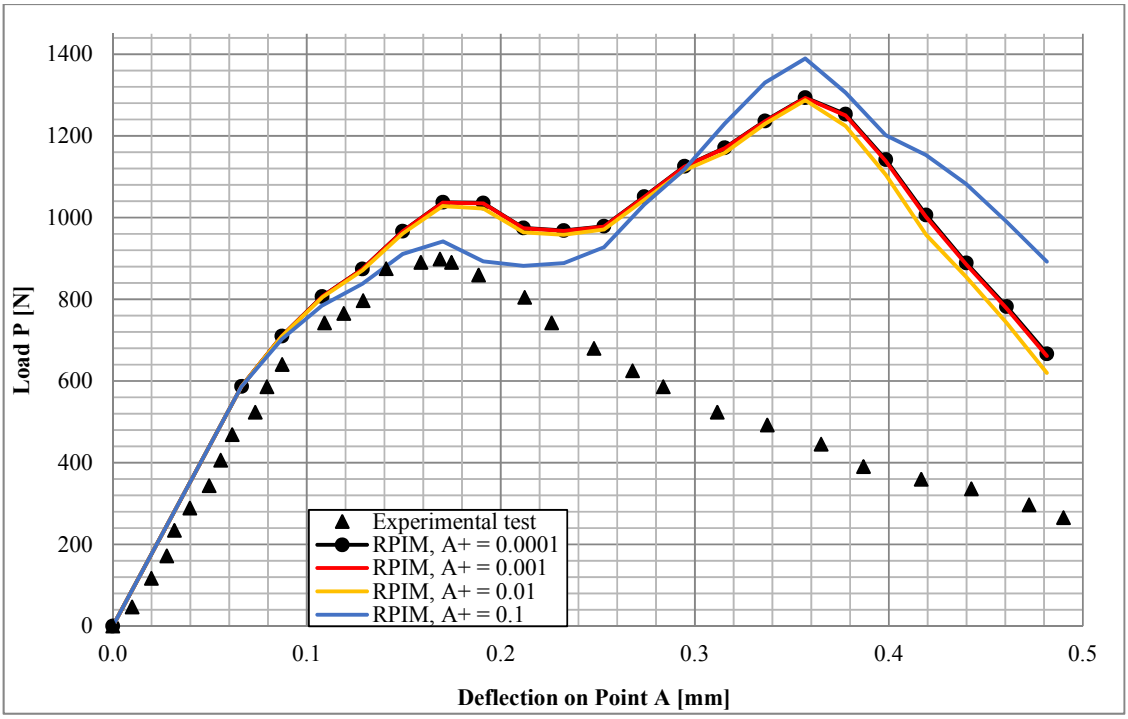

Figure 87: Study of A^+ for the response of load P versus the deflection of point A on the first refined discretization, the 2nd-order weight function with $n_p = 0.8$

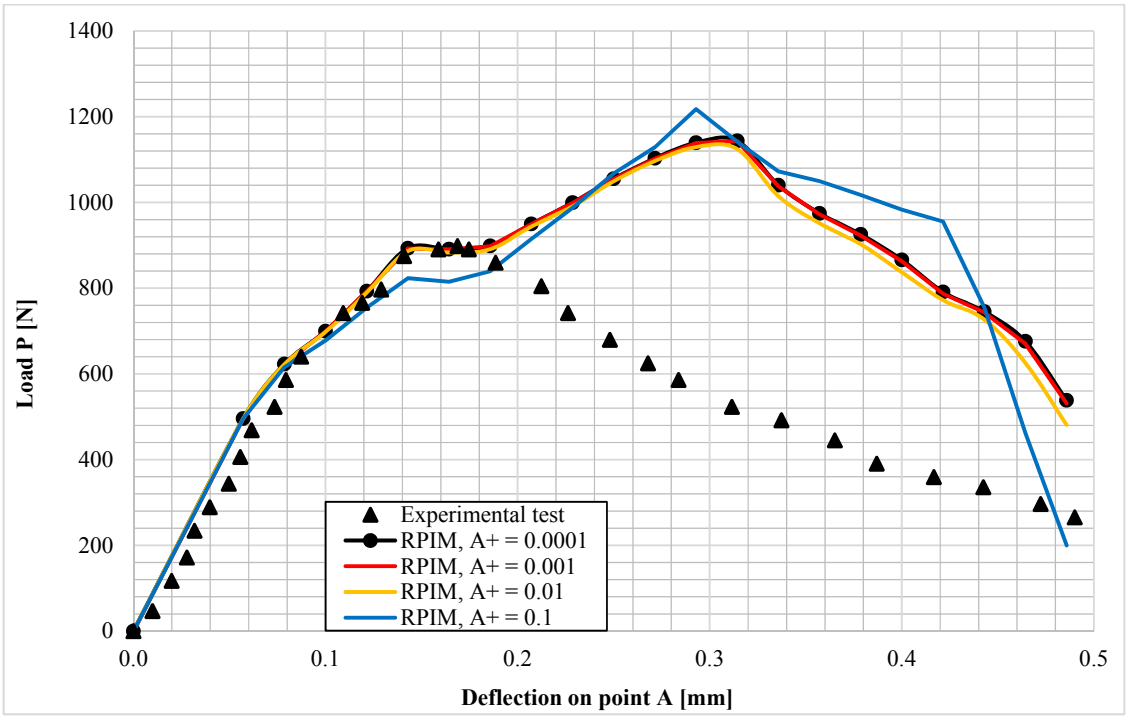

Figure 88: Study of A^+ for the response of load P versus the deflection of point A on the second refined discretization, the 2nd -order weight function with $n_p = 0.8$

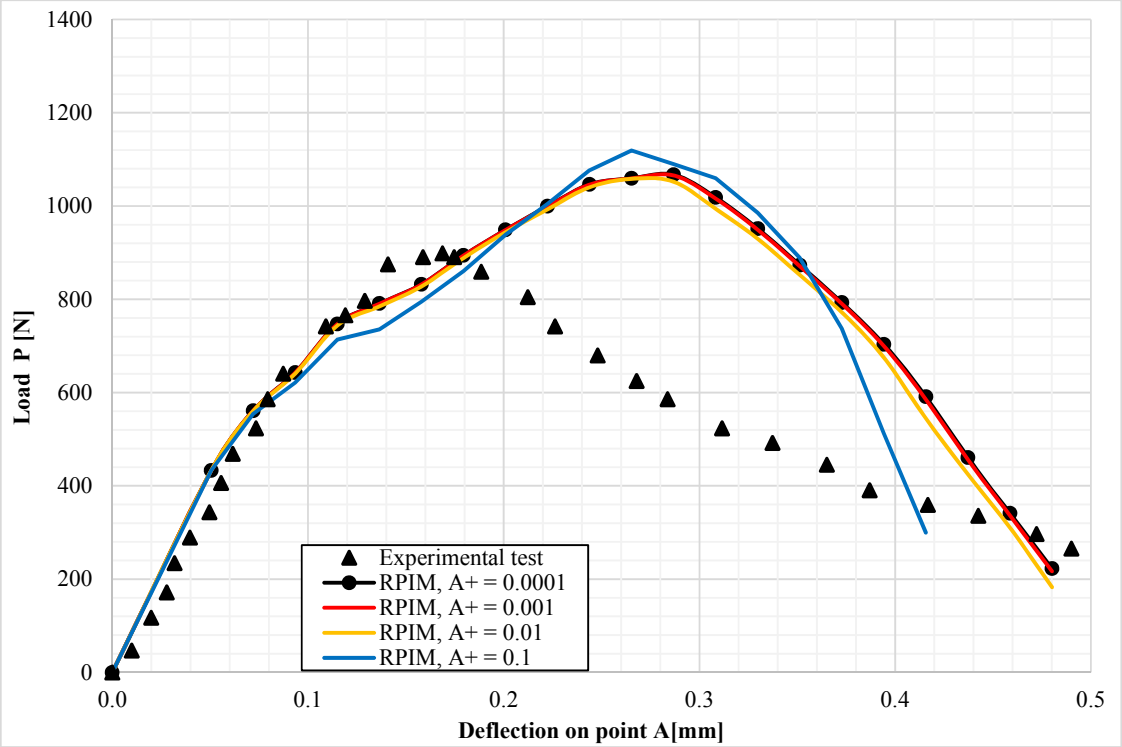

Figure 89: Study of A^+ for the response of load P versus the deflection of point A on the third refined discretization, the 2nd -order weight function with $n_p = 0.8$

The same procedure is conducted on the 3rd order weight function taking account into the various values of A^+ for all the refined discretizations shown in Figure 90, Figure 91 and Figure 92.

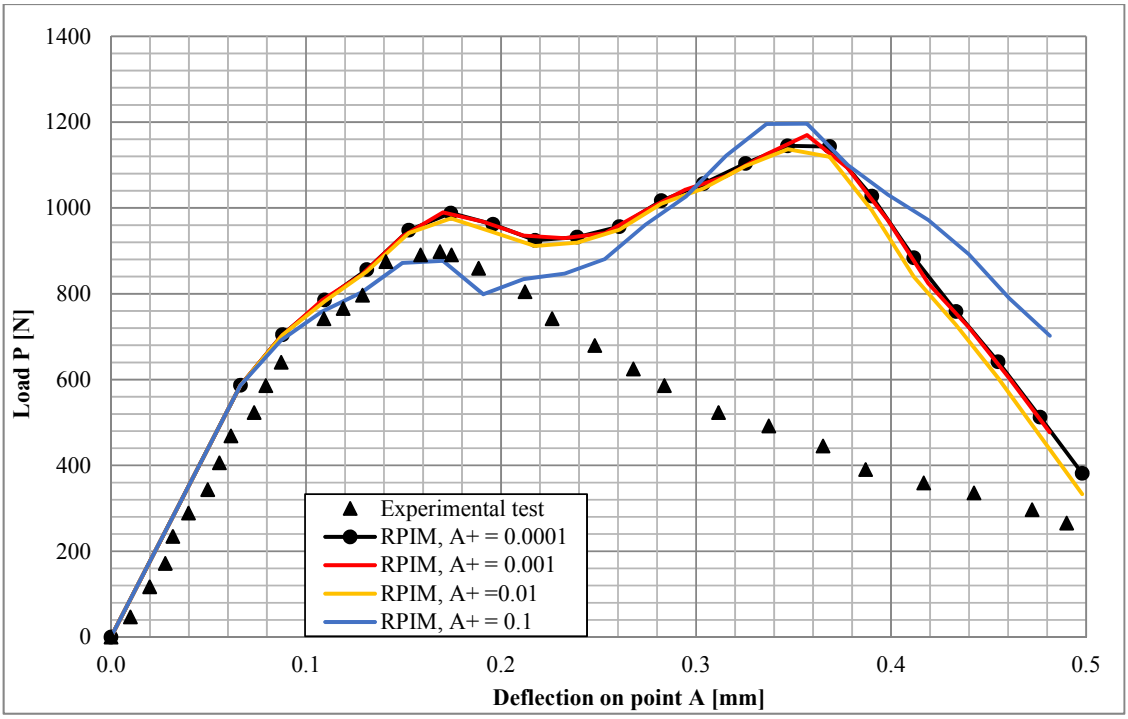

Figure 90: Study of A^+ for the response of load P versus the deflection of point A on the first refined discretization, the 3rd -order weight function with $n_p = 0.8$

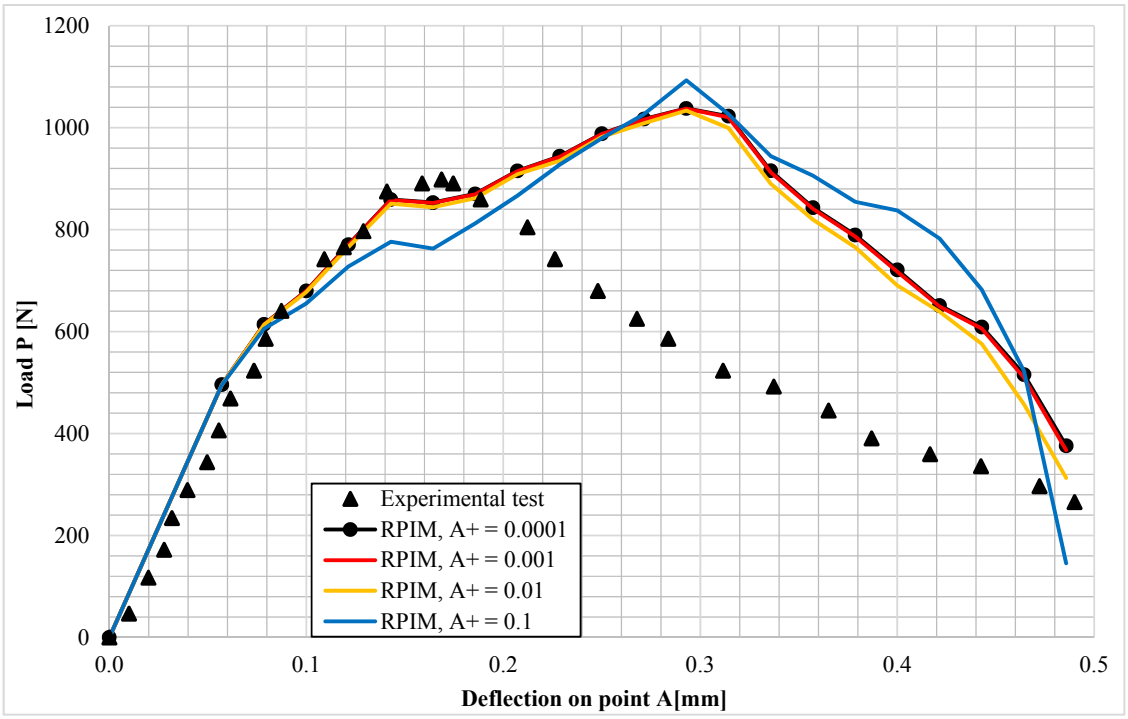

Figure 91: Study of A^+ for the response of load P versus the deflection of point A on the second refined discretization, the 3rd -order weight function with $n_p = 0.8$

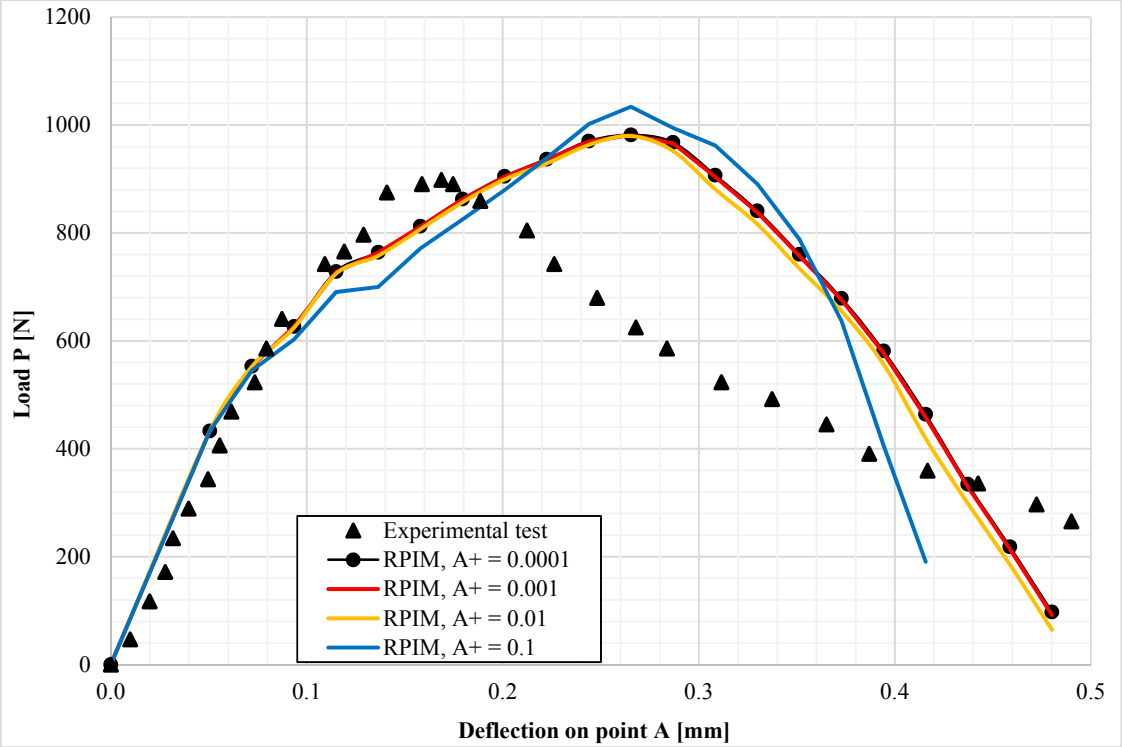

Figure 92: Study of A^+ for the response of load P versus the deflection of point A on the third refined discretization, the 3rd -order weight function with $n_p = 0.8$

The variation of the characteristic length and $\bar{H}^+$ variable are computed based on Equations (96-a) and (95-a) repetitively reported on Table 25.

Table 25: variation of the characteristic length and H variable

A^+	$l_{ch}(m)$	$\bar{H}^+ \ (m^{-1})$	$\frac{1}{\bar{H}^+} \ (m)$
1×10^{-1}	1.08×10^{-2}	4.244	0.226
1×10^{-2}	1.1×10^{-3}	4.244	0.226
1×10^{-3}	1.1296×10^{-4}	4.244	0.226
1×10^{-4}	1.1302×10^{-5}	4.244	0.226

The results represented on Table 25 present the acceptable values for all variables according to the damage mechanics criteria. They satisfy the corresponding conditions expressed in Equations (95-b) and (96-c) in which:

$$A^{+} \geq 0 \quad and \ \frac{1}{\bar{H}^{+}} \geq l_{ch}$$

In all analyses, the curve related to $A^{+} = 0.1$ behaves differently compared to the other ones. Somehow it experiences some unexpected fluctuations during the process. Hence it is recommended not to consider that.

Although the results related to the other values $A^{+} = 0.01, 0.001 \ and \ 0.0001$ vary similarly and they have a good agreement with the experimental curve, there must be one value optimized here. However, the optimized value could be selected the middle one which is $A^{+} = 0.001$.

Regarding the behavior of weigh function order, it is visible that the 2nd order weight function increases the peak load point leading to delay the damage phenomenon. Because the damage initiates after reaching the ultimate elastic value where the concavity of the curves changed. Hence it is rational to discard the 2nd order weight function.

Considering all the convergence studies, it is possible to represent all the optimized values for localized damage formalism as seen on Table 26.

Table 26: The optimum values of damage localization in three point bending beam

$n_p = 0.8$	3rd order weight function	$A^{+} = 0.001$	$l_{ch} = 1.1296 \times 10^{-4}\ (m)$

According to the results presented on Table 24 and Table 26, it is important to mention that *RGP* value is affected by the discretization size meaning that it is a function of the number of nodes.

Considering all, it is possible to analyze a denser refined mesh of three point bending beam so-called “the final one” with regard to the optimum localized damage values.

7.2.4 The Final Refined Discretization

In order to finalize the refinement study, within the scope of the localized damage for three point bending beam, a denser mesh so-called "Final Discretization" with the total number of 2941 nodes and 6300 integration points is considered, as represented in Figure 93.

The main goal of this study is to observe the efficiency and performance of the numerical algorithm in the presence of the optimum values reported from the previous studies.

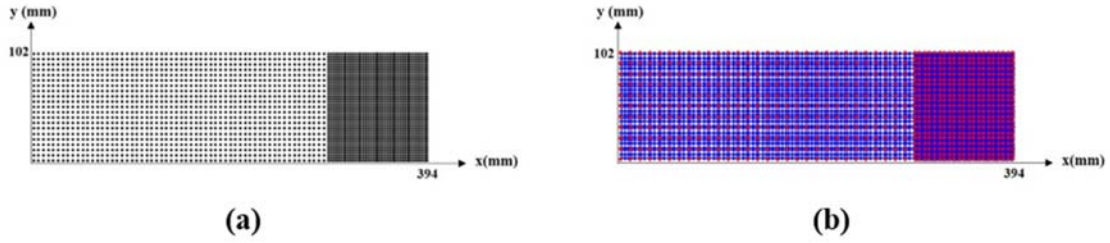

Figure 93: Final refined discretization for three point bending beam: (a) 2941 nodes and (b) 6300 Gauss points

It is necessary to mention that the total displacement enforcement is considered as u = 0.32 *(mm)* to capture better performance of the localized damage algorithm. The divisions along *x* and *y* directions are 81 and 21 respectively. So, it is possible to compute the average distance between nodes within Equation (113-b) as follows:

$$h = 0.0049\ (m)$$

Consequently, consider $n_p = 0.8$, *RGP* is calculated from Equation (113-a) as:

$$RGP = n_p\, h = 0.8 * 0.0049 = 0.0039\ (m)$$

Consider the 3rd order weight function and the other optimum variables for damage localization aspect, the response of load P - deflection on point A is captured for this analysis shown in Figure 95. The variation of damage versus effective strain in the case of non-local and localized tensile damage in addition to total damage at gp_c is presented in Figure 96. The corresponding integration point is introduced in Figure 94.

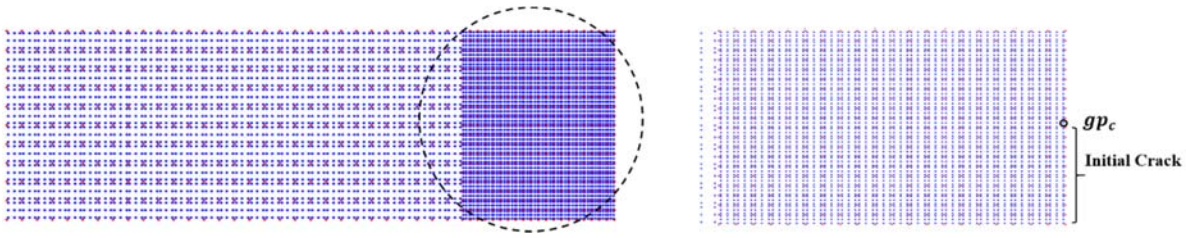

Figure 94: The detection of gp_c for the final refined discretization in three point bending beam

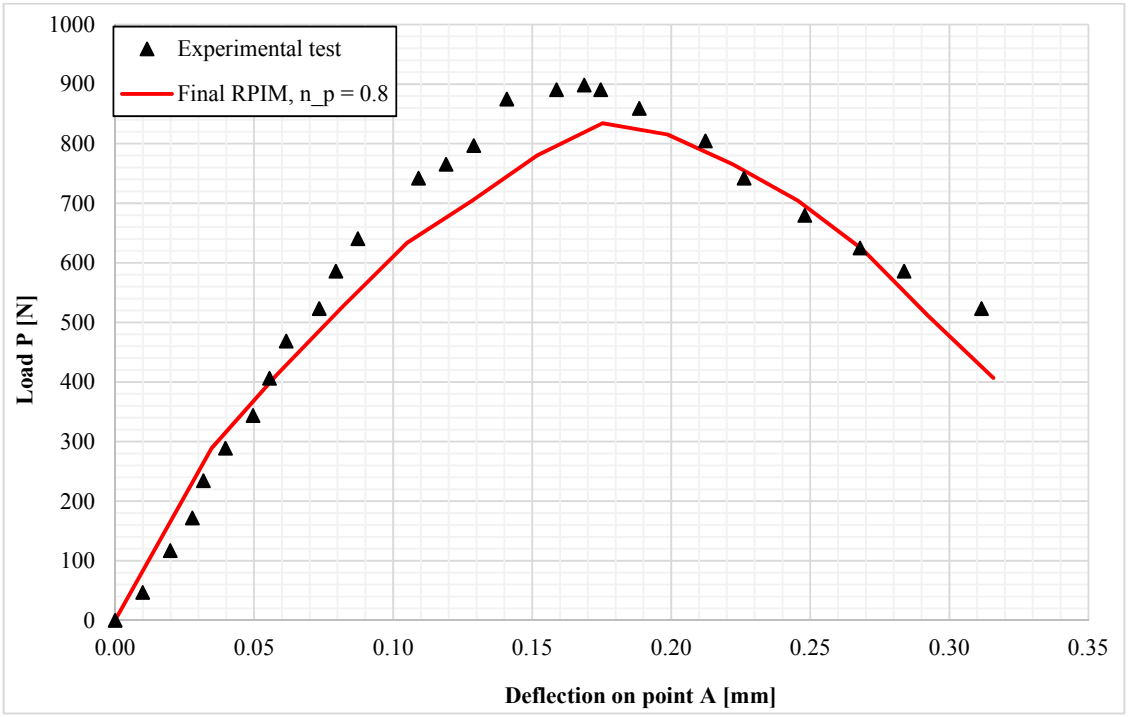

Figure 95: Load *P* in terms of deflection on point *A* for final refined discretization with 2941 nodes, 3rd order weight function if $n_p = 0.8$

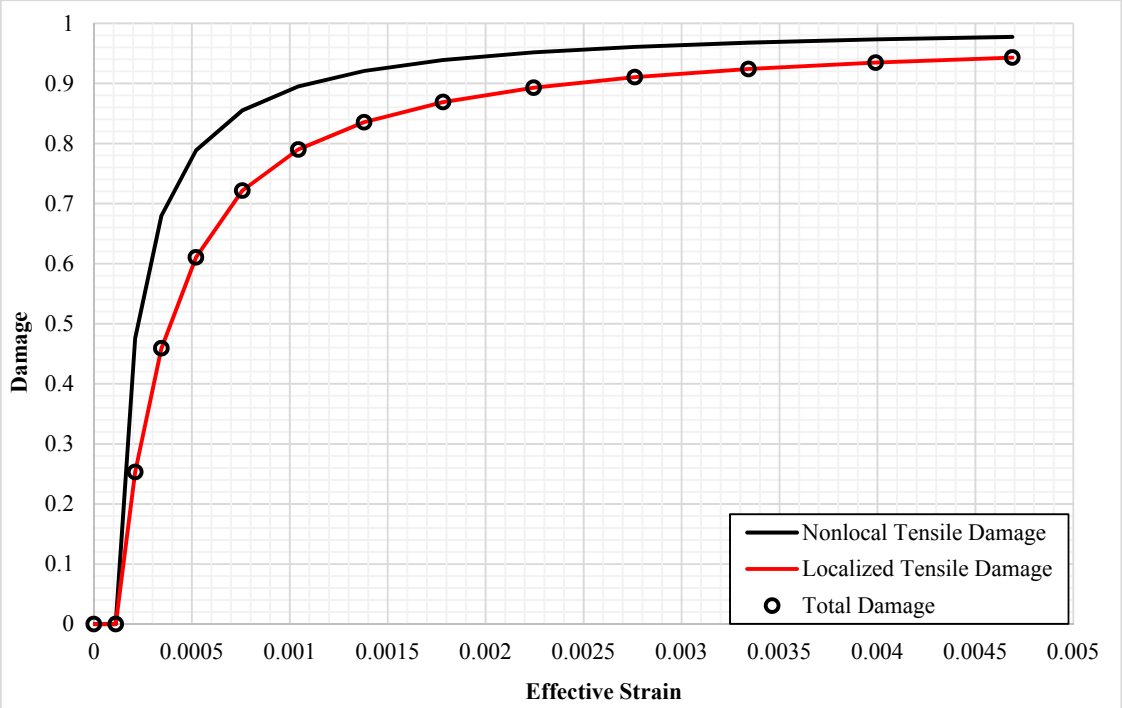

Figure 96: Variation of damage at gp_c obtained for final refined with 3rd order weight function if $n_p = 0.8$

Referring to Figure 95, it is observable that the RPIM solution agrees very well with the experimental one and it satisfies the target of this work. Thus, this agreement proves the efficiency of the convergence study and most importantly the optimization procedure. To clarify this notification, all the curves with regard to the optimum n_p value for the four refined discretizations are shown in Figure 97.

In fact, this figure is the complete version of Figure 86.

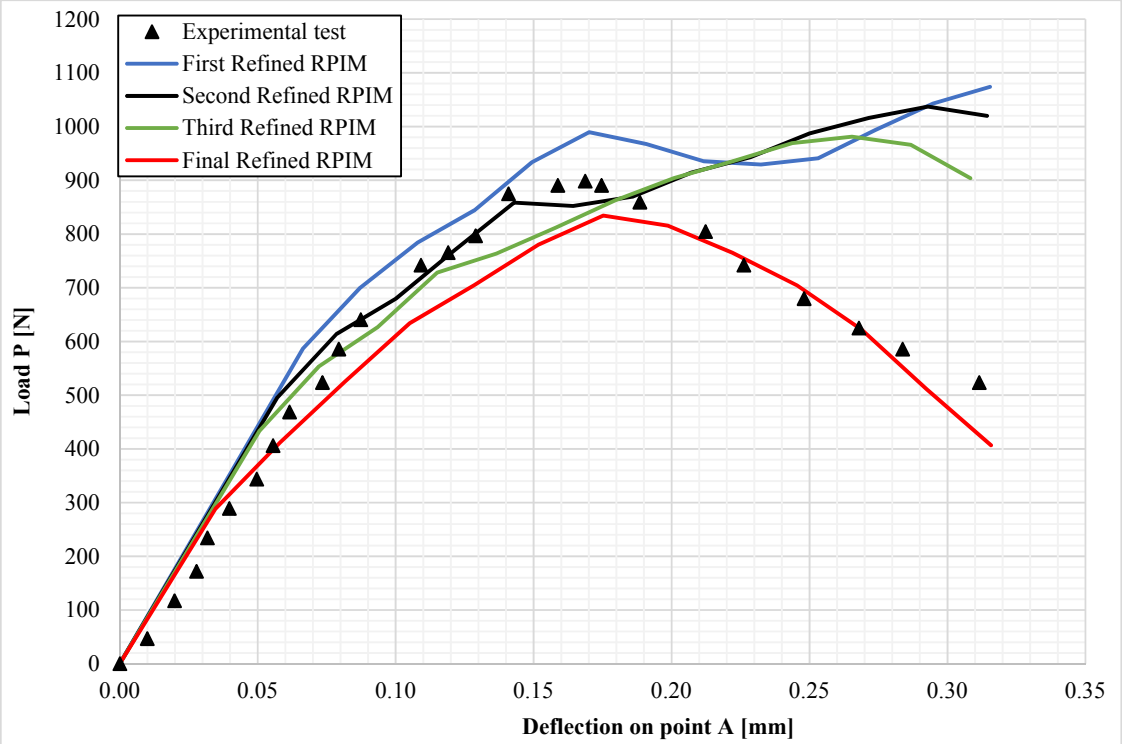

Figure 97: Load P in terms of deflection on point A for all refined discretizations for 3rd order weight function and $n_p = 0.8$

7.2.4.1 Graphical Representations of the Internal and Damage Variables

In this part, profiles of the tensile, compressive and total damage contours are presented to catch the progress of the analysis related to three point bending test when the final RPIM discretization is considered. They are captured in each increment of displacement enforcement. In addition, the profile of total equivalent von Mises effective stress in total and damaged states are demonstrated.

7.2.4.1.1 Damage Contours

The corresponding contours are captured in the following displacement enforcement stages as shown on Table 27.

Table 27: The corresponding displacement enforcement for graphical representations

	First stage	Second stage	Third stage
Displacement enforcement (mm)	1.2841E-01	1.7526E-01	3.1581E-01

The obtained contours, related to the damage profiles based on the particular displacement enforcement stages (see Table 27), are presented in Figure 98.

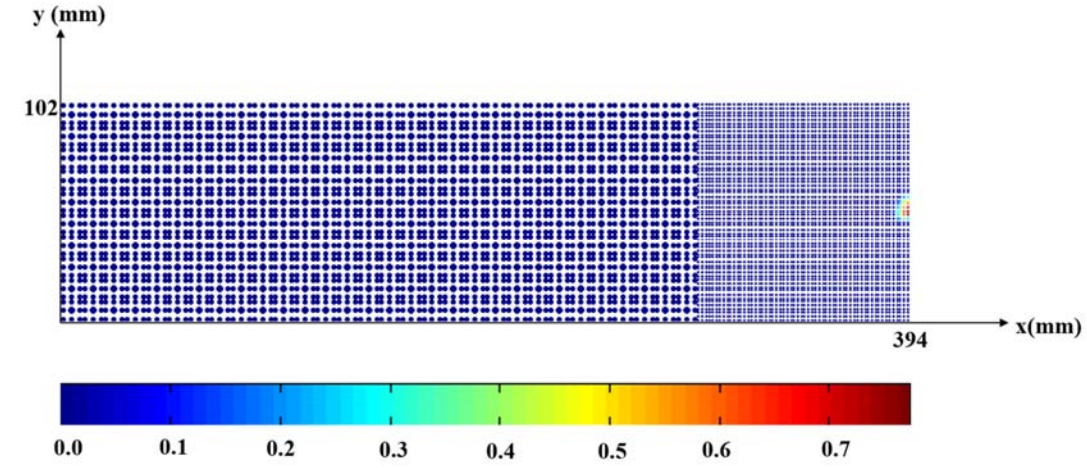

(a)

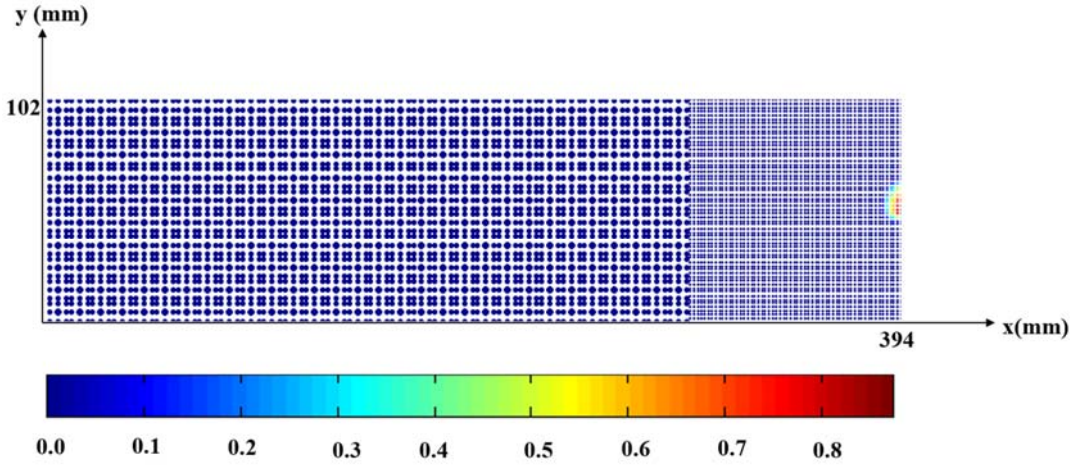

(b)

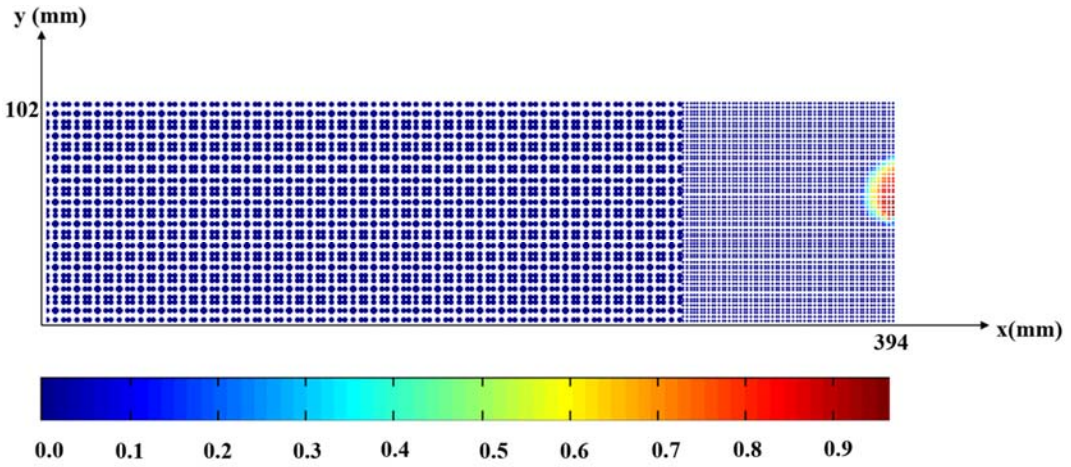

(c)

Figure 98: The damage contour on three point bending beam for (a) first stage, (b) second stage and (c) third stage of enforced displacement

It is important to mention that the tensile damage contours are the same as the damage ones. Thus, it is not necessary to repeat them.

7.2.4.1.2 Compressive Damage Contour

The compressive damage profile for this three point bending is presented in Figure 99. This profile remains as zero value during all the displacement enforcement stages.

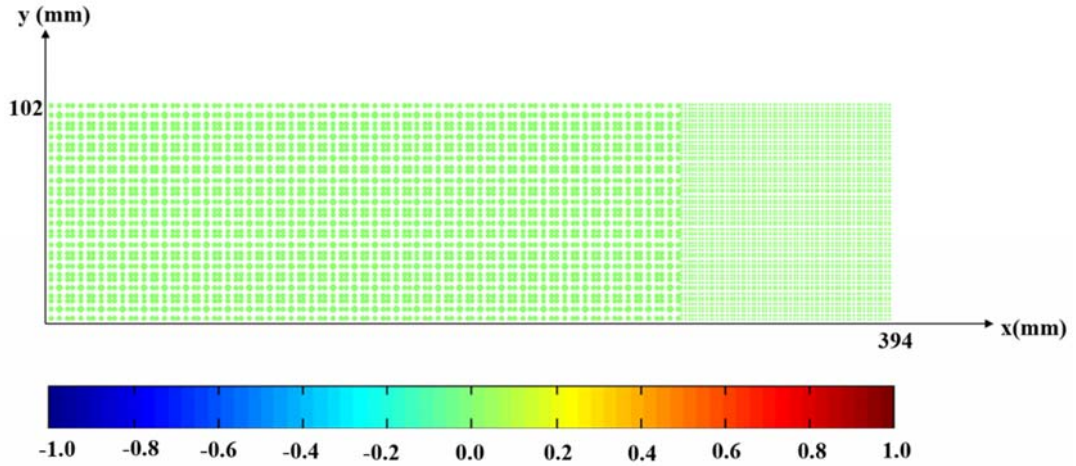

Figure 99: Compressive damage contour on the three point bending beam

7.2.4.1.3 Equivalent Von Mises Total Stress

The profile of equivalent von Mises effective stress in total elastic state is shown in Figure 100. This figure shows an increasing trend of the total effective stress value when the enforced displacement grows.

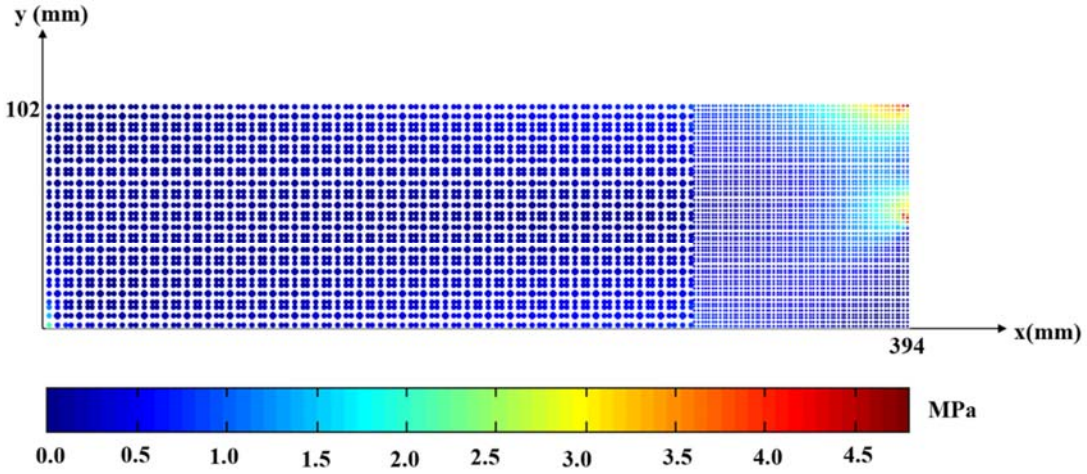

(a)

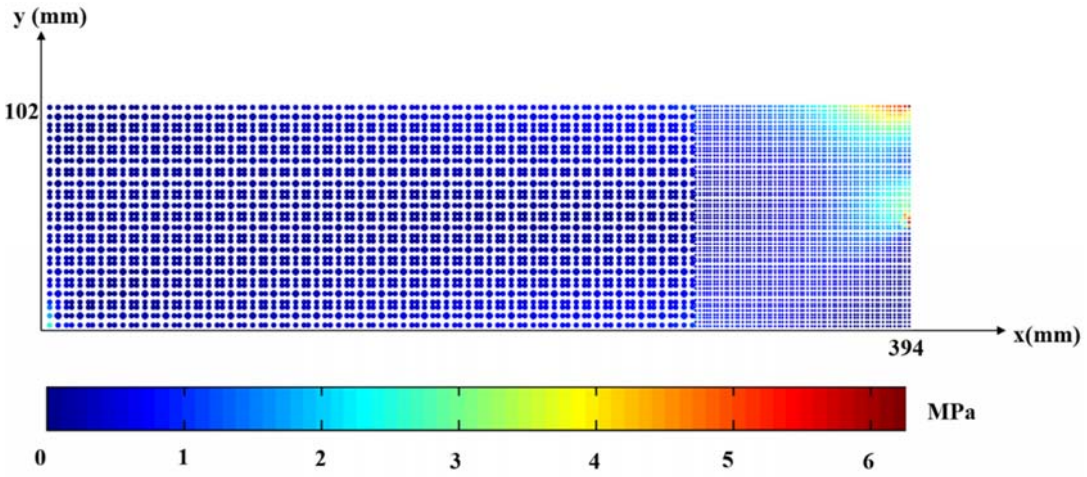

(b)

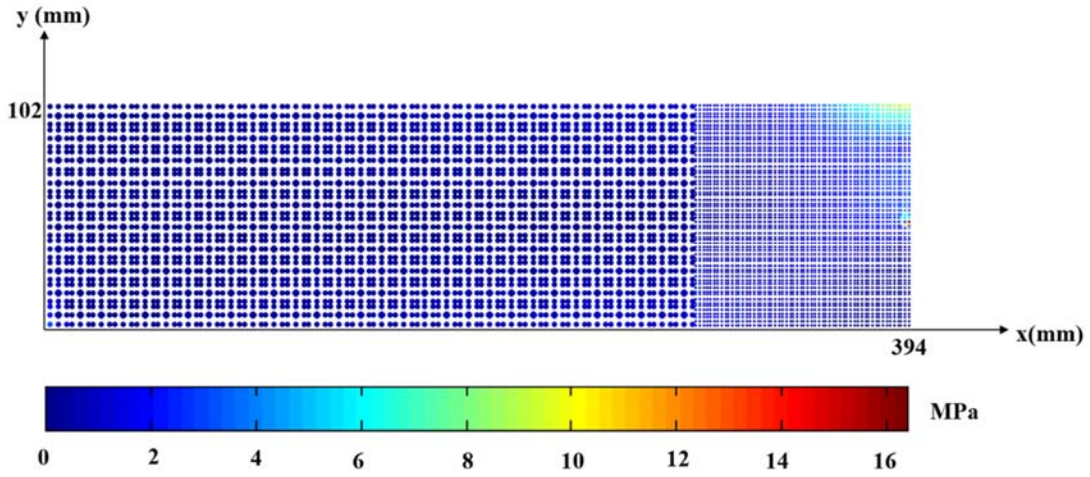

(c)

Figure 100: The total stress profile on three point bending beam for (a) first stage, (b) second stage and (c) third stage of enforced displacement

As seen in Figure 100, it is visible that the stress is increasing in the crack area. It already exceeds the maximum uniaxial tensile strength causing the tensile damage happens in the material (Figure 100-c).

7.2.4.1.4 Equivalent Von Mises Damaged Stress

The equivalent effective von Mises stress map in damaged state for three point bending test is presented in Figure 101.

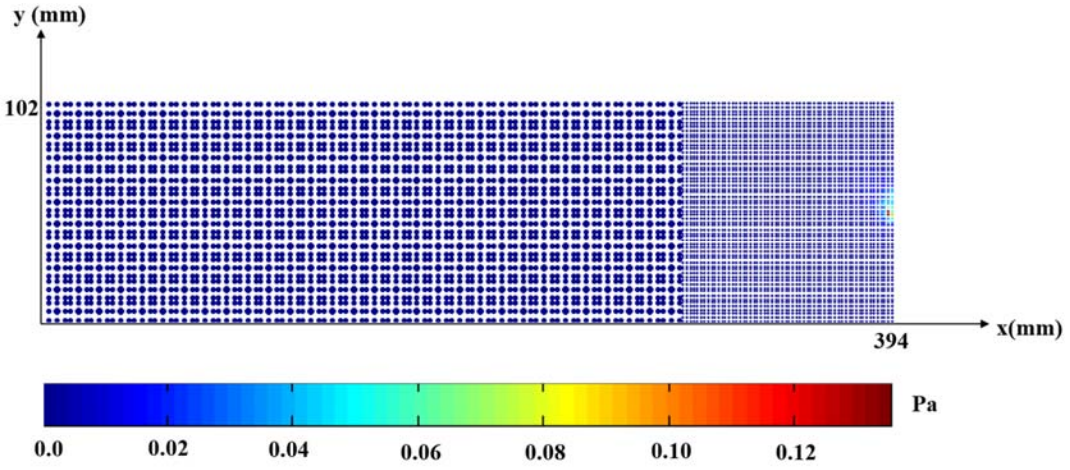

(a)

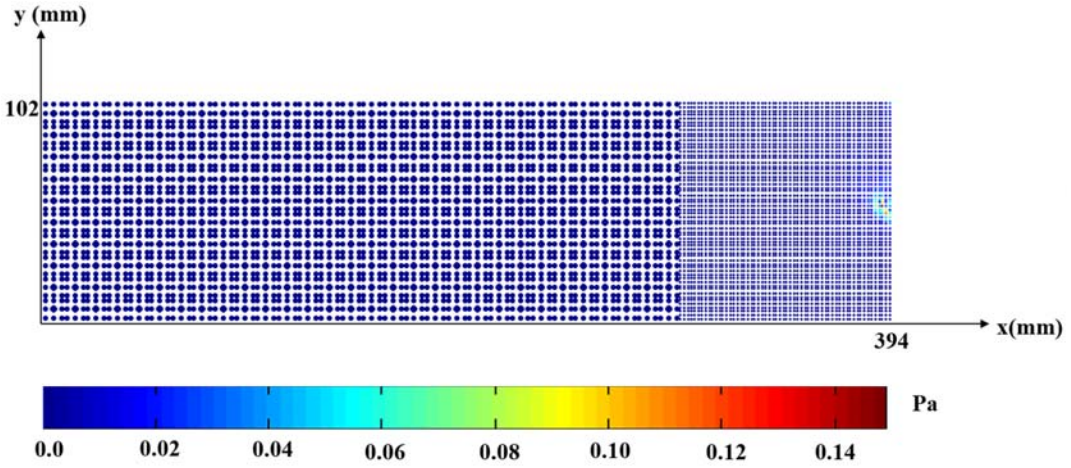

(b)

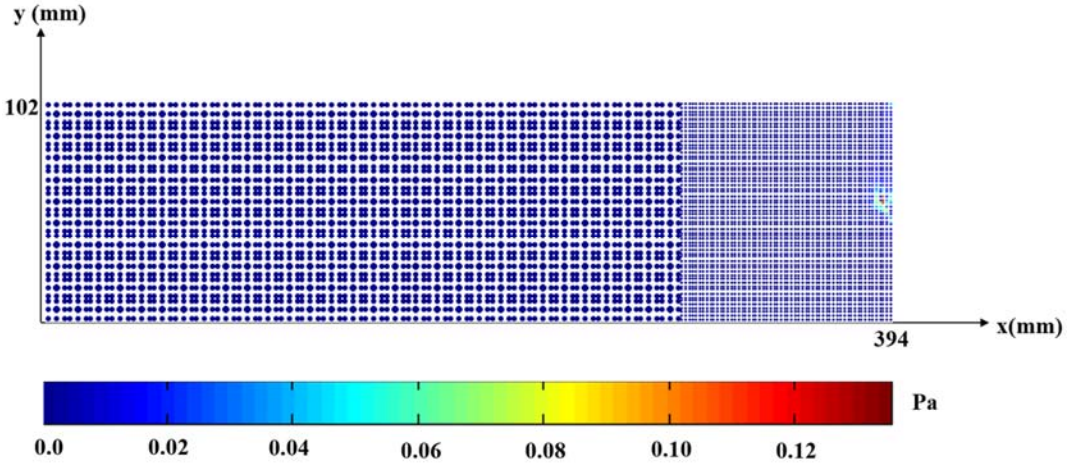

(c)

Figure 101: The damaged stress profile on three point bending beam for (a) first stage, (b) second stage and (c) third stage of enforced displacement

It is nothing worth to mention that the damaged stress accounted for very low values. This has a good agreement with the literature. Once the material starts to be damaged, the stiffness matrix is decreasing significantly. Hence the material becomes softer leading to decrease the internal force. Consequently, the stress in damaged state declines. Besides, the damaged stress is concentrated on the crack tip where it initiates to propagate (the non-dark blue area in the profiles)

7.2.4.2 Study of Irregular Mesh

Based on the analysis presented in Section 7.2.4, it is possible to perform the algorithm on the irregular discretization using RPIM formulation extended to the rate-independent damage mechanics with localized damage parameters. First of all, the geometry and essential boundary conditions are shown in Figure 102.

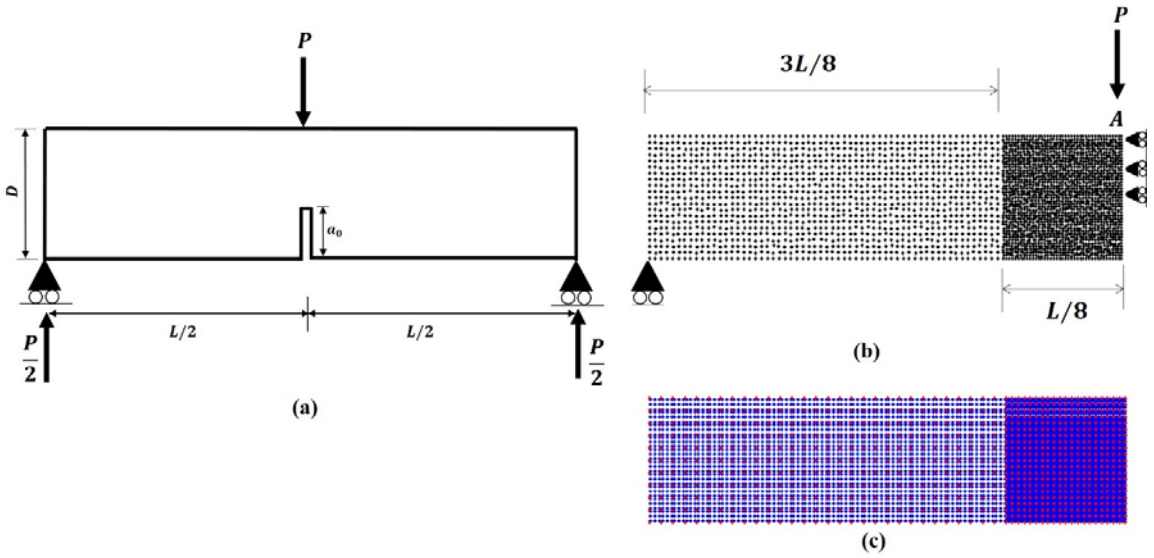

Figure 102: The single-edge-notched beam subjected to three point bending (a) geometry, (b) the refined irregular mesh with the essential boundary conditions and (c) integration points

In this part we can benefit from the previous work where the theory of RPIM irregularity was introduced in Section 5.1.4 for axisymmetric plates. With regard to Equation (126), the irregularity parameter for this analysis is chosen as $\lambda = 10$. The material properties, geometric and damage characteristics are the same as the similar regular case.

As done before, so as for obtaining the more accurate results in the irregular nodal distribution, the analysis should be performed for several times while the coefficients and parameters are the same for all of them. Then, the average value is driven to compare with the experimental solution (Malvar & Warren, 1988). Thus, there are 7 basic results obtained for this irregular study as demonstrated in Figure 103.

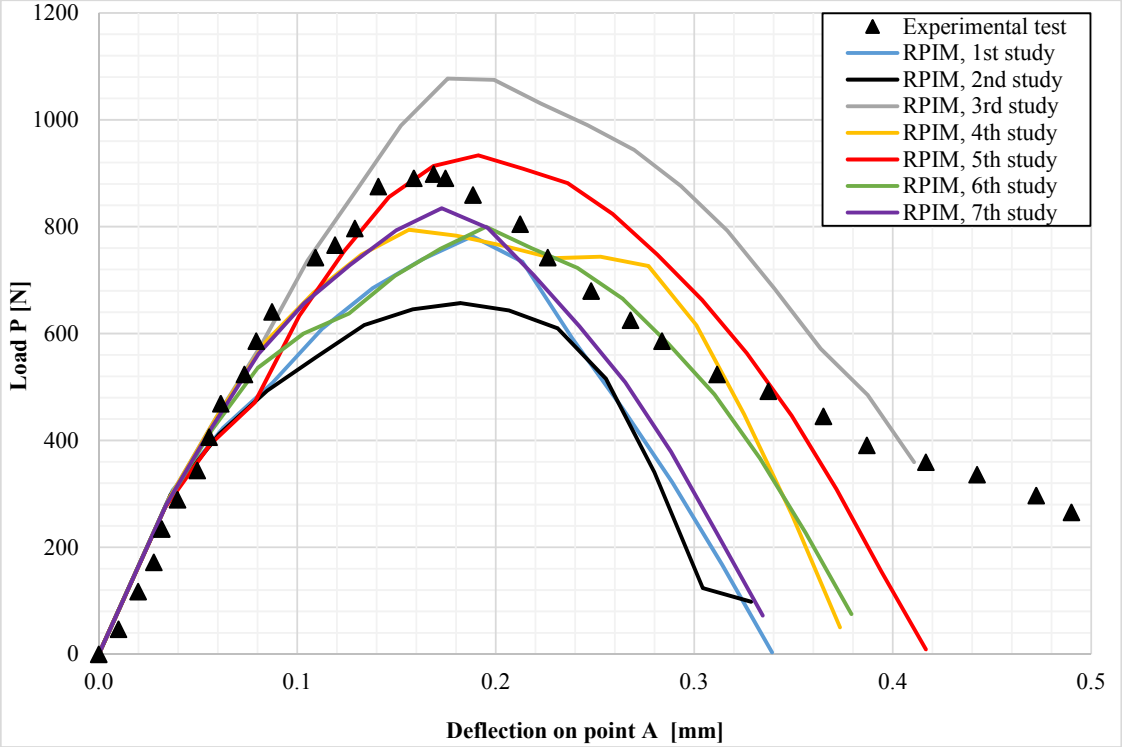

Figure 103: Basic responses of load *P*- deflection on point *A* obtained for irregular discretization with 2941 number of nodes in the case of damage localization

Considering all the 7 irregular results for this example, it is possible to calculate their average and then compare to the experimental solution and also the similar regular result as well (the regular result relevant to this study was presented in Figure 95), subsequently the outcome is shown in Figure 104.

It is nothing worth to mention that the optimum parameters of localized damage perform very well with the irregular nodal distribution as well as the regular case ($n_p = 0.8$ and 3rd order weight function).

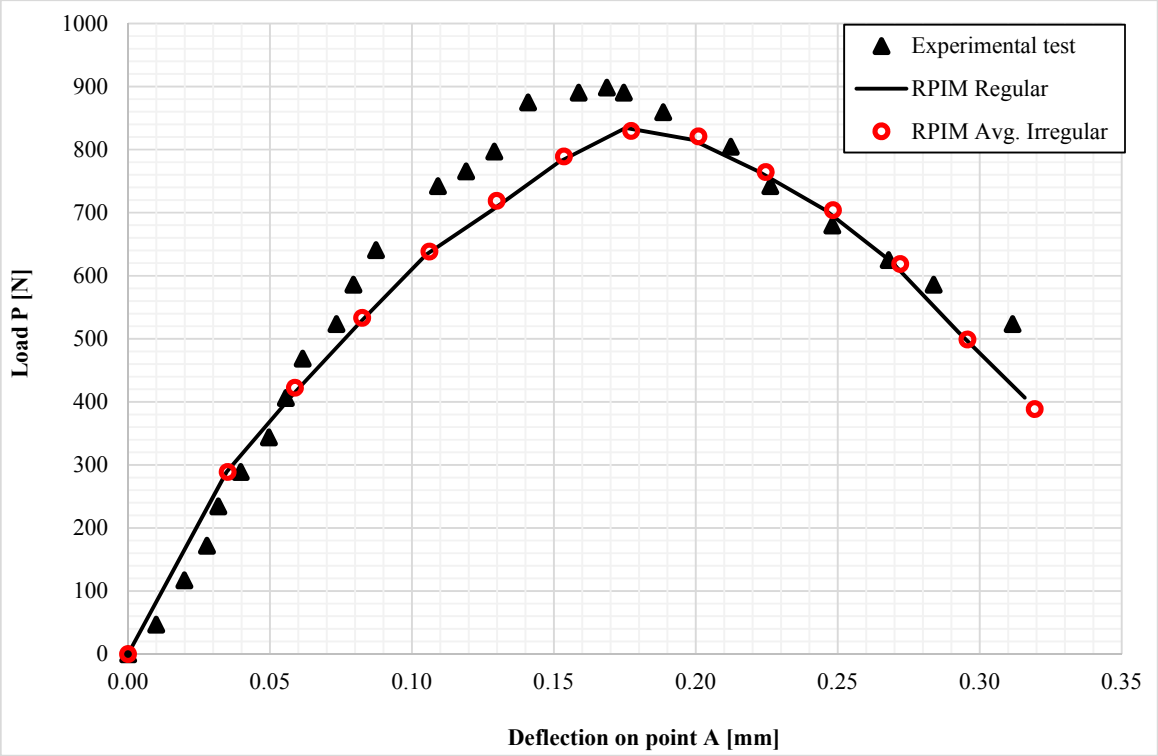

Figure 104: Response of load P in terms of deflection on point A for three point bending test within localized RPIM damage formalism obtained for the regular and average irregular discretizations

Figure 104 certifies that the average irregular result has a good agreement with the regular one and both of them are validated with the experimental curve of the load *P*- the deflection on point *A* response.

7.2.4.3 Modified Irregular Mesh

To end the analysis of three point bending beam, this section is devoted to the specific rearrangement of the irregular nodal distribution. The procedure is described briefly here, in order to obtain a milder curve of the load *P*- the deflection on point *A*, a small change in the arrangement of the node is applied.

Thus, the RPIM algorithm is ordered to rearrange these three nodes close to the regular nodal distribution. This change is not significant in the discretization, since only 3 nodes are affected by this rearrangement, but it might influence the solution dramatically.

Subsequently, the corresponding change is defined in the part of irregular discretization by forcing the mentioned 3 nodes to be arranged regularly. Figure 105 clarifies the abovementioned description.

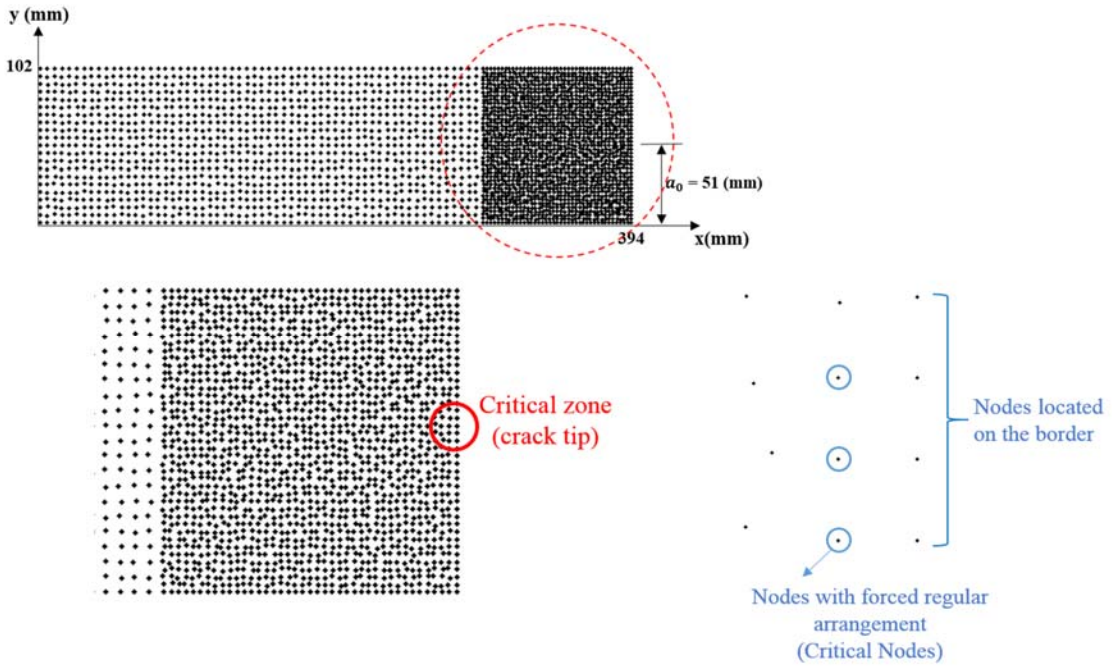

Figure 105: The rearrangement on the critical nodes situated at the crack tip for the modified irregular mesh in three point bending beam

For this specific analysis (with 2941 nodes and 6300 integration points), it should be remarked that the mesh routine, defined to change the arrangement of the nodes, never rearranges the discretization in the critical zone for more than 3 single nodes. Because it is controlled within the specific conditions in advance. But it would be distinct for the other discretization patterns. However, the nodes located at the border are forced to be regularly discretized, which is not relevant to this stage (see Figure 105).

With regard to the mentioned aspect, using the rearranged irregular mesh it is possible to obtain the response of load in terms of the deflection.

So, the analysis has been repeated for 7 times with the same property for the irregular discretization ($\lambda = 10$) with the optimum localized parameters mentioned before. The outcome of this work is shown in Figure 106.

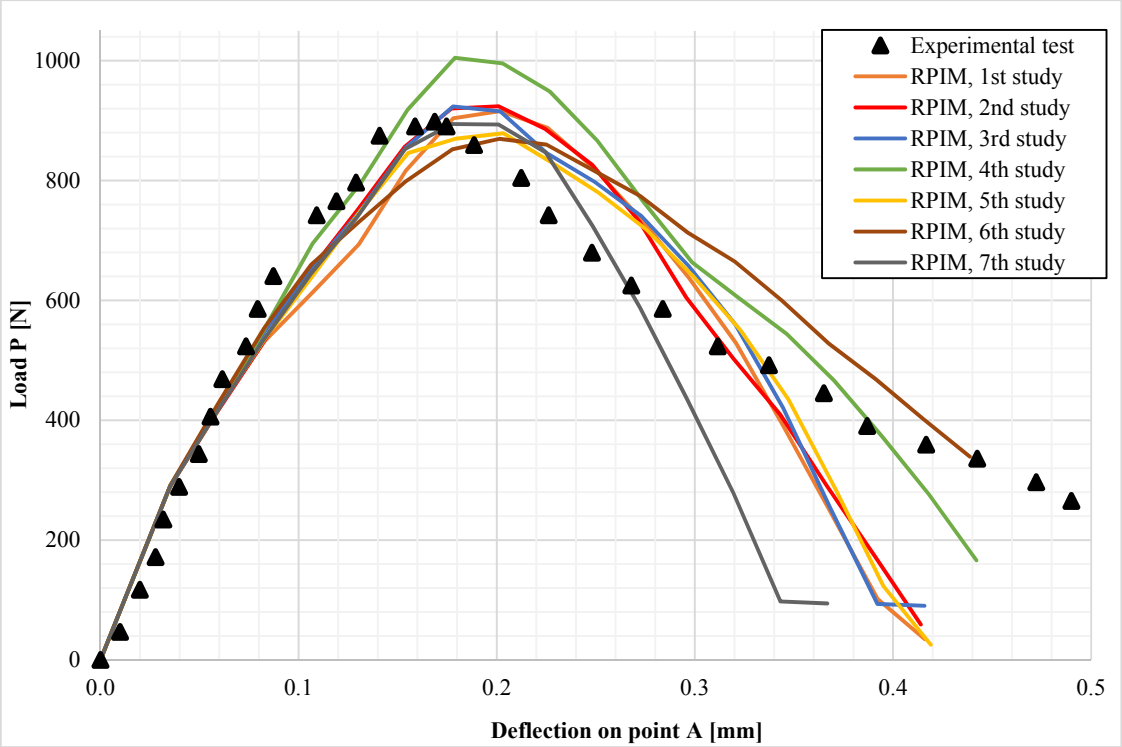

Figure 106: Basic responses of load P- deflection on point A obtained for the modified irregular mesh with regard to the optimum localized parameters

Comparing the basic irregular results presented in Figure 103 and the modified ones shown in Figure 106, it is visible that the current curves of load - deflection are milder and closer to the experimental solution (Malvar & Warren, 1988). There is an expected variation after reaching the peak load point in the former results.

Consequently, in order to finish this research task, the average modified results are compared to the experimental solution (Malvar & Warren, 1988) and similar regular result (Figure 95). Therefore, Figure 107 demonstrates the final graphical representation.

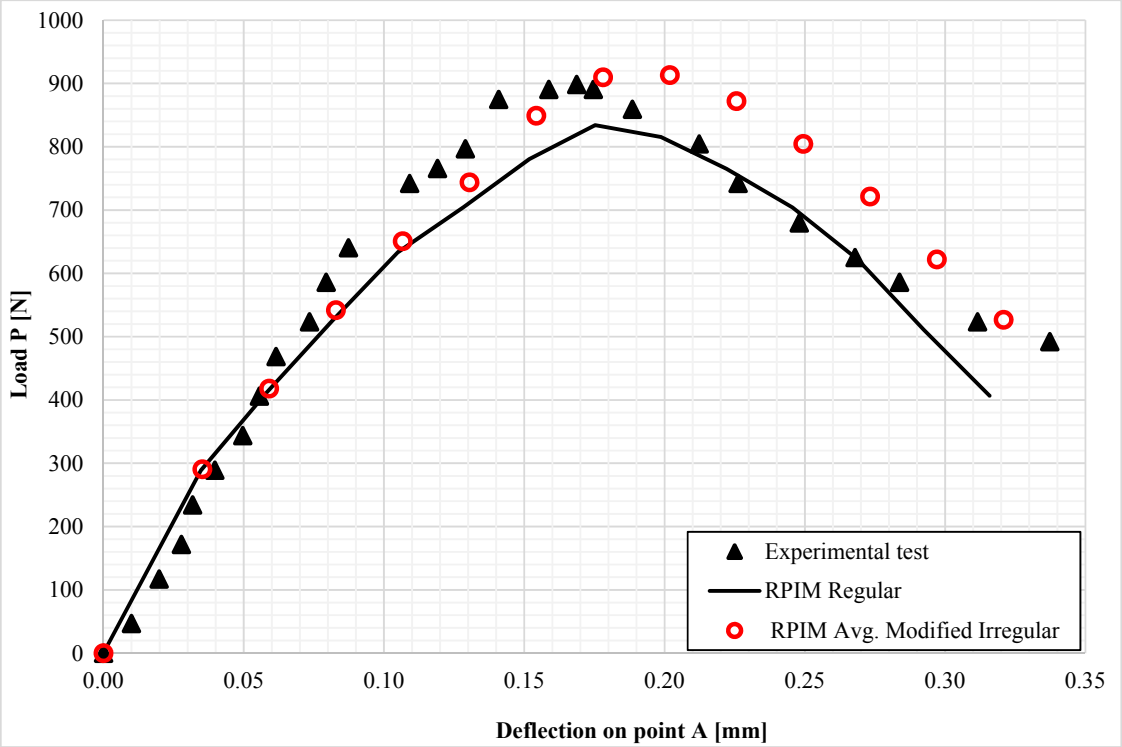

Figure 107: Response of load P – deflection on point A for three point bending test within localized damage formalism obtained for regular and average irregular mesh with refinement

Figure 107 indicates the behavior of load *P* versus deflection on point *A* for three point bending beam obtained from regular and modified irregular meshes in the sense of the localized damage. It is observable that the curve of average irregular is getting a bit far away from the experimental result after reaching the peak load compared to the similar graph presented in Figure 104 (where the irregular and regular curves are almost matched together).

Figure 108 indicates a resume of all the analyses done for regular, irregular and modified irregular meshes. Considering this figure, it is rational to conclude that, the main targets of this work have been satisfied.

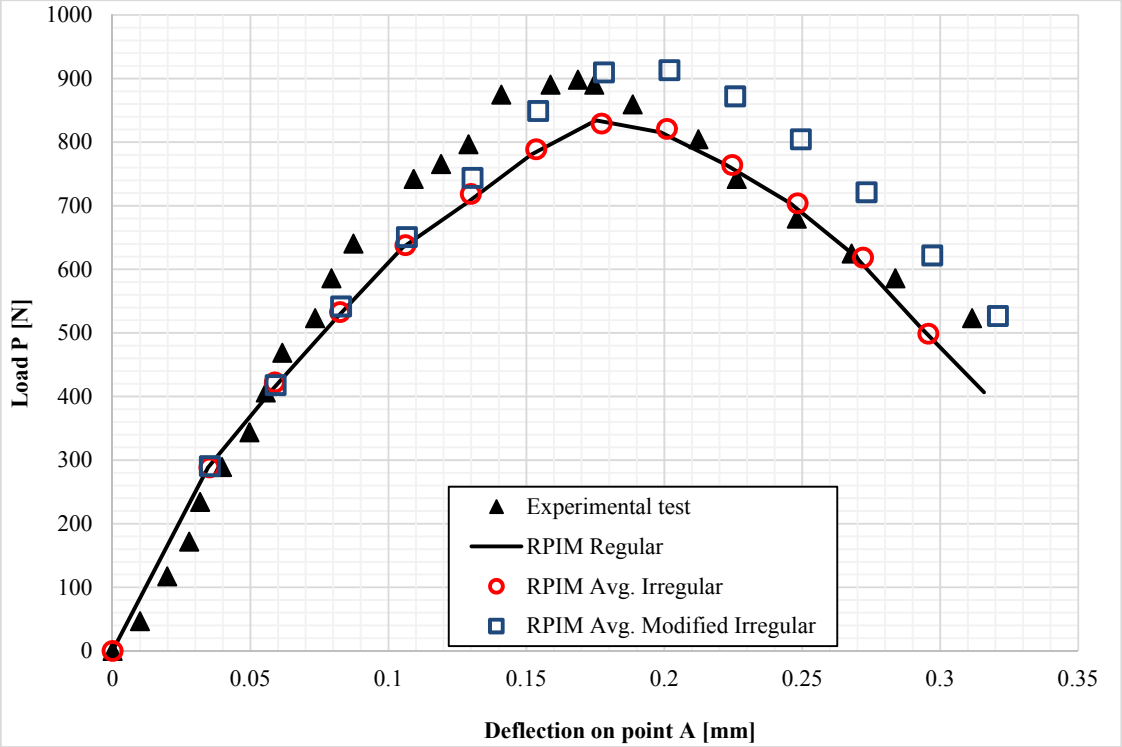

Figure 108: The comparison between regular, irregular and modified irregular meshes obtained for three point bending beam

The importance of performing modified irregular mesh is referred to the basic irregular analyses shown in Figure 103. As it is observable, the corresponding curves are satisfactory till reaching the peak load, after that they start to diverge significantly from the experimental result. This behavior is not very convenient for the analyses. Thus, in order to eliminate this variation, the rearrangement of the nodes in the critical zone (which seems to affect the solution) has been proposed. Consequently, the suitable basic results of the irregular analyses have been obtained Figure 106 with regard to the modified irregular discretization.

The observation of Figure 108, including all the results together, permits to verify that the regular mesh of three point bending beam agreeing very well with the experimental solution (Malvar & Warren, 1988). Besides, the average irregular solution has a good agreement with the experiment regardless the non-mild variations of the 7 basic solutions for that Figure 103. Although the average modified irregular result overlaps the

experimental curve a bit after reaching the peak load point, the 7 basic results (Figure 106) match the experimental results acceptably. Hence the objective of the modified analysis is relevant to the basic irregular solution and verify them with the experiment.

Overall, all the obtained results are valid with the experimental solution with regard to the optimum parameters for damage localization formalism in RPIM meshless method.

7.3 Compact Tension Test

The last benchmark studied here is a compact tension specimen as seen in Figure 109, it was tested for the first time at LMT Cachan (Legendre, 1984). There are some observations and experimental results reported by (Legendre, 1984) and (Mazars & Pijaudier-Cabot, 1996) showing the global behaviour of the structure during linear elastic damage mechanics (LEDM) and linear elastic fracture mechanics (LEFM). This study has been categorized as a combination of damage and fracture mechanics because micro cracks evolve to a macro crack. It means that the analysis starts with damage mechanics and ends with the fracture phenomenon (Mazars & Pijaudier-Cabot, 1996).

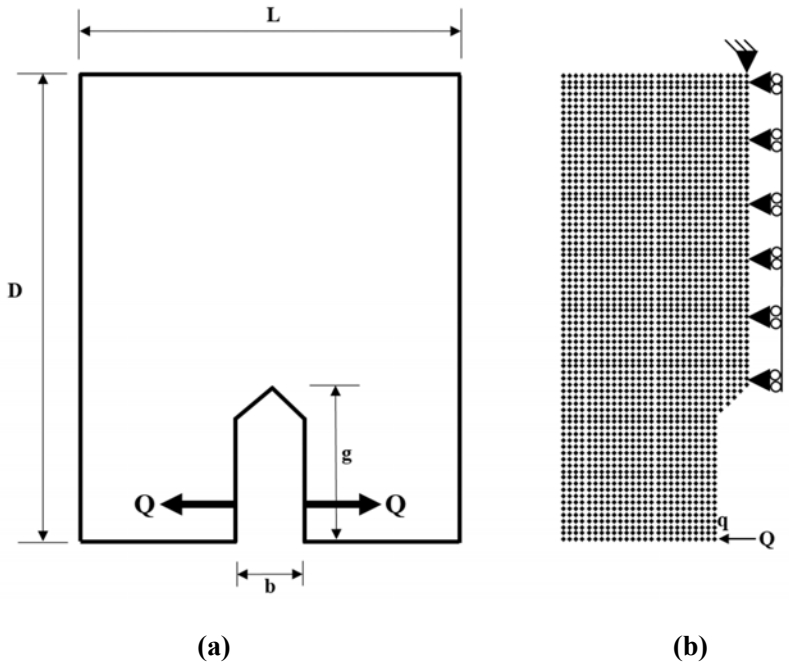

Figure 109: Compact tension specimen: (a) Geometry and (b) Regular mesh and essential boundary conditions

Figure 109-a indicates the geometry of the specimen containing an empty space so-called "hole" in the middle bottom with the specific dimensions. As seen in Figure 109-b, it is noticeable that only half of the specimen will is considered due to its symmetry. This assumption reduces the computational costs and increases the efficiency of the RPIM formulations. Furthermore, this figure illustrates the essential boundary conditions applied on the specimen. Like the other studies, here, a displacement controlled analysis is performed, where the displacement is enforced at point *q* shown as *Q*. Moreover, the nodes located on the right border are not allowed to move along *x* direction.

This study performs with the different nodal distributions for the compact tension specimen considering the localized damage formalism.

In order to start the analysis through RPIM formulation, it is necessary to predefine some properties and coefficients presented on Table 28.

Table 28: Geometric properties of compact tension specimen (Mazars & Pijaudier-Cabot, 1996)

Parameter	Value
Length	$L = 60 \times 10^{-2}(m)$
Width	$D = 75 \times 10^{-2}(m)$
Thickness	$e = 10 \times 10^{-2}(m)$
Hole length	$b = 10 \times 10^{-2}(m)$
Hole width	$g = 25 \times 10^{-2}(m)$

The material properties and damage characteristics of concrete used in this example are represented on the following Table 29 and Table 30.

Table 29: Material properties of the model (Mazars & Pijaudier-Cabot, 1996)

Property	Value
Young`s modulus	$E = 34.5 \times 10^{9}(Pa)$
Poisson's ratio	$\nu = 0.2$
Maximum uniaxial tensile strength	$f_0^+ = 4.2435 \times 10^{6}(Pa)$
Maximum uniaxial compressive strength	$f_0^- = 29 \times 10^{6}(Pa)$
Maximum uniaxial tensile strain	$\varepsilon_0^+ = 1.23 \times 10^{-4}$
Maximum uniaxial compressive strain	$\varepsilon_0^- = 8.4058 \times 10^{-4}$
Fracture energy	$G_t = 102\ (N/m)$

Table 30: Damage characteristics for compact tension test

Parameter	Value
In tension	$A^+ = 0.1663$
In compression (Cervera et al., 1996)	$A^- = 1$
In compression (Cervera et al., 1996)	$B^- = 0.89$
Characteristic length (Mazars & Pijaudier-Cabot, 1996)	$l_{ch} = 3 \times 10^{-2}(m)$

Regarding the characteristic length and A^+, it must be noted that the scenario varies here compared to the previous examples. In this study, the characteristic length is chosen as $l_{ch} = 3 \times 10^{-2}(m)$ based on the fixed value for the FEM analysis proposed by (Mazars & Pijaudier-Cabot, 1996). Hence the tensile coefficient is adopted in accordance with Equation (96-a) as follows:

$$\bar{H}^+ = 2.5586\ (m^{-1})$$

$$A^+ = 0.1663\ \geq 0$$

$$\frac{1}{\bar{H}^+} = 0.3908\ (m)\ \ \geq\ \ l_{ch} = 0.03\ (m)$$

The abovementioned relations prove that all the corresponding variables have an agreement with the damage mechanics concept.

Moreover, there exist some important configurations relevant to the non-linear elastic damage algorithm presented on Table 31. A displacement controlled based on the rate-independent elastic damage routine as introduced in the previous examples (see Box 1, Box 2 and Box 3.)

Table 31: Algorithm configuration

Description
Total displacement enforcement $u = 2.25 \times 10^{-4}\ (m)$
Average displacement increment = $1.3543 \times 10^{-5}\ (m)$
Tolerance = 10^{-6}
Total increment = 15
Maximum number of iteration in each increment = 500

In addition to the afore-mentioned information relevant to the LEDM procedure, it is necessary to indicate the features of the localized damage model used in the LEFM process.

The optimized values demonstrated on Table 26 are also useful here. Hence the 3rd -order weight function with regard to $n_p = 0.8$ are considered here, as well as for proceeding the localized damage concept, based on the theory and equations introduced in Section 4.3.

In this study, distinct regular discretizations are considered as shown in Figure 110.

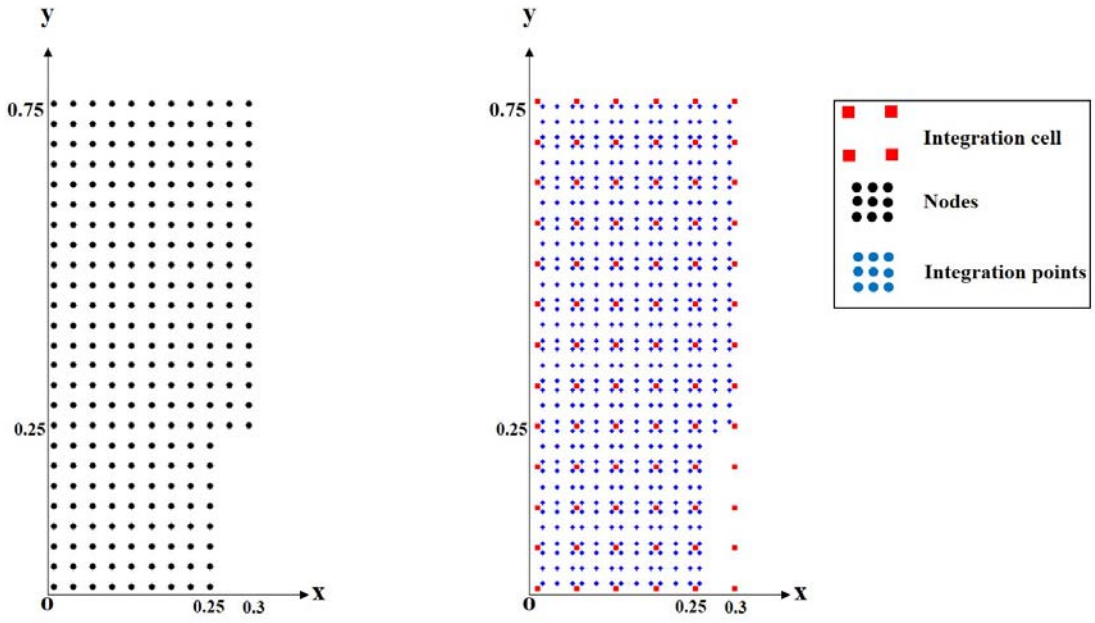

(a)

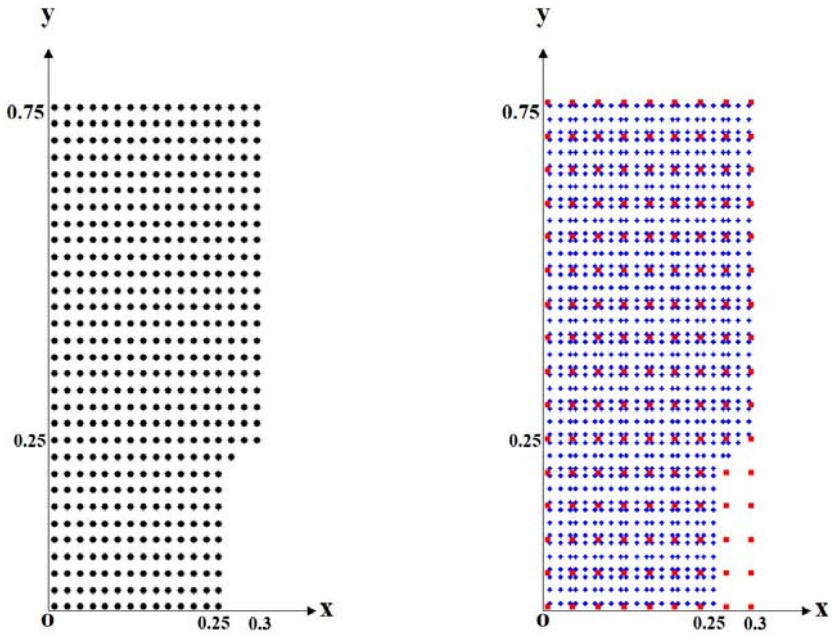

(b)

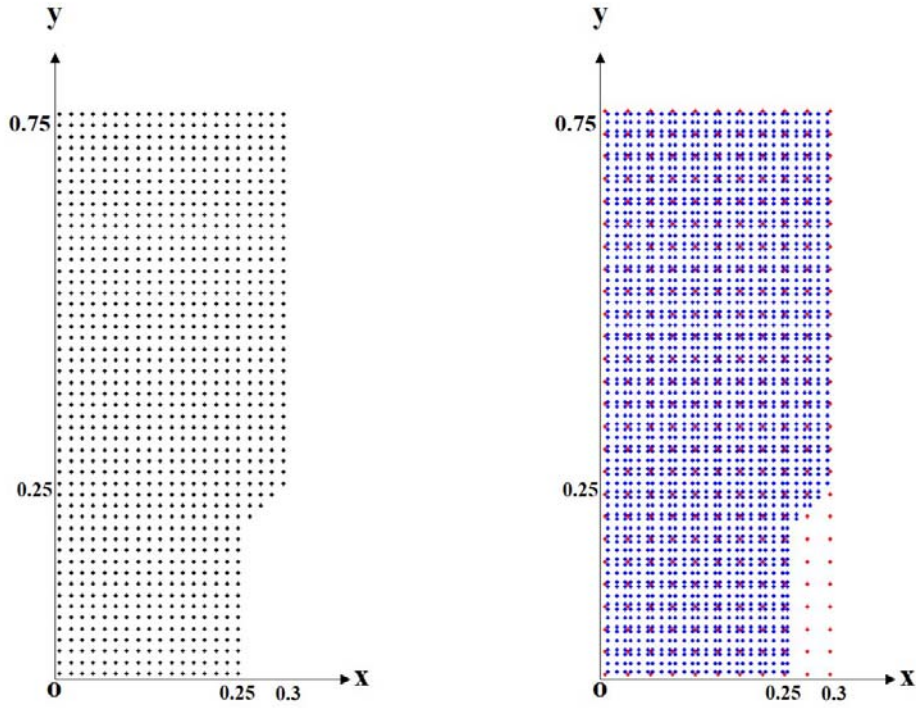

(c)

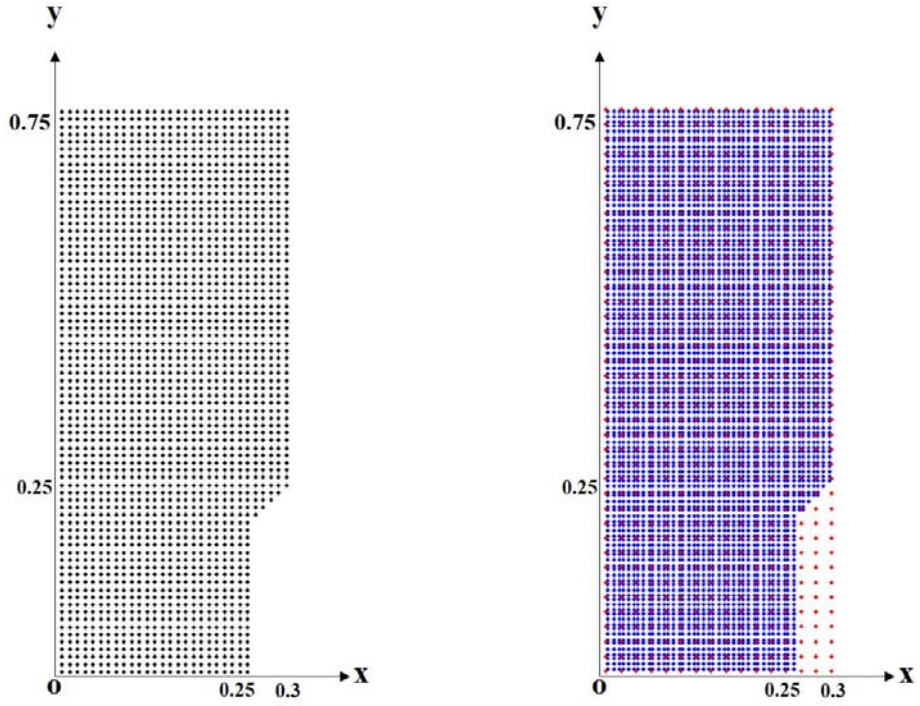

(d)

Figure 110: Different regular discretizations used in the compact tension test (a) 1st pattern, (b) 2nd pattern, (c) 3rd pattern and (d) 4th pattern

Consider Figure 110, the properties relevant to each discretization pattern is represented on Table 32. In addition to that all RGP values used in this analysis are introduced on the mentioned table.

Table 32: Properties for the discretizations in the compact tension specimen analysis

Discretization	Divisions along x	Divisions along y	Number of nodes	Number of integration points	RGP
1st pattern	11	25	259	517	0.0240 (m)
2nd pattern	17	31	498	1025	0.0150 (m)
3rd pattern	21	51	1009	2138	0.0120 (m)
4th pattern	30	76	2165	4887	0.0083 (m)

In accordance with Table 32, to obtain the localized damage parameters (*RGP* and *h*) for this study, Equations (113-a, b) are adopted as follows:

$$h = \frac{L/_2}{divisions\ along\ x}$$

$$RGP = n_p h = 0.8 * h$$

where only half of the total length is considered due to the symmetric geometry. Therefore, the computed results are demonstrated on Table 33.

Table 33: Variation of h and RGP for compact tension specimen

Discretization	Divisions along x	Divisions along y	n_p	*h (m)*	*RGP (m)*
1st pattern	11	25	0.8	0.0300	0.0240
2nd pattern	17	31	0.8	0.0187	0.0150
3rdpattern	21	51	0.8	0.0150	0.0120
4th pattern	30	76	0.8	0.0103	0.0083

Until here, all the initial information required for the analysis has been introduced, now it will be briefly described the objectives:

1- Verify the experimental curve of load *Q* versus hole mouth opening *q* reported by (Legendre, 1984) and (Mazars & Pijaudier-Cabot, 1996) in Figure 111 ;

2- Measure of the equivalent crack length (*a*) at a certain point *B* discussed next with regard to the numerical solution presented by (Mazars & Pijaudier-Cabot, 1996).

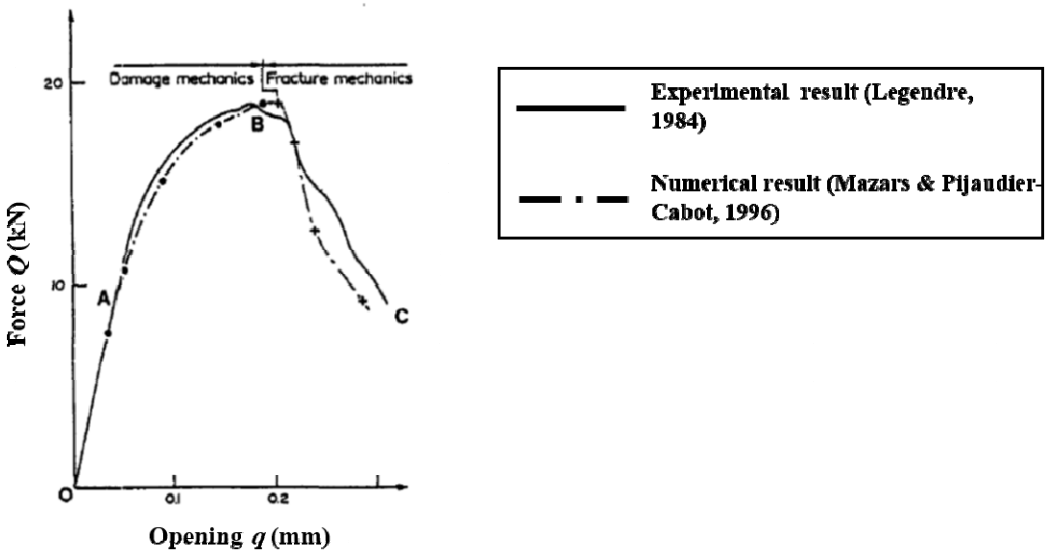

Figure 111: The global behavior of the compact tension test performed from damage to fracture (Mazars & Pijaudier-Cabot, 1996)

It is possible to perform the analysis of various regular meshes shown in Figure 110 based on the geometry and essential boundary conditions indicated in Figure 109. First, a convergence study should be conducted on these distinct discretization patterns to observe the global behaviour of the material in the elastic, damage (LEDM) and fracture mechanics (LEFM).

The response of horizontal force *(Q)* correlated with of the mouth opening of the hole *(q)* for different regular nodal distributions on compact tension test compared to the experimental solution is presented in Figure 112.

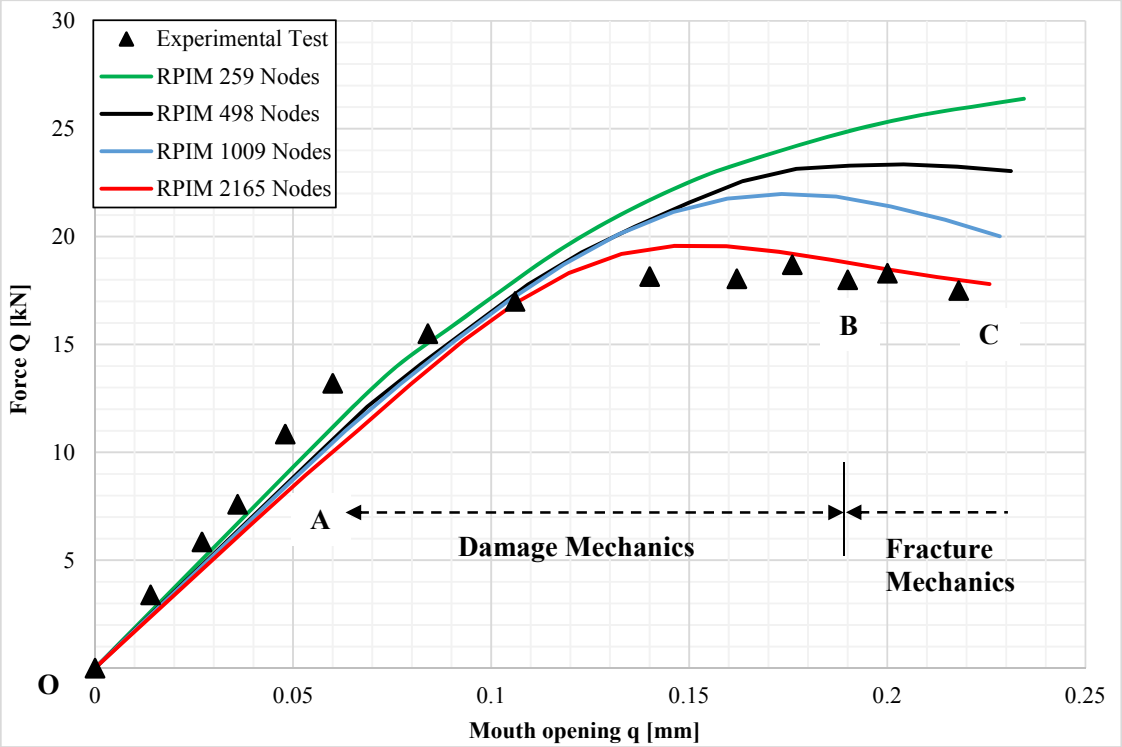

Figure 112: Response of load versus mouth opening obtained for different meshes compared to experimental curve (Mazars & Pijaudier-Cabot, 1996)

Figure 112 indicates that the accuracy of the RPIM increases when the denser discretization is considered. Thus, as a resume, the suitable solution is obtained where the mesh includes 2165 nodes in RPIM formulations (the divisions are 30 and 76 along *x* and *y* directions respectively).

As shown in Figure 112, the global behaviour of the compact tension test under compressive displacement enforcement is divided in the following stages:

First of all, the material experiences a linear elastic behaviour (*OA* line). After that, the material initiates to get softer so that the stiffness is decreasing. It means that the material is encountering linear damage mechanics with micro cracks while the macro cracks have not been yet created, *AB* curve. At the end, the material undergoes to the linear fracture mechanics, where the micro cracks evolve to the macro cracks (*BC* curve).

In the last stage, some parts of material have been already damaged and probably the existing cracks initiate to propagate along the *Oy* direction. Hence the failure of the structure might be predicated after.

It is important to mention that the non-local damage algorithm is applied on LEDM (see Box 2) while the localized damage routine (Box 3) is used to evaluate LEFM in the material, which are as *OB* and *BC* curves, respectively.

7.3.1 Assessment on Point B

Based on the observation reported by (Legendre, 1984) and (Mazars & Pijaudier-Cabot, 1996), there is an interface point between LEDM and LEFM known as *point B* (see Figure 112). It is possible to infer that the damage parameter accounted for the maximum value at this point (*d=1*). This point provides some important information and features related to the damage and fracture phenomena. It is visible from Figure 112 that point *B* is identified in the numerical curve with the following components:

$$B = (q_B, Q_B) \cong (0.195\ (mm), 18(kN))$$

The obtained results from RPIM analyses regarding the value of horizontal force at point *B* is shown on Table 34.

Table 34: The RPIM result of force at point B obtained for different discretization patterns compared to the experimental one

Number of nodes	Number of integration points	Experimental value [kN]	RPIM value [kN]	Error %
259	517	18	24.7783	37.66
498	1025	18	23.2946	29.41
1009	2138	18	21.6282	20.16
2165	4887	18	18.7602	4.22

Since point *B* is located between damage and fracture states meaning that the material has already had some micro cracks, so it is possible to measure the equivalent crack length *(a)*. Hence it is required to obtain this value for the RPIM analyses as presented on Table 35. Numerical value *($a = 0.13\ m$)* has been reported by (Mazars & Pijaudier-Cabot, 1996).

Table 35: The equivalent crack length (*a*) obtained from damage profile for different discretization patterns at point B

Number of Nodes	Number of integration points	Experimental value [m]	RPIM value [m]	Error %
259	517	0.13	0.0573	55.92
498	1025	0.13	0.0847	34.85
1009	2138	0.13	0.1048	19.38
2165	4887	0.13	0.1331	2.38

According to the results presented on Table 35, it is important to mention that the more accurate value, belonging to the equivalent crack length, is achieved when the discretization contains 2165 number of nodes. Indeed, Figure 113 demonstrates the variation of the equivalent crack length in terms of the mesh size compared to the experimental solution (Legendre, 1984). This diagram clarifies the concept of equivalent crack length in relation with the number of nodes in RPIM formulations.

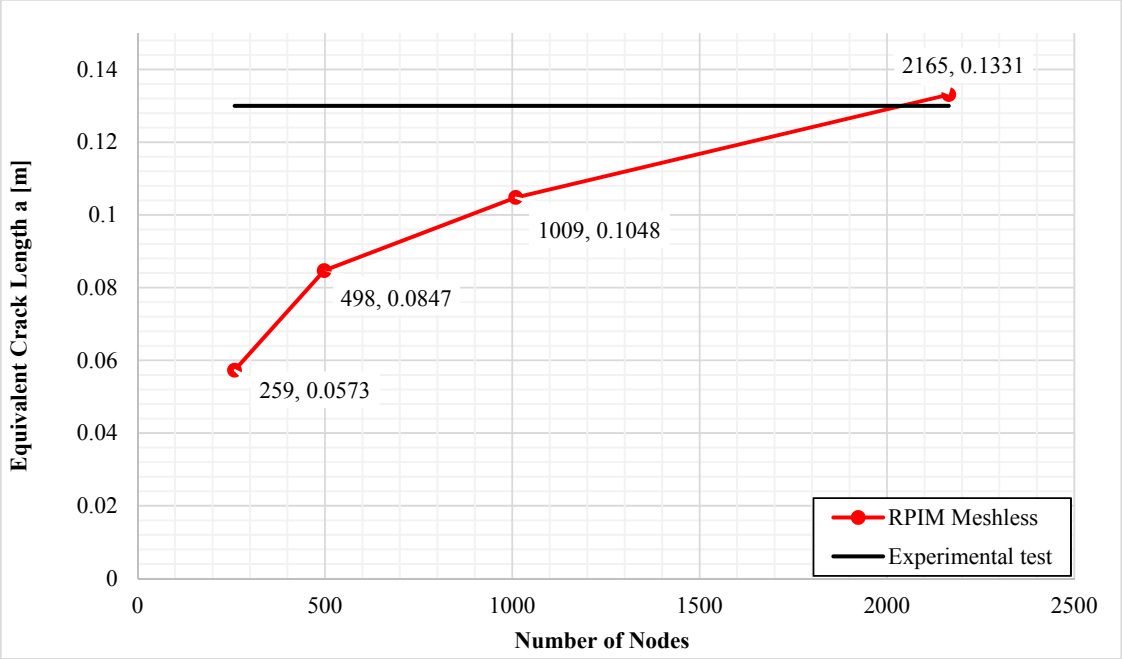

Figure 113: The variation of equivalent crack length at point *B* obtained for all regular patterns

It is observable form the above figure that the solution is converging when the number of nodes is equal to 2165. In addition to the aforementioned explanation, it is possible to verify the experimental value of equivalent crack length using the distribution of the damage

parameters on the specimen at point *B*. Hence, the profiles of the tensile, compressive and total damage variables for all the regular RPIM studies are demonstrated in the next plots.

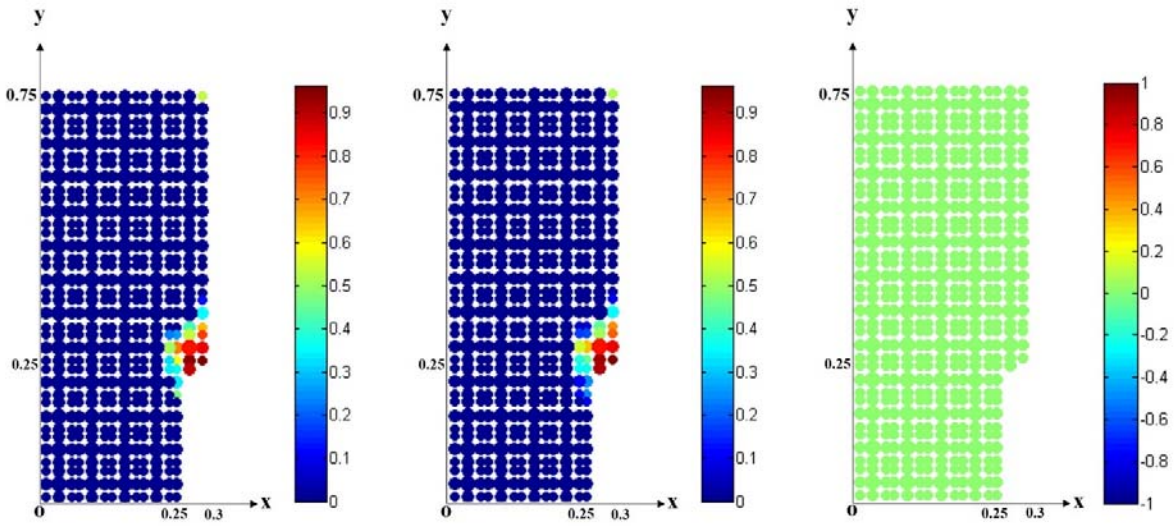

(a) (b) (c)

Figure 114: Distribution of damage for 259 nodes at point B; (a) total damage, (b) tensile damage and (c) compressive damage

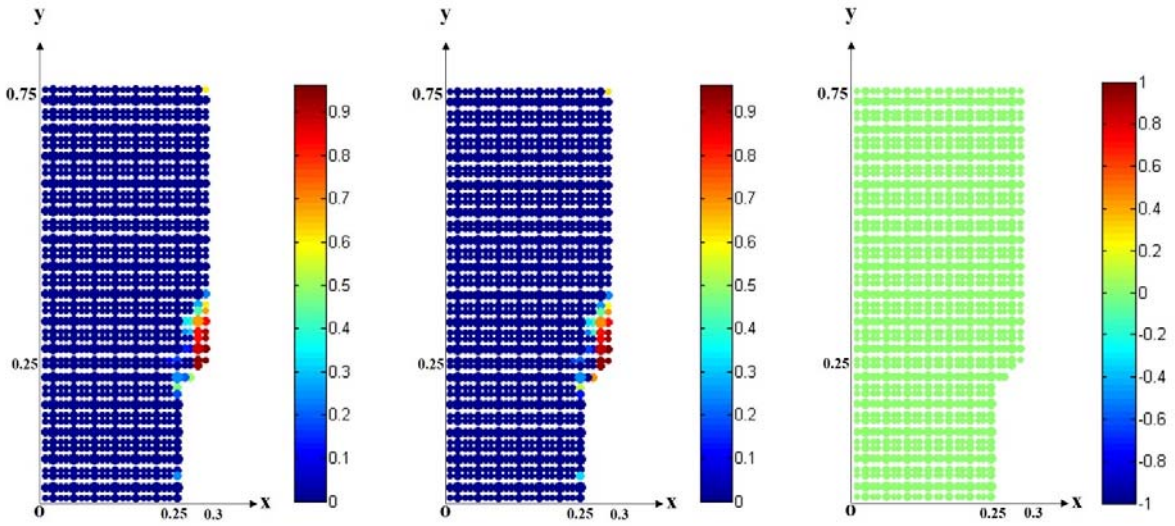

(a) (b) (c)

Figure 115 : Distribution of damage for 498 nodes at point B; (a) total damage, (b) tensile damage and (c) compressive damage

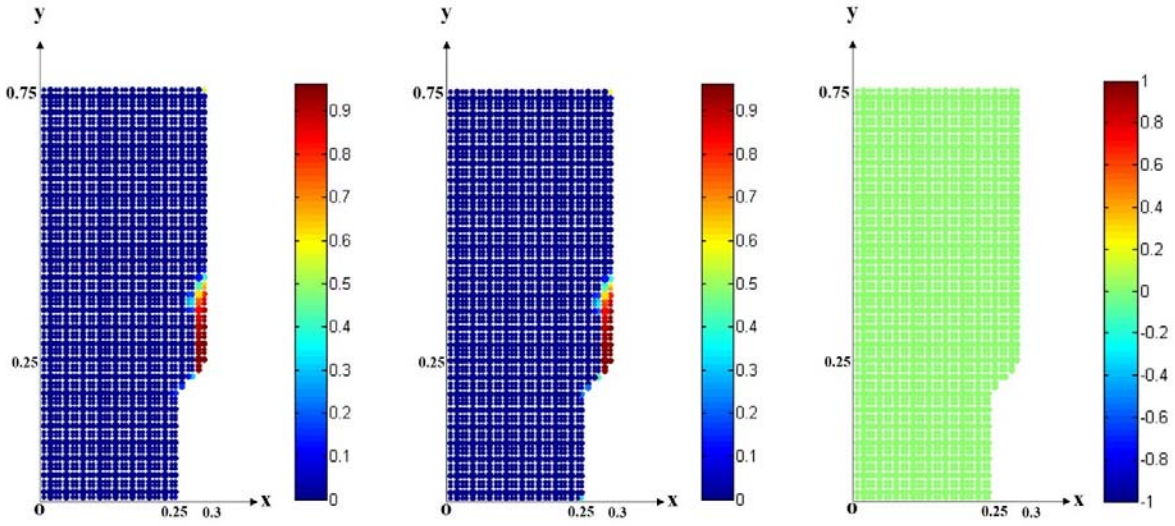

(a) (b) (c)

Figure 116: Distribution of damage for 1009 nodes at point B; (a) total damage, (b) tensile damage and (c) compressive damage

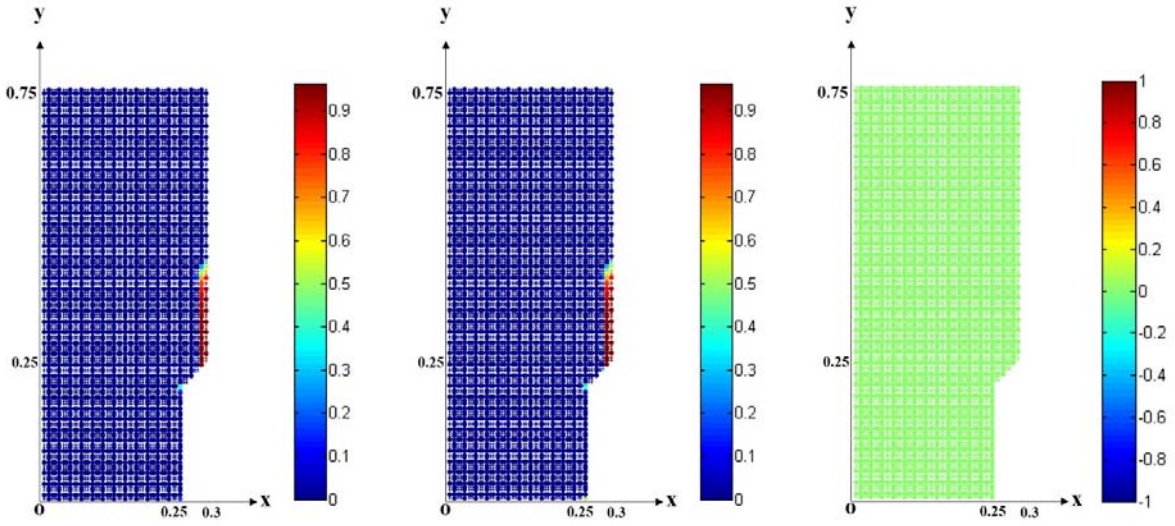

(a) (b) (c)

Figure 117: Distribution of damage for 2165 nodes at point B; (a) total damage, (b) tensile damage and (c) compressive damage

Figure 114, Figure 115, Figure 116 and Figure 117 were obtained for the damage parameters for different regular discretizations at point *B*.

It must be remarked that there is no compressive damage in all discretization patterns. This matter is related to the high value of the maximum uniaxial compressive strength. This high value permits the material to resist against the compressive effect strongly.

Therefore, the material is only influenced by the tensile damage. So, the total damage is the same as the tensile one.

7.3.2 Graphical Representations of Internal Variables

It is possible to present the variation of the internal variables such as effective total stress and damaged stress. The latter one is also identified as the Cauchy elastic stress tensor. However, only the results related to the densest discretization with 2165 node corresponding to the regular study (corresponds to the discretization presented in Figure 110-d).

It is also essential to mention that all the values are computed in the form of equivalent Von mises stress based on Equation (51).

In fact, the program is enable to produce all the stress profiles at the end of each increment of displacement enforcement. Since there are 15 increments considered here, it is extra details if we present all of them, hence only some essential profiles of stress (in some displacement enforcement increments shown on Table 36) will be presented in the following Figure 118, Figure 119 and Figure 120. These figures have the potential to indicate the progress of the process in pseud time stepping scheme.

It is important to mention that all the stress profiles are mapped on the integration points (Gauss Points) due to the nature of the RPIM formulation.

Table 36: The displacement enforcement value in relation with the increments

Increment	**2nd**	**8th**	**14th**
Displacement enforcement (mm)	5.3182E-02	1.32831E-01	2.12529E-01

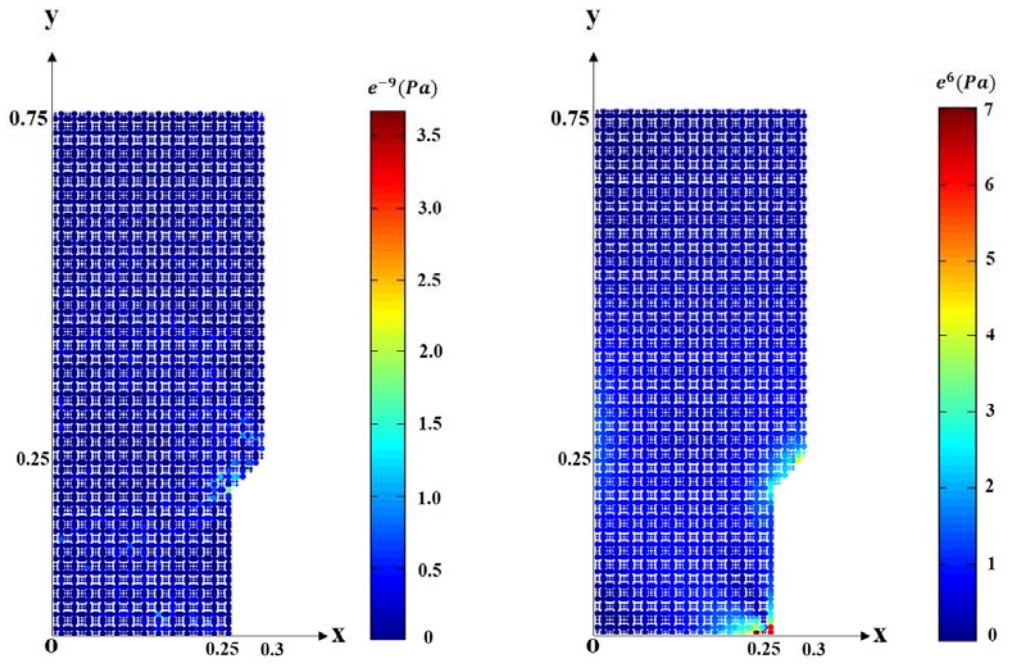

(a) (b)

Figure 118: Equivalent Von-mises Stress profile on compact tension specimen for 2165 nodes at the 2nd increment (a): damaged state and (b) total state

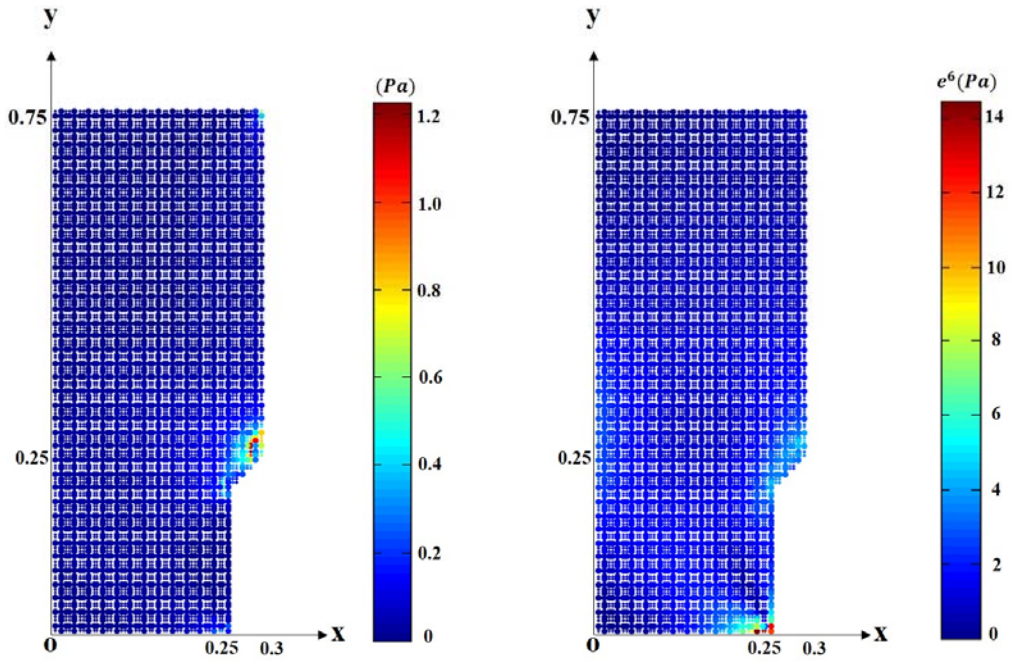

(a) (b)

Figure 119 : Equivalent Von-mises Stress profile on compact tension specimen for 2165 nodes at the 8th increment (a): damaged state and (b) total state

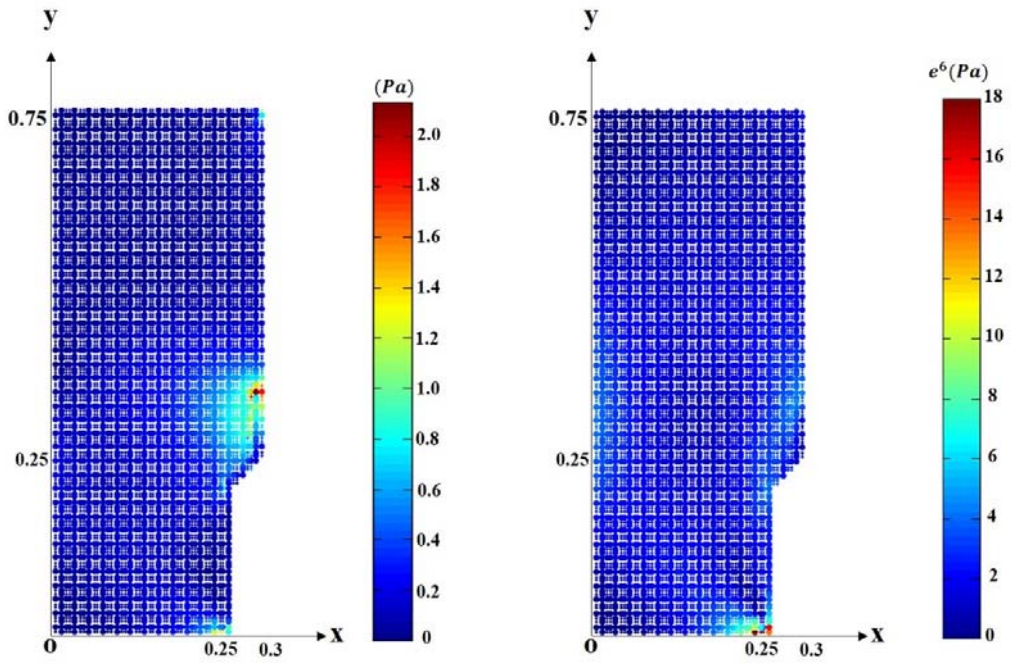

(a) **(b)**

Figure 120: Equivalent Von-mises Stress profile on compact tension specimen for 2165 nodes at the 14th increment (a): damaged state and (b) total state

The stress maps indicate that the damage initiates from the tip of the hole, where the crack is propagated from.

On the other hand, the value of the total elastic stress (see the legend bar on Figure 120-b) reaches the maximum amount of $\tilde{\bar{\sigma}} = 18\ (Pa)$ which is located between the maximum uniaxial tensile and compressive strengths, therefore;

$$f_0^+ < \tilde{\bar{\sigma}} < f_0^- \xrightarrow{so\ that} 4.2435 \times 10^6\ (Pa) < 18 \times 10^6\ (Pa) < 29 \times 10^6\ (Pa)$$

Meaning that the material does not reach the maximum uniaxial compressive. That is why no compressive effects are observed in this analysis and the compressive damage remains for zero value during all the increments.

Taking account into the theory of continuum damage mechanics, the aforementioned issue is typically normal in concrete structures, because they are known due to their high compressive resistance.

Regarding the localized damage parameters as introduced previously, it is possible to produce the damage parameters in terms of effective strain (should be computed on equivalent von Mises state, Equation (53)) to distinguish the difference between non-local damage and localized one. Therefore, it is necessary to choose a specific Gauss point (integration point) in the critical zone and then plot the damage variables on in the both non-local and localized states.

Considering the results obtained for this study, it has been proved that the crack is forming in the material during the displacement enforcement stages. Thus, the best position is near crack tip zone (yellow highlighted area in Figure 121). Indeed the corresponding critical Gauss point has been selected as gp_c (see Figure 121).

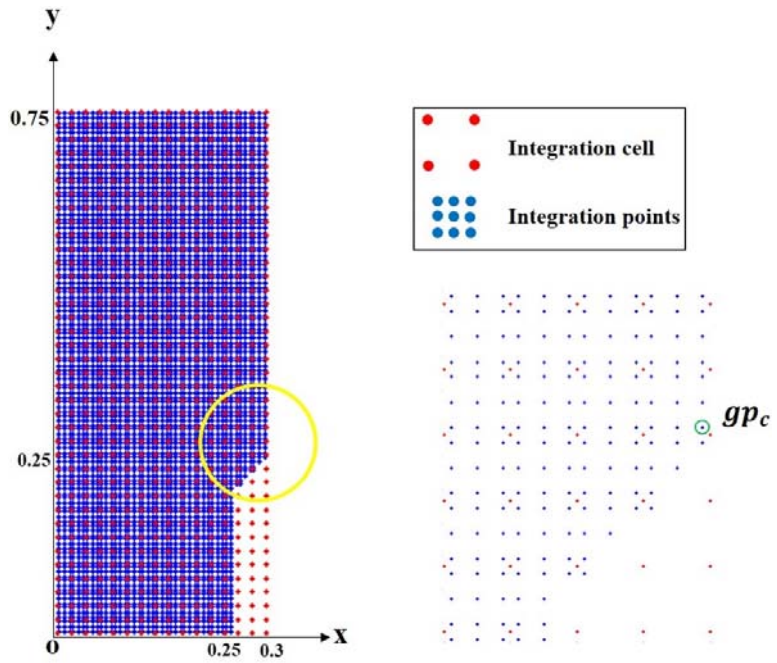

Figure 121: Detection of the critical integration point gp_c in the compact tension test

As shown in Figure 121, the yellow highlighted area is related to the place that the crack is almost situated at. If the yellow area is magnified, it is possible to observe the corresponding integration point that the damage variation is going to be measured on. Selecting this point as the studied one for damage parameters in terms of effective strain allows us to observe the evaluation of damage from the beginning of the process.

Following the afore-mentioned description, the variation of damage parameter in terms of equivalent strain is plotted in Figure 122.

It is nothing worth to mention that the compressive damage does not appear in the evaluation since it is equal to zero during the procedure.

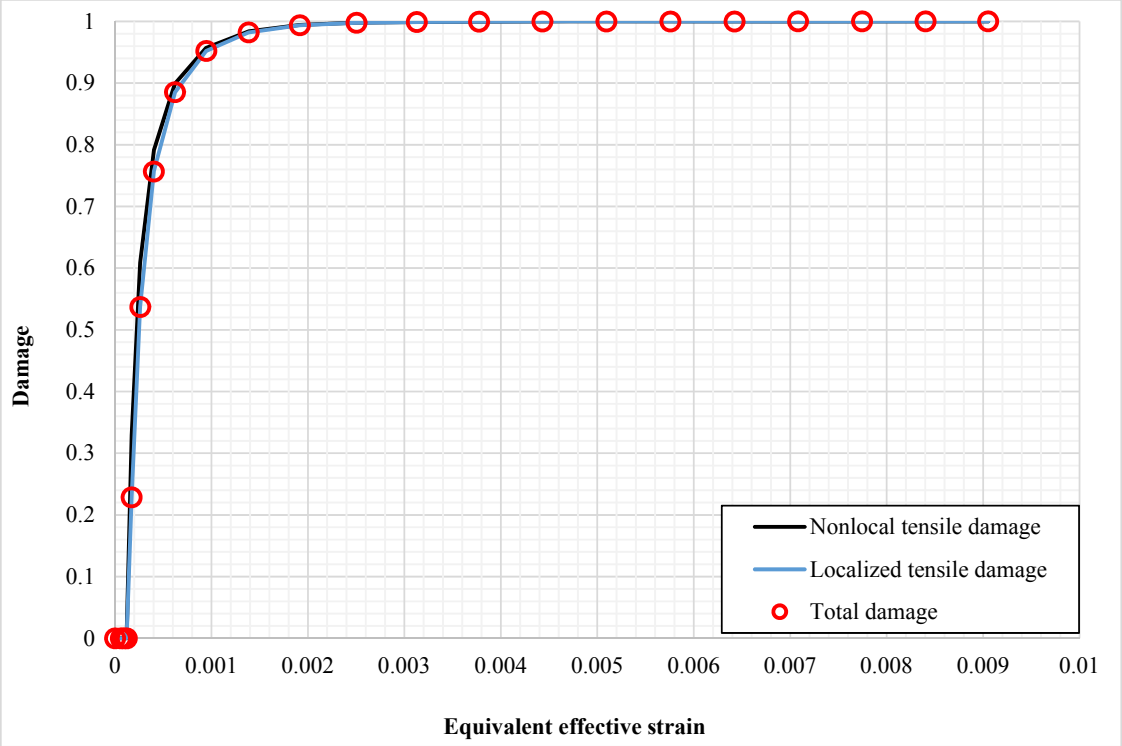

Figure 122: the damage evolution on gp_c obtained for non-local tensile, localized tensile and total damage when the RPIM discretization contains 2165 nodes

Figure 122 demonstrates the damage evolution in terms of effective strain with regard to the non-local and localized aspects.

It is essential to indicate that the objective of the localization is to smooth the damage by sharing the damage value of an interest point with the other points around (they are located inside the circle with the radius of RGP). Hence the localized damage trend must be smoother than the non-local behavior. According to Figure 122, this phenomenon is almost satisfied. Although the variation is not that much high, the curve related to the local tensile damage accounted for the slower slope compared to the sharp slope of the non-local curve

(the black and blue curves respectively). As a final remark, the curve indicated with the red circles is relevant to the total damage which is the same as the localized tensile damage. It has a good agreement with the target of the damage localization. Since tensile damage variable has been smoothed with regard to the zero value of the compressive one, the total damage is derived only form the tensile one and they should be the same. So, the localized damage algorithm was successfully applied, showing a very good agreement.

7.3.3 First Study on the Irregular Mesh

This part is devoted to the random arrangement of the nodes. As it was mentioned before (Sections 5.1.4 and 7.2.4.2), there are some aspects that should be described in advance.

First of all, the specimen is discretized into divisions along each direction (x and y) accounted for the same values as it was finalized for the regular study (30 by 76). So, the regular discretization is formed containing 2165 nodes and 4887 integration points. Afterwards the nodes are arranged randomly in accordance with the chosen irregularity parameter (λ) as introduced in Equation (126). This parameter controls the irregularity and affects the solution significantly. Thus it should be chosen carefully.

So, it is better to start with a small value of λ to achieve a proper irregular mesh (see Figure 13). The irregularity parameter is chosen as $\lambda = 10$ .Indeed, the geometry of the compact tension test with the irregular discretization is shown in Figure 123.

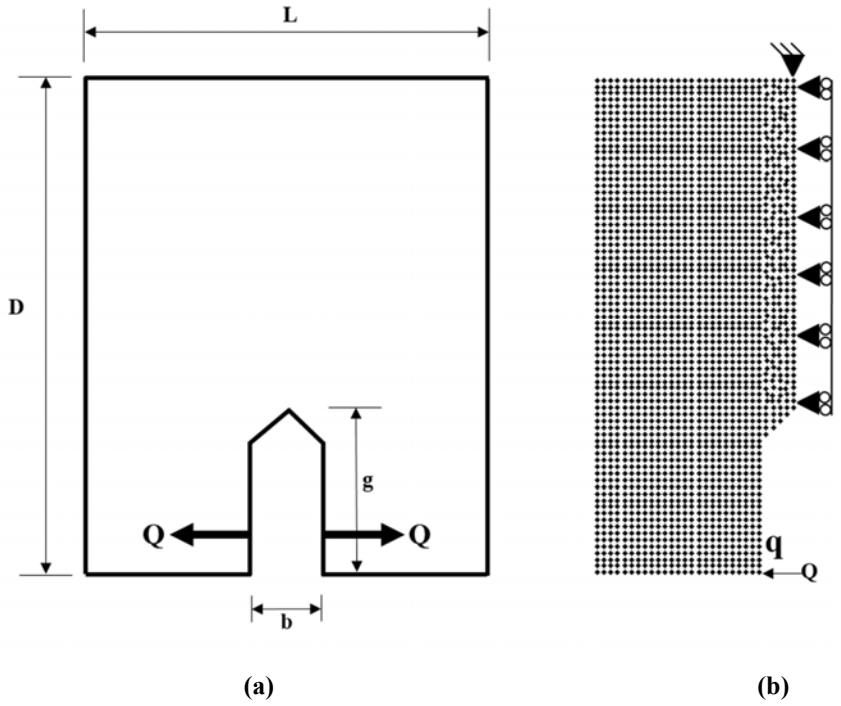

Figure 123: Compact tension specimen: (a) Geometry and (b) Irregular mesh when $\lambda = 10$ and essential boundary conditions

Figure 123-a demonstrates the geometry of the compact tension specimen. Figure 123-b shows the irregular discretization with regard to $\lambda = 10$. It is visible from the figure that the irregular effect is only applied on the right side of the specimen due to the prediction of the crack propagation in this zone. In fact, this area could be called the critical location in the perspective of the presence of micro and macro cracks after. Hence the critical area covers all the nodes situated along the hole directions from its tip to the top edge of the specimen. Indeed the geometric and material properties are presented on Table 28 and Table 29, respectively. Moreover, the damage characteristics and algorithm configurations are introduced on Table 30 and Table 31.

In accordance with Table 33, the amount of *RGP* in the case of localized damage state is *RGP* = 0.0083 (m).

The results regarding the horizontal load (Q) in terms of mouth opening of the hole (q) are obtained. Since the more accurate results of irregular study is obtained when several analyses studies, it will be done for 11 times with the fixed properties as shown in Figure 124.

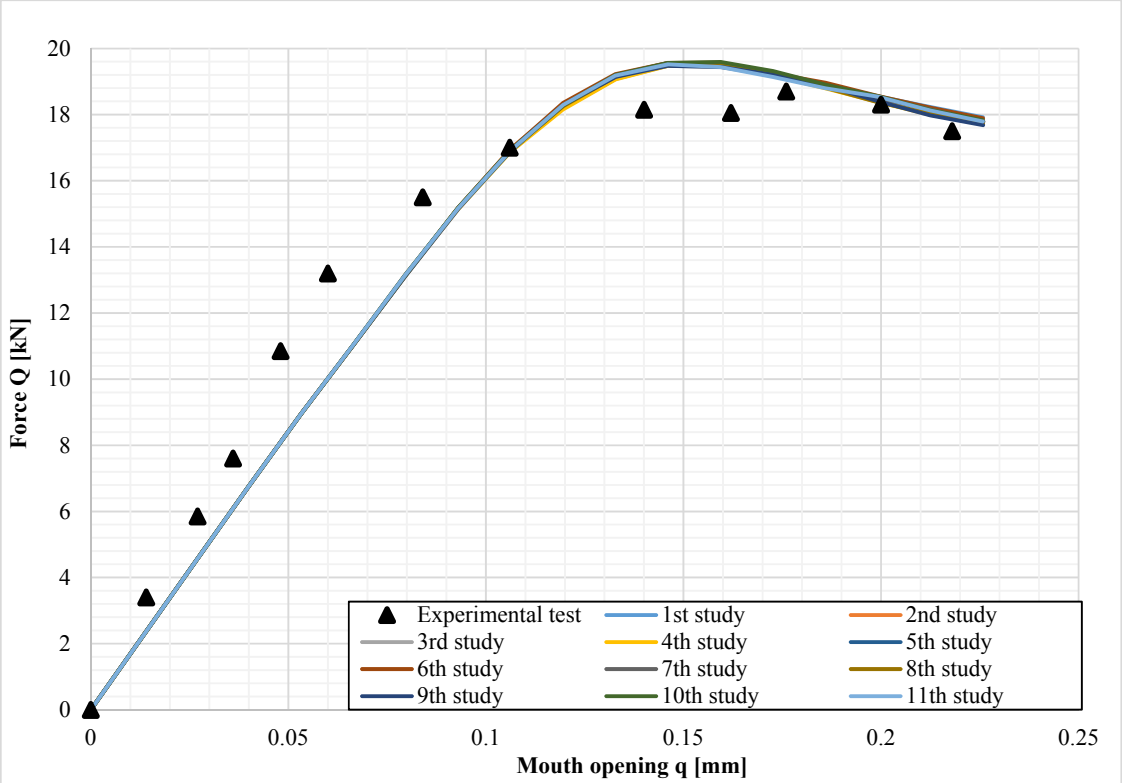

Figure 124: Study of the irregular mesh obtained for the response of load Q- mouth opening q in RPIM for compact tension specimen - localized damage formulation

Figure 124 indicates that the RPIM curves agree in an acceptable way with the experimental solution which proves the proper performance of the localized elastic damage algorithm within RPIM formalism.

Consequently, it is possible to take the average from the 11 irregular results and then compare to the similar regular solution and most importantly with the experimental result as illustrated in Figure 125.

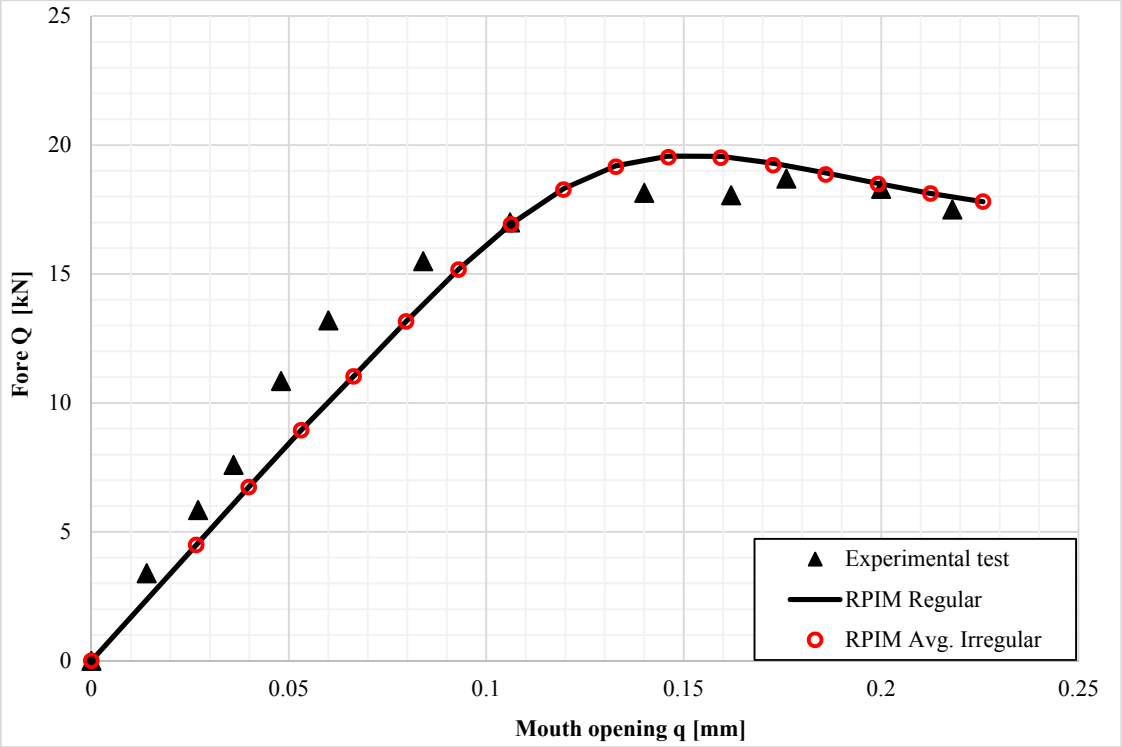

Figure 125: The response of load- mouth opening in compact tension test obtained for regular and average irregular results compared to experimental one, $\lambda = 10$

As seen in Figure 125, the regular and irregular curves undergo almost the same trend and they agree well with the experimental result particularly from damage to fracture mechanics.

It must be remarked that the regular curve has been extracted from Figure 112.

In order to verify the functionality of irregular study in the RPIM formalism extended to elastic damage and fracture mechanics for a particular case of localized damaged parameter, it is possible to study another irregular case of compact tension test.

7.3.4 Second Study on the Irregular Mesh

To finish the irregular study, another analysis is considered here with a change in irregularity parameter. It is noticeable to mention that all the parameters and properties are the same as previous example (Section 7.3.3) while the irregularity parameter is decreased to $\lambda = 5$. Hence more irregular arrangement of the nodes should be obtained. The

geometry and the nodal discretization with the essential boundary conditions of this example are illustrated in Figure 126.

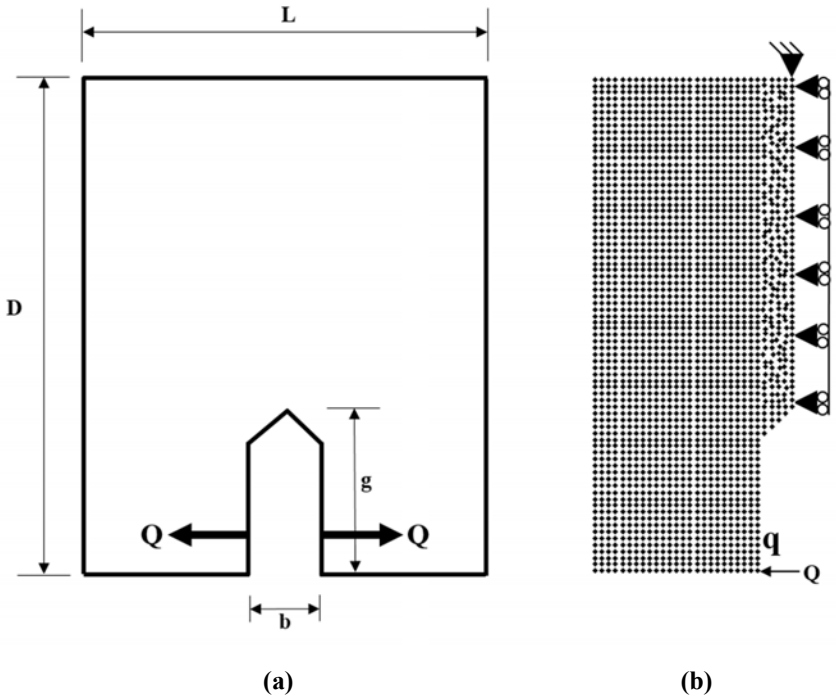

Figure 126: Compact tension specimen: (a) Geometry and (b) Irregular discretization when $\lambda = 5$

As it is visible in Figure 126-b, a more irregular nodal arrangement is obtained due to decrease of the irregularity parameter. The analysis is performed and the obtained response of *Q*-*q* for the new irregular case is captured. Then, there will be a comparison between the current result and all the others (previous irregular, regular and experimental test) shown in Figure 127.

Regarding Figure 127, it should be noted that curves related to irregular 1 and 2 are associated with the analyses if $\lambda = 10$ and $\lambda = 5$ respectively. Consequently, changing in the irregularity parameter does not affect the final solution significantly and the obtained results for both irregular cases have a good agreement with the regular and experimental solution (Mazars & Pijaudier-Cabot, 1996).

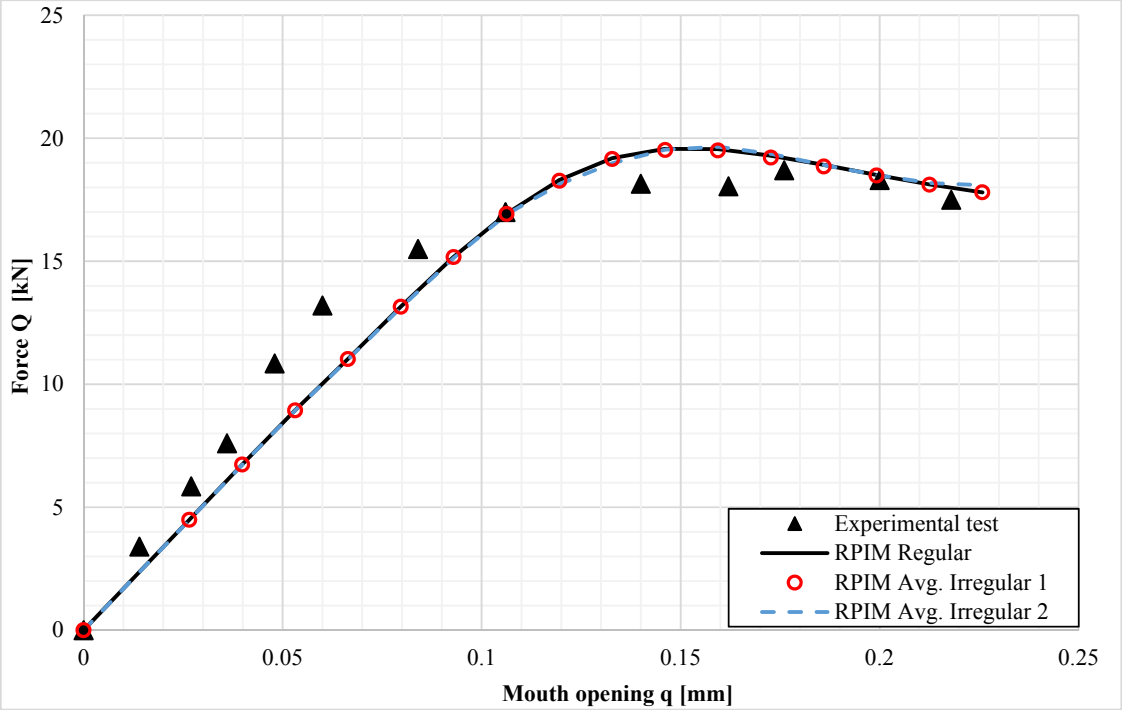

Figure 127: Results of load vs. mouth opening for irregular mesh obtained for different irregularity parameters compared to the regular result and experimental test

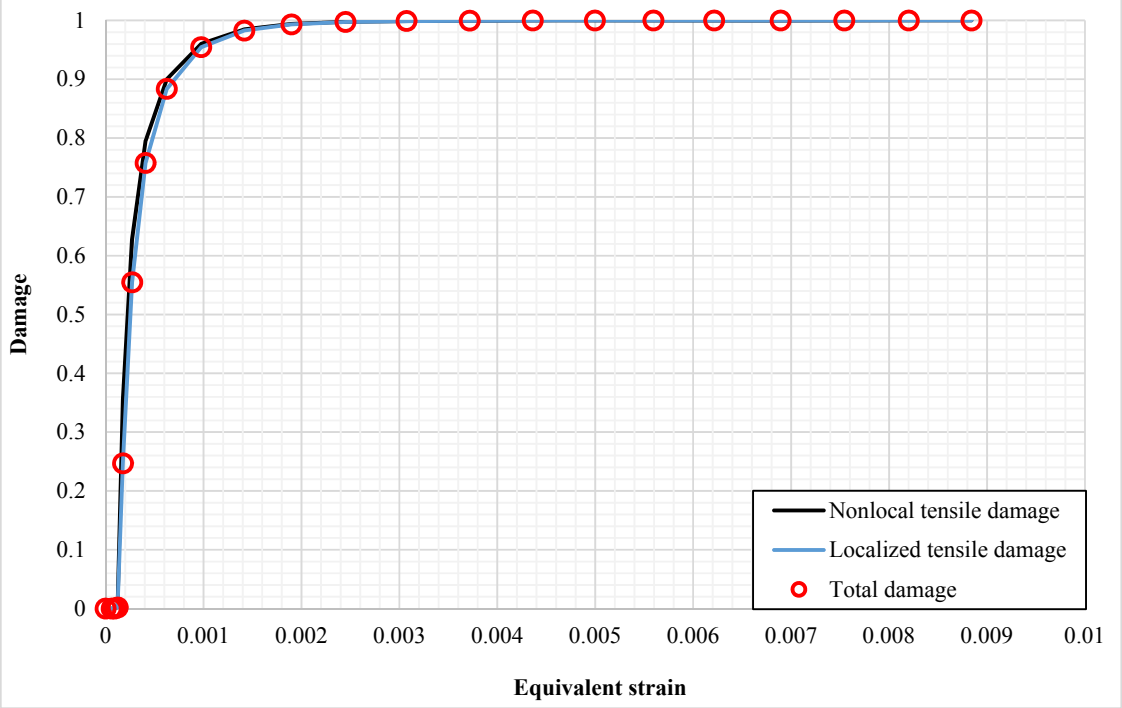

Figure 128: Damage evolution at gp_c obtained for non-local tensile, localized tensile and total damage in the second irregular mesh ss

Considering all irregular analyses, it is rational to conclude that this RPIM study is not significantly sensitive to the irregularity parameter.

It is possible to put the attention to the evolution of damage variables at the critical integration point gp_c(as shown in Figure 121) in terms of effective strain, Figure 128.

Figure 128 demonstrates the diagram of damage parameter in terms of equivalent strain (Computed from von Mises equivalent strain presented in Equation (53)) when the irregular mesh with $\lambda = 5$ is considered. The observation and clarification of this plot is the same as the one for Figure 122.

As a resume of the irregular studies, it is possible to conclude that the RPIM solution is not significantly sensitive to the irregularity parameter and both obtained results for *Q*-*q* agree well with the experimental solution (Legendre, 1984).

Chapter 8

8.1 General Conclusions

In this work the Radial Point Interpolation Method (RPIM) was presented and developed.

First the RPIM formulations were extended to the analysis of circular plates using a 2D axisymmetric deformation theory. It was found that the construction of the background integration cell should respect the construction 3×3 integration points inside each integration cell. This construction allows to obtain solutions showing acceptable errors (below 0.8%) without increasing significantly the computational cost of the analysis.

Concerning the influence-domain size, the obtained results indicate that the influence-domain of each interest point $\boldsymbol{x}_I$ should be formed with the closest $N_I = 20$ nodes, following a radial search.

Additionally, this present work shows that the RPIM axisymmetric formulation possesses the final converged value which is consistently accurate. The distinct relevant benchmarks were analysed. It was verified that the RPIM provides precise results regardless the thickness of the studied plate or the kind of the applied load or displacement constrains in the plate edge. The obtained stress profiles indicate that the RPIM, despite the lack of the compatibility property, is capable of producing smooth stress fields.

Second, the RPIM formalism was extended with a non-local damage mechanics theory which the non-linear analysis of damage in concrete structures are formulated within a rate-independent constitutive elastic damage model. The return-mapping damage stage permits to obtain the required internal variable fields such as damage variables, stress and strain tensors and, most importantly, the displacement field. The enforced displacement is applicable for both compressive and tensile states and the algorithm evolves through a

pseudo-time stepping scheme. Furthermore, the damage criteria relies on a Helmholtz free energy function connected to the fracture energy release. Some of the advantages of the proposed methodology are: (a) it uses the principal effective stress instead of general stress tensor which permits to eliminate the repetitive computations; (b) the non-linear behaviour of concrete structures can be studied using the isotropic damage model here implemented, in both tensile and compressive loadings separately (c) Since the proposed approach is explicit, it seems suitable for micro-scale study of concrete structures; (d) the methodology is not sensitive to the nodal discretization and it is capable to produce accurate and stable results with irregular nodal distributions.

8.2 Discussion of the Obtained Results

Considering the numerical benchmarks, it is concluded that the proposed return-mapping damage algorithm has the potential to provide results very close to FEM and experimental solutions; it was enhanced the higher accuracy of RPIM with regard to FEM for the different discretizations.

Additionally, this work studied some parameters characterising the damage phenomenon under tensile and compressive enforced displacement, which control the stress-strain response and particularly the load *P*- deflection on point *A* trend. As introduced before, they are known as A^+ in tension and A^-, B^- in compression. According to the captured results, these parameters influence significantly the results. The variation of these parameters modify the peak value of the stress and the load. Furthermore, they have the potential to change the damage behaviour after reaching the mentioned peak values. Some particular values of A^+ , A^-, B^- could force the solution to reach the failure sharply. On the other hand, changing the values of these parameters permit to smooth the stress-strain curve, which was observed in the biaxial and uniaxial tests. In this work, the optimum values of these parameters were considered based on the literature. Additionally, this work provided a simple equation to calculate efficiently the characteristic length in meshless methods.

Also, the return-mapping non-linear elastic damage algorithm is developed to the localized damage formalism. The analysis of three point bending beam subjected to the compressive

enforced displacement was done using the RPIM formulations, to implement the rate-independent elastic damage mechanics for concrete material for the normal RPIM discretization as presented with regard to the damage localization formalism. Since the obtained results were far away from the experimental one (Malvar & Warren, 1988), a refined nodal distribution has been proposed for three point bending beam. Consider three different refined discretizations patterns, it purposed to obtain: (1) the optimum values of damage localization parameters such as n_p, the weight function order and $A^+$and (2) the more accurate result in the presence of the irregular nodal distribution. Following the objectives, the convergence studies have been performed on the three RPIM discretization patterns. Consequently, the optimum values of damage localization variables have been determined as $n_p = 0.8$, $A^+ = 0.001$ and the 3rd order weight function.

After that, consider the optimized localized damage parameters, a denser discretization is analyzed to evaluate the performance and efficiency of the algorithm. It was discretized for 81 by 21divisons long *x* and *y* including 2941 and 6300 number of nodes and integration points respectively where the obtained results possess a good agreement with the experimental solution proposed by (Malvar & Warren, 1988).

Subsequently, the variation of non-local tensile, localized tensile and total damage at the specific integration point known as gp_c agreeing very well with the theory of localization phenomenon (Jirásek, 1998). Afterwards, several graphical representations of the internal variables such as total and damaged stress fields in addition to the damage contours have been captured for various enforced displacement stages.

Considering the optimum values of the localized damage parameters obtained for the regular discretization, the RPIM irregular analysis has been performed to observe the behavior of the algorithm in the presence of the random nodal distribution. Subsequently, the results have been obtained for 7 basic responses of load versus deflection. In the next step, the average of irregular results has been compared to the similar regular and experimental solution. Since the 7 basic irregular results overlap the experimental one after peak load, it was recommended to rearrange the nodal discretization for three nodes situated at the crack tip. Hence the irregular analysis has been performed again for the modified nodal discretization. Other 7 basic responses of the load-deflection have been

obtained. Consequently, the variation of the curve around the peak load has been eliminated significantly. Thus, the last irregular results agree in an acceptable way with the experimental curve. Therefore, the objectives of the study have been gained and the three point bending beam test with regard to the localized damage formalism finished here.

As a final remark, it must be noted that the RPIM formulations extended to the continuum damage algorithm performs very well in the presence of the localized damage formalism and it gains accurate results for both regular and irregular discretizations. In addition, the profile of stress and damage variable experience smooth trends.

Finally, with regard to the localized damage formalism, another benchmark has been studied known as compact tension test. It was required to obtain (1) the horizontal force in terms of hole mouth opening in the presence of the compressive displacement enforcement and (b) the equivalent crack length where the macro cracks are formed in the interface between damage and fracture states. In order to gain the objectives, several distinct RPIM regular discretizations have been used to evaluate the performance and efficiency of the algorithm to obtain the more accurate results.

Within the convergence studies on the discretization size, the response of load-opening has been verified though using the densest discretization with 2165 nodes. After that, it was focused on a certain point locating at the interface between damage and fracture phenomena known as point *B*. The equivalent crack length is converging in the presence the densest mesh and the result was obtained with a low error (2.38 %) compared to the experimental value reported by (Mazars & Pijaudier-Cabot, 1996). Following that, the main objectives of the study have been satisfied.

Therefore, consider point *B*, the graphical representations of the damage variables in the case of non-local and localized states have been indicated. The profiles experience a smooth behaviour while the crack area accounted for the higher values. In the same way, the profiles of effective total stress and damaged stress were indicated.

To end this analysis, the RPIM irregular discretizations with 2165 nodes have been performed in order to observe the result when random nodal distribution is considered. It was done with regard to two different irregularity parameter ($\lambda = 10, \lambda = 5$). Afterwards,

the 11 basic irregular results have been gained if $\lambda = 10$ and the average solution has been compared to the similar regular discretization and experimental solutions. After that the analysis performs for the second irregularity parameter ($\lambda = 5$). All the results have been shown in a single figure to measure the differences. The non-local tensile, localized tensile and total damage have been plotted at the certain gauss point gp_c to observe the variation of damage phenomenon.

It must remarked that the compressive damage remains for zero value for all the analyses, since the total stress has not yet reached the maximum uniaxial compressive strength.

This study was conducted from damage to fracture mechanics. It means that the micro cracks are created in the damage phase first, once the fracture occurs, the micro cracks transform to the macro cracks. Hence at the end of the procedure, there might be failure of the material.

The irregular results show that the RPIM solution is not significantly sensitive to the irregularity parameter (λ) due to obtaining almost the same results for two different irregular studies.

8.3 Suggestions for Further Research

The present work would be helpful for those who are interested in numerical methods such as Finite Element Method and Meshless Method and most importantly in the field of continuum damage mechanics. In addition, it would be useful to study fracture mechanics since the continuum damage mechanics theory was linked to the fracture mechanics in an elegant way.

Precisely, the current job has the potential to be developed for the following topics:

1- Large deformation analysis useful for the concrete dams, bridges and reinforced concrete beams;
2- Composite materials; for example applicable for the aircrafts;
3- Damage in cellular materials particularly appropriate for the trabecular bones, (brittle material behavior);
4- Ductile damage material behavior for mostly metallic components such as rails, structural steel bridges.

Bibliography

Atluri, S. N., & Zhu, T. (1998). A new Meshless Local Petrov-Galerkin (MLPG) approach in computational mechanics. *Computational Mechanics*.

Bathe, K. (1982). *Finite Element Procedures in Engineering Analysis*. New Jersey: Prentice-Hall, Inc.

Bažant, Z., & Pijaudier-Cabot, G. (1989). Measurement of Characteristic Length of Nonlocal Continuum. *Engineering Mechanics*, *115(4)*, 755–767.

Belinha, J., Dinis, L. M. J. S., & Jorge, R. M. N. (2013). Composite laminated plate analysis using the natural radial element method. *Composite Structures*, *103*, 50–67.

Belinha, J., Dinis, L. M. J. S., & Natal Jorge, R. M. (2013a). Analysis of thick plates by the natural radial element method. *International Journal of Mechanical Sciences*, *76*, 33–48.

Belinha, J., Dinis, L. M. J. S., & Natal Jorge, R. M. (2013b). The natural radial element method. *Int. J. Numer. Methods Eng*, *93*(12), 1286–1313. http://doi.org/10.1002/nme

Belytschko, T., Lu, Y. Y., & Gu, L. (1994). Element-free Galerkin methods. *International Journal for Numerical Methods in Engineering*, *37*(2), 229–256. http://doi.org/10.1002/nme.1620370205

Bonet, J., & Wood, R. D. (2008). *Nonlinear Continuum Mechanics for Finite Element Analysis*. *Communications in Numerical Methods in Engineering* (Vol. 24). Cambridge University Press. http://doi.org/10.1017/CBO9780511755446

Cervera, M., Oliver, J., & Faria, R. (1995). Seismic evaluation of concrete dams via continuum damage models. *Earthquake Engineering & Structural Dynamics*, *24*(9), 1225–1245. http://doi.org/10.1002/eqe.4290240905

Cervera, M., Oliver, J., & Manzoli, O. (1996). A Rate-dependent Isotrpic Damage Model for Seismic Analysis of Concrete Dams. *Earthquake Engineering and Structural Dynamics*, *25*, 987–1010.

Chen, W. F., & Han, D. J. (1988). *Plasticity for Structural Engineers*. Springer-Verlag, New York. Retrieved from http://bookzz.org/book/2110763/6e84c1

Comi, C., & Perego, U. (2001). Fracture energy based bi-dissipative damage model for concrete. *International Journal Of Solids And Structures*, *38*(36-37), 6427–6454. http://doi.org/10.1016/S0020-7683(01)00066-X

Crisfield, M. A. (1991). *Non-Linear Finite Element Analysis of Solids and Structures, Essentials*. London: John Wiley & Sons Ltd.

Crisfield, M. A. (1996). *Non-linear Finite Element Analysis of Solids and Structures* (Vol. 2). Wiley.

Dinis, L. M. J. S., Jorge, R. M. N., & Belinha, J. (2007). Analysis of 3D solids using the natural neighbour radial point interpolation method. *Comput. Methods Appl. Mech. Eng.*, *196*(no. 13-16), 2009–2028.

Dinis, L. M. J. S., Jorge, R. M. N., & Belinha, J. (2010). A 3D shell-like approach using a natural neighbour meshless method: Isotropic and orthotropic thin structures. *Composite Structures*, *92*(5), 1132–1142.

Dinis, L. M. J. S., Natal Jorge, R. M., & Belinha, J. (2008). Analysis of plates and laminates using the natural neighbour radial point interpolation method. *Engineering Analysis with Boundary Elements*, *32*(3), 267–279.

Dinis, L. M. J. S., Natal Jorge, R. M., & Belinha, J. (2011). A natural neighbour meshless method with a 3D shell-like approach in the dynamic analysis of thin 3D structures. *Thin-Walled Struct.*, *49*(1), 185–196.

Faria, R. M. C. M. de. (1994). *Avaliação do comportamento sísmico de barragens de betão através de um modelo de dano contínuo*. Porto.

Faria, R., & Oliver, J. (1993). A rate dependent plastic-damage constitutive model for large scale computations in concrete structures. *CIMNE Monograph*, (17).

Faria, R., Oliver, J., & Cervera, M. (1998). A strain-based plastic viscous-damage model for massive concrete structures. *International Journal of Solids and Structures*.

Feenstra, P. H. (1993). *Computational aspects of biaxial stress in plain and reinforced concrete | Feenstra P. | digital library bookzz*. Delft University, the Netherlands. Retrieved from http://bookzz.org/book/494850/186515

Ferreira, A. J. M., Kansa, E. J., Fasshauer, G. E., & Leitao, V. M. A. (2009). *Progress on Meshless Methods, Computational Methods in Applied Sciences*. Springer.

Ferronato, M., Mazzia, A., Pini, G., & Gambolati, G. (2007). A meshless method for axi-symmetric poroelastic simulations : Numerical study. *International Journal for Numerical Methods in Engineering*, *70*, 1346–1365. http://doi.org/10.1002/nme

Fichant, S., La Borderie, C., & Pijaudier-Cabot, G. (1998). A comparative study of isotropic and anisotropic descriptions of damage in concrete structures. *Studies in Applied Mechanics*, *46*(C), 259–274. Retrieved from http://booksc.org/book/100745

Ford. (1963). *Advanced Mechanics of Materials*. London: Longmans.

Fung, Y., Tong, P., & Bechtel, S. (2003). Classical and Computational Solid Mechanics. *Applied Mechanics Reviews*.

Ghaffarzadeh, H. (2014). Assessment of Effective Parameters on Rbf-BASED Meshfree Method for Wave Propagation Modeling. In *the Latest Trends in Engineering Mechanics, Structures, Engineering Geology*. Salerno, Italy.

Ghaffarzadeh, H., & Mansouri, A. (2013). Numerical Modeling of Wave Propagation using RBF-based Meshless Method. In *Future Trends in Structural, Civil, Environmental and Mechanical Engineering*.

Gopalaratnam, V. S., & Shah, S. P. (1985). Softening response of plain concrete in direct tension. *Journal Proceedings*, *82*(3), 310–323. Retrieved from http://booksc.org/book/2649578

Hayati, A. N., Ahmadi, M. M., & Sadrnejad, S. A. (2012). Analysis of Axisymmetric Problems by Element-Free Galerkin Method. *International Journal of Modeling and Optimization*, *2*(6), 712–717. http://doi.org/10.7763/IJMO.2012.V2.217

He, W., Wu, Y.-F., Liew, K. M., & Wu, Z. (2006). A 2D total strain based constitutive model for predicting the behaviors of concrete structures. *International Journal of Engineering Science*, *44*(18-19), 1280–1303. http://doi.org/10.1016/j.ijengsci.2006.07.007

Idelsohn, S. R., & Pin, F. Del. (2003). The meshless finite element method. *International Journal for Numerical Methods in Engineering*, *58*(6), 893–912. http://doi.org/10.1002/nme.798

J. Belinha. (2014). *Meshless Methods in Biomechanics: Bone Tissue Remodelling Analysis* (Vol. 16). Springer Netherlands. Retrieved from http://bookzz.org/book/2348567/ccd9ed

Jankowiak, T., & Lodygowski, T. (2005). Identification of parameters of concrete damage plasticity constitutive model. *Foundations of Civil and Environmental …*, (6), 53–69. Retrieved from http://www.ikb.poznan.pl/fcee/2005.06/full/fcee_2005-06_053-069_identification_of_parameters_of_concrete.pdf

Jirásek, M. (1998). Nonlocal models for damage and fracture: Comparison of approaches. *International Journal of Solids and Structures*, *35*(31-32), 4133–4145. http://doi.org/10.1016/S0020-7683(97)00306-5

Ju, J. W. (1990). Isotropic and Anisotropic Damage Variables in Continuum Damage Mechanics. *Journal of Engineering Mechanics*.

Kachanov, L. M. (1986). *Introduction to Continuum Damage Mechanics*. Martinus Nijhoff Publishers, Dordrecht, the Netherlands.

Kansa, E. J. (1990a). Multiquadrics—A scattered data approximation scheme with applications to computational fluid-dynamics—I surface approximations and partial derivative estimates. *Computers & Mathematics with Applications*.

Kansa, E. J. (1990b). Multiquadrics—A scattered data approximation scheme with applications to computational fluid-dynamics—II solutions to parabolic, hyperbolic and elliptic partial differential equations. *Computers & Mathematics with Applications*.

Karsan, I. D., & Jirsan, J. O. (1969). Behavior of Concrete Under Compressive Loadings. *Journal of the Structural Devision*, *95*(ST12), 2543–2563.

Kazimi, S. M. A. (1982). *Solid Mechanics*. Tata McGraw-Hill.

Khan, A. R., Al-Gadhib, A. H., & Baluch, M. H. (2007). Elasto-damage Model for High Strength Concrete Subjected to Multiaxial Loading. *International Journal of Damage Mechanics*. http://doi.org/10.1177/1056789506065914

Krajcinovic, D., & Fonseka, G. (1981). the Continuum Damage Theory of Britle Materials, Part 1: General Theroy. *ASME Journal of Applied Mechanics*, *48*, 809–815.

Krajcinovic, D., & Fonseka, G. (1983). the Continuum Damage theory for Brittle Material. *ASME Journal of Applied Mechanics*, *50*, 355–360.

Kupfer, H., Hilsdorf, H. K., & Rusch, H. (1969). Behavior of Concrete Under Biaxial Stresses. *Journal of the American Concrete Institute*, *66*(8), 656–666. Retrieved from http://www.concrete.org/publications/internationalconcreteabstractsportal.aspx?m=details&i=7388

La Borderie, C., Berthaud, Y., & Pijaudier-Cabot, G. (1990). Crack closure effect in continuum damage mechanics. numerical implementation. In *Second International Conference, At Zell am See* (p. COMPUTER AIDED ANALYSIS AND DESIGN OF CONCRETE STR).

Labadi, Y., & Hannachi, N. E. (2005). Numerical Simulation of Brittle Damage in Concrete. *Strength of Materials*, 268–281.

Lee, J., & Fenves, G. L. (1998). Plastic-Damage Model for Cyclic Loading of Concrete Structures. *Journal of Engineering Mechanics*.

Lee, J., & Fenves, G. L. (2001). A return-mapping algorithm for plastic-damage models: 3-D and plane stress formulation | Jeeho Lee; Gregory L. Fenves | digital library booksc. *International Journal for Numerical Methods in Engineering*, *50*(2), 487–506. http://doi.org/10.1002/1097-0207(20010120)50:23.0.

Legendre, J. (1984). *Prevision de la ruine des structures en beton par une approche combinee : mecanique de l'endommagement-mecanique de la rupture.* Universite Paris 6 - LMT Cachan.

Liew, K. M., Zhao, X., & Ferreira, A. J. M. (2011). A review of meshless methods for laminated and functionally graded plates and shells. *Composite Structures*, *93*(8), 2031–2041. http://doi.org/10.1016/j.compstruct.2011.02.018

Liu, G. R. (2001). A point assembly method for stress analysis for two-dimensional solids. *International Journal of Solids and Structures*, *39*(1), 261–276.

Liu, G. R. (2009). *Mesh Free Methods, Moving beyond the Finite Element Method* (2nd ed.). Boca Raton: CRC Press LLC.

Liu, G. R., & Gu, Y. T. (2001). A point interpolation method for two-dimensional solids. *International Journal for Numerical Methods in Engineering*, *50*(4), 937–951.

Liu, G. R., Jiang, Y., Chen, L., Zhang, G. Y., & Zhang, Y. W. (2011). A singular cell-based smoothed radial point interpolation method for fracture problems. *Computers and Structures*, *89*(13-14), 1378–1396.

Liu, G. R., Zhang, G. Y., Wang, Y. Y., Zhong, Z. H., Li, G. Y., & Han, X. (2007). A nodal integration technique for meshfree radial point interpolation method (NI-RPIM). *International Journal of Solids and Structures*, *44*(11-12), 3840–3860.

Liu, W. K., Jun, S., & Zhang, Y. F. (1995). Reproducing kernel particle methods. *International Journal for Numerical Methods in Fluids*, *20*(8-9), 1081–1106. http://doi.org/10.1002/fld.1650200824

Lowes, L. N. (1999). Finite Element Modeling of Reinforced Concrete Beam-Column Bridge Connections_Chapter 5. *PhD Thesis*, 4–6.

Lubliner, J. (1972). On the thermodynamic foundations of non-linear solid mechanics. *International Journal of Non-Linear Mechanics*.

Malvar, J., & Warren, G. (1988). Fracture Energy for Three-Point Bend Tests on Single-Edge Notched Beams. *Naval Civil Engineering Laboratory*, (March), 1–28. Retrieved from http://booksc.org/book/12505223

Mazars, J., & Pijaudier-Cabot, G. (1989). Continuum Damage Theory —Application to Concrete. *Journal of Engineering Mechanics*, *115*(2), 345–365.

Mazars, J., & Pijaudier-Cabot, G. (1996). From damage to fracture mechanics and conversely: A combined approach. *International Journal of Solids and Structures*, *33*(20-22), 3327–3342. http://doi.org/10.1016/0020-7683(96)00015-7

Murakami, S. (1983). Notion of Continuum Damage Mechanics and its Application to Anisotropic Creep Damage Theory. *Journal of Engineering Materials and Technology*.

Nayroles, B., Touzot, G., & Villon, P. (1992). Generalizing the finite element method: Diffuse approximation and diffuse elements. *Computational Mechanics*, *10*(5), 307–318.

Nguyen, G. D., & Houlsby, G. T. (2008). A coupled damage-plasticity model for concrete based on thermodynamic principles: Part I: Model formulation and parameter identification. *International Journal for Numerical and Analytical Methods in Geomechanics*, *32*(4), 353–389.

Nguyen, V. P., Rabczuk, T., Bordas, S., & Duflot, M. (2008). Meshless methods: A review and computer implementation aspects. *Mathematics and Computers in Simulation*.

O. C. Zienkiewicz and R. L. Taylor. (1994). *The Finite Element Method* (4th ed.). London: McGraw-Hill Book Company Europe.

Oliver, J., Cervera, M., Oller, S., & Lubliner, J. (1990). Isotropic Damage Models and Smeared Crack Analysis of Concrete. In *the 2nd Conference on Computer Aided Analysis and Design of Concrete Structures* (pp. 945–957). Zell am See.

Oñate, E., Idelsohn, S., Zienkiewicz, O. C., & Taylor, R. L. (1996). A finite point method in computational mechanics. Applications to convective transport and fluid flow. *International Journal for Numerical Methods in Engineering*, *39*, 3839–3866.

Raju, I. S., & Chen, T. (2001). Meshless Petrov-Galerkin method applied to axisymmetric problems. *American Institute of Aeronautics and Astronautics*, *1253*, 1–12.

Raju, I. S., & Chen, T. (2003). A Computationally Efficient Meshless Local Petrov-Galerkin Method for Axisymmetric Problems. *American Institute of Aeronautics and Astronautics*, *1673*, 1–14.

Randles, P. W., & Libersky, L. D. (1996). Smoothed Particle Hydrodynamics: Some recent improvements and applications. *Computer Methods in Applied Mechanics and Engineering*, *139*(1–4), 375–408. Retrieved from http://www.sciencedirect.com/science/article/pii/S0045782596010900\nhttp://www.sciencedirect.com/science/article/pii/S0045782596010900/pdf?md5=34ab4ea19bb6ae930e08da51d979019d&pid=1-s2.0-S0045782596010900-main.pdf

Resende, L., & Martin, J. (1984). A Progressive Damage Continuum Model for Granular Materials. *Computer Methods in Applied Mechanics and Engineering*, *42*, 1–18.

Roth, S.-N., Léger, P., & Soulaïmani, A. (2015). A combined XFEM–damage mechanics approach for concrete crack propagation. *Computer Methods in Applied Mechanics and Engineering*, *283*, 923–955. http://doi.org/10.1016/j.cma.2014.10.043

Salari, M. R., Saeb, S., Willam, K. J., Patchet, S. J., & Carrasco, R. C. (2004). A coupled elastoplastic damage model for geomaterials. *Computer Methods in Applied Mechanics and Engineering*, *193*(27-29), 2625–2643.

Shao, J. F., Jia, Y., Kondo, D., & Chiarelli, A. S. (2006). A coupled elastoplastic damage model for semi-brittle materials and extension to unsaturated conditions. *Mechanics of Materials*, *38*(3), 218–232. http://doi.org/10.1016/j.mechmat.2005.07.002

Simo, J. C. (1992). Algorithms for static and dynamic multiplicative plasticity that preserve the classical return mapping schemes of the infinitesimal theory. *Computer Methods in Applied Mechanics and Engineering*.

Simo, J. C., & Ju, J. W. (1987). Strain- and stress-based continuum damage models - I. Formulation. *International Journal of Solids and Structures*, *23*(7), 821–840. Retrieved from http://www.sciencedirect.com/science/article/pii/0020768387900837

Simo, J., & Taylor, R. (1986). A return mapping algorithm for plane stress elastoplasticity. *International Journal for Numerical ...*, *22*(3), 649–670. Retrieved from http://doi.wiley.com/10.1002/nme.1620220310\nhttp://onlinelibrary.wiley.com/doi/10.1002/nme.1620220310/abstract

Sladek, V., Sladek, J., & Zhang, C. (2008). Local integral equation formulation for axially symmetric problems involving elastic FGM. *Engineering Analysis with Boundary Elements*, *32*(12), 1012–1024. http://doi.org/10.1016/j.enganabound.2007.09.006

Sumarac, D., Sekulovic, M., & Krajcinovic, D. (2003). Fracture of Reinforced Concrete Beams Subjected to Three Point Bending. *International Journal of Damage Mechanics*.

Tao, X., & Phillips, D. V. (2005). A simplified isotropic damage model for concrete under bi-axial stress states. *Cement and Concrete Composites*, *27*(6), 716–726.

Timoshenko, S., & Woinowsky-Krieger, S. (n.d.). *Theory of Plates and Shells* (2nd ed.). New York: McGraw-Hill International Editions.

Timoshenko, S., & Woinowsky-Krieger, S. (n.d.). *Theory of Plates and Shells* (2sd ed.). New York: McGraw-Hill International Editions.

Voyiadjis, G., & Taqieddin, Z. (2009). Elastic Plastic and Damage Model for Concrete Materials: Part I-Theoretical Formulation. *International Journal of Structural Changes in Solids*, *1*(1), 31–59. Retrieved from https://journals.tdl.org/IJSCS/article/view/2313/0

Wang, J. G., & Liu, G. R. (2002a). A point interpolation meshless method based on radial basis functions. *International Journal for Numerical Methods in Engineering*, *54*(11), 1623–1648.

Wang, J. G., & Liu, G. R. (2002b). On the optimal shape parameters of radial basis functions used for 2-D meshless methods. *Computer Methods in Applied Mechanics and Engineering*, *191*(23-24), 2611–2630.

Wang, J. G., Liu, G. R., & Wu, Y. G. (2001). A point interpolation method for simulating dissipation process of consolidation. *Computer Methods in Applied Mechanics and Engineering*, *190*(45), 5907–5922.

Willam, K., Rhee, I., & Beylkin, G. (2001). Multiresolution analysis of elastic degradation in heterogeneous materials. *Meccanica*, *36*(1), 131–150. Retrieved from <Go to ISI>://WOS:000171148000010

Wu, C. T., Hu, W., & Guo, Y. (2014). the Recent Update of LS-DYNA Meshfree and Advanced FEM for Manufacturing Application. *Livermore Software Technology Corporation, LS-DYNA Forum, Bamberg,*.

Wu, J. Y., Li, J., & Faria, R. (2006). An energy release rate-based plastic-damage model for concrete. *International Journal of Solids and Structures*, *43*(3-4), 583–612.

Yu, R. C., Ruiz, G., & Chaves, E. W. V. (2008). A comparative study between discrete and continuum models to simulate concrete fracture. *Engineering Fracture Mechanics*, *75*(1), 117–127. Retrieved from http://www.sciencedirect.com/science/article/pii/S0013794407001567#

Zhao, X., Liu, G. R., Dai, K. Y., Zhong, Z. H., Li, G. Y., & Han, X. (2008). A linearly conforming radial point interpolation method (LC-RPIM) for shells. *Comput. Mech.*, *43*(3), 403–413.

Zhao, X., Liu, G. R., Dai, K. Y., Zhong, Z. H., Li, G. Y., & Han, X. (2009). Free-vibration analysis of shells via a linearly conforming radial point interpolation method (LC-RPIM). *Finite Elements in Analysis and Design*, *45*(12), 917–924.